Mobilization of terrestrial organic matter from thawing Arctic permafrost regions: Insights from lignin-derived phenols and their compound-specific radiocarbon ages

Kumulative Dissertation

zur Erlangung des akademischen Grades

eines Doktors der Naturwissenschaften

-Dr. rer. nat.-

am Fachbereich Geowissenschaften

der Universität Bremen

vorgelegt von

Mengli Cao

Bremerhaven, 2023

Gutachter der Dissertation:

Prof. Dr. Gesine Mollenhauer

Dr. Tommaso Tesi

Ph.D. Colloquium

Permafrost OC mobilization Permafrost OC mobilization from two sub-Arctic river catchments under climate warming: Lessons learned from lignin biomarkers.

November 10, 2023

Versicherung an Eides Statt / *Affirmation in lieu of an oath*

gem. § 5 Abs. 5 der Promotionsordnung vom 18.06.2018 /

according to § 5 (5) of the Doctoral Degree Rules and Regulations of 18 June, 2018

Ich / I, Mengli cao

(Vorname / First *Name*, Name / *Name*, Anschrift / *Address*, ggf. Matr.-Nr. / *student ID no., if applicable)*

versichere an Eides Statt durch meine Unterschrift, dass ich die vorliegende Dissertation selbständig und ohne fremde Hilfe angefertigt und alle Stellen, die ich wörtlich dem Sinne nach aus Veröffentlichungen entnommen habe, als solche kenntlich gemacht habe, mich auch keiner anderen als der angegebenen Literatur oder sonstiger Hilfsmittel bedient habe und die zu Prüfungszwecken beigelegte elektronische Version (PDF) der Dissertation mit der abgegebenen gedruckten Version identisch ist. / *With my signature I affirm in lieu of an oath that I prepared the submitted dissertation independently and without illicit assistance from third parties, that I appropriately referenced any text or content from other sources, that I used only literature and resources listed in the dissertation, and that the electronic (PDF) and printed versions of the dissertation are identical.*

Ich versichere an Eides Statt, dass ich die vorgenannten Angaben nach bestem Wissen und Gewissen gemacht habe und dass die Angaben der Wahrheit entsprechen und ich nichts verschwiegen habe. */ I affirm in lieu of an oath that the information provided herein to the best of my knowledge is true and complete.*

Die Strafbarkeit einer falschen eidesstattlichen Versicherung ist mir bekannt, namentlich die Strafandrohung gemäß § 156 StGB bis zu drei Jahren Freiheitsstrafe oder Geldstrafe bei vorsätzlicher Begehung der Tat bzw. gemäß § 161 Abs. 1 StGB bis zu einem Jahr Freiheitsstrafe oder Geldstrafe bei fahrlässiger Begehung. / *I am aware that a false affidavit is a criminal offence which is punishable by law in accordance with § 156 of the German Criminal Code (StGB) with up to three years imprisonment or a fine in case of intention, or in accordance with § 161 (1) of the German Criminal Code with up to one year imprisonment or a fine in case of negligence.*

Bremerhaven, 15/11/2023

Ort / *Place*, Datum / *Date*

Unterschrift / *Signature*

TABLE OF CONTENT

Abstract

Global climate change is expected to have a huge impact on Arctic warming, leading to an increased remobilization of permafrost organic carbon. More than twice as much carbon as in the atmosphere is contained in permafrost soils, and may upon destabilization expose large amounts of organic matter to microbial degradation and release climate-forcing greenhouse gases. As an important link in the land-ocean continuum, rivers are important pathways for permafrost OC remobilization. Arctic ocean sediments are thus receptors of terrestrial OC remobilization for a large part of the circum-Arctic drainage basin and offer an archive to study past terrestrial OC remobilization as during the last deglaciation.

This thesis studies terrestrial OC in sub-Arctic ocean sediments to study OC remobilization from permafrost regions across temporal and spatial scales. A detailed study of two sediment cores from the Bering Sea and Okhotsk Sea, allowed the reconstruction of vegetation development, permafrost OC mobilization, and transport pathways of permafrost OC remobilization during the last deglaciation. Vegetation development and permafrost OC remobilization have been investigated by analyses of the mass accumulation rate of terrestrial biomarkers (lignin phenols and lipids). To study the influence of climatic conditions on the stability of inland permafrost soils, the sea surface temperature of the Bering Sea was investigated (TEX^{L}_{86}). For the study of terrestrial OC remobilization from different carbon pools, compound-specific radiocarbon analysis (CSRA) was applied to terrestrial compounds (lignin-derived phenols). A modified method for the purification of lignin-derived phenols was used for CSRA.

Downcore records of lignin flux from the Yukon and Amur basins covering the early deglaciation to the Holocene are discussed in the first study. It was found that vegetation change and permafrost remobilization occurred earlier in the Yukon than in the Amur basin. The retreat of sea ice coupled with increased sea surface temperatures in the Bering Sea and adjacent ocean areas during the early deglaciation (19.0-14.6 kyr) might have promoted early permafrost mobilization. The results reveal that lipids and lignin might have been delivered to the ocean by identical processes, i.e., runoff and erosion, which is not consistent with previous studies of modern Arctic river systems.

A simplified procedure for the purification of lignin phenols based on the published method by Feng et al., (2013b) and an evaluation of the fraction of modern carbon ($F^{14}C$) and the mass of the associated procedural blank is described in the second study. Lignin phenols were purified only by one HLB SPE cartridge (Waters Oasis, 200 mg, 6 mL). Samples were eluted from the HLB cartridge with 60 mL ethyl acetate to achieve a clean-up of lignin-derived phenols. Single compound separation and collection was achieved by HPLC on a

Phenomenex Synergi Polar-RP column at 40 °C. The blank carbon contribution of the entire method, as determined with reference compounds, was found to be 4.17 ± 0.35 μgC with an $F^{14}C$ of 0.55 ± 0.04.

In the third study, the revised method of lignin purification was applied to obtain first downcore CSRA records of lignin-derived phenols from sediment cores retrieved off the Yukon and Amur Basins. The radiocarbon ages of phenols from sediments of the Bering and Okhotsk Seas are expected to reflect inputs from at least two different terrigenous sources that are characterized by different ages and degradation degrees during the last deglaciation. The age offsets between lignin phenols and fatty acids were controlled by surface discharge in the Yukon and Amur Basins. Deep OC enriched in long-chain lipids can be mobilized both through coastal erosion and thawing of inland thermokarst which can be transported to marine sediments by surface runoff in the last deglaciation. The radiocarbon ages of lignin phenols and long-chain fatty acids are controlled by processes that are affected by climate change, and the ^{14}C age offset between lipids and lignin phenols can be used as palaeo-proxy for these changing processes.

The fourth study investigates lignin phenols flux and radiocarbon ages in short cores off the Lena River, covering the last century. The vegetation in the Lena Basin is a mixture of woody gymnosperm and non-woody angiosperm sources and has not changed significantly in the past century. Young and old terrigenous carbon pools both affect the $\Delta^{14}C$ values of phenols in the two sediment cores. The $\Delta^{14}C$ values of lignin phenols in shallow Laptev Sea sediments may be treated as an indicator of runoff.

This thesis highlights the vulnerability of permafrost OC to Arctic warming over time and space, thus contributing to a better understanding of climate-carbon couplings in the Earth system.

Zusammenfassung

Es wird erwartet, dass der globale Klimawandel enorme Auswirkungen auf die Erwärmung der Arktis haben wird, und zur verstärkten Remobilisierung von im Permafrost gespeichertem organischen Kohlenstoff (OC) führen kann. Permafrostböden enthalten mehr als doppelt so viel Kohlenstoff wie die vorindustrielle Atmosphäre, und die Destabilisierung von Permafrostböden könnte große Mengen organischer Materie für mikrobiellen Abbau verfügbar machen und Treibhausgase freisetzen. Als wichtiges Bindeglied im Land-Ozean-Kontinuum sind Flüsse von entscheidender Bedeutung für die Remobilisierung von OC aus dem Permafrost. Der durch arktische Flüsse remobilisierte terrestrische OC wird während des Transportes teilweise abgebaut, wodurch Treibhausgase freigesetzt werden, während der verbleibende Teil in den Arktischen Ozean exportiert und in Meeresbecken abgelagert wird. Arktische und subarktische Ozeansedimente sind somit Empfänger für terrestrischen OC aus einem großen Teil des zirkumarktischen Einzugsgebiets und bieten ein Archiv für die Untersuchung früherer terrestrischer OC-Remobilisierung, wie beispielsweise während der letzten Deglaziation.

Diese Dissertation untersucht terrestrischen OC in subarktischen Schelfsedimenten, um die OC-Remobilisierung aus Permafrostregionen über zeitliche und räumliche Skalen hinweg zu verstehen. Eine detaillierte Untersuchung von zwei Sedimentkernen aus dem Beringmeer und dem Ochotskischen Meer erlaubte es, die Vegetationsentwicklung, die Mobilisierung und die Transportwege von Permafrost-OC während der letzten Deglaziation zu rekonstruieren. Die Vegetationsentwicklung und die OC-Remobilisierung wurden anhand der Massenakkumulationsraten terrestrischer Biomarker (Lignin-Phenole und Lipide) beschrieben. Um den Einfluß klimatischer Bedingungen auf die Stabilität von Permafrostböden im Landesinneren zu untersuchen, wurde die Oberflächentemperatur des Beringmeeres rekonstruiert (TEX^{L}_{86}). Zur Untersuchung der terrestrischen OC-Remobilisierung aus verschiedenen Kohlenstoffpools wurden komponentenspezifische Radiokarbonanalysen (CSRA) von Lignin-Phenolen durchgeführt. Dafür wurde eine modifizierte Methode zur Aufreinigung der Phenole angewandt.

Downcore-Aufzeichnungen der Ligninflüsse in die Yukon- und Amur-Becken, die die frühe Deglaziation bis zum Holozän umfassen sind in der ersten Studie diskutiert. Es zeigte sich, dass Vegetationsveränderungen und Permafrostremobilisierung im Yukon-Becken früher auftraten als im Amur-Becken. Der Rückgang des Meereises in Verbindung mit steigenden Oberflächentemperaturen im Beringmeer und angrenzenden Meeresgebieten während der frühen Deglaziation (19,0–14,6 ka) könnten eine frühere Permafrostmobilisierung gefördert haben. Die Ergebnisse zeigen, dass Lipide und Lignin möglicherweise durch identische

Prozesse, nämlich Abfluss und Erosion, in den Ozean gelangt sind, was im Widerspruch zu früheren Studien moderner arktischer Flusssysteme steht.

Die zweite Studie beschreibt ein vereinfachtes Verfahren zur Aufreinigung von Lignin-Phenolen, basierend auf der von Feng et al. (2013b) veröffentlichten Methode und bewerten den Anteil an modernem Kohlenstoff ($F^{14}C$) und die Masse des zugehörigen Verfahrensblanks. Lignin-Phenole zur ersten Trennung nur durch eine HLB-SPE-Kartusche gereinigt. Die Proben wurden mit 60 mL Ethylacetat von der HLB-Kartusche eluiert um eine Aufreinigung der Ligninphenole zu erreichen. Die Trennung und Sammlung einzelner Komponenten erfolgte im Anschluss mittels Hochdruckflüssigkeitschromatographie (HPLC) auf einer Phenomenex Synergi Polar-RP-Säule bei 40 °C. Der Kohlenstoffblank der gesamten Methode wurde mit Referenzkomponenten als 4,17 ± 0,35 mgC und einen $F^{14}C$ Wert von 0,55 ± 0,04 bestimmt.

In der dritten Studie wurde die modifizierte Aufreinigungsmethode angewendet um erste Downcore-CSRA-Daten von Lignin-Phenolen aus Sedimentkernen des Yukon- und Amur-Beckens zu erhalten. Die Radiokohlenstoffalter von Phenolen in den Sedimenten aus dem Bering- und Ochotskischen Meer spiegeln vermutlich Einträge aus mindestens zwei verschiedenen terrigenen Quellen wider, die sich durch ein unterschiedliches Alter und einen unterschiedlichen Abbaugrad während der letzten Enteisung auszeichnen. Der Altersunterschied zwischen Ligninphenolen und Fettsäuren wurde durch Oberflächenabfluss im Yukon- und Amur-Becken kontrolliert. Mit langkettigen Lipiden angereichertes tiefes OC kann sowohl durch Küstenerosion als auch durch auftauenden Thermokarst im Landesinneren mobilisiert werden und durch Oberflächenabfluss bei der letzten Enteisung in Meeressedimente transportiert werden. Das Radiokarbonalter von Ligninphenolen und langkettigen Fettsäuren wird durch Prozesse bestimmt die durch den Klimawandel beeinflusst sind. Der ^{14}C-Altersversatz zwischen Lipiden und Ligninphenolen kann als Paläo-Proxy für diese wechselnden Prozesse verwendet werden.

Die vierte Studie untersucht den Fluss von Ligninphenolen und das Alter von Radiokohlenstoff in kurzen Bohrkernen vor dem Fluss Lena und deckt das letzte Jahrhundert ab. Die Vegetation im Lena-Becken ist eine Mischung aus holzigen Gymnospermen und nichtholzigen Angiospermen und hat sich im letzten Jahrhundert nicht wesentlich verändert. Sowohl junge als auch alte terrigene Kohlenstoffvorkommen beeinflussen die $\Delta^{14}C$-Werte von Phenolen in den beiden Sedimentkernen. Die $\Delta^{14}C$-Werte von Ligninphenolen in flachen Sedimenten der Laptewsee können als Indikator für den Abfluss betrachtet werden.

Diese Dissertation zeigt die Anfälligkeit von Permafrost-OC gegenüber der Erwärmung der Arktis auf und trägt so zu einem besseren Verständnis der Klima-Kohlenstoffkreislauf-Kopplungen im Erdsystem bei.

1. Introduction

1.1. Modern Arctic and its role in the global climate system

The Arctic is a polar region located in the northernmost part of the Earth. The area can be defined as north of the Arctic Circle (about 66° 34' N), the approximate southern limit of the midnight sun and the polar night (Fig. 1.1). The Arctic is characterized by cold winters and cool summers. The average winter temperatures in the Arctic can go as low as -40 °C, and the coldest recorded temperature is approximately -68 °C. The land within the Arctic region has seasonally varying snow and ice cover, with predominantly treeless permafrost containing tundra. Arctic vegetation is composed of plants, such as dwarf shrubs, graminoids, herbs, lichens, and mosses, which all grow relatively close to the ground. Trees cannot grow in the Arctic, but in its warmest parts, shrubs are common; sedges, mosses and lichens can form thick layers. In the coldest parts of the Arctic, much of the ground is bare; non-vascular plants such as lichens and mosses predominate, along with a few scattered grasses and forbs.

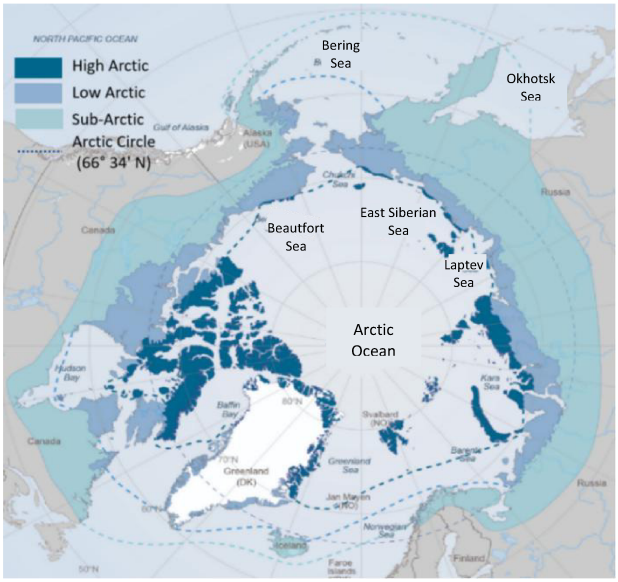

Figure 1.1 Map of the Arctic and sub-Arctic (source: Arctic Biodiversity Trends 2010: Selected indicators of change report by the Conservation of Arctic Flora and Fauna (CAFF), *https://arcticportal.org/maps/download/arctic-definitions/2425-arctic-sub-regions*).

The sub-Arctic zone is a region in the Northern Hemisphere immediately south of the Arctic (Fig. 1.1), north of humid continental regions and covering much of Alaska, Canada, Iceland, the north of Scandinavia, Siberia, and the Cairngorms. Generally, sub-Arctic regions fall between 50° N and 70° N latitude, depending on local climates. Subarctic temperatures are above 10 °C for at least one and at most three months of the year. Precipitation tends to be low due to the low moisture content of the cold air, and vegetation is characteristic of

the taiga. Even though the diversity may be low, the area and numbers are high, and the taiga (boreal) forest is the largest forest biome on the planet, with most of the forests located in Russia and Canada.

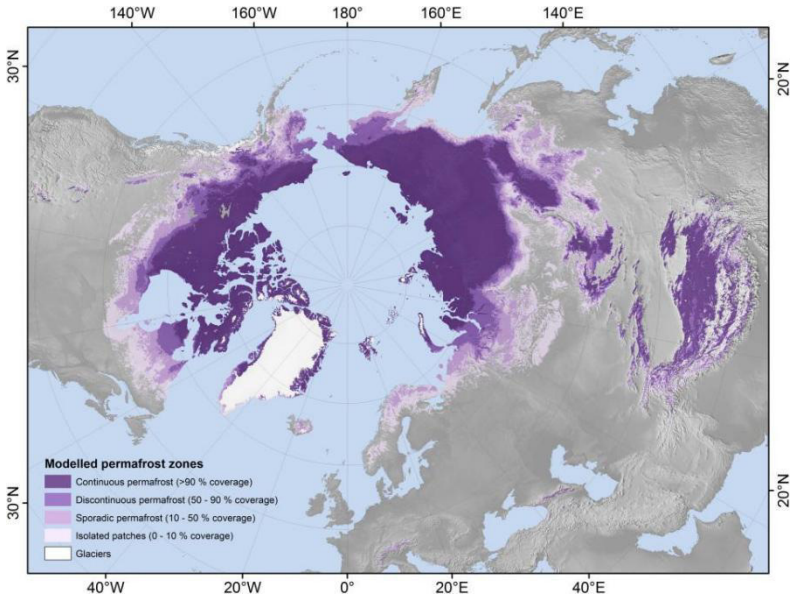

Figure 1.2. Extent of permafrost on the Northern Hemisphere (Obu et al., 2019).

Aside from the low temperature, the Arctic is unique in comparison to other world regions, as most of the terrestrial surface around the Arctic Ocean is covered by permafrost. Permafrost is defined as frozen ground, such as soil, rock, and ice, which remains colder than 0 ℃ for at least 2 consecutive years (Washburn, 1980). The permafrost distribution is controlled by long-term mean air temperature, so permafrost distributes primarily in high latitudes, at high elevations, and in the bottom of shallow shelf of the Arctic Ocean (submarine permafrost). Based on the proportion of the land area underlain by frozen material, permafrost regions can be divided into four types: continuous permafrost with ＞90% coverage, discontinuous permafrost with 50–90% coverage, sporadic permafrost with 10–50% coverage, and isolated permafrost has ＜10% coverage (FAO and ITPS, 2021, Fig. 1.2). Permafrost underlies ~ 25% of the Northern Hemisphere (Olefeldt et al., 2016; Obu et al., 2019; Overduin et al., 2019). The majority of Arctic permafrost has been present since the Pleistocene or the Last Glacial Maximum (LGM) (Froese et al., 2008; Mackelprang et al. 2017; Abramov et al., 2021). The depth of permafrost is a first-order approximation of age, where deeper layers were deposited further in the past (Miner et al., 2021).

Global warming is one of the most important challenges that humans are facing in the 21st century. Climate change has caused increasingly irreversible losses in terrestrial, freshwater and coastal and open ocean marine ecosystems. If global warming increase by 2 ℃ in the coming decades of this century, snowmelt water availability for irrigation is projected to

decline in some snowmelt water dependent river basins by up to 20%, and global glacier mass loss of 18 ± 13% (IPCC, 2022). Since 2000, Arctic temperatures have risen about twice as fast as global temperatures (Fig. 1.3). Arctic amplification—more intense warming in the Arctic than the rest of the globe—is consistent with both theoretical understanding of Earth's climate system and model projections of global warming. With melting sea ice and decreasing snow cover, warming in the Arctic regions causes more sunlight to be absorbed, which allows for more warming. Arctic ecosystems are thus likely to be more severely affected by warming than other regions on earth.

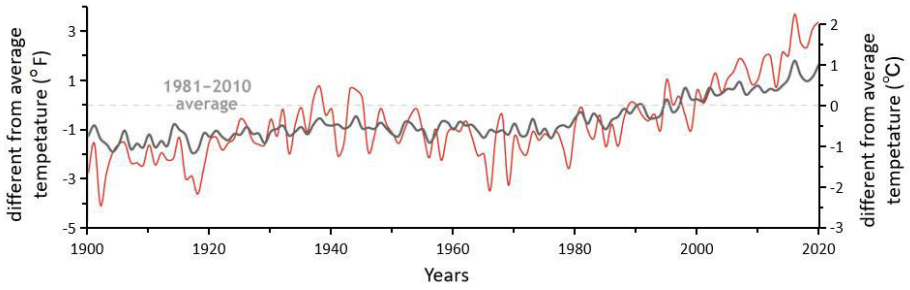

Figure 1.3 Yearly temperatures over the Arctic (red) and the entire globe (gray) compared to the 1981–2010 average (source: NOAA Climate.gov, *https://www.climate.gov/media/11762*).

1.2. Permafrost OC in the Arctic regions

Permafrost consists with a combination of soil, rocks and sand that are held together by ice. Near the surface, permafrost soils contain large quantities of organic carbon (OC), and lower permafrost layers contain soils made mostly of minerals. The cold temperature and unique processes of permafrost have led to the accumulation of large stocks of soil OC in permafrost regions (Hugelius et al., 2014). The OC stored in Arctic permafrost regions is about 1300 ± 200 Gt (Hugelius et al., 2014; Schuur et al., 2015) which means although the permafrost regions account for only 22% of global soil area (Obu et al., 2019), they contain ＞42% of carbon storage in global soil (Schuur et al., 2015; Jackson et al., 2017). About one third of Arctic permafrost OC is present in the uppermost meter, while the larger part is locked in frozen sediments below 3 m depth (Hugelius et al., 2014) of which about one third is stored in silty to fine sandy deposits called Yedoma or Ice Complex deposit (ICD) (Schirrmeister et al., 2011; Strauss et al., 2017). ICD was deposited in unglaciated areas of the circum-Arctic region during the late Pleistocene, and widespread in Beringia (Schirrmeister et al., 2013) (Fig. 1.4). The ICD is characterized by very high ground ice content (40–60 wt% absolute) (Schirrmeister et al., 2010). The mean OC contents of ICD, typically 2–5% (Schirrmeister et al., 2011; Strauss et al., 2013), are higher and more decomposable than in most thawed

mineral soils because fresh organic inputs from the tundra-steppe ecosystem were buried and frozen into rapidly accumulating sediment (Zimov et al., 2006).

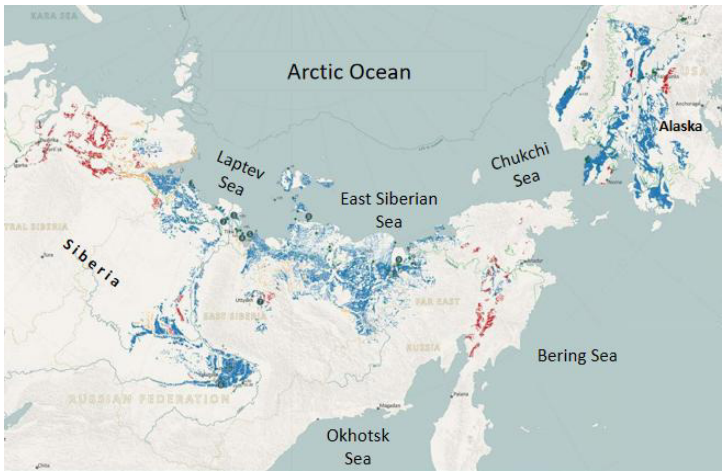

Figure 1.4 Yedoma in Northern Hemisphere distribution and spatial distribution of the confidence classes: confirmed (blue), likely (orange) and uncertain (red) (Strauss et al., 2021, *https://apgc.awi.de*).

There is widespread evidence and documentation of recent permafrost thawing. Since the 1980s, permafrost near the depth of zero annual amplitude has warmed by 1 to 3 °C in some Arctic regions (Smith et al., 2022). Given that permafrost is a key component of Arctic landscapes, any changes can have substantial consequences for natural systems. For instance, the warming and the subsequent thawing of permafrost can affect landscape stability, causing subsidence of the ground surface, slope instability, rock glacier acceleration and changes to hydrological processes (Gruber and Haeberli, 2007; Kokelj and Jorgenson, 2013; Marcer et al., 2021). A major concern is the potential role that permafrost thaw will play in causing feedback to climate change, given the sheer size of the permafrost region soil carbon pool, which is 55–68% greater than the atmospheric OC pool in 2020 (Friedlingstein et al., 2020). The melting of ground ice causes structural sediment collapse and thus exposes ancient sedimentary organic matter to microbial degradation that could increase emissions of CO_2 and CH_4 to the atmosphere (Schuur et al., 2008; Nitze et al., 2018; Turetsky et al., 2020). CO_2 and CH_4 are the most influential long-lived greenhouse gases (Schuur et al., 2015; Voigt et al., 2020). A comprehensive synthesis estimated that CO_2 and CH_4 emissions from thawing permafrost across the Arctic region could release between 5 and 15% from the permafrost carbon pool over decades and centuries under business-as-usual warming scenarios (representative concentration pathway 8.5) (Schuur et al., 2015, 2022). This proportion is equivalent to a cumulative 67–237 Pg C by 2100 (Schneider von Deimling et al., 2015; Schuur et al., 2022). This magnitude of the annual release of ~ 0.5–2 Pg C per year causes a positive feedback loop to climate change and constitutes one important 'tipping element' of the climate system (Lenton et al., 2019). CO_2 concentrations in the atmosphere are projected

to be between 530 and 980 ppm by 2100 based on current trends (Forster et al., 2007). The Bering Sea winter sea ice would be lost by the time atmospheric concentrations reach 685 ppm, which would be reached in ~ 2080 (Jones et al., 2020a).

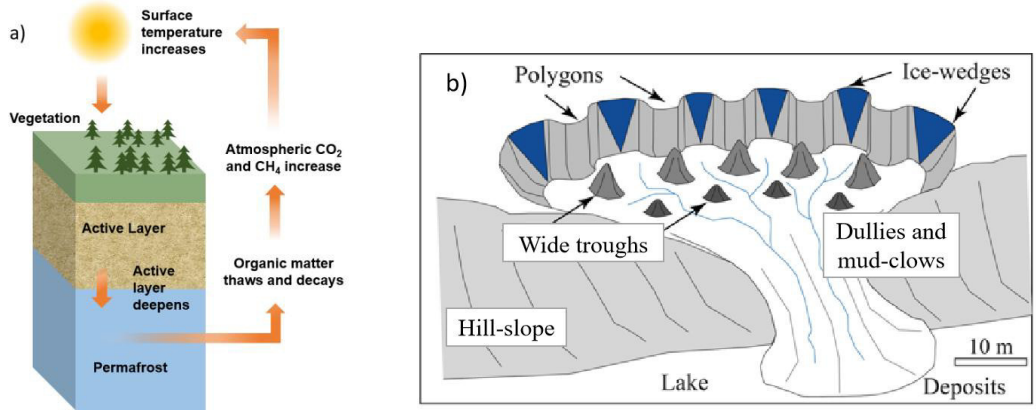

Figure 1.5 a) The permafrost carbon feedback is an amplification of surface warming due to the thaw of organic material currently frozen in permafrost, which will then decay and release CO_2 and CH_4 into the atmosphere (adapted from UNEP, *https://www.unep.org/resources/report/policy-implications-warming-permafrost*). b) The melting of ice wedges along the banks of thermokarst lakes forms highly degraded conical polygons with wide troughs in eastern Siberia (Costard et al., 2020).

1.3. Remobilization of permafrost OC

Permafrost thawing due to climate change can occur through gradual deepening of the active layer, through the development of thermokarst landforms in lowlands and wetlands, and by thermo-erosion along coasts, river banks and lake shores (Grosse et al., 2011; Schuur et al., 2015; Olefeldt et al., 2016; Strauss et al., 2017).

A layer of soil on top of permafrost does not stay frozen all year long. This layer is called the active layer (Fig. 1.5a). In the colder regions, the ground rarely thaws even in the summer. There, the active layer is very thin—only 10 to 15 centimeters. In the warmer permafrost regions, the active layer can achieve several meters thick. The top-down thawing is by long-term thickening of the surface layer on the top of permafrost subjects to seasonal thawing and freezing (Hinkel and Nelson, 2003). Deepening of the seasonally thawed active layer can gradually mobilize permafrost OC, whereas thermokarst formation and coastal erosion abruptly release deeper stores of ancient permafrost OC (Vonk et al., 2012; Olefeldt et al., 2016).

Abrupt thaw of permafrost may be the norm for many parts of the Arctic landscape (Jorgenson et al., 2006; Walter Anthony et al., 2014). Abrupt permafrost thaw occurs when warming melts ground ice, causing the land surface to collapse into the volume previously occupied by ice (i.e. thermokarst) (Schuur et al., 2015) (Fig. 1.5b). Abrupt thaw will probably occur in <20% of the permafrost zone but could affect half of permafrost OC through the collapsing ground, rapid erosion and landslides (Turetsky et al., 2020). The gradual thaw

slowly affects soil by centimeters over decades, but the abrupt thaw can affect many meters of permafrost soil in periods of days to several years (Grosse et al., 2011). According to the modelling results, Turetsky et al. (2020) found that gradual thaw emissions from the studied 18 million km^2 permafrost region ranged about 613–802 $TgCO_2$ yr^{-1} during 2000 to 2100, which is similar to the abrupt thaw emissions from 2.5 million km^2 permafrost region (624 $TgCO_2$ yr^{-1}) during the same time. Permafrost OC remobilized through gradual thaw and abrupt thaw inland may be transported to the oceans by surface runoffs.

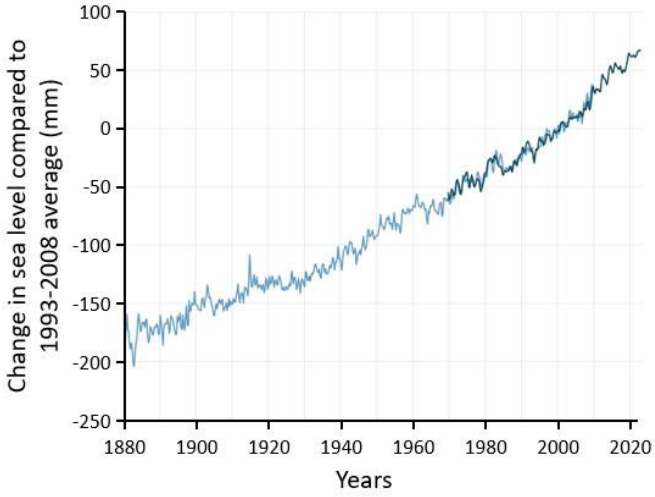

Figure 1.6 Seasonal sea level estimates from Church and White (2011) (light blue line) and University of Hawaii Fast Delivery sea level data (dark blue). The values are shown as change in sea level in millimeters compared to the 1993–2008 average (source: *NOAA Climate.gov*).

The global mean sea level has risen about 21–24 centimeters since 1880 (Fig. 1.6). In 2021, the global mean sea level was 97 millimeters above the levels recorded in 1993, making it the highest annual average in the satellite record (1993–present). The rising sea level is mostly due to a combination of melt water from glaciers and ice sheets as well as the thermal expansion of seawater as it warms (Frederikse et al., 2020). In the Arctic, an acceleration in sea level rise will enhance the erosion of the Arctic coast through higher storm surges (Lantuit et al., 2012). Permafrost coasts are particularly vulnerable to climate warming, warm air acts upon the soil column from the top to down and laterally inwards from the bluff face. This combination leads to rapid ground-ice melting and permafrost thawing, making the coast more susceptible to erosion (Kupilik et al., 2020; Lim et al., 2020; Irrgang et al., 2022) (Fig. 1.7). From the modern observation, the OC flux from erosion of permafrost coasts are comparable with that from Arctic river basins (Rachold et al., 2000). The overall annual input of OC from coastal erosion to the Arctic Ocean is estimated to be 14.0 Tg, which is higher than the amount of particle OC provided by Arctic rivers (Wegner et al., 2015). The mean annual erosion rates along stretches of unlithified permafrost coasts in Alaska, Canada and Siberia have increases more than two times since the early 2000s compared with the latter half of the twentieth century (Jones et al., 2020b; Irrgang et al., 2022). Coastal erosion along permafrost coasts is expected to continue at high rates or even accelerate in response to further climate warming.

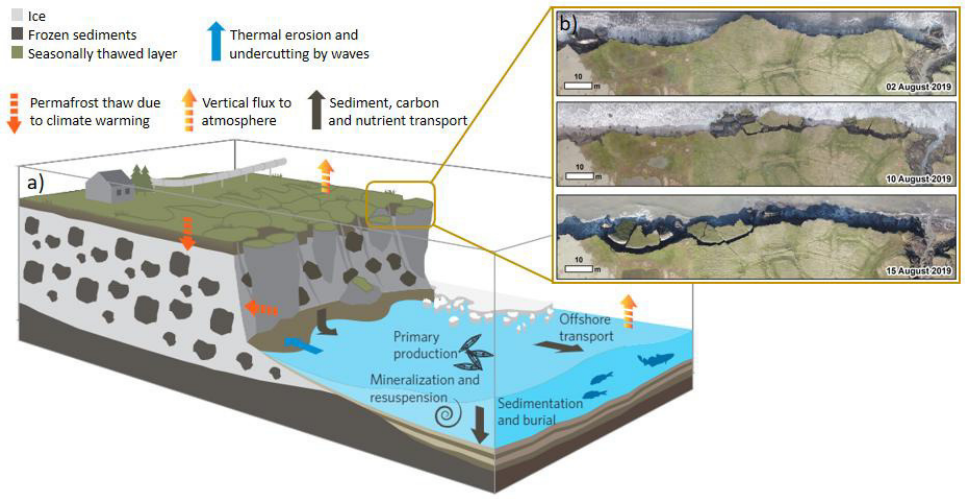

Figure 1.7 a) Physical processes that contribute to morphodynamic changes along permafrost coasts. Increasing air temperatures and occurrence of flooding from streams and the ocean contribute to permafrost degradation and ground subsidence. Increasing sea levels, higher and more frequent extreme water levels and more powerful waves contribute to accelerating erosion of the Arctic coast (adapted from Fritz et al., 2017). b) Aerial UAV orthoimages showing rapid erosion of permafrost coastal bluffs (Alaska Beaufort Sea Coast) in early August 2019 (image credit: Benjamin Jones, *https://researchoutreach.org*).

1.4. Translocation of permafrost OC by rivers

The Arctic is strongly influenced by huge river discharge which is equivalent to 10% of the global runoff (Holmes et al., 2002). The watersheds of the 6 largest Arctic rivers (Mackenzie, Yukon, Kolyma, Lena, Yenisei, and Ob) cover more than 10×10^6 km^2 of surface area including biomass OC in vegetation, soil, and methane hydrates. Among these large carbon pools, soil OC stores 1400–1850 PgC, which represents roughly 50% of the global soil OC (Tarnocai et al., 2009). These watersheds are predominantly covered by permafrost. It is possible that this massive washout of permafrost OC extended spatially to other nearby Arctic watersheds and shelf seas. Records of Arctic river discharge since the early 1930s reveal a long-term increase in freshwater flux to the Arctic Ocean (Peterson et al. 2002; McClelland et al., 2006; Holmes et al., 2021) (Fig. 1.8), potentially resulting in greater riverine export of terrigenous OC to the ocean. Amon et al. (2012) found that the dissolved OC discharge from the 6 largest Arctic rivers could increase under a warmer climate.

Active layer deepening and the development of various thermokarst landforms each cause characteristic changes to soil environmental conditions and thus influence both the potential for soil OC erosion and in situ rates of organic matter degradation. Rivers transfer terrestrial OC from inland to ocean basins, playing a key role in the global carbon cycle. During fluvial transit, organic matter may be oxidized and emitted to the atmosphere as CO_2 or preserved and transported to downstream depositional sinks. Previous studies found that the large Arctic watersheds are currently net sinks for CO_2, net sources for CH_4 (McGuire et al., 2009),

and deliver between 25 and 36 TgC yr^{-1} in the form of dissolved OC to the Arctic Ocean (Raymond et al., 2007; Holmes et al., 2012). Protective physico-chemical mechanisms and sediment transit time may regulate the magnitude and rate of organic matter oxidation (Repasch et al., 2021; Jia et al., 2023; Martens et al., 2023). In coastal mountains with short, steep rivers linking to the ocean, fluvial particulate OC may be efficiently transferred to depocentres (Hilton et al., 2011; Bianchi et al., 2018). In continental settings, fluvial transit times of sediments can exceed 20 kyr (Dosseto et al., 2008; Torres et al., 2020), and many large rivers have been characterized as net CO_2 sources due to degassing from channels and floodplains (Mayorga et al., 2005; Raymond et al., 2013).

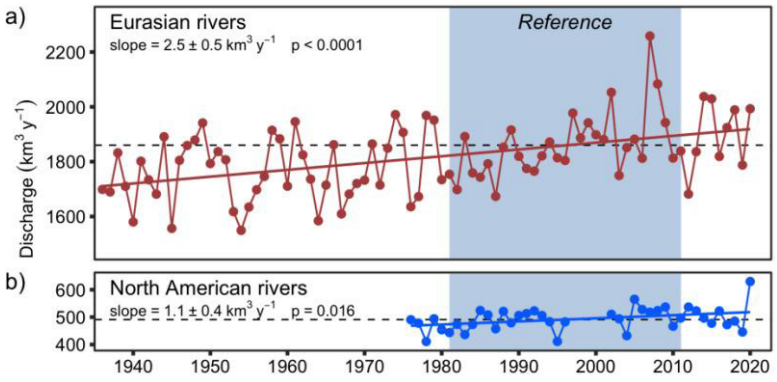

Figure 1.8 Long-term trends in annual discharge (km^3 yr^{-1}) for a) Eurasian and b) North American Arctic rivers through 2020. Gaps in the North American rivers time series span from 1996 through 2001 due to missing Yukon data (1996 to 2001) and missing Mackenzie data (1997 and 1998). Dashed lines show the mean annual discharge throughout the 1981-2010 reference period for the Eurasian (1860 km^3 yr^{-1}) and North American (491 km^3 yr^{-1}) rivers. Eurasian rivers include Kolyma, Yenisey, Lena, Ob', Pechora, and Severnaya Dvina rivers. Mackenzie and Yukon are the North American rivers (Holmes et al., 2021).

1.5. Carbon isotopes used to trace terrigenous OC

There are three naturally occurring carbon isotopes: the stables ^{12}C and ^{13}C, and the radioactive ^{14}C, of which ^{14}C exists in nature only in trace amounts and is produced by cosmic rays (Fig. 1.9). During the carbon cycle, the isotope exchange reactions cause inorganic carbon (such as carbonate) to enrich heavy isotopes (such as ^{13}C). The organic cycle of carbon, such as the dynamic fractionation effect of photosynthesis, leads to the enrichment of light isotopes (such as ^{12}C) in biogenic carbon (organic matter). This results in the carbon isotope fractionation in the carbon cycle between organisms and atmospheric CO_2 in terrestrial ecosystems (Tieszen and Boutton, 1989). $\delta^{13}C$ is a measure of the ratio of the two stable isotopes of carbon—^{13}C and ^{12}C—reported in parts per thousand (‰) (Drever, 1997). The definition is:

$$\delta^{13}C = (((^{13}C/^{12}C)\text{sample} / (^{13}C/^{12}C)\text{standard}) - 1) \times 1000 \quad (1.5)$$

The OC biosynthesized by terrestrial vascular plants uptake atmospheric CO_2 by the C4 pathway has an average $\delta^{13}C$ value of around -14‰ with a range of -16‰ to -10‰ (O'Leary, 1988; Meyers, 1997; Dittmar and Stubbins, 2014). While OC produced by C3 plants is characterized by a low average $\delta^{13}C$ value of approximately -27‰ with a full range of -33‰ to -24‰ (O'Leary, 1988; Glaser et al., 2005; Dittmar and Stubbins, 2014). The $\delta^{13}C$ of OC derived from plants can be further influenced by processing in the environment. The balance of photosynthetic source contributions and OC processing results in riverine dissolved OC with $\delta^{13}C$ values ranging from approximately -30‰ to -25‰ (Bauer et al., 2002), which is similar to the $\delta^{13}C$ values of freshwater plankton range (Mayer, 1994). In contrast, the $\delta^{13}C$ of dissolved OC ranges from approximately -28‰ to -18‰ (Bauer et al., 2002) across the global oceans, and the marine OC is produced by utilizing marine dissolved inorganic carbon so that the $\delta^{13}C$ values of marine OC are about -22‰ to -19‰ (Fontugne and Jouanneau, 1987).

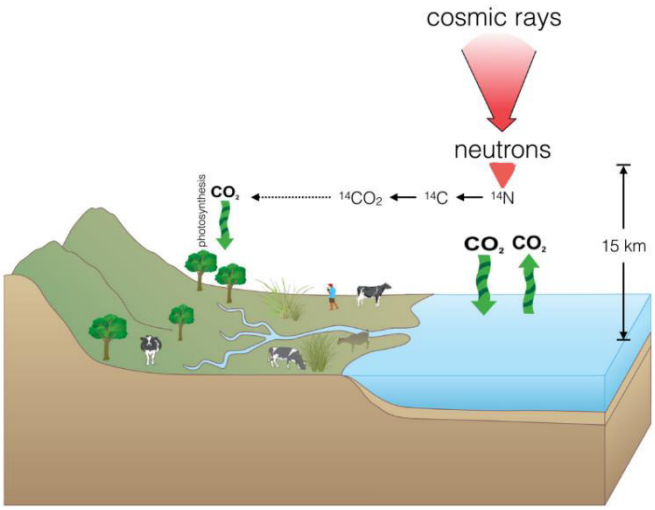

Figure 1.9 Simplified illustration of radiocarbon production, oxidation, absorption, and distribution throughout the Earth's reservoirs (Alves et al., 2018).

The natural radiocarbon isotope (^{14}C) is mainly derived from the reaction of neutrons produced by cosmic rays in the upper atmosphere with the stable nitrogen isotope ^{14}N, and the resulting ^{14}C combines with atmospheric oxygen to form carbon dioxide ($^{14}CO_2$) (Fig. 1.9). $^{14}CO_2$ enters the lower atmosphere and enters the ocean through sea-air exchange and vertical mixing, becoming an inorganic carbon source for the life activities of terrestrial and marine organisms. The gas exchange between surface sea water dissolved inorganic carbon ($DI^{14}C$) and atmospheric $^{14}CO_2$ is limited, which delays the isotopic equilibration between both carbon pools (Kusch, 2010). Both processes reach a stable balance causing an age offset between the atmosphere and surface ocean, which is termed reservoir age. The reservoir age increases with increasing water depth. The reservoir age of sea water $DI^{14}C$ will be

incorporated into marine organisms and has to be considered when interpreting ^{14}C data from marine samples (Kusch, 2010).

^{14}C is widely present in the atmosphere, land, ocean and living organisms, which makes ^{14}C a powerful tracer for understanding the biogeochemical carbon cycle process and studying carbon exchange between different carbon pools. The resultant ^{14}C has a radioactive half-life of 5730 ± 30 years (Godwin, 1962). The ^{14}C content of CO_2, dissolved OC, and other carbon pools are routinely expressed as $\Delta^{14}C$ with units of parts per million (Stuiver and Polach, 1977). $\Delta^{14}C$ compositions reveal additional information on the sources of OC that could not be obtained by $\delta^{13}C$ values. For example, ^{14}C compositions can be used to distinguish freshly synthesized OC from pre-aged soil OC, although they have similar $\delta^{13}C$ values. Bulk OC consists of a complex mixture of compounds from different sources and with different residence times and distinct fates, such as fresh vegetation OC origin and pre-aged terrestrial OC inputs from erosion. ^{14}C compositions on bulk OC level are not enough for characterizing the provenances and ages of the major components. Thus, ^{14}C compositions of source specific compounds are needed to provide insights into the turnover of the OC at the molecular level.

By using the compound-specific radiocarbon analysis (CSRA) of biomarkers, organic matter sources in natural environmental systems can be basically divided into three categories from the perspective of "age", including young marine OC and terrigenous vascular plant residues ($\Delta^{14}C$ = 0 ± 50‰, modern < 100 years), aged soil OC (millennial scale) and weathered carbon of ancient sedimentary rocks (petrogenic carbon; $\Delta^{14}C$ = -1000‰, million years scale) (Hedges, 1992; Villinski et al., 2008). The $\Delta^{14}C$ end-member of ICD is -966 ± 45‰ as reported in Tesi et al. (2016). The $\Delta^{14}C$ end-member of the active layer from the uppermost metre of Siberian soils located in the continuous permafrost domain is -232 ± 147‰ (Tesi et al., 2016). Based on dual-carbon isotope- ($\delta^{13}C$ and $\Delta^{14}C$) of TOC and lignin concentration, Tesi et al. (2016) found that the material held in the active layer was the major carbon source during the Younger Dyers to Preboreal transition (YD-PB) (70–80%) resulting large quantity of soil carbon released in the Lena River basin. Winterfeld et al. (2018) found the mobilization of glacial permafrost carbon during the last glacial-interglacial transition to be an additional and significant source of greenhouse gases to the atmosphere, and coastal erosion was the main cause for this permafrost OC mobilization based on lipids flux and radiocarbon age. ^{14}C compositions of long-chain *n*-alkanoic acids and lignin can represent the cycling of pre-aged terrestrial OC as they are of vascular plant origin, but might have undergone different turnover in soils and/or rivers before transport to oceans and deposition in sediments.

1.6. Biomarkers used to reconstruct paleoenvironment

The geological record encompasses a wide range of climate states that can help explore the response of regional climate and terrestrial ecosystems to external forcing (Tierney et al., 2020). The abundance, distribution, and isotope composition of source-specific organic molecules—termed biomarkers—preserved in a variety of sedimentary deposits provide an additional window into ancient terrestrial environments (Fig. 1.10). The most common biomarkers used for the reconstruction of the terrestrial paleoenvironment are lignin (Hedges & Mann 1979) and long-chain *n*-alkyl compounds (e.g., *n*-alkanes, *n*-alkanoic acids) (Eglinton and Hamilton, 1967).

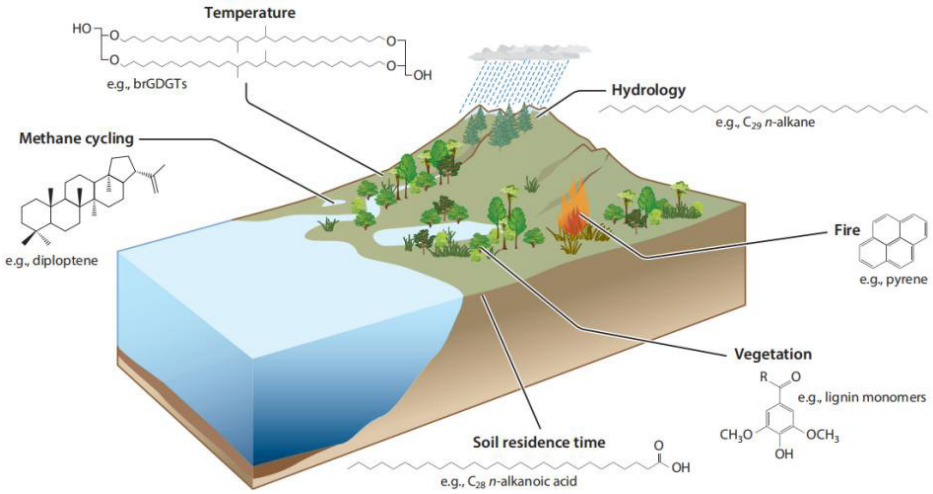

Figure 1.10 Terrestrial biomarkers in the environment. Abbreviation: brGDGT, branched glycerol dialkyl glycerol tetraether (Inglis et al., 2022).

1.6.1. Lignin

Lignin is synthesized by vascular plants and can exist in different environments, such as soils and sediments. Lignin is a key component of wood (30–50%) and other plant tissues and is a heterogeneous polymer containing a variety of monomeric building blocks. The lignin macromolecule turns over relatively rapidly in soils (Schmidt et al., 2011), partly because it is relatively concentrated in soil aggregates rather than mineral associated fine soil fractions (Amelung et al., 1999, 2002), and lignin turnover in soils is mainly regulated by temperature (Jia et al., 2023). Previous studies found the efficient delivery of vascular plant debris during storm, flood, and high-precipitation events (Hilton et al., 2008; Smith et al., 2013), suggesting increased transfer of surface detrital carbon in high-runoff systems. Runoff exerts a strong control on the $\Delta^{14}C$ values of lignin phenols in Arctic river systems (Feng et al., 2013a), where younger lignin is transported by rivers with a higher mean annual runoff rate.

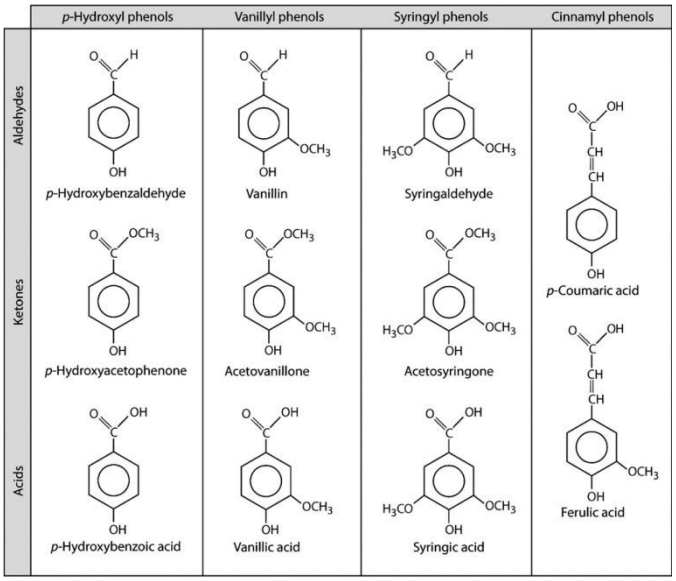

Figure 1.11 The structural formulas of eleven characteristic lignin phenolic monomers produced after the alkaline CuO oxidation (Thevenot et al., 2010).

After oxidation with copper oxide (CuO), lignin polymers can produce several characteristic methoxylated phenols that can be analyzed by gas chromatography (GC). The most commonly used eleven phenolic monomers are shown in Figure 1.11. According to their structure, these phenolic monomers can be divided into 4 groups (Fig. 1.11). The vanillyl phenols (V) include vanillin (Vl), acetovanillone (Vn), and vanillic acid (Vd). Syringyl phenols (S) include syringaldehyde (Sl), ancetosyringone (Sn), and syringic acid (Sd). Cinnamyl phenols (C) include *p*-coumaric acid (p-Cd) and ferulic acid (Fd). These eight phenolic monomers derive only from lignin. The para-hydroxybenzenes (P), including *p*-hydroxybenzaldehyde (Pl), *p*-hydroxybenzophenone (Pn), and *p*-hydroxybenzoic acid (Pd), might also be yielded by non-lignin precursor, e.g., amino acid (Hedges and Parker, 1976). The compositions of these phenolic monomers vary in different plant types, the C/V and S/V ratios thus can distinguish lignin between woody and non-woody tissues of angiosperms and gymnosperms (Hedges and Mann, 1979). The degradability varies with species and plant tissue type, the ratios of vanillic acid to vanillin $(Ad/Al)_v$ and syringic acid to syringaldehyde $(Ad/Al)_s$ can indicate the degradation degree of lignin (Ertel and Hedges, 1985). Syringyl phenols are reported to degrade faster than vanillyl phenols in both aquatic and terrestrial environments, leading to lower S/V ratios with increasing degradation (Hedges et al., 1988; Opsahl and Benner, 1995; Otto et al., 2005). Previous studies have found precursors of cinnamyl phenols to be highly labile compared to syringyl and vanillyl precursors in conifer needles (Hedges and Weliky, 1989), cypress needles, mangrove leaves and cordgrass (Opsahl and Benner, 1995), indicating the C/V ratios decrease with progressive degradation. P-phenols may derive from protein and they are enriched in *Sphagnum* and peat (Erickson and Miksche, 1974; Goñi and Hedges, 1995; Goñi et al., 2000; Amon et al., 2012). The P/V ratio indicates a contribution of mosses or peat. Typical ratios of S/V, C/V, P/V and $(Ad/Al)_v$ taken from the literature are in Table 1.1.

Table 1.1 Lignin phenol parameters in different source material.

Source	S/V	C/V	P/V	$(Ad/Al)_v$	Reference
Gymnosperm woody	0.03	0.04	0.04	0.19	Hedges and Mann, 1979; Hedges and Parker, 1976; Prokushkin et al. (in preparation)*
Gymnosperm needels	0.04	0.17	0.07	0.32	Hedges and Mann, 1979; Hedges and Parker, 1976; Williams et al., 1998; Prokushkin et al. (in preparation)
Angiosperm woddy	2.42	0.05	0.03	0.15	Hedges and Mann, 1979; Hedges and Parker, 1976; Prokushkin et al. (in preparation)
Angiosperm leaves	0.98	0.7	0.72	0.24	Hedges and Mann, 1979; Hedges and Parker, 1976; Prokushkin et al. (in preparation)
Grasses	1.23	1.19	0.06	0.19	Prokushkin et al. (in preparation)
Moss	2.34	0.26	9.0	0.82	Prokushkin et al. (in preparation)
Wetland plants	1.9	3.05	0.5	0.22	Williams et al., 1998
Peat (*Sphagnum* sp.)	0.82	0.77	6.06	0.27	Prokushkin et al. (in preparation)
Peat	0.82	0.88	1.49	0.34	Williams et al., 1998
Boreal forest soil-organic horizon	0.24	0.42	0.22	0.42	Houel et al., 2006
Boreal forest soil-inorganic horizon	0.11	1.18	0.85	1.65	Houel et al., 2006

* data reported in Amon et al. (2012)

1.6.2. Lipids

Lipids are one of the principal structural components of living cells. The commonly used lipid biomarkers include fatty acids, *n*-alkanes and glycerol dialkyl glycerol tetraether lipids (GDGTs).

Fatty acids are usually used as biomarkers to identify sources and fate of organic matter in marine environments (Harvey, 1994) due to their structural diversity and high biological specificity (Parkes, 1987). For example, fatty acids with greater than 24 carbon atoms are synthesized mostly by vascular plants (Volkman et al., 1980), and are considered indicative of terrestrial higher plant markers in sediments (Scribe et al., 1991; Carrie et al., 1998) (Table 1.2). Short-chain (C_{16} and $C_{18)}$ fatty acids also exist in all plants but only account for a small proportion compared to their long-chain homologs, and short-chain *n*-alkanoic acids are dominantly produced by algae (Meyers, 1997). Compared to the long-chain homologs, short-chain *n*-alkanoic acids are labile and selectively decomposed. Thus, short-chain fatty acids can be used to reflect marine and terrestrial modern autochthonous OC inputs (Table 1.2).

Table 1.2 Some fatty acids used as biomarkers to identify the sources of the organic matter in sediments.

Fatty acids	Sources	References
C14:0, C16:1ω7, C20:4ω6, C20:5ω3	Diatom	Volkman et al., 1989; Carrie et al., 1998; Mudge et al., 1998,
C15:0, C17:0, C18:1ω7	Bacteria	Parkes and Taylor, 1983; Volkman et al., 1989; Canuel and Martens, 1993
C18:2ω6, C18:3ω3, C18:3ω6	Macroalgae	Volkman et al., 1989; Mudge et al., 1998
C18:1ω9, C22:6ω3	Dinoflagellate	Carrie et al., 1998; Zimmerman and Canuel, 2001
C22:1ω9, C24:1ω9	Zooplankton	Carrie et al., 1998; Venturini et al., 2012
Ubiquitous fatty acids (C16:0, C18:0)	Detrital materials	Carrie et al., 1998; David et al., 2019
Long chain fatty acids (C24:0–C30:0)	Terrestrial plants	Volkman et al., 1980; Scribe et al., 1991; Meyers, 1997; Carrie et al., 1998; Dunn et al., 2008

N-alkanes are widely found in bacteria, fungi, macroaquatic plants and terrestrial vascular plants. The composition and distribution characteristics of *n*-alkanes from different biological sources are different. The epidermal leaf wax of terrestrial higher plants contains *n*-alkanes with long carbon chains (nC_{25}–nC_{33}), usually nC_{27}, nC_{29} or nC_{31} as the main peak carbon, which has obvious odd-carbon predominance (Fig. 1.12). The *n*-alkanes of bacteria, algae and other lower organisms have shorter carbon chains (nC_{14}–nC_{20}), and are usually an unimodal distribution of nC_{16}, nC_{17} or nC_{19}, with no obvious odd-even predominance. The distribution of *n*-alkanes of submerged and floating aquatic macroplants is between the middle carbon chain nC_{21} and nC_{25}, with nC_{21}, nC_{23} or nC_{25} as the main peak, which has obvious odd carbon predominance (Fig. 1.12). The distribution of *n*-alkanes in endangered aquatic macroplants is similar to that of terrestrial higher plants (Cranwell et al., 1987; Rieley et al., 1991; Ficken et al., 2000; Jeng, 2006; Cranwell, 2010). The terrestrial and emergent plants showed similar n-alkane distributions, maximizing at nC_{29} or nC_{31}. However, the submerged/floating plants maximized at nC_{23} or nC_{25} *n*-alkane (Fig. 1.2).

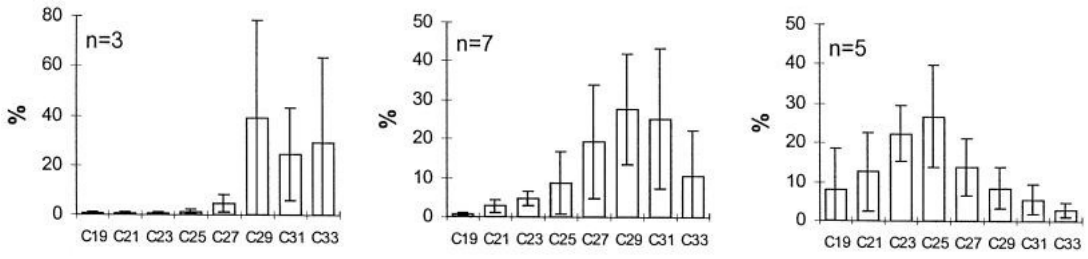

Figure 1.12 Histograms of the distributions of the *n*-alkanes for n species of plant from the three categories: terrestrial (left), emergent (middle) and submerged/floating (right) plants. Only odd carbon number distributions are shown for the *n*-alkanes. Bars represent 1 standard deviation (Ficken et al., 2000).

Compare with lignin, plant-derived long chain lipids chemically associated with soil minerals (Kögel-Knabner et al., 2008; Grant et al., 2022), while short-chain lipids that include microbial contributions may turn over relatively quickly in the soil (Wiesenberg et al., 2008). In the Arctic permafrost regions, long chain lipids predominantly trace ancient OC that is remobilized through coastal erosion and thermokarst (Feng et al., 2013a, 2015b; Winterfeld et al., 2018; Meyer et al., 2019). The $\Delta^{14}C$ values of long chain lipids in river sediments are most strongly correlated with the watershed coverage of continuous permafrost in the Arctic.
GDGTs are a class of membrane lipids synthesized by archaea and some bacteria (Karner et al., 2001; Herndl et al., 2005; Weijers et al., 2006a, 2007), making them useful biomarkers for these organisms in the geological record (Fig. 1.10). Because the number of cyclopentane moieties in a GDGT compound is related to the temperature of the growth environment, with increasing numbers of cyclopentane rings resulting in increased thermal stability and allowing for survival at higher temperatures, GDGT distribution and abundance can be employed as paleoclimate proxies.

1.7. Study area

1.7.1. The Bering Sea and the Yukon Basin

The Bering Sea is a marginal sea of the Northern Pacific Ocean (Fig. 1.13). It is bordered on the east and northeast by Alaska, on the west by the Russian Far East and the Kamchatka Peninsula, on the south by the Alaska Peninsula and the Aleutian Islands and on the far north by the Bering Strait, which connects the Bering Sea to the Chukchi Sea (Fig. 1.13). During the LGM, expansive continental ice sheets lowered the globally averaged sea level by ~ 130 m, exposing a land bridge at the Bering Strait (Pico et al., 2020). During the subsequent deglaciation, sea level rose rapidly and ultimately flooded the Bering Strait, linking the Arctic and Pacific Oceans (Jakobsson et al., 2017; Pico et al., 2020). The Bering Sea serves as a transition between the ice-free North Pacific and perennially ice-covered Arctic Ocean. Ice initially forms near the Bering Strait or along the south facing coastlines and is advected southwest by the prevailing easterly winds (Stabeno et al., 2001). At present, sea ice generally forms in November over the continental shelf areas of the Bering Sea and reaches its maximum extent in March. By June, sea ice has generally retreated farther north than the Bering Strait. The sub-Arctic climate over the Bering Sea is driven by the variability and seasonal evolution of the Aleutian Low-pressure system, controlling sea-ice coverage, cold and warm air-mass distribution, as well as snow fall and melt on surrounding land masses (Overland et al., 1999; Pickart et al., 2009). Drainage is basically achieved by the Yukon River from Alaska, and the Anadyr River from Chukotka. Continental runoff brings both fresh water and detrital sediments to the Bering Sea (Bailey, 2005).

The Yukon River is a major watercourse in northwestern North America and the longest river in Alaska (Fig. 1.13) with an area of 857,300 km^2 and the annual flow of about 210 km^3 to the Bearing Sea (Holmes et al., 2012). Dissolved OC discharge of the Yukon River is roughly 1.5 TgC per year (Raymond et al., 2007; Holmes et al., 2012). Low flows in winter and high discharge in summer, with the peak flood in June due to snowmelt runoff (Yang et al., 2014). Yukon River annual flow at the basin outlet increased by 8% over the past 40 years; summer flows have a higher fluctuation, and peak snowmelt flow slightly increases with its timing shifted to an earlier date (Ge et al., 2013; Yang et al., 2014). It has a higher mean elevation (690 m) and higher maximum elevation (6100 m) than other polar rivers, such as the Lena River (Amon et al., 2012). The Yukon basin was mostly unglaciated during the LGM but had permafrost (Schirrmeister et al., 2013). Although part of the permafrost in the Yukon basin thawed during the last deglaciation (Meyer et al., 2019; Wang et al., 2021), most of the basin is still covered by permafrost today. The basin is underlain by 16% continuous permafrost and 70% discontinuous permafrost at present (Brabets et al., 2000; Holmes et al., 2012). Yukon basin mean annual air temperature is about -5 ℃ with annual total precipitation of 380 mm.

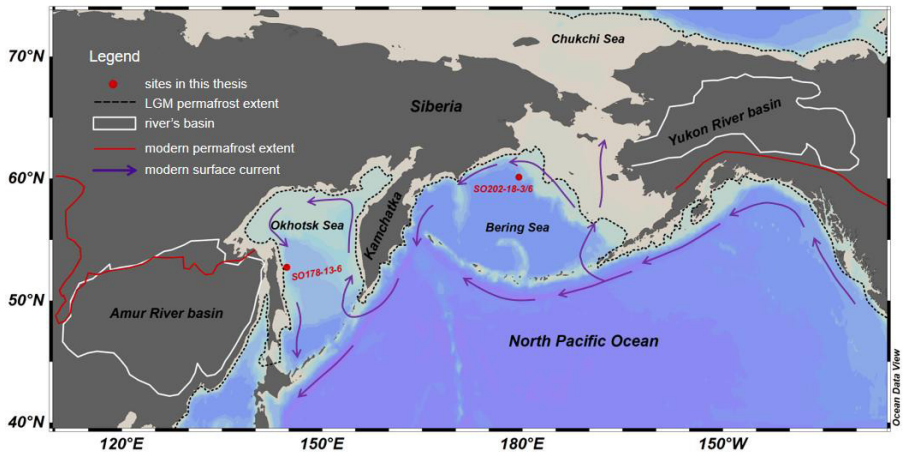

Figure 1.13 Map of the Bering Sea and Okhotsk Sea with adjoining oceans and land masses as well as the location of the study sites (red dot) (adapted from Cao et al., 2023).

As sea level rose during the transition from the Pleistocene to the Holocene, the vast non-glaciated landmass extending from northeastern Siberia to northwestern Canada (Beringia) was transformed. The dry, treeless landscape was replaced by the present– mosaic of boreal forest, peatlands and thaw lakes bordered by epicontinental seas —an environment dramatically different from any during the preceding 100,000 years. Pollen records from Alaska and the Yukon Territory indicate the vegetation was herb and forb dominated, with grass, sedge, and *Artemisia* being the most common taxa during the most recent glaciation (from 29 to 18 kyr) (Bigelow et al., 2013). Sites in western Alaska contain more *Thalictrum*

(a mesic indicator) than sites to the east (Ager, 2003; Zazula et al., 2006). From the LGM to about 16 kyr, the dominant pollen records remain unchanging (mostly graminoids and forbs), but after about 16 kyr, birch pollen becomes significant across the region, from western Alaska to the Mackenzie River (Anderson et al., 2003; Bigelow et al., 2013). This change in the pollen records marks a significant shift in the vegetation from a dominantly herbaceous tundra to a dominant shrub tundra, probably reflecting both increasing summer warmth and increased moisture (Finney et al., 2004). By about 10 kyr, the alder pollen frequency increased rapidly in northwestern and southwestern Alaskan pollen cores (Bigelow et al., 2013; Kaufman et al., 2015). In the Alaskan interior, alder frequencies crossed 20% by about 7–8 kyr (Anderson et al., 2003; Kaufman et al., 2015). The last major tree species to appear in the north is lodgepole pine (*Pinus contorta ssp. latifolia*). It appears in the south since 2 kyr (Kettlehole Pond), where it replaced the local spruce vegetation (Bigelow et al., 2013). Pine reached its current limit northwest of Whitehorse about 400 years ago (MacDonald and Cwynar, 1985; Bigelow et al., 2013). Approximately 20% of the Yukon River catchment is covered by spruce forest, white (*P. glauca*) in well drained sites and black (*P. mariana*) in lowland sites (Brabets et al., 2000), about 40% by grassland, 20% by shrubland, and 8% by open water and wetlands associated with the low land areas (Amon et al., 2012).

1.7.2. The Okhotsk Sea and the Amur Basin

The Okhotsk Sea is a marginal sea of the western Pacific Ocean (Fig. 1.13). It is located between Russia's Kamchatka Peninsula on the east, the Kuril Islands on the southeast, Japan's island of Hokkaido on the south, the island of Sakhalin along the west, and a stretch of eastern Siberian coast along the west and north. Most of the continental shore is high and rocky, dissected by large rivers, e.g., the Amur, Tugur, Uda. Large quantities of continental sediment flow into the sea, primarily from the Amur River. Other sources of sediment include coastal erosion and volcanic activity. The northeastern, northern, and western regions of the sea experience severe weather during the winter, because of the influence of the Asian continent; from October through April these areas experience very cold air temperatures, are constantly covered with ice, and have very little precipitation. In short, a continental climate pervades these parts of the sea. To the south and southeast the proximity of the Pacific results in a milder marine climate. The Okhotsk Sea is characterized as the source region of the North Pacific Intermediate Water (Wong et al., 1998; Okazaki et al., 2014) and the southernmost region of seasonal sea ice in the Northern Hemisphere today (Kimura and Wakatsuchi, 2000). The relatively shallow and bounded nature of the sea favours seasonal sea-ice formation. Specifically, the continental shelf under the northwestern part of the Okhotsk Sea is the active sea-ice production area owing to the northerly winter wind. Climatologically, initial freezing occurs in late fall and becomes maximum from late

February to early March, with ice melting by June. The Okhotsk Sea is the coldest sea in East Asia. The coldest months in the sea are January and February, and the warmest are July and August.

The Amur River is the world's tenth longest river and the longest river in the Russian Far East, forming the border between the Russian Far East and Northeastern China. The Amur and its tributaries drain a basin of about 1.85×10^6 km^2. The Amur basin's climate is affected by its northern location—between 45° and 55° N—and by the monsoon winds that shape the climate of all East Asia. In winter polar, continental air masses dominate, resulting dry, frigid weather. Mean January temperatures range from -20 °C at Harbin on the Sungari River in China to -33 °C in the northern interior parts of the basin. In summer the predominant subtropical maritime air masses provide mean July temperatures of between 22 °C and 18 °C over the area. Precipitation in the Amur basin is uneven. It is heaviest in the maritime and southern sections, where it ranges between 600 and 900 mm annually. In the middle regions, the annual rate does not exceed 600 mm, and in the western, continental regions it averages 300 to 400 mm. The peak comes in the summer months when more than half the annual total typically falls. The river is fed principally by the monsoon rains that fall in summer and autumn. The rainwater discharges quickly into the river, resulting in a period of flooding that extends from May to October. After September the floodwaters began to abate. The river reaches its lowest level in March and April, before the spring flood, which is fed mainly by the runoff of melted snow and which is much smaller than the monsoon floods that occur in summer and autumn. The mean discharge of the Amur at its mouth is about 10,900 m^3 per second. The mean annual discharge of the Amur is about 394 m^3. The annual sediment discharge averages 57 million tons. Much of the Amur basin lies in the taiga vegetation zone. Larch is the predominant species, particularly in boggy areas, with some pine, spruce, and fir on drier land. In the east are found the Korean pine (*Pinus koraiensis*) and the Amur cork tree (*Phellodendron amurense*). In the west, the Argun River traverses a region of steppe grassland. In the Da and Xiao Hinggan ranges south of the Amur are found broad-leaved and mixed broad-leaved and conifer forests dominated by Mongolian oak (*Quercus mongolica*), pine, and daurian larch.

1.7.3. The Laptev Sea and the Lena Basin

The Laptev Sea is a marginal sea of the Arctic Ocean (Fig. 1.14). It is located between the northern coast of Siberia, the Taimyr Peninsula, Severnaya Zemlya and the New Siberian Islands. The Kara Sea lies to the west, the East Siberian Sea to the east. The sea has a severe climate with temperatures below 0 °C over more than nine months per year. More than half of the sea rests on a continental shelf with average depths below 50 m, and the areas south from 76° N are shallower than 25 m. The Laptev Sea is a major source of Arctic sea ice, ice

formation starts usually in September on the north and October on the south. With an average outflow of 483,000 km^2 per year over the period 1979–1995, it contributes more sea ice than the Barents Sea, Kara Sea, East Siberian Sea and Chukchi Sea combined (Alexandrov et al., 2000). The ice formation results in a large continuous sheet of ice, with a thickness of up to 2 meters in the south-eastern part of the sea as well as near the coast (Alexandrov et al., 2000). The water salinity is significantly affected by the thawing of ice and river runoff. Most of the river runoff (about 70%) is contributed by the Lena River.

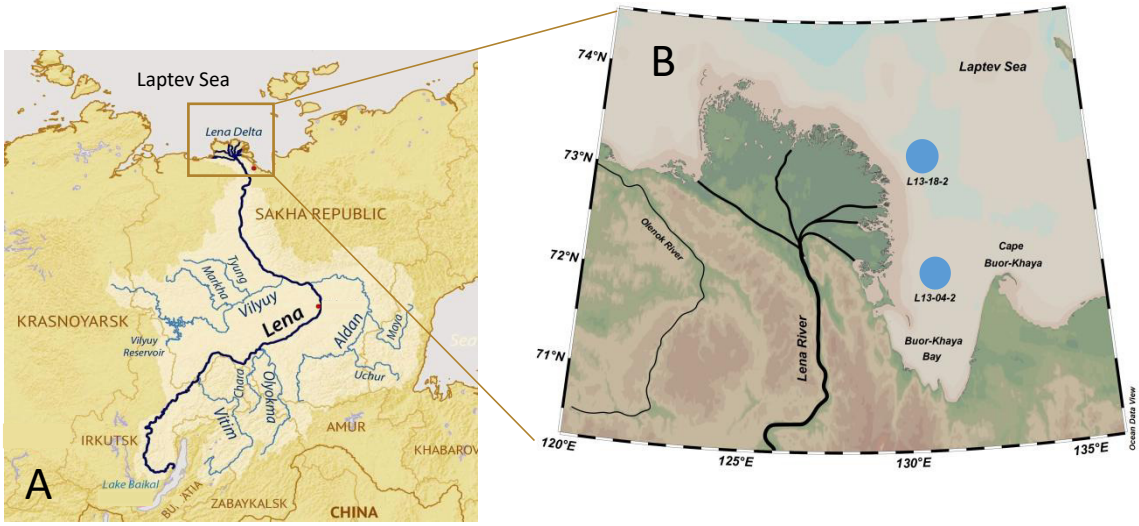

Figure 1.14 Map of (A) the Lena Basin (source: *http://ultima0thule.blogspot.com*) and (B) Lena Delta. Blue dots in map B are the location of the study sites.

The Lena River originates from the Baikal Mountains in the south-central Siberian Plateau and flows northeast and north, entering into the Arctic Ocean via the Laptev Sea (Fig. 1.14). Lena River is the longest river entirely within Russia, with a length of 4,294 km and a mean annual discharge is 489 m^3 per year. Its drainage area is about 2,490,000 km^2, and permafrost underlies most of the catchment, 77% of which is continuous permafrost (Brown et al., 2002). At the end of the Lena River there is a large delta that extends 100 kilometers into the Laptev Sea and is about 400 km wide. The Lena Delta is the largest delta in the Arctic Ocean. The Lena Basin lies in a zone of continental moderate and sub-arctic climate (Liu and Yang, 2011). Precipitation is highest during April–October (total precipitation at Yakutsk = 152 mm), peaking in July and subsequently decreasing during November–March (Hudson and Thompson, 2019). Temperature peak in July, after which snow accumulation commences, reaching a maximum extent in November, before snowmelt begins in March (Ye et al. 2003). The lowest and highest river flows occur during winter and summer, respectively. The basin is sparsely populated and vegetation is largely natural comprising forests (84%), shrublands (9%), grasslands (3%), croplands (2%) and wetlands (1%) (Liu and Yang 2011). Forests dominate the southwest and tundra dominates the north. The central

valley of the Lena River has wide expanses of steppe grasslands, while the floodplains of the river are characterized by typical taiga coniferous forests, along with peat bogs and swamps. Alder, willow, and birches grown in this region. Further north, in the river's lower course, typical tundra types of vegetation prevail, with mosses, lichens, Arctic poppies, and Whitlow grasses covering the land surface in most areas.

1.8. Objectives

Permafrost OC comprises a mixture of OC from late Pleistocene ICD and from the active layer in the Arctic, and ICD is mainly eroded by coastal erosion, while active layer permafrost OC is predominantly delivered by fluvial transport (Vonk et al., 2012; Tesi et al., 2014). Alteration in permafrost coverage affects the availability of various hydrological conduits, and thus mobilization pathways of OC associated with different permafrost depths and structures (Guo et al., 2007; Gustafsson et al., 2011). Previous studies suggest that the remobilization patterns of permafrost OC may be different for different regions in the Arctic (Tesi et al., 2016; Winterfeld et al., 2018; Martens et al., 2020; Cao et al., 2023), and we need to consider multiple terrestrial OC proxies at molecular levels to differentiate the fate for different allochthonous components in the Arctic systems. Published studies show that climate warming during the last deglaciation caused terrestrial OC fluxes to the East Siberian Arctic Shelf (Vonk et al., 2012; Keskitalo et al., 2017), Chukchi Sea (Martens et al., 2019), Okhotsk Sea (Winterfeld et al., 2018), and Beaufort Sea (Wu et al., 2022) enhanced based on biomarker records in sediments, and most of the OC enters ocean as a result of coastal erosion. Laterally transported permafrost OC in Arctic Ocean sediments thereby provides an integrated signal to trace inland and coastal remobilization of permafrost OC and permits studies of large-scale permafrost OC remobilization with increasing importance in a warming climate. During the global warming from the end of the LGM to the early Holocene, virtually every component of the climate system underwent large-scale change, sometimes at extraordinary rates (Peltier, 2004; Liu et al., 2009; Clark et al., 2012). There were several episodes of large and rapid sea-level rise and abrupt climate change during the last deglaciation (Monnin et al., 2001; Rasmussen et al., 2008; Lambeck et al., 2014). Therefore, the evolution of global climate during the last deglaciation is an outstanding analogue to chronicle the dynamics of permafrost OC remobilization in the Arctic. This thesis utilizes sediment records of transported permafrost OC in Arctic ocean to improve the understanding of how climate warming triggers permafrost OC remobilization and affects carbon cycling in the Arctic during the last deglaciation.

Although substantial research efforts have been made in investigating terrestrial OC in the Arctic and sub-Arctic regions, several issues are still unexplored and/or under debate. Previous studies have reconstructed the mobilization of terrigenous OC from degrading

permafrost in the Okhotsk (Winterfeld et al., 2018) and the Bering Seas (Meyer et al., 2019) based on long-chain *n*-alkyl lipid results. However, no records exist that combine lignin and *n*-alkane data to explore the potentially different transport of terrestrial OC archived in Arctic marine sediments during the last deglaciation. Therefore, multiple biomarkers and isotopes are used to address the following research objectives and hypotheses:

1. The major objective was to exploit the potential of lignin phenols as a paleoenvironmental biomarker in the Yukon and Amur Basins during the last deglaciation, and to learn about the paleo-vegetation development in the two basins. Based on lipids and lignin data to better understand the terrigenous OC accumulation and what controls them.

2. Compared with CSRA on lipids, the CSRA of lignin is rather challenging. In this study, we modified to the previous published method for CSRA of lignin phenols (Feng et al., 2013b) and evaluated the $F^{14}C$ and the mass of the associated procedural blank following the approach of Sun et al. (2020).

3. Since lignin is one of the major biomarkers of terrestrial vascular plants, the ^{14}C composition of lignin can provide new evidences to resolve if there is evidence for mobilization of ancient carbon from the lignin phenol CSRA. This study tests if there is a difference between the radiocarbon ages of lipids and lignin, and the linkage between this age difference and the thawing processes within the catchments occurring during the last deglaciation in the Yukon and Amur Basins.

4. Further, we want to know if the supply and age of lignin phenols from the Lena watershed changed over the past century.

2. Material and methods

2.1. Sampling

The thesis focuses on sediment cores SO202-18-6/3 and SO178-13-6 from the Bering Sea and Okhotsk Sea (Fig. 1.13). The piston core SO202-18-3 (60.13° N, 179.44° W; water depth: 1111 m) and neighboring kasten core SO202-18-6 (60.13° N, 179.44° W; water depth: 1107 m) were recovered from the northeastern continental slope of the Bering Sea in 2009 during R/V Sonne cruise SO202-INOPEX (Gersonde, 2012). The two cores can be treated as one composite record according to their ultrahigh-resolution micro-X-ray-fluorescence data, sediment facies analysis of laminae and radiocarbon dating results (Kühn et al., 2014). It represents an apparently continuous sedimentary sequence dated back to the Last Glacial (~25 ka) (Kühn et al., 2014). Selected samples from core SO202-18-6 (n = 20, 10−589 cm core depth, 6.23−12.65 ka) and from core SO202-18-3 (n = 29, 447−1423 cm core depth, 12.99−24.1 ka) with an average temporal resolution of ~ 510 years were analyzed for lignin contents.

The 23.7 m long piston core SO178-13-6 (52.73° N, 144.71° E; water depth: 713 m) was collected from the Sakhalin margin in the Okhotsk Sea during the expedition SO178-KOMEX with R/V Sonne (Dullo et al., 2004) (Fig. 1.13), with the lowermost interval corresponding to ~17.5 ka (Max et al., 2014). Selected samples (n = 51, 100−2340 cm core depth, 1.11−17.27 ka) from core SO178-13-6 were analyzed for lignin derived phenol contents with an average temporal resolution of ~340 years. Samples from 6 depths were selected for CSRA of lignin phenols and long-chain fatty acids.

L13-18-2 and L13-04-2 were recovered during an expedition conducted in 2013 (Kattein, 2018). The cores were taken about 30 km off the mouths of two main channels of the Lena River (Fig. 1.14). Both core sites are located east of the delta in the adjacent Laptev Sea. L13-18-2, which was taken off the mouth of the Trofimovskaya channel is a 24 cm long core covering the last 80 years of sedimentation. Upon retrieval it was sampled every 1 cm down-core. L13-04-2, which was recovered in the Buor-Khaya Bay, off the mouth of the Bykovskaya channel is of 25 cm length and covers the last 150 years. It was sampled at the surface (0-1cm) and downcore from there every 2 cm. All samples were put into pre-combusted glass jars and stored frozen at -20 °C until analysis.

2.2. Chronology

The chronology of core SO202-18-6/3 is constrained by accelerator mass spectrometry (AMS) ^{14}C dating of calcareous foraminifera. Radiocarbon-based age models for the two cores are

revised based on Kühn et al. (2014, 2015) for cores SO202-18-6/3, Max et al. (2014) and Lembke-Jene et al. (2017) for core SO178-13-6. We used the program Calib 8.20 Marine 20 calibration curves (Heaton et al., 2020; Stuiver and Reimer, 1993) for initial age determinations.

Choice of ΔR in the North Pacific Ocean has been discussed in detail by Kühn et al. (2014). These authors propose that calculated reservoir ages range within 730–990 yr in the Bølling–Allerød (mean reservoir age: 875 yr), 800–1100 yr in the Younger Dryas (mean reservoir age: 910 yr) and 765–775 yr in the Preboreal (mean reservoir age: 770 yr) in the Bering Sea. For the sediment core SO178-13-6, Lembke-Jene et al. (2017) used a regional reservoir age correction (ΔR) value of 500 ± 50 yr, in line with published correction values for the Okhotsk Sea (Kuzmin et al., 2007) and earlier works (Max et al., 2012; Okazaki et al., 2014). The age-depth model has been established by the "CLAMS" software of Blaauw (2010), which was used in Lembke-Jene et al. (2017). The final best-fit runs were performed in CLAMS with 10,000 iterations using a smooth spline function for matching all age control points in their respective 2σ calibrated age distribution ranges.

2.3. Methods

2.3.1. Carbon isotope composition of TOC ($\delta^{13}C$)

The stable carbon isotope composition of organic matter ($\delta^{13}C$) was analyzed by a Thermo Fisher Scientific Delta-V-Advantage gas mass spectrometer equipped with a FLASH elemental analyser EA 2000 and a CONFLO IV gas mixing system in the Stable Isotope Laboratory of the Alfred Wegener Institute for Polar and Marine Research in Potsdam. Sediments were freeze-dried, ground, and homogenized. Removal of carbonates was performed by adding hydrochloric acid. An aliquot of the sample is weighed to a tin capsule according to the OC content of the sample (1 mg to max. 80 mg corresponding to about 0.2 mg OC). The sample is combusted at 1020 °C under O_2 atmosphere and the OC quantitatively transferred to CO_2. The sample CO_2 is separated from other gases in the reduction tube and the elemental analyser. For carbon isotope measurements, the CO_2 gas is transferred with Helium as a carrier gas via the CONFLO IV gas mixing system and a capillary to the mass spectrometer, where the carbon isotope composition is determined relative to laboratory standards of known isotopic composition. $\delta^{13}C$ of the sample is given in ‰ relative to V-PDB. The standard deviation (1σ) is generally better than $\delta^{13}C = \pm 0.15$‰.

2.3.2. Lignin-phenol analysis

The extraction of lignin phenols was carried out based on the method of Goñi and Montgomery (2000) and as described in Sun et al. (2017). Dried samples were oxidized with

copper oxide (CuO, ~ 500 mg) and ~ 50 mg ferrous ammonium sulfate ($(NH_4)_2Fe(SO_4)_2 \cdot 6H_2O$) in 2N sodium hydroxide (NaOH) under anoxic conditions (Fig. 2.2). The oxidation was conducted with a CEM MARS5 microwave accelerated reaction system at 150 ℃ for 90 min. After oxidation, known quantities of recovery standards (ethyl vanillin and trans-cinnamic acid) were added to the oxidation products. Oxidation products were transfer to centrifuge tubes and centrifuged for 10 min (2000 revolutions per minute). The alkaline supernatants were transfer to 40 mL vilas and acidified to pH 1 with 37% hydrochloric acid (HCl). The reaction products were subsequently recovered by two successive extractions with ethyl acetate (EtAc). The combined EtAc extracts were evaporated under a stream of nitrogen, then re-dissolved in 400 µL pyridine.

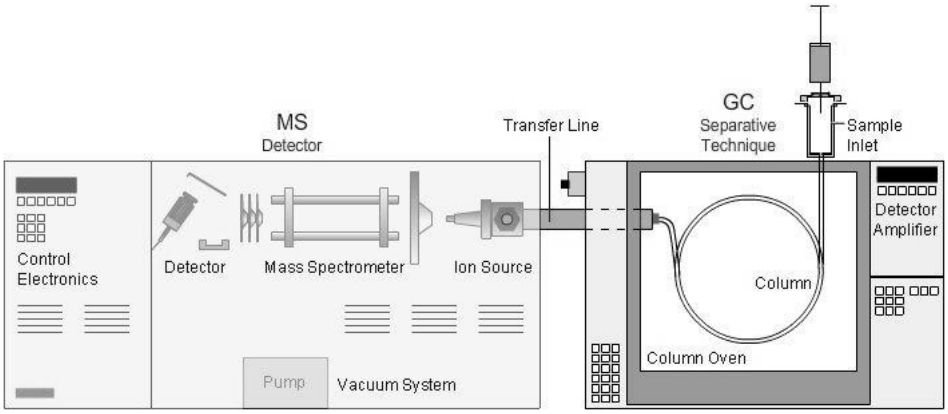

Figure 2.1. Schematic diagram of gas chromatograph–mass spectrometer (GC-MS) (Hussain and Maqbool, 2014).

Prior to injection into the gas chromatograph–mass spectrometer (GC–MS) (Fig. 2.1), an aliquot (30 µL) was derivatized with 30 µL bis-trimethylsilyl-trifluoroacetamide (BSTFA) + 1% trimethylchlorosilane (TMCS) (60 ℃, 30 min). An Agilent 6850 GC coupled to an Agilent 5975C VL MSD quadrupole MS operating in electron impact ionization (70 eV) and fullscan (m/z 50–600) mode was used for analysis. The source temperature of the MS was set to 230 ℃ and the quadrupole to 150 ℃. The GC was equipped with a DB-1 MS column (30 m × 0.25 mm i.d., film thickness 0.25 µm). Helium was used as a carrier gas at a constant flow rate of 1.2 mL min^{-1}. Samples were injected in splitless mode in a split/splitless injector (S/SL) held at 280 ℃. The temperature of the GC–MS column was programmed from 100 ℃ (initially held for 8 min) and ramped at 4 ℃ min^{-1} to 220 ℃, then at 10 ℃ min^{-1} to 300 ℃, with a final hold time of 5 min.

Lignin phenols were identified based on retention time and mass spectra. Quantification was achieved by peak areas of the respective compounds and using individual five point response factor equations obtained from mixtures of commercially available standards analyzed periodically. The content of lignin phenols should be around 10 ng. The yields of Pl, Vl and Sl were corrected by the recovery rate of ethyl vanillin, and the recovery rate of trans-

cinnamic acid was applied to correct the yield of other lignin-derived compounds and 3,5Bd (Goñi et al., 2000; Goñi and Montgomery, 2000).

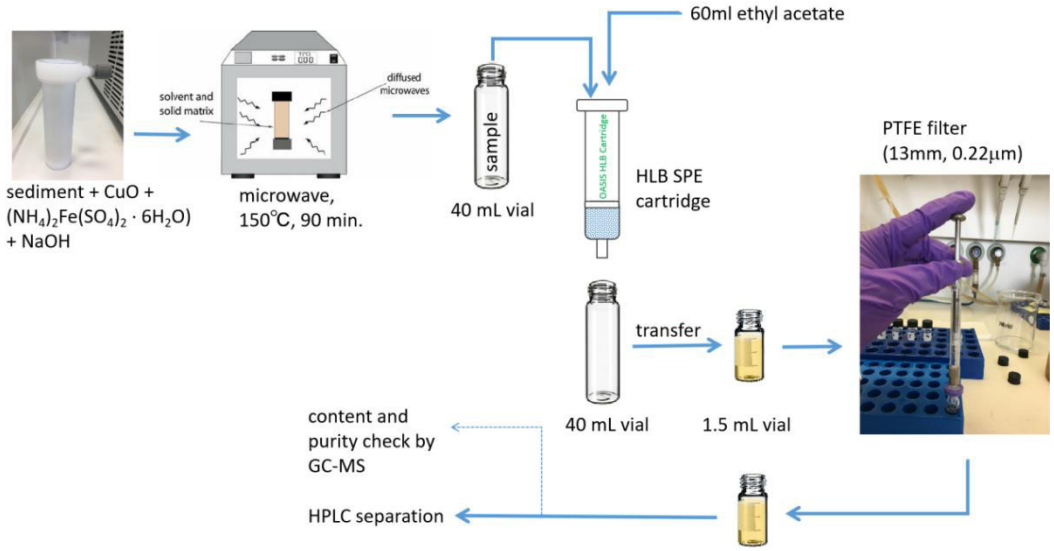

Figure 2.2. A simplified flow chart of the extraction and SPE separation for lignin phenols from sediments.

2.3.3. Compound-specific radiocarbon analyses—lignin phenols

After lignin phenols were extracted with EtAc, samples need to be purified first with solid phase extraction (SPE) (Fig. 2.2). The HLB SPE cartridges (Waters Oasis, 200 mg, 6 mL) were activated by rinsing the cartridges with 6 mL methanol, subsequently the cartridge was sealed on the bottom with a Luer cap and 5 mL methanol were added overnight. On the next day, the cartridges were successively rinsed with 6 mL Milli-Q water (twice), 6 mL methanol (twice), and 6 mL EtAc (twice). Samples were redissolved in 1 mL EtAc and loaded onto activated HLB cartridges, then eluted with 59 mL EtAc (Fig. 2.2). The top of the cartridges was covered with a piece of clean aluminum foil which can prevent external impurities from falling into the sample during rinsing. The eluates were dried and transferred to 1.5 mL vial with 1 mL EtAc and filtered with PTFE filter (13 mm, 0.22 µm) (Fig. 2.2). The filtrate was dried under a gentle stream of nitrogen (40 °C) and subsequently re-dissolved in 150 µL methanol for next HPLC separation.

Table 2.1 The binary gradient of mobile phases of the HPLC method to separate lignin phenols. Solvent A: methanol/acetonitrile (1:1, v:v); Solvent B: acetic acid solution (0.2 %). Flow rate = 0.8 mL/min.

Time (min)	0.0	3.0	8.0	15.0	20.0	25.0	33.0	40.0	45.0	54.0	55.0	62.5
A (%)	10	10	15	20	20	25	25	30	100	100	10	10

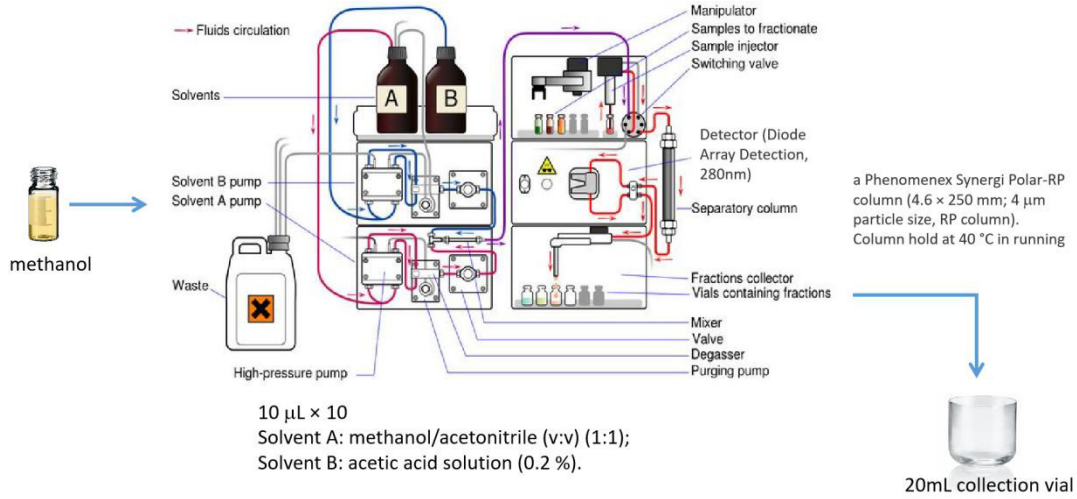

Figure 2.3. HPLC separation of lignin phenols. Digram of HPLC is from *https://chemdictionary.org/hplc/*

Abundance of lignin phenols were determined on a Agilent 1200 HPLC system coupled to a diode array detector (DAD). The HPLC was equipped with a Phenomenex Synergi Polar-RP column (4.6×250 mm; 4 µm particle size, RP column) hold at 40 °C in running and a binary gradient program of increasing polarity using solvent A (methanol:acetonitrile (v:v) = 1:1) and solvent B (acetic acid solution, 0.2 %) (Table 2.1) was used to achieve chromatographic separation of the major lignin phenols (Fig. 2.3). Following HPLC fraction collection, isolated fractions were transferred to 40 mL vials, and the HPLC collection containers were rinsed with 3×0.5 mL Milli-Q water and 3×0.5 mL EtAc. The lignin phenols were recovered from the washing by liquid-liquid extraction with 3×3 mL EtAc. Isolated fractions were dried under a stream of nitrogen (40 °C), then transferred to 4 mL vials and stored in the fridge (4 °C) until further radiocarbon measurement. A small aliquot of purified phenols was used to check identity and purity by GC-MS.

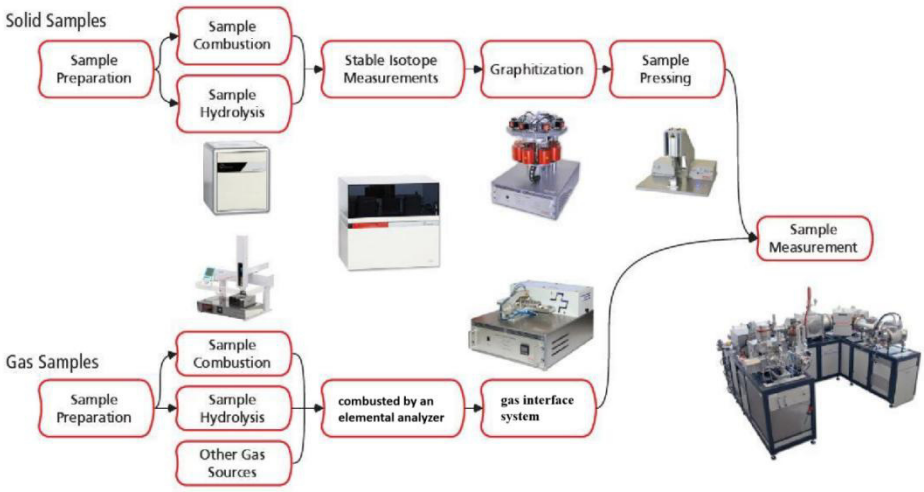

Figure 2.4. A simplified flow chart of radiocarbon measurement by MICADAS.

Radiocarbon measurements followed the protocol described in Mollenhauer et al. (2021). Briefly, isolated lignin phenol fractions were transferred (3 times) to 25 µL tin capsules with a minimum amount of methanol and kept in a holding tray (20 min.). Following the third transfer the holding tray was placed in a desiccator and stored evacuated (150 mbar) inside an oven (40 °C) for 48 h. After drying in the desiccator and oven, samples were folded as small as possible. Each tin ball was stored in a labeled 1.5 mL glass vial until analysis. Analyses were carried out by a Mini Carbon Dating System (MICADAS; Synal et al., 2007). Samples were combusted using an elemental analyzer coupled to MICADAS via the gas interface system (Wacker et al., 2013) (Fig. 2.4). The radiocarbon data are normalized to and corrected by standards NIST oxalic acid II and phthalic acid.

Radiocarbon dating of organic matter in sediment samples was similar as above. Briefly, freeze-dried samples were weighed into silver boats and the inorganic carbon was removed with 6 M hydrochloric acid covered and dried on a 60 °C heating plate. After carbonate removal, samples in the silver boats were folded into a tin boat to be combusted in the elemental analyzer at 950 °C. The resulting gas was transferred into the automated graphitization system (Wacker et al., 2010) for graphitization to produce graphite targets for measurement in the MICADAS (Fig. 2.4).

Radiocarbon data are reported as fraction modern carbon ($F^{14}C$). The initial radiocarbon content was calculated using the following equation (Schefuß et al., 2016):

$$\Delta^{14}C_{initial} = (F^{14}C\ e^{\lambda t} - 1) \times 1000\ ‰ \quad (2.1)$$

$F^{14}C$ is the measured fraction modern, λ is the decay constant ($1/8267\ yr^{-1}$) of ^{14}C, and t is time since deposition in years. The radiocarbon age, referred as to conventional radiocarbon age (T) is calculated as following:

$$T = -8033 \times \ln(F^{14}C) \quad (2.2)$$

The radiocarbon content of the past atmosphere differed from the modern atmosphere, conventional radiocarbon ages can not be directly converted into calendar ages. The reporting of true calendar ages requires conventional radiocarbon ages to be compared with other geochronological ages that have been independently derived. All independent derivations are included in international calibration data set such as IntCal 20 (Heaton et al., 2020; Stuiver and Reimer, 1993). The atmospheric radiocarbon content at the time of deposition ($\Delta^{14}C_{atm}$) was taken from the atmospheric $\Delta^{14}C$ record of IntCal 20 (Heaton et al., 2020; Stuiver and

Reimer, 1993). The offset of the initial radiocarbon contents of OC fractions to that of the past atmosphere ($\Delta^{14}C_{atm}$) is calculated as (Schefuß et al., 2016):

$$\Delta\Delta^{14}C_{initial} = \Delta^{14}C_{initial} - \Delta^{14}C_{atm} \quad (2.2)$$

The apparent initial (conventional) ^{14}C age is calculated from the initial radiocarbon content (Schefuß et al., 2016):

$$^{14}C \text{ age} = -8033 \times \ln[(1 + \Delta^{14}C_{initial}/1000) / (1 + \Delta^{14}C_{atm}/1000)] \text{ (year)} \quad (2.3)$$

In this thesis, the radiocarbon ages of TOC and biomarkers used in discussion are the conventional ^{14}C age, the $\Delta^{14}C$ values are the initial radiocarbon content $\Delta^{14}C$.

2.3.4. GDGTs analyses

The GDGTs data were obtained together with the same total lipid extracts that were used for *n*-alkane data published by Meyer et al. (2019). The isoprenoid GDGTs were determined using the methodology described in Meyer et al. (2016). In brief, the internal standard of GDGTs (C_{46}-GDGT) was added to known amounts of dry sediment, and total lipid extracts were obtained by ultrasonication with dichloromethane:methanol = 9:1 (vol vol^{-1}) three times. After extraction and saponification, neutral compounds (including GDGTs) were recovered with *n*-hexane. Different compound classes were separated by 1% deactivated SiO_2 column chromatography. Polar compounds (including GDGTs) were eluted with methanol:dichloromethane = 1:1 (vol vol^{-1}). Afterward they were dissolved in hexane:isopropanol = 99:1 (vol vol^{-1}) and filtered with a polytetrafluoroethylene filter (0.45 µm pore size). Samples were brought to a concentration of 2 µg μL^{-1} prior to GDGT analysis. GDGTs were analyzed by HPLC and a single quadrupole mass spectrometer (Meyer et al., 2017).

3. Manuscipt I

Deglacial records of terrigenous organic matter accumulation off the Yukon and Amur rivers based on lignin phenols and long-chain *n*-alkanes

Mengli Cao[1] , Jens Hefter[1], Ralf Tiedemann[1,2], Lester Lembke-Jene[1], Vera D. Meyer[3], and Gesine Mollenhauer[1,2,3]

[1] Alfred-Wegener-Institut, Helmholtz-Zentrum für Polar-und Meeresforschung (AWI), 27570 Bremerhaven, Germany

[2] Department of Geosciences, University of Bremen, 28359 Bremen, Germany

[3] MARUM–Center for Marine Environmental Sciences, University of Bremen, 28359, Bremen, Germany

Published in *Climate of the Past* 2023, Vol. 19, 159-178

Abstract

Arctic warming and sea level change will lead to widespread permafrost thaw and subsequent mobilization. Sedimentary records of past warming events during the Last Glacial–interglacial transition can be used to study the conditions under which permafrost mobilization occurs and which changes in vegetation on land are associated with such warming. The Amur and Yukon rivers discharging into the Okhotsk and Bering seas, respectively, drain catchments that have been, or remain until today, covered by permafrost. Here we study two marine sediment cores recovered off the mouths of these rivers. We use lignin phenols as biomarkers, which are excellently suited for the reconstruction of terrestrial higher plant vegetation, and compare them with previously published lipid biomarker data. We find that in the Yukon basin, vegetation change and wetland expansion began already in the early deglaciation (ED; 14.6–19 ka). This timing is different from observed changes in the Okhotsk Sea reflecting input from the Amur basin, where wetland expansion and vegetation change occurred later in the Pre-Boreal (PB). In the two basins, angiosperm contribution and wetland extent all reached maxima during the PB, both decreasing and stabilizing after the PB. The permafrost of the Amur basin began to become remobilized in the PB. Retreat of sea ice coupled with increased sea surface temperatures in the Bering Sea during the ED might

have promoted early permafrost mobilization. In modern Arctic river systems, lignin and *n*-alkanes are transported from land to the ocean via different pathways, i.e., surface runoff vs. erosion of deeper deposits, respectively. However, accumulation rates of lignin phenols and lipids are similar in our records, suggesting that under conditions of rapid sea level rise and shelf flooding, both types of terrestrial biomarkers are delivered by the same transport pathway. This finding suggests that the fate of terrigenous organic matter in the Arctic differs on both temporal and spatial scales.

3.1. Introduction

Climate warming caused by anthropogenic perturbation affects the Arctic more strongly than other regions of the world. Warming climate induces environmental changes that accelerate degradation of organic matter (OM) stored in permafrost and promote greenhouse gas release (Strauss et al., 2013; Hugelius et al., 2014; Schuur et al., 2015). Permafrost, or permanently frozen ground, is soil, sediment or rock that remains at or below 0 °C for at least 2 consecutive years. It occurs both on land and on the continental shelves offshore and underlies about 22% of the Earth's land surface (Brown et al., 2002; Wild et al., 2022). Permafrost regions around the world store twice as much carbon as is contained in the atmosphere at present (Hugelius et al., 2014; Friedlingstein et al., 2020). Across the northern circumpolar permafrost regions, the surface permafrost carbon pool (0–3 m depth) amounts to 1035±150 Pg (Hugelius et al., 2014). Warming climate may lead to increased mobilization of this carbon pool, while it also affects the type and extent of the vegetation cover, which in turn influences permafrost stability.

During the most recent interval of rapid global warming from the end of the Last Glacial Maximum (LGM) to the early Holocene (~ 19–11 ka), the climate system underwent large-scale change (Clark et al., 2012). Viau et al. (2008) found that the summer temperatures in eastern Beringia (the non-glaciated region between the Eurasian and the Laurentian ice sheet during the Late Pleistocene) during the LGM were approximately 4 °C lower than the present and increased rather rapidly toward the Holocene. Sea ice extent and distribution changed dramatically, with consequences for atmospheric moisture content (Ballantyne et al., 2013) and increased heat transport from the oceans to the continental interiors (Lawrence et al., 2008). The increase in precipitation inland as a result of sea ice retreating affects the stability of permafrost in the Arctic (Vaks et al., 2020). Together with increasing air temperatures during the deglaciation, sea ice retreat may thus have led to rising ground temperatures, active layer deepening and permafrost degradation.

Increased moisture due to sea ice retreat leads to heavier winter snowfall inland (Liu et al., 2012; Park et al., 2013). Menard et al. (1998) reported that ground surface temperature was higher where ground is covered by thick snow and shrubs and trees than where it was covered

by both thin snow and vegetation (moss and lichen). During the last deglacial toward the Holocene, warming ground ice melted, causing the land surface to collapse into space previously occupied by ice wedges, a process called thermokarst. This led to the formation of thermokarst lakes and thermoerosional valleys as well as rivers and also likely the release of carbon from thawed deposits (Walter et al., 2006; Walter Anthony et al., 2014). During millennia following the formation of thermokarst lakes, mosses and other plants grew in and around them, which may in part have offset permafrost carbon release (Walter Anthony et al., 2014; Schuur et al., 2015; Turetsky et al., 2020). Several studies suggested major deglacial changes in the vegetation of permafrostaffected areas during the last deglaciation, including the Lena river basin (Tesi et al., 2016), the Yukon Territory (Fritz et al., 2012), the Amur river basin (Seki et al., 2012), and the Sakhalin peninsula and Hokkaido (Igarashi and Zharov, 2011), the latter two bounding the Okhotsk Sea to the northwest and north. Vegetation has a profound impact on distribution and thickness of active layers and permafrost in cold regions; for example, evidence exists that permafrost temperature in the tundra is lower than in the boreal forest in northwestern Canada (Smith et al., 1998), illustrating the strong effects of vegetation on permafrost stability. Changes in vegetation should therefore be considered when investigating permafrost stability in a changing climate.

Biomarker compositions, distributions and contents in marine sediments can help to elucidate the vegetation development in adjacent land areas (Winterfeld et al., 2015, 2018; Keskitalo et al., 2017; Martens et al., 2019; Wu et al., 2022). Lignin is a biopolymer exclusively biosynthesized by vascular plants. The relative abundance of individual phenolic monomers varies between different plant types, and the different phenols also differ in their stability towards degradation (Hedges and Mann, 1979; Hedges et al., 1988; Lobbes et al., 2000; Feng et al., 2013a; Wild et al., 2022). Ratios between different phenolic monomers are thus sensitive indicators for vegetation type and depositional history of OM originating from land plants (Hedges and Mann, 1979; Hedges et al., 1988).

Previous studies found that the delivery of lignin from land to the ocean is mainly controlled by surface discharge in modern Arctic river systems (Feng et al., 2013a) and has the potential to provide information on surface runoff processes and wetland extent (Tesi et al., 2016; Feng et al., 2015a). Long-chain *n*-alkanes with a strong predominance of the odd carbon number homologues, as well as even-numbered long-chain *n*-alkanoic acids, derived from the epicuticular waxes of vascular and aquatic plants (Eglinton and Hamilton, 1967). In contrast to lignin phenols, sedimentary records of *n*-alkanes, due to their recalcitrance, likely trace terrigenous OM which has been mobilized from thawing permafrost deposits in modern Arctic river systems (Feng et al., 2013a) and may be transported into the marine sediment primarily following coastal erosion during shelf flooding (Winterfeld et al., 2018). Previous studies have reconstructed the mobilization of terrigenous OM from degrading permafrost in

the Okhotsk (Winterfeld et al., 2018) and Bering shelves (Meyer et al., 2019) during the last deglaciation based on long-chain n-alkyl lipid results. However, no records exist that combine lignin and *n*-alkane data to explore the potentially different transport of terrestrial OM archived in Arctic marine sediments during the last deglaciation.

Biomarker records can also be used to infer environmental conditions like sea surface temperatures (SSTs) or sea ice extent that influence heat and moisture transport from the ocean to the continents. A commonly used proxy for the reconstruction of SSTs is the TEX_{86}, which relies on the relative abundance of so-called isoprenoid glycerol dialkyl glycerol tetraether lipids (GDGTs) with different numbers of cyclopentyl moieties (Schouten et al., 2002). These compounds are derived from the membranes of marine Thaumarchaeota and have been found to record temperature conditions of their habitat. Sea ice reconstructions rely on the abundance of highly branched isoprenoids derived from diatoms adapted to life in sea ice (IP_{25}; Belt et al., 2007). Applying the TEX_{86} temperature proxy, Meyer et al. (2016) found that atmospheric teleconnections with the North Atlantic were a widespread control on SST in the northwestern Pacific and its marginal seas during the past 15.5 kyr. The TEX_{86}-derived SST records imply that the strength of the atmospheric teleconnections with the North Atlantic decreased during the deglaciation, and summer insolation and CO_2 concentration in the atmosphere were important factors driving the SST evolution during this time (Meyer et al., 2016). GDGTs can also be used to reconstruct terrigenous input to the ocean, when the relative abundance of branched GDGTs derived mainly from soil bacteria and of isoprenoid GDGTs is quantified by the branched and isoprenoid tetraether (BIT) index (Hopmans et al., 2004). According to lignin phenols and the BIT index, Seki et al. (2014a) found that terrestrial OM from the Amur river is a major source of OM in the North Pacific Ocean at present and that terrestrial OM in surface sediments is dominated by gymnosperms in the Okhotsk Sea.

In this study, we present downcore records of lignin phenols from the early deglaciation to the Holocene obtained from sediment cores from off the Amur and Yukon rivers draining permafrost affected by deglacial climate change. These sites in the Okhotsk and Bering seas, respectively, record conditions at two contrasting river-dominated continental margins in the North Pacific area. We interpret the lignin phenol records in the context of vegetation and wetland development and investigate the temporal evolution of the different pathways of terrigenous OM export to the ocean by comparing different types of terrigenous biomarker records, i.e., *n*-alkanes from published studies and new lignin phenol data as well as BIT index values. We further investigate new and published biomarker-based reconstructions of SST, as well as published biomarker-based sea ice reconstructions, to unravel the controls on terrigenous OM transport to the ocean from thawing permafrost landscapes.

3.2. Study area

The Bering Sea is located north of the Pacific Ocean (Fig. 3.1). The Yukon River is the fourth-largest river in North America in terms of annual discharge and drains into the Bering Sea (Holmes et al., 2012). The deglacial sediments from the Bering Sea contain records of both sea-level-rise-induced erosion of the vast Bering Shelf and runoff from the Yukon River (Kennedy et al., 2010; Meyer et al., 2019). The Yukon basin was mostly unglaciated during the LGM but had permafrost (Schirrmeister et al., 2013). Although some permafrost in the Yukon basin thawed during the last deglaciation (Meyer et al., 2019; Wang et al., 2021), most of the basin is still covered by permafrost today (Fig. 3.1). Arctic coastal erosion is rapid today, with average rates of erosion at 0.5 m yr^{-1} (Lantuit et al., 2012; Irrgang et al., 2022). Sea level rise will lead to greater wave impact on arctic shorelines, which increases the coastal erosion (Lantuit et al., 2012). This suggests that during past times of rapid sea level increase like in the B/A and PB periods, coastal erosion was more intense than it is today (Lambeck et al., 2014; Fig. 2b). Coastal erosion causes a large amount of terrigenous OM to enter the ocean (Couture et al., 2018; Winterfeld et al., 2018), suggesting that during past periods of sea level rise, erosive forces similar to those today or even stronger were at play supplying vast quantities of terrigenous materials to marine sediments. Pollen records indicate there were no significant changes in vegetation pattern from the LGM to about 16 ka, but after about 16 ka, birch (one of the first trees to develop after the glacier retreated) pollen became significantly more abundant from western Alaska to the Mackenzie River (Bigelow, 2013). In the early Holocene, significant *Populus–Salix* (cottonwood–willow) woodland development occurred in interior Alaska and in the Yukon Territory (Bigelow, 2013), suggesting both increasing summer temperature and moisture. Alder grows in a warmer and wetter environment than birch, and it is a common genus in Yukon Holocene pollen records (Schweger et al., 2011). Today the catchment of the Yukon River is covered by spruce forest (20%), grassland (40%), shrubland (20%), and open water and wetlands associated with the lowland areas (8%) (Amon et al., 2012).

The Okhotsk Sea, a semi-enclosed marginal sea located in the west of the North Pacific, is known as the southernmost region of seasonal sea ice in the Northern Hemisphere today (Fig. 3.1). The continental slope off Sakhalin Island in the Okhotsk Sea receives runoff from the Amur river, the largest river catchment in East Asia. The Amur is also one of the largest rivers in the world in terms of the annual total output of dissolved OM and substantially influences the formation of seasonal sea ice (Nakatsuka et al., 2004). The river originates in the western part of Northeast China and flows east, forming the border between China and Russia. The catchment of the Amur transitioned from complete permafrost coverage during the LGM (Vandenberghe et al., 2014) to almost entirely permafrost-free conditions at present. The climate of the Amur basin today is largely determined by continental patterns from Asia,

as the Asia monsoon influences the amount of precipitation from the Pacific transported to this region during the summer. Previous studies found that herbaceous plants were the predominant vegetation in the Last Glacial periods in the Amur basin and were replaced by gymnosperms during the deglaciation and Holocene (Bazarova et al., 2008; Seki et al., 2012). These authors concluded that the variations in vegetation change agree well with climate changes in eastern Russia, with dry conditions in the Last Glacial followed by wetter climate in the deglaciation and early Holocene (Seki et al., 2012). Now, the vegetation of the Amur basin belongs mostly to the Taiga zone, with larch as the most common species in the area. The upper reaches of the Amur basin belong to the coniferous continental taiga at present. The central areas are dominated by mixed coniferous and broad-leaved forests, and the coniferous larch forests are the predominant vegetation in the lower Amur basin.

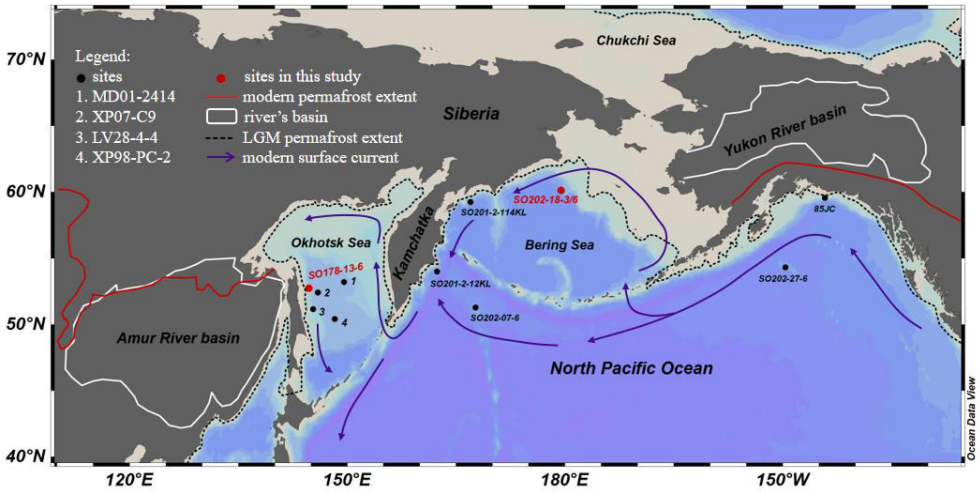

Figure 3.1 Study area. Red dots indicate locations of sediment cores investigated in this study; black dots denote cores described in previous studies. (1) Site MD01-2414 (Lattaud et al., 2019; Lo et al., 2018), (2) Site XP07-C9 (Seki et al., 2012), (3) Site LV28-4-4 (Winterfeld et al., 2018), (4) Site XP98-PC-2 (Seki et al., 2014b).

3.3. Material and methods

3.3.1. Sampling and age control

The piston core SO202-18-3 (60.13° N, 179.44° W; water depth: 1111 m) and neighboring kasten core SO202-18-6 (60.13◦ N, 179.44◦ W; water depth: 1107 m) were recovered from the northeastern continental slope of the Bering Sea in 2009 during R/V Sonne cruise SO202-INOPEX (Gersonde, 2012). The two cores can be treated as one composite record according to their ultrahigh-resolution micro-X-ray-fluorescence data, sediment facies analysis of laminae and radiocarbon dating results (Kühn et al., 2014). It represents an apparently continuous sedimentary sequence dated back to the Last Glacial (~ 25 ka) (Kühn et al., 2014). Selected samples from core SO202-18-6 (n=20, 10–589 cm core depth, 6.23–12.65 ka) and

from core SO202-18-3 (n=29, 447–1423 cm core depth, 12.99–24.1 ka) with an average temporal resolution of ~ 510 years were analyzed for lignin-derived phenol contents.

The 23.7 m long piston core SO178-13-6 (52.73° N, 144.71° E) was collected from the Sakhalin margin in the Okhotsk Sea during the expedition SO178-KOMEX with R/V Sonne (Dullo et al., 2004) (Fig. 3.1), with the lowermost interval corresponding to ~ 17.5 ka (Max et al., 2014). Selected samples (n=51, 100–2340 cm core depth, 1.11–17.27 ka) from core SO178-13-6 were analyzed for lignin-derived phenol contents with an average temporal resolution of ~ 340 years. Radiocarbon-based age models for the two cores are from Kühn et al. (2014) for core SO202-18-3/6 and Lembke-Jene et al. (2017) for core SO178-13-6. The time interval covered by the records is subdivided into five intervals: the early deglaciation (ED; 19–14.6 ka), the B/A (14.6–12.9 ka), the Younger Dryas (YD; 12.9–11.5 ka), the Pre-Boreal (PB; 11.5–9 ka) and the Holocene (< 9 ka).

3.3.2. Laboratory analyses

The extraction of lignin phenols was carried out based on the method of Goñi and Montgomery (2000) and as described in Sun et al. (2017). Dried samples were oxidized with CuO (~ 500 mg) and ~ 50 mg ferrous ammonium sulfate in 12.5 mL 2N NaOH under anoxic conditions. The oxidation was conducted with a CEM MARS5 microwave accelerated reaction system at 150 °C for 90 min. After oxidation, known quantities of recovery standards (ethyl vanillin and trans-cinnamic acid) were added to the oxidation products. The alkaline supernatant was acidified to pH 1 with 37 % HCl. The reaction products were subsequently recovered by two successive extractions with ethyl acetate. The combined ethyl acetate extracts were evaporated under a stream of nitrogen, then re-dissolved in 400 µL pyridine. Prior to injection into the gas chromatograph–mass spectrometer (GC–MS), an aliquot (30 µL) was derivatized with 30 µL bis-trimethylsilyl-trifluoroacetamide (BSTFA) + 1 % trimethylchlorosilane (TMCS) (60 °C, 30 min). An Agilent 6850 GC coupled to an Agilent 5975C VL MSD quadrupole MS operating in electron impact ionization (70 eV) and fullscan (m/z 50–600) mode was used for analysis. The source temperature of the MS was set to 230 °C and the quadrupole to 150 °C. The GC was equipped with a DB-1 MS column (30 m × 0.25 mm i.d., film thickness 0.25 µm). Helium was used as a carrier gas at a constant flow rate of 1.2 mL min^{-1}. Samples were injected in splitless mode in a split/splitless injector (S/SL) held at 280 °C. The temperature of the GC–MS column was programmed from 100 °C (initially held for 8 min) and ramped at 4 °C min^{-1} to 220 °C, then at 10° C min^{-1} to 300 °C, with a final hold time of 5 min.

Eight lignin-derived phenols were analyzed in this study. They can be classifified into three groups according to their plant sources and structures:

1. vanillyl phenols (V) consisting of vanillin (Vl), acetovanillone (Vn) and vanillic acid (Vd);

2. syringyl phenols (S), comprising syringaldehyde (Sl), acetosyringone (Sn) and syringic acid (Sd);

3. cinnamyl phenols (C) that include p-coumaric acid (*p*-Cd) and ferulic acid (Fd).

Vanillyl phenols can be found in all vascular plants; syringyl phenols exist only in angiosperms. Cinnamyl phenols are exclusively present in non-woody tissues of vascular plants. Therefore, the S/V and C/V ratios can be used to distinguish lignin between woody and non-woody tissues of angiosperms and gymnosperms (Hedges and Mann, 1979) (Fig. 3.4). Since S and C phenols are more easily degraded than V phenols during lignin degradation, these two ratios can also be impacted by the degradation degree of lignin (Hedges et al., 1988; Otto and Simpson, 2006) (Fig. 3.4). Microbial degradation of lignin increases the relative abundance of phenolic acids of V and S phenols, and the ratios of vanillic acid to vanillin $(Ad/Al)_v$ and syringic acid to syringaldehyde $(Ad/Al)_s$ are commonly used to reconstruct the degradation degree of lignin (Ertel and Hedges, 1985; Hedges et al., 1988; Otto and Simpson, 2006) (Fig. 3.4).

Besides, we also included some other oxidation products that do not necessarily originate from lignin, such as 3,5-dihydroxybenzoic acid (3,5Bd) and para-hydroxybenzenes (P) like *p*-hydroxybenzaldehyde (Pl), *p*-hydroxybenzophenone (Pn) and *p*-hydroxybenzoic acid (Pd). Unlike lignin-derived phenols (V, S and C), 3,5Bd is absent in plant tissues but most enriched in peat (Goñi et al., 2000; Amon et al., 2012). The 3,5Bd/V ratio can be used as a tracer for wetland extent and to determine the degree of degradation for terrigenous OM (Fig. 3.4).

These compounds were identified based on retention time and mass spectra. Quantification was achieved by peak areas of the respective compounds and using individual five point response factor equations obtained from mixtures of commercially available standards analyzed periodically. The yields of Pl, Vl and Sl were corrected by the recovery rate of ethyl vanillin, and the recovery rate of trans-cinnamic acid was applied to correct the yield of other lignin-derived compounds and 3,5Bd (Goñi et al., 2000; Goñi and Montgomery, 2000). The standard deviation was determined from repeated measurements of a laboratory internal standard sediment extract (n=12), and for the carbon-normalized concentration of the sum of the eight lignin phenols (Λ8, mg 100 mg^{-1} OC) it equals 0.31.

Mass accumulation rates (MARs) of vascular-plantderived lignin phenols were calculated as follows:

$$MAR = SR \times \rho\ , \tag{3.1}$$

$$MAR\text{-}lignin = MAR \times \Sigma 8 : 100, \tag{3.2}$$

where MAR is the mass accumulation rate in grams per square centimeter per year, SR is the sedimentation rate in centimeters per year, and ρ is the dry bulk density in grams per cubic centimeter. MAR-lignin is the mass accumulation rate of lignin (mg cm^{-2} yr^{-1}). Σ8 represents the content of the eight lignin phenols in milligrams per 10 g of dry sediment.

According to previous studies, the odd-numbered *n*-alkanes in the range of C_{23} to C_{33} are almost exclusively terrigenous (Eglinton and Hamilton, 1967; Otto and Simpson, 2005). Therefore, we can use the medium- to long-chain-length (high molecular weight, HMW) *n*-alkanes to reflect the contribution of terrigenous OM. Lignin MARs were compared to published MARs of HMW *n*-alkanes from the Okhotsk Sea (Winterfeld et al., 2018) and the Bering Sea (Meyer et al., 2019). The MARs of HMW *n*-alkanes from the Bering Sea were recalculated from the published data (Meyer et al., 2019) in order to compare the results of the two sediment cores. The HMW *n*-alkanes quantified for the Bering Sea and Okhotsk Sea sediment cores are C_{23}, C_{25}, C_{27}, C_{29}, C_{31} and C_{33} (Fig. 3.2).

Alkanes also have been shown to provide a second marker for wetland extent via the Paq index (Ficken et al., 2000). It represents the relative proportion of medium-chain-length *n*-alkanes (C_{23} and C_{25}) to long-chain *n*-alkanes (C_{29} and C_{31}). The Paq ratios shown in our paper have been published by others. The Paq ratio of the SO202-18-3/6 core was published by Meyer et al. (2019). The Paq ratio of the SO178-13-6 core was published by Winterfeld et al. (2018). We also cited the Paq ratio of the XP07-C9 core (Seki et al., 2012), which was retrieved from the Okhotsk Sea (Fig. 3.1).

We further report here the relative abundances of isoprenoid GDGT lipids. These data were obtained together with the same total lipid extracts that were used for *n*-alkane data published by Meyer et al. (2019). The isoprenoid GDGTs were determined using the methodology described in Meyer et al. (2016). In brief, the internal standard of GDGTs (C_{46}-GDGT) was added to known amounts of dry sediment, and total lipid extracts were obtained by ultrasonication with dichloromethane:methanol = 9:1 (vol vol^{-1}) three times. After extraction and saponification, neutral compounds (including GDGTs) were recovered with n-hexane. Different compound classes were separated by 1% deactivated SiO_2 column chromatography. Polar compounds (including GDGTs) were eluted with methanol:dichloromethane = 1 : 1 (vol vol^{-1}). Afterward they were dissolved in hexane:isopropanol = 99 : 1 (vol vol^{-1}) and filtered with a polytetrafluoroethylene filter (0.45 µm pore size). Samples were brought to a concentration of 2 µg μL^{-1} prior to GDGT analysis. GDGTs were analyzed by high-performance liquid chromatography and a single quadrupole mass spectrometer (see Meyer et al., 2017, for more details).

The TEX_{86} index can be used as a SST proxy (Schouten et al., 2002), with the modified version TEX^{L}_{86} being applicable in settings where SST is below 15 °C (Kim et al., 2010). The regional calibration of SST and TEX^{L}_{86} is based on Seki et al. (2014b).

$$TEX^{L}_{86} = \log(GDGT\text{-}2/(GDGT\text{-}1 + GDGT\text{-}2 + GDGT\text{-}3)) \quad (3.3)$$

$$SST = 27.2 \times TEX^{L}_{86} + 21.8 \quad (3.4)$$

The GDGT-1, GDGT-2 and GDGT-3 are isoprenoid tetraether lipids with 1, 2 and 3 cyclopentane rings, which were detected by a single-quadrupole mass spectrometer. The MS detector was set for selected-ion monitoring of the following (M + H)+ ions: m/z 1300.3 (GDGT-1), 1298.3 (GDGT-2) and 1296.3 (GDGT-3) (Meyer et al., 2016). SST is the sea surface temperature in degrees Celsius.

The BIT index proxy is based on the abundance ratio of branched GDGTs to isoprenoid GDGTs (Hopmans et al., 2004); higher BIT values suggest more contributions from terrestrial soil OM (Weijers et al., 2006b; Fig. 3.3). The BIT index is calculated as BIT = (GDGT-I + GDGT-II + GDGT-III)/(GDGT-I + GDGT-II + GDGT-III + GDGT-IV). GDGT-I, GDGT-II and GDGT-III refer to the concentration of branched GDGT; GDGT-IV refers to the concentration of isoprenoid GDGT (crenarchaeol). The MS detector was set for selected-ion monitoring of the following (M + H)+ ions: m/z 1022 (GDGT-I), 1036 (GDGT-II), 1050 (GDGT-III) and 1292.3 (GDGT-IV) (Meyer et al., 2016).

3.4. Results

3.4.1. Lignin concentrations and MARs

Lignin phenol concentrations were 0.19–1.43 mg 100 mg^{-1} OC (Λ8) or 0.20–1.07 mg 10 g^{-1} sediment (Σ8) in the Bering Sea sediments and 0.32–1.29 mg 100 mg^{-1} OC or 0.40–2.16 mg 10 g^{-1} sediment in the Okhotsk Sea record. Overall, the MAR of lignin is lower in the Bering Sea than in the Okhotsk Sea (Fig. 3.2c and d). During the ED, the lignin MAR began to increase in the Bering Sea sediment and kept increasing until it reached a maximum (17.70 μg cm^{-2} yr^{-1}) at the B/A–YD transition (Fig. 3.2c). After the B/A, the lignin MAR started to decrease in the Bering Sea until the onset of the YD. The lignin MAR in the Bering Sea reached a more pronounced but short maximum (20.61 μg cm^{-2} yr^{-1}) at the YD–PB transition, followed by a decrease to the Holocene. The lignin MAR in the Okhotsk Sea is more variable than in the Bering Sea record (Fig. 3.2d). The lignin MAR shows an initial maximum in the B/A but reaches a more pronounced second peak (31.16 μg cm^{-2} yr^{-1}) in the early PB. Similar to the Bering Sea, the lignin MAR decreased after about 11 ka and into the Holocene; however, the lignin MAR in the Okhotsk Sea sediment featured a rather broad maximum between B/A and early Holocene.

Deglacial changes in the MARs of HMW *n*-alkanes have previously been reported for the same cores (Meyer et al., 2019; Winterfeld et al., 2018). The MAR of lignin and HMW *n*-

alkanes changed mostly synchronously in the Bering Sea, but in the Okhotsk Sea, the increase in lignin MAR occurred later than in n-alkane MAR and notably also later than in the Bering Sea (Fig. 3.2c and d); n-alkane MAR in the Okhotsk Sea featured two similar maxima in the B/A and during the YD–PB transition, while the lignin MAR maximum in the B/A is less pronounced than that at the YD–PB transition. Lignin MARs are more variable than n-alkane MARs between 10 and 7.8 ka.

3.4.2. Sea surface temperature in the Bering Sea (BIT and TEX^{L}_{86})

Most BIT values in the Bering Sea are below the commonly assumed threshold value of 0.3 (Fig. 3.3Ic), above which SST reconstructions are potentially biased by terrigenous iso-GDGTs (Weijers et al., 2006b). We are confident that in our study area, marine-derived GDGTs dominate over terrigenous GDGTs, suggesting that TEX^{L}_{86} is not biased by terrigenous input.

The SST estimates derived from the TEX^{L}_{86} index are shown in Fig. 3.3Ic. The deglacial evolution of the TEX^{L}_{86}-derived SST shows an overall warming, from ~ 4.5 °C at 23.4 ka to 10.8 °C at 12.0 ka. The SST in the Bering Sea remained rather constant during the LGM and the ED. The onset of the B/A is characterized by an abrupt temperature increase of ~ 2 °C, followed by a decrease at the end of the B/A. At the end of the YD, the SST abruptly increased by ~ 2 °C while staying rather constant from 11.5 to 10 ka. At the end of the PB, the SST decreased slowly by 1 °C from 10.5 to 9.0 ka. During the Holocene, the SST ranged between 8.0 and 9.7 °C.

3.4.3. Lignin source and degradation indicators

Vegetation development can be assessed using the S/V (angiosperm vs. gymnosperm) and C/V ratios (woody tissues vs. non-woody tissues) (Hedges and Mann, 1979). The 3,5Bd/V and Paq ratios can be used to indicate the change in wetland extent in the study area (Goñi et al., 2000; Amon et al., 2012). Similar to (Ad/Al)s and (Ad/Al)v ratios, S/V, C/V and 3,5Bd/V ratios are also affected by degradation processes (Ertel and Hedges, 1985; Hedges et al., 1988; Otto and Simpson, 2006).

The S/V and C/V ratios yielded values of 0.36–0.86 and 0.11–0.46 in the Bering Sea (Fig. 3.4Ia and b), while slightly higher ratios of 0.41–0.92 and 0.19–0.70 were obtained in the Okhotsk Sea (Fig. 4IIa and b). The standard deviations for S/V and C/V are 0.08 and 0.10, respectively. In the Bering Sea, the S/V ratios began to increase from 18 ka and kept increasing until they reached a maximum in the transition of the YD to the PB. The change in C/V values was not as obvious as S/V values, but they also reached their maximum at the YD–PB transition. Subsequently, S/V and C/V ratios decreased during the Holocene and reached minima at the top of the core.

In the Okhotsk Sea, the S/V values increase slowly from the ED to PB, but the C/V ratios do not display an obvious increase over the same time, except for a maximum in C/V ratios around 15 ka. Minimum values were found in the ED, and values remained rather low before the YD–PB transition. After reaching maxima in the PB, S/V and C/V ratios decreased during the Holocene, stabilizing at a higher level than during the ED.

In the Bering Sea, the 3,5Bd/V ratio ranged from 0.09 to 0.20 (Fig. 3.4Id) (standard deviation: 0.02). From the end of the LGM to the YD, the 3,5Bd/V ratio decreased slowly but began to increase and reached a small local maximum at the YD–PB transition. During the Holocene, the 3,5Bd/V ratio decreased again and reached the lowest values near the top of the core.

The 3,5Bd/V ratios in the core from the Okhotsk Sea range from 0.10 to 0.23 (Fig. 3.4IId) (standard deviation: 0.02). The values were rather uniform throughout the record, with the exception of a maximum during the PB, and the ratio remained rather stable afterwards.

The $(Ad/Al)_s$ and $(Ad/Al)_v$ ratios ranged from 0.19 to 0.80 (standard deviation: 0.24) and 0.51 to 1.04 (standard deviation: 0.26), respectively, in the Bering Sea (Fig. 3.4Ie and f). Maxima in $(Ad/Al)_s$ and $(Ad/Al)_v$ were reached in the Holocene and YD. The Ad/Al ratio in the Bering Sea showed low values during the PB and increased towards the early Holocene, when the highest values of Ad/Al were obtained.

In the Okhotsk Sea, the $(Ad/Al)_s$ and $(Ad/Al)_v$ ratios are overall similar and range from 0.30 to 0.79 (standard deviation: 0.24) and from 0.22 to 0.89 (standard deviation: 0.26), respectively (Fig. 3.4IIe and f). The $(Ad/Al)_v$ ratio decreased slowly until 10.5 ka, when the biomarker MARs reached maxima. All minima and maxima in both indices occurred in the PB. Throughout the rest of the Holocene, Ad/Al values remained rather constant.

3.5. Discussion

3.5.1. Terrigenous OM mobilization during the last deglaciation

Permafrost remobilization has a strong impact on local topography, vegetation and OM fate (Feng et al., 2013a; Walter Anthony et al., 2014). We observed distinct MAR peaks of terrigenous biomarkers in both sediment cores, but the temporal evolution of MARs and the relative magnitude of change differ between the sites.

In the Bering Sea, lignin MAR began to increase at ~ 17.5 ka, which coincides with the onset of sea level rise (Fig. 3.2). Wang et al. (2021) found that the Alaskan mountain glaciers and Laurentide and Cordilleranice sheets reached their maximum extent from 20 to 16.5 ka, suggesting permafrost of the Yukon basin may not have begun to be remobilized during this time. The Yukon River discharge did not increase until 16.5 ka (Wang et al., 2021), and the terrigenous OM transported by surface runoff thus may not have increased at ~ 17.5 ka. Keskitalo et al. (2017) found that the OM flux accumulated on the East Siberian Shelf during

the PB–Holocene transition was high, and this OM was characterized by high S/V (0.28–0.90; mean value is 0.50) and C/V values (0.19–0.60; mean value is 0.35) (Fig. 3.5). These authors suggested the ice complex deposit (ICD) as a significant source of OM in the East Siberian Sea during this time. Previous studies indicated that ICD samples yield relatively high S/V and C/V ratios ranging from 0.47 to 1.01 and from 0.03 to 0.82, indicating the OM is likely to stem from grass-like material typical of a tundra or steppe biome (Schirrmeister et al., 2013; Tesi et al., 2014; Winterfeld et al., 2015). The S/V (0.50–0.75; mean value is 0.62) and C/V (0.22–0.36; mean value is 0.28) values of the Bering Sea sediment core from 24 to 17.5 ka are high (Fig. 3.4I), which may indicate that this terrestrial OM is likewise derived from the ICD. The organic-rich ICD on the coasts of the Bering Sea might have been inundated or eroded by rising sea level in the ED, which may contribute to the lignin MAR in the Bering Sea at ~ 17.5 ka.

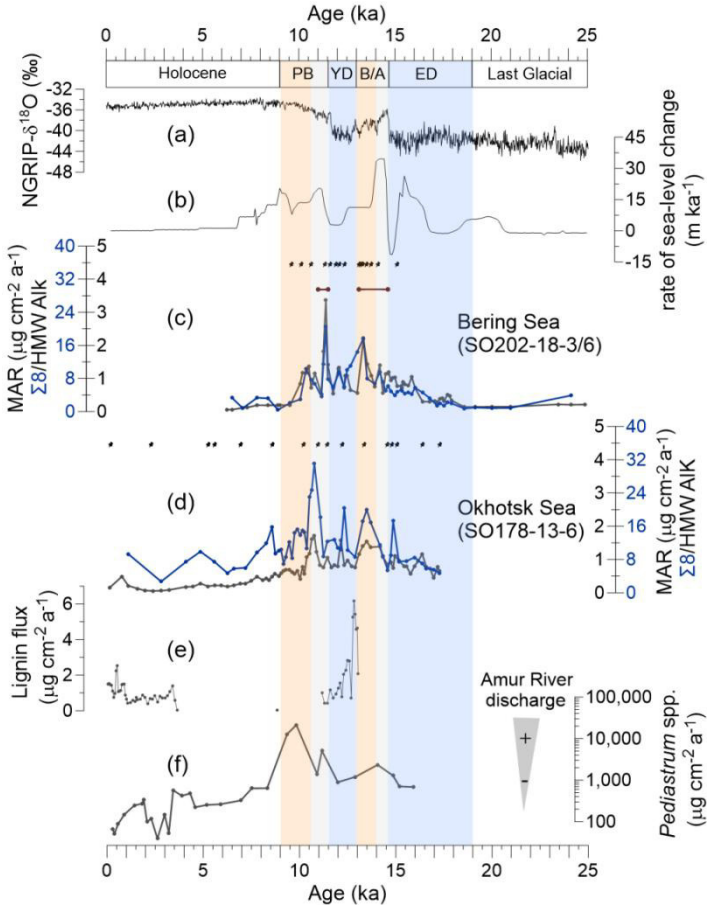

Figure 3.2 Proxy records of terrestrial organic matter supply and environmental records of deglacial changes. (a) Greenland NGRIP $\delta^{18}O$ (Rasmussen et al., 2008). (b) Global rate of sea level change (Lambeck et al., 2014). (c) Mass accumulation rate (MAR) of lignin phenols (blue) and high-molecular-weight (HMW) *n*-alkanes (black; Meyer et al., 2019) from core SO202-18-3/6. (d) MAR of lignin phenols (blue) and HMW *n*-alkanes (black; Winterfeld et al., 2018) from core SO178-13-6. Pin marks at the top of (c) and (d) show age control points, the accelerator mass spectrometry ^{14}C dates for SO202-18-3/6 (Kühn et al., 2014) and SO178-13-6 (Max et al., 2012). Brown bars in panel (c) indicate laminated/layered (anoxic) core sections (Kühn et al., 2014). (e) Lignin flux from core 4-PC1 (Chukchi Sea, Martens et al., 2019). (f) Accumulation rate of chlorophycean freshwater algae *Pediastrum* spp. from core LV28-4-4 (Winterfeld et al., 2018). Blue boxes represent the cold spells the early deglaciation (ED) and Younger Dryas (YD). Orange boxes are for the warm phases Bølling–Allerød (B/A) and Pre-Boreal (PB). Gray boxes highlight the periods of meltwater pulse 1A (MWP-1A) and 1B (MWP-1B).

HMW *n*-alkane accumulation in the Bering Shelf started to increase around 16.5 ka (Fig. 3.2), which coincides with the beginning retreat of Alaskan glaciers (Dyke, 2004). The glacial meltwaters drained through the Yukon River and enhanced fluvial discharge to the Bering Sea (Wang et al., 2021). The ICD in Alaska and Beringia might have started to be remobilized at ~ 16.5 ka (Meyer et al., 2019; Wang et al., 2021), subsequently enhancing the MAR of ICD-derived OM off the Bering Shelf. Thus, the increased S/V, C/V and Paq values near 17.5 ka (Fig. 3.4Ia–c) lend support to the notion that permafrost of the Yukon basin may have begun to be remobilized in the ED.

Retreat of sea ice will increase the SST, and open waters increase the moisture content of the atmosphere, so the transport of heat from the ocean via atmospheric pathways to continental interiors increases (Ballantyne et al., 2013; Vaks et al., 2020). Praetorius et al. (2015) found that SST warming commenced around 16.5 ka (core 85JC; Fig. 3.3If) in the northern Gulf of Alaska, and Méheust et al. (2018) observed rising SST of the northeastern Pacific by ~ 1.5 °C near 16 ka (core SO202-27-6; Fig. 3.3Ie) which agrees with our TEX^{L}_{86} SST record (core SO202-18-3/6; Fig. 3.3Ic). The same authors reconstructed sea ice extent based on the IP_{25} proxy to decrease from around 16 ka in the northeastern Pacific (Fig. 3Ie). Jones et al. (2020a) reported that the sea ice in the Bering Sea is highly sensitive to small changes in winter insolation and atmospheric CO_2. Further evidence for regional climate warming in the hinterland of Alaska is provided by the Brooks Range glacial melting during a time of widespread cooling in the Northern Hemisphere (Dyke, 2004; Wang et al., 2021). Combined evidence from SST and sea ice reconstructions as well as records of glacial melting thus suggest that the permafrost of the Yukon basin may have begun to be remobilized at ~ 16 ka.

In the B/A, all biomarker fluxes increased and reached short maxima (Fig. 2c and d). The rate of sea level rise also reached a maximum since the LGM. If *n*-alkanes had been transported to the ocean primarily through coastal erosion, as is the case with the modern Arctic river transport systems (Feng et al., 2013a), then *n*-alkane MAR would have been at its maximum, but it was not. Warming may have caused widespread permafrost thaw in the Yukon basin in the B/A. At this time, SST increased, sea ice cover decreased (Méheust et al., 2018), and river discharge increased (Wang et al., 2021). Each process, or all of them combined, may have promoted diatom bloom events (Kühn et al., 2014; Fig. 3.2). The increase in S/V and decrease in $(Ad/Al)_{s,v}$ during the B/A indicate that the OM deposited in the Bering Sea during the B/A may have been derived from ICD. Similar to our findings, Martens et al. (2019) found relatively high lignin fluxes in the Chukchi Sea during the B/A (Fig. 3.2e) and showed that lignin deposited during this period was poorly degraded. The authors interpreted this degradation state as permafrost OM from ICD being the dominant source. The relative contribution of ICD and the main pathway of transportation (abrupt thaw or gradual thaw on

land) cannot be deduced from our data alone. Further analyses may reveal possible ICD contributions to lignin exported to the marine realm during this interval.

During the YD–PB transition, the Northern Hemisphere experienced an abrupt temperature increase; the maxima of biomarker MAR (Fig. 3.2c) indicate that the permafrost remobilization in the Yukon basin reached a peak at this time. The Yukon River discharge increased during the PB (Wang et al., 2021), which can also promote lignin flux. Evidence for widespread permafrost decomposition and wetland expansion at the same time has been reported from the Bering Sea (Meyer et al., 2019), the Siberian Arctic (Tesi et al., 2016; Martens et al., 2020) and eastern Beringia (Kaufman et al., 2015). Bering Sea sediments deposited during the time intervals of lignin MAR peaks were laminated (Fig. 3.2c), indicating that increased export productivity and terrigenous OM supply may have promoted anoxic conditions during the YD–PB transition (Kühn et al., 2014).

The rate of sea level change was lower during the PB than that in the B/A, but the MARs of *n*-alkanes and lignin reached maxima, and the discharge of the Yukon also increased from the B/A to the PB. Therefore, both coastal erosion and surface runoff may affect the transport of *n*-alkanes and lignin from land to ocean in the Yukon basin during the last deglaciation.

Different from the Bering Sea records, lignin MAR did not yet increase in the Okhotsk Sea during the ED (Fig. 3.2d), except for a short peak at the transition from the ED to the B/A. The discharge of the Amur river was low, but the MAR of lignin increased at the transition from the ED to the B/A when the rate of sea level change was rapid. At the same time, the *n*-alkane MAR did not change significantly (Fig. 3.2). This suggests that both lignin MARs in Okhotsk Sea sediment are affected by coastal erosion during the last deglaciation.

SSTs were higher in the northeastern Pacific and the Bering Sea than in the northwestern Pacific and Okhotsk Sea during the ED, and the IP_{25} value was relatively high in the Okhotsk Sea (Fig. 3.3IIc), indicating the sea ice of the Okhotsk Sea did not begin to retreat in the ED (Lo et al., 2018). Caissie et al. (2010) found that the first detectable concentration of alkenones in the Bering Sea sediment at 16.7 ka occurred earlier than in the Okhotsk Sea, although the Bering Sea is located further north than the Okhotsk Sea. As a result of prevailing sea ice cover, the permafrost of the Amur basin may have remained stable in the ED (Vaks et al., 2013, 2020; Winterfeld et al., 2018; Meyer et al., 2019).

The rate of sea level change reached a peak during MWP-1A (Fig. 3.2d), which likely also caused an increase in the rate of coastal erosion. Thus, the increased biomarker MAR during the B/A (Fig. 3.2) may be attributed largely to coastal erosion. This suggests that both types of biomarkers are supplied via the same erosive process during the B/A, in contrast to findings from the modern-day Arctic.

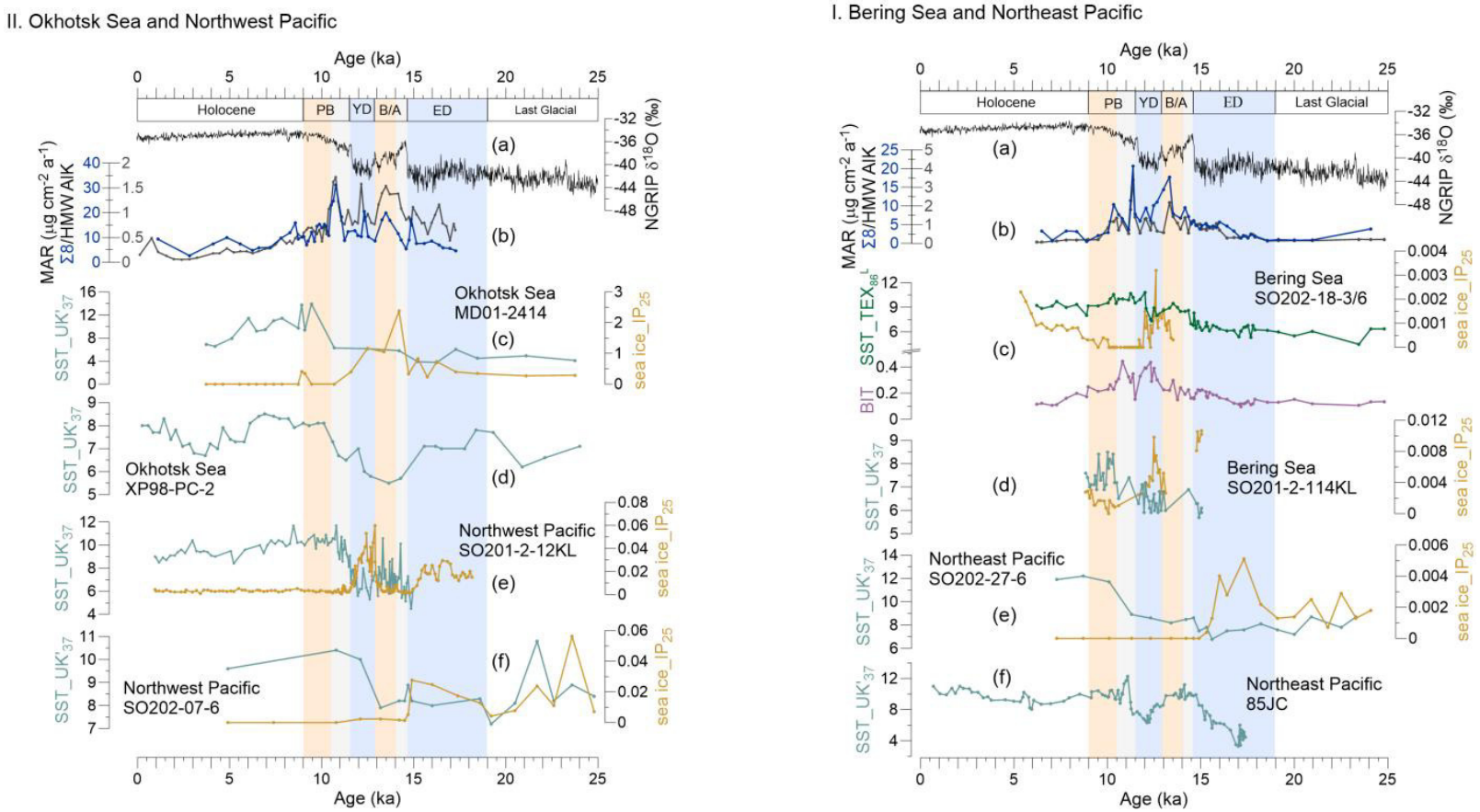

Figure 3.3 Records of sea surface temperature (SST) and sea ice (IP_{25}) in the Bering Sea and northeastern Pacific and the Okhotsk Sea and northwestern Pacific during the past 25 kyr. (a) NGRIP-$\delta^{18}O$ from Greenland (Rasmussen et al., 2008). (b) MAR of biomarkers. I (c) The green line reflects SST (TEX^{L}_{86}), and the purple line shows the BIT from this study, SO202-18-3/6. The orange line denotes the IP_{25} obtained for this core by Méheust et al. (2018). (d) SST and IP_{25} for core SO202-2-114KL (Max et al., 2012; Méheust et al., 2016). (e) SST and IP_{25} for core SO202-27-6 in the northeastern Pacific (Méheust et al., 2018). (f) SST for core 85JC (Praetorius et al., 2015). II (c) SST and IP_{25} of the core MD01-2414 in the Okhotsk Sea (Lattaud et al., 2019; Lo et al., 2018). (d) SST for core XP98-PC-2 (Seki et al., 2014b). (e) SST and IP_{25} for core SO201-2-12KL in the northwestern Pacific (Max et al., 2012; Méheust et al., 2016). (f) SST and IP_{25} for core SO202-07-6 (Méheust et al., 2018). The units of the SST and IP_{25} are degrees Celsius and micrograms per gram sediment, respectively. Blue boxes represent intervals with prevailing colder climate conditions during the early deglaciation (ED) and Younger Dryas (YD); orange boxes are for the warm phases Bølling–Allerød (B/A) and Pre-Boreal (PB). Gray boxes highlight the periods of meltwater pulse 1A (MWP-1A) and 1B (MWP-1B).

From the YD to the PB, the Northern Hemisphere experienced an abrupt temperature increase, and the SST of the North Pacific increased significantly (Max et al., 2012; Riethdorf et al., 2013; Méheust et al., 2016, 2018; Meyer et al., 2016, 2017). All biomarker MARs in the Okhotsk Sea increased and reached maxima in the YD–PB transition. The permafrost of the Amur basin may have begun to be remobilized coevally with previously reported periods of stalagmite growth starting after the PB in the south of Siberia, which indicates the decay of permafrost and opening of water conduits into the caves (Vaks et al., 2013, 2020). A pronounced lignin flflux maximum occurred during MWP-1B, coinciding with a period of enhanced discharge from the Amur river. This implies that hinterland permafrost thawing played a more important role in the land–ocean OM transport during the later deglaciation, which may have had an impact on the oxygen content and nutrient concentration in the Okhotsk Sea Intermediate Water in the MWP-1B (Lembke-Jene et al., 2017).

MARs decrease drastically after maxima in both the Okhotsk and Bering seas (Fig. 3.2c and d). The Amur basin was completely covered with permafrost during the LGM (Vandenberghe et al., 2014), and almost all of the permafrost was lost until today as a result of permafrost mobilization during the last deglaciation. Thus, the contribution of permafrost OM from the Amur basin to the marine sediment began to decrease in the early Holocene in agreement with the results of Seki et al. (2012).

In summary, the permafrost of the Amur basin began to be remobilized in the PB later than in the Yukon basin. We suggest that this was caused by decreased sea ice or increased SST in the Bering Sea during the ED, while the Okhotsk Sea remained ice-covered. We found that during the last deglaciation, lignin and *n*-alkanes were supplied from land to the ocean via the same combined processes in the Yukon and Amur basins, including surface runoff and coastal erosion.

3.5.2. Vegetation changes in the two river basins

3.5.2.1. Yukon River basin

As the climate warmed during the transition from the LGM to the ED, moisture increased, and an increasing number of thermokarst lakes developed in Alaska, especially after about 16–14 ka (Bigelow, 2013; Walter et al., 2007). We observe an increase in S/V ratios from the ED to the B/A, indicating increasing contributions of angiosperms around this time, extending into the B/A (Fig. 3.4Ia). The S/V and C/V ratios are also influenced by the degradation of lignin, with increasing ratios suggesting a lower degradation state (Hedges et al., 1988; Otto and Simpson, 2006), but there is no parallel decrease in the more commonly used degradation indicator, i.e., the Ad/Al ratios, at the same time (Fig. 3.4Ie and f). As the permafrost had begun to be remobilized in the Yukon basin during the ED, the S/V suggests that the cover of angiosperms in this basin increased

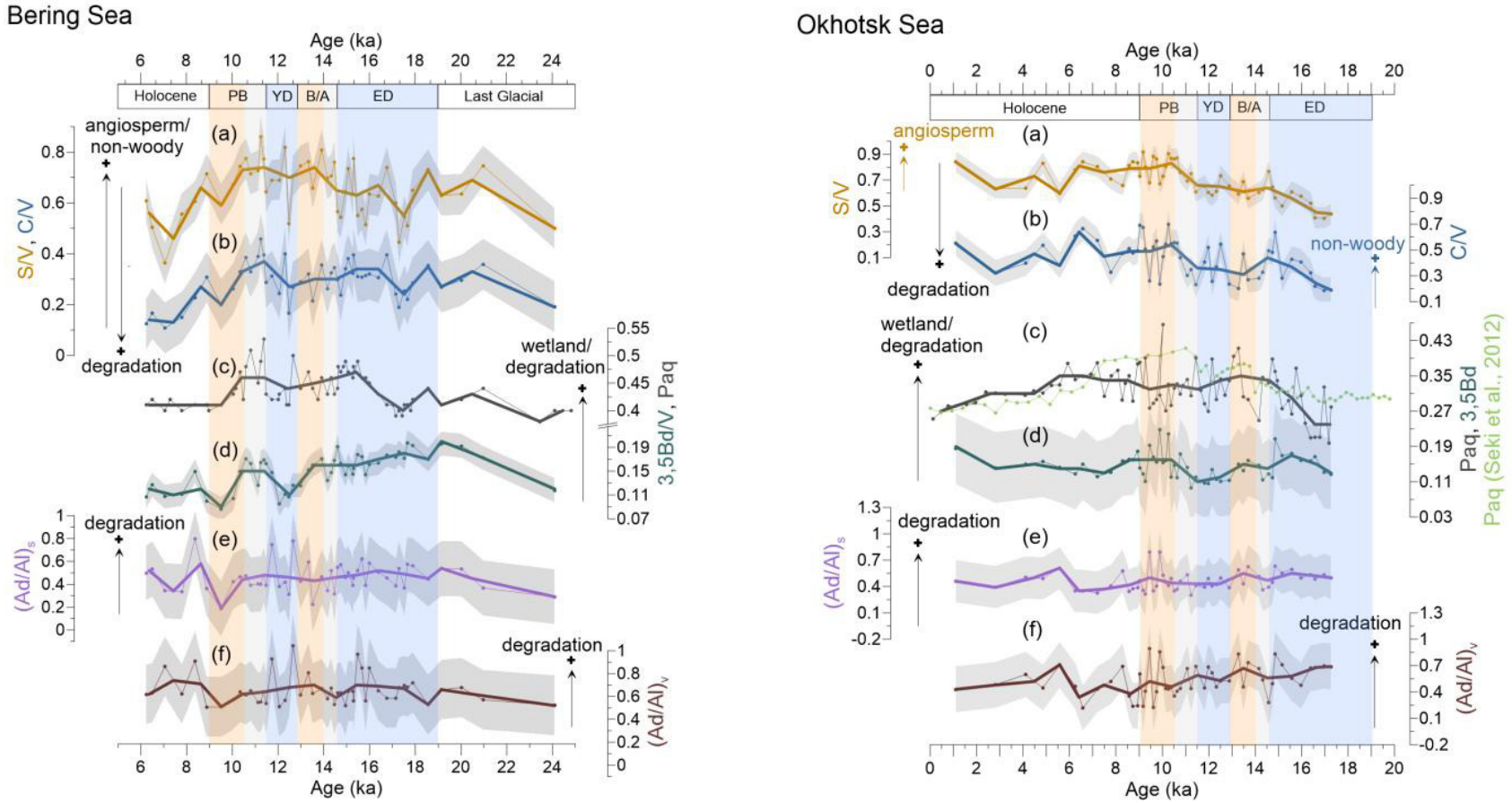

Figure 3.4 Records of lignin and non-lignin phenol indices compared with the Paq index in Bering Sea (I) and Okhotsk Sea (II) sediments. (a, b) S/V and C/V ratios reflect the vegetation change and/or degree of lignin degradation in the respective river basins. (c, d) 3,5Bd/V and Paq ratios represent the wetland extent or degree of degradation in the respective catchments. In panel II, showing records from the Okhotsk Sea, the light-green line represents the Paq of a nearby core, XP07-C9 (Seki et al., 2012). (e, f) The Ad/Al can reflect the degradation of lignin phenols. Shaded gray areas illustrate the uncertainty in these indices. Bold lines are the 1 kyr averages of the corresponding indices. Blue boxes represent the cold spells the early deglaciation (ED) and Younger Dryas (YD); orange boxes are for the warm phases Bølling– Allerød (B/A) and Pre-Boreal (PB). Gray boxes highlight the periods of meltwater pulse 1A (MWP-1A) and 1B (MWP-1B).

During the transition of ED–B/A, the rate of sea level change was rapid, implying that the distance of our study site to the river mouth must have changed. The degree of OM degradation, however, did not change significantly at the same time (Fig. 3.4e and f). Reports that the degradation degree of Lena river-derived OM and surface sediments of Buor-Khaya Bay are similar (Winterfeld et al., 2015) suggest that the oxidative degradation of lignin occurred mainly on land, in agreement with our results. We thus posit that transport within the ocean that might have increased in distance and duration in response to the sea level change may only have a limited impact on OM degradation in the Bering Sea. The S/V and C/V can thus be regarded to mainly reflect vegetation development in the transition of ED–B/A. Anderson et al. (2003) also found birch pollen becoming significantly more prevalent after about 16 ka from western Alaska to the Mackenzie River, suggesting that these regions were characterized by glacier retreating and more favorable climatic conditions. Coevally, the Paq index (Fig. 3.4Ic) shows an increase, indicating wetland expansion.

There is evidence that herb-dominated tundra was replaced by *Betula–Salix* (birch–willow) shrub tundra around Trout Lake (the northern Yukon) during the B/A (Fritz et al., 2012) as the climate warmed and became more humid than during the ED. In line with these observations, our C/V ratios indicate that the contribution of non-woody plant tissues was lower in the B/A than in the ED (Fig. 3.4Ib).

After the B/A, the summer temperatures during the YD dropped by ~ 1.5 °C (Fritz et al., 2012); thus cold-adapted non-arboreal plants briefly increased in abundance (Fritz et al., 2012). The S/V ratios indicate that the non-woody angiosperm plants' contribution reached a maximum in the Yukon basin during the YD–PB transition (Fig. 3.4Ia). The MARs of biomarkers in the Bering Sea also reached maxima during this transition (Fig. 3.2c). Since the opening of the Bering Strait (~ 11 ka; Jakobsson et al., 2017), a trend of increase in *Betula* (birch) was observed in eastern Beringia (Fritz et al., 2012; Kaufman et al., 2015), which indicates a progressively more maritime climate developing in response to changes in the marine environment (Igarashi and Zharov, 2011). Vegetation development and permafrost remobilization both contribute to the biomarker MARs (Fig. 3.2c). The BIT values higher than 0.3 from 13 to 10.5 ka (Fig. 3.3Ic) further support this interpretation while at the same time indicating that in these intervals, TEX^{L}_{86} cannot be used to reflect the sea surface temperature change. Additionally, the intensification of oxygen-minimum zones in the Bering Sea during the B/A (Fig. 3.2c) may be related to the increase in surface runoff (freshwater and OM fluxes; Kühn et al., 2014).

Since vegetation responds to changes in both temperature and moisture, significant *Populus/Salix* (cottonwood/willow) woodland development occurred in interior Alaska and the Yukon Territory during the early Holocene (Anderson et al., 2003). However, the expansion of these angiosperm plants is not reflected in our S/V record (Fig. 4Ia); the

interpretation of S/V ratios may be complicated by the influence of degradation processes during the early Holocene. Pollen assemblages from northern Siberian soils have shown that woody plants occurred only after the onset of the Holocene (Binney et al., 2009), which agrees with a decrease in the C/V ratios since the early PB into the early Holocene (Fig. 3.4Ib).

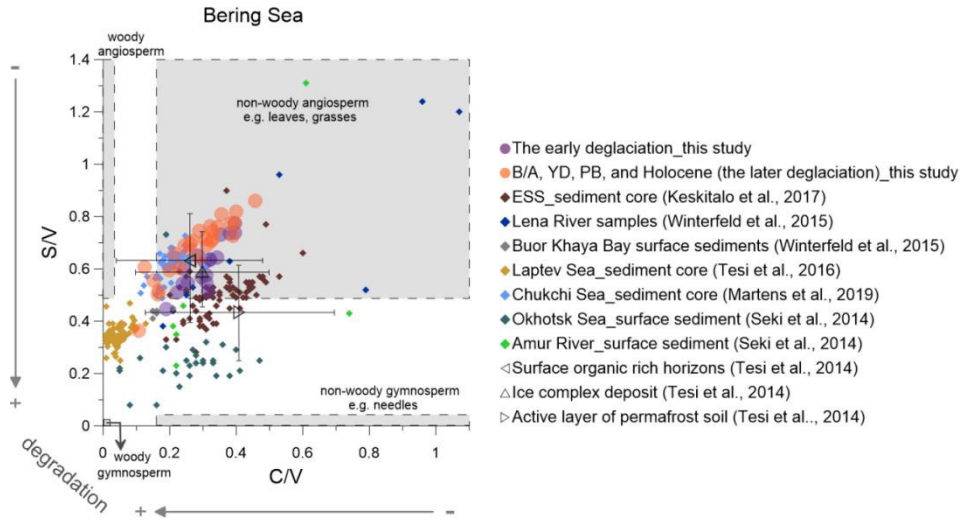

Figure 3.5 Lignin indicators of terrigenous material in the Bering sediment (solid circles) compared with published data (Martens et al., 2019; Keskitalo et al., 2017; Tesi et al., 2016; Seki et al., 2014a; Winterfeld et al., 2015). The early deglaciation is from 19 to 14.6 ka, and after the early deglaciation is the later deglaciation. The dark triangles represent the ratio of S/V and C/V from surface soils, ice complex deposits and active layer permafrost (Tesi et al., 2014). ESS is short for the East Siberian Shelf.

We compare our S/V and C/V ratios with published values from sediment cores, surface sediments and suspended materials in the Arctic and sub-Arctic (Fig. 3.5). Such plots can help to identify the main types of plant tissues the lignin phenols are derived from and enable the detection of potential degradation effects.

The S/V and C/V ratios from our Bering Sea core compare favorably with those from a core recovered from the Chukchi Shelf covering parts of the B/A and the YD as well

as the late Holocene (Martens et al., 2019) (Fig. 3.5). This may suggest that a similar type of vegetation prevailed across much of Beringia. After the opening of the Bering Strait, Pacific waters flowed into the Chukchi Sea, and it is conceivable that the terrestrial material transported to the Bering Sea by the Yukon River may have been in part transported into the Chukchi Sea. The top of our core dates to the early Holocene, a period that was characterized by more widespread broadleaf angiosperm vegetation than today, which might explain the offset between our early Holocene S/V and C/V ratios and those reported for Yukon River surface sediment (S/V: 0.28; C/V: 0.14) (Feng et al., 2015a) and dissolved organic carbon in the Yukon (S/V: 0.47; C/V: 0.14) (Amon et al., 2012) at present. Degradation of lignin in sediments may explain some of the discrepancies between sediment data and S/V and C/V

ratios reported from suspended materials collected in the modern Lena river (Fig. 5). As the Amur river catchment is dominated by gymnosperms at present (Seki et al., 2014a), the S/V ratios of the Amur river and Okhotsk Sea surface sediments (Seki et al., 2014a) are lower than in the Bering Sea core (Fig. 3.5).

The highest values of the 3,5Bd/V ratio correlate with the enhanced degradation of lignin phenols around 17.5 ka (Fig. 3.4Id). This suggests that degraded OM is the dominant source of the lignin phenols at this time, in agreement with previous studies (Meyer et al., 2016, 2019). Global meltwater pulses according to Lambeck et al. (2014) occurred during the following periods: MWP-1A from 14.6 to 14.0 ka and MWP-1B from 11.5 to 10.5 ka. The 3,5Bd/V and $(Ad/Al)_s$ ratios decreased slowly from the ED to the MWP-1A, which indicates that the change in 3,5Bd/V values from the LGM to the early B/A reflects a variable degree of OM degradation, rather than expansion of wetlands or peatlands. The 3,5Bd/V also featured a short maximum during the late YD and early PB, when the 3,5Bd/V signal is likely dominantly ascribed to increases in wetland or peatland sources, as there is no parallel maximum in Ad/Al ratios (Fig. 3.4Id–f).

This pattern of 3,5Bd/V change is not in agreement with the Paq ratio determined for the same core earlier (Meyer et al., 2019), although both proxies may reflect wetland expansion (Goñi et al., 2000; Amon et al., 2012). The temporal evolution of Paq is similar to that of S/V and C/V, where Paq began to increase in the ED and reached its maximum in the YD–PB transition (Fig. 3.4Ic), indicating that the proxies are influenced to some extent by degradation.

The Ad/Al ratios decreased when the biomarker MAR peaked during MWP-1B (Fig. 3.4IIe and f), which may correspond to better preservation during rapid burial or higher contribution of ICD OM and fresh angiosperm debris. This better preservation is in agreement with previous studies (Anderson et al., 2003; Meyer et al., 2019). Kühn et al. (2014) found that increases in biological export production and remineralization of OM in the Bering Sea during the B/A and PB reduced oxygen concentration to below 0.1 mL L^{-1} and caused the occurrence of laminated sediments (Fig. 3.2c). This anoxic condition in the Bering Sea during the B/A and PB also slowed down rates of OM decomposition and increased the accumulation of OM.

In summary, our data together with published evidence indicate that in the Yukon basin, vegetation change and wetland expansion began in the ED. Angiosperm plant contribution and wetland extent all reached their maxima during the PB, both decreasing and stabilizing at lower levels after the PB. During the PB, terrigenous OM appeared least degraded, suggesting rapid supply and burial of rather wellpreserved terrigenous OM.

3.5.2.2. Amur River basin

The lowest contribution of non-woody angiosperms as indicated by low S/V and C/V ratios occurred at 16.6 ka (Fig. 3.4IIa and b). Subsequently, both ratios increased and reached maxima during the PB, suggesting the expansion of angiosperms and non-woody tissues contributing substantially to lignin. After the PB, the S/V decreased rapidly and remained stable during the Holocene, while the C/V ratio showed a second maximum at 9.2 ka, suggesting an increasing contribution of non-woody angiosperms in the PB (Fig. 3.4IIa and b). In agreement with our data, published lipid records provide evidence that the vegetation in the Amur basin did not change significantly in the ED (Seki et al., 2012). Winterfeld et al. (2018) found a general synchronicity of Amur river discharge and the northward extent of monsoon precipitation in the early Holocene. Climate warming associated with high moisture supply allowed the expansion of birch–alder forests in the Amur basin in the PB (Bazarova et al., 2008; Igarashi and Zharov, 2011).

C/V and S/V ratios indicate that the contribution of non-woody gymnosperm tissue was higher in the early than in the later deglaciation (Fig. 3.6), similar to what has been reported from East Siberian Shelf records (Keskitalo et al., 2017). The YD caused only minor vegetation changes in the East Asian hinterland (Igarashi and Zharov, 2011). Our lignin records for this period are in agreement with previous studies that indicated that the lower Amur river basin mainly featured shrub birch-alder forests and rare Pinus (Bazarova et al., 2008; Seki et al., 2012).

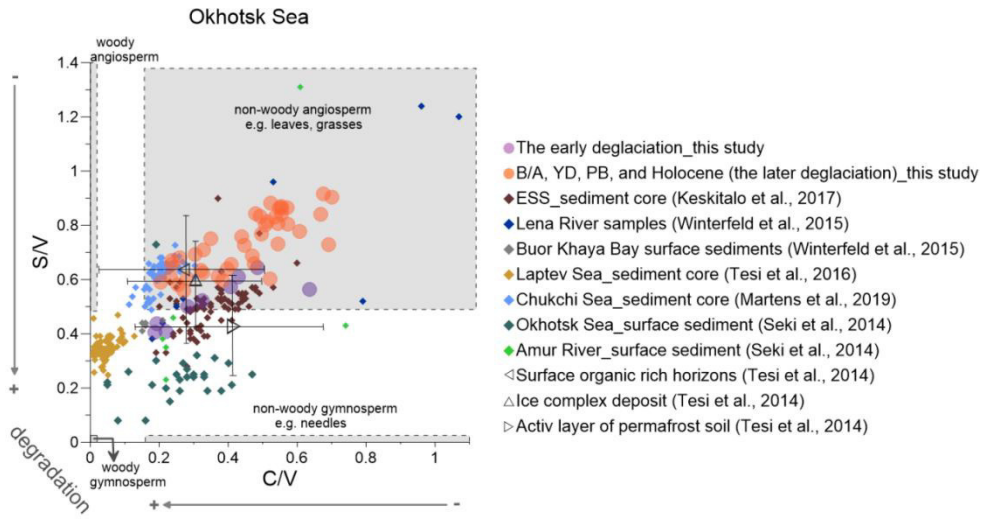

Figure 3.6 Lignin indicators of terrigenous material in the Okhotsk Sea sediment (solid circles) compared with published data (Martens et al., 2019; Keskitalo et al., 2017; Tesi et al., 2016; Seki et al., 2014a; Winterfeld et al., 2015). The early deglaciation is from 19 to 14.6 ka, and after the early deglaciation is the later deglaciation. The dark triangles represent the ratio of S/V and C/V from surface soils, ice complex deposits and active layer permafrost (Tesi et al., 2014). ESS is short for the East Siberian Shelf.

Non-woody angiosperm plant contributions to the Okhotsk Sea sediment strongly increased during the PB (Fig. 3.4IIa and b), when the summer insolation and regional temperatures reached the highest values since the LGM. Significant vegetation changes in the Amur basin thus started in the PB period, temporally offset from the Yukon basin, and the contribution of angiosperms from 14.6 to 9 ka appears to be higher than during the ED (Fig. 3.6). Bazarova et al. (2008) reported based on pollen analyses that a turning point in vegetation development in the Amur basin occurred at a boundary of 10 ka. The middle Amur depression registered the first appearance of broad-leaved species of pollen and a prevalence of spores over arboreal pollen at that time (Bazarova et al., 2008). The C/V ratio did not decrease as rapidly as the S/V ratio after the peak and showed a second maximum at ~ 9 ka. Some pollen of Picea (such as *P. glauca* and *P. mariana*) yields exceptionally high quantities of cinnamyl phenols (Hu et al., 1999), which may have affected the C/V ratio as the end-member of woody/non-woody tissues. An et al. (2000) concluded that lakes were deepest and most extensive around 10 ka in northeastern China (the upper Amur basin), and 3,5Bd/V and Paq values reached maxima at the same time (Fig. 3.4IId and c), suggesting wetland extent peaked during the PB. Therefore, wetland plants that have broad leaves, such as sedges, may also have a positive influence on the C/V ratio.

The S/V and C/V data from the Holocene part of our core do not agree with published values for the Okhotsk Sea and Amur river surface sediments (Fig. 3.6). During the past 250 years, vegetation was marked by significant rises in gymnosperms, such as pines, combined with the reduction in the swamp area and a large increase in fire activity (Yu et al., 2017), likely resulting in higher contributions of gymnosperm to the surface sediment, while these changes are not resolved in the samples analyzed for our record.

The 3,5Bd/V and Paq ratios of the Okhotsk Sea both display relatively high values during the PB (Fig. 3.4IIc and d). Seki et al. (2012) found high Paq values during the PB in a nearby sediment core XP07-C9, and the values in their core were higher than in ours (Fig. 3.4IIc). Spores of *Sphagnum* show a distinct peak during the PB (Morley et al., 1991), reflecting an expansion of mesic and boggy habitats. Our records together with published evidence thus suggest that permafrost destabilization and wetland expansion in the Amur basin occurred only at the beginning of the PB, while those processes were initiated much earlier in the Yukon basin.

The Ad/Al values were decreasing until 10.5 ka and reached minima during the PB (Fig. 3.4e and f), indicating that low temperatures on land on the one hand and rapid burial in marine sediments during shelf flooding and coastal erosion during MWP-1B on the other hand contributed to the Ad/Al signals. The 1 ka averages of the S/V and C/V ratios show similar minima to the Ad/Al ratios from the ED to the PB (Fig. 3.4II), suggesting that degradation processes exert a strong control on the S/V and C/V ratios during a time when vegetation did

not change in the Amur basin. In the course of climate amelioration from around 11.6 ka (Tarasov et al., 2009), the rates of vegetation development, wetland expansion and Amur river discharge (Fig. 3.2f) all displayed maxima in the PB. Generally, higher Ad/Al values in the later part of the PB suggest that fluvial runoff supplied more degraded lignin. Aerobic degradation of OM in soils by fungi has also been shown to increase Ad/Al values (Goñi et al., 1993). Since the oxidative degradation occurred mainly on land (Winterfeld et al., 2015), and lateral transport is likely short, this increased degradation is unlikely to occur in the ocean. The Okhotsk Sea shelf is narrower than the Bering and Siberian shelves; the lateral shelf transport times (i.e., the cumulative time a particle spends in sedimentation–resuspension cycles) of the Okhotsk shelf are therefore likely to be much shorter than what has been reported for the Laptev shelf (Bröder et al., 2018), further supporting our interpretation.

The rate of sea level change in the Bering Sea (Manley, 2002) is slower than the global average rate (Lambeck et al., 2014). The effect of sea level change on the degradation process of terrestrial OM in the Bering Sea is limited. We are not aware of a published local reconstruction of sea level change for the Okhotsk Sea from 20 ka to the present, but we suggest that, since the shelf of the Okhotsk Sea is narrower than that of the Bering Sea, the effect of sea level change on the Okhotsk shelf may be neglected. Pre-aged OM and young OM can be transported from land to the marine

sediments in a variety of ways, such as coastal erosion and surface runoff, but the relative contribution of different carbon pools could not be quantified by lignin and *n*-alkane fluxes or other parameters (S/V, C/V, 3,5Bd/V, Ad/Al and Paq), as they appear to be transported through the same pathways during the last deglaciation. Further investigation using compound-specific radiocarbon analysis is needed to quantify the contribution of different carbon pools in marine sediments.

In summary, our records indicate that in the Amur basin vegetation change and wetland expansion began during the PB and in the early Holocene, in agreement with previous paleo-vegetation studies. This timing is different from observed changes in the Yukon basin. However, similar to the Yukon basin, the wetland extent and non-woody angiosperm contribution were reduced and stabilized after the PB in the Amur basin. The increased vegetation and wetland indices, as well as increased degradation of lignin in the Okhotsk Sea sediment at the end of the PB, may be related to changes in the source of OM (shelf and coastal erosion vs. river transported material).

3.6. Conclusions

By analyzing mass accumulation rates of terrigenous biomarkers in sediments from the Bering and Okhotsk seas, we provide the first downcore records of lignin from the Yukon

and Amur basins covering the early deglaciation to the Holocene. We find that vegetation changed earlier in the Yukon than in the Amur basin. Although S/V, C/V and 3,5Bd/V ratios can reflect vegetation change and wetland development, the degradation state of lignin strongly overprints these proxy signals and should be considered to be a function of temperature, transport distance and burial rate. Similar to changes in vegetation, we observe that degradation and remobilization of permafrost of the Yukon basin also occurred earlier than in the Amur basin. Sea ice extent and SSTs of adjacent ocean areas might have had a strong influence on the timing of hinterland permafrost mobilization. Our study reveals that lignin transported by surface runoff may account for significant proportions of lignin during inland warming, but the export of lignin and lipids does not always occur via different pathways, as both biomarker groups can be contributed from rapidly eroding deep deposits during phases of rapid permafrost thaw. In contrast to modern-day evidence suggesting different pathways for lipid and lignin biomarker transport, our records imply that during glacial peaks of permafrost decomposition, lipids and lignin might have been delivered to the ocean by identical processes, i.e., runoff and erosion.

Author contributions

MC measured and compiled lignin data and wrote the manuscript with the help of all co-authors. JH was responsible for all biomarker analyses. LLJ and RT provided samples. VDM carried out sea surface temperature measurements of SO202-18-3/6. GM designed the study. All authors participated in the discussion of results and conclusions and contributed to the final version of the paper.

Acknowledgments

We thank the masters and crews of R/V Sonne for their professional support during cruises SO202 (INOPEX) and SO178 (KOMEX). Hartmut Kühn is acknowledged for providing total organic carbon and dry bulk density data of site SO202-18-3/6. Mengli Cao thanks the China Scholarship Council and POLMAR (Helmholtz Graduate School for Polar and Marine Research) for additional support. We are also grateful to the laboratory and computer staff at the Alfred Wegener Institute.

4. Manuscript II

Assessment of blanks associated with the isolation and purification of lignin phenols for compound-specific radiocarbon analysis

Mengli Cao[1], Hendrik Grotheer[1,3], Gesine Mollenhauer[1,2,3], Jens Hefter[1]

[1]Alfred-Wegener-Institut, Helmholtz-Zentrum für Polar-und Meeresforschung (AWI), 27570 Bremerhaven, Germany.
[2]Department of Geosciences, University of Bremen, 28359 Bremen, Germany.
[3]MARUM-Center for Marine Environmental Sciences, University of Bremen, 28359 Bremen, Germany.

In preparation for *Limnology and Oceanography: methods*

Abstract

Compound-specific radiocarbon analysis (CSRA) is a powerful technique that can be used to constrain the cycling of organic matter between reservoirs. The technique allows, for example, to investigate timescales of organic matter transfer from land to oceans, and terrigenous biomarkers like long-chain *n*-alkyl lipids or lignin-derived phenols are useful targets for such studies. However, the procedures used for isolating and purifying these biomarkers, including the phenolic monomers of lignin for CSRA typically require a sequence of wet chemical preparation steps and are prone to introduce extraneous (blank) carbon into the samples. These procedural blanks will potentially lead to erroneous interpretation of lignin CRSA results, making the assessment of procedural blanks an important prerequisite. We describe a revised method for the purification of lignin phenols from sediment based on a previously published method and evaluate the fraction of modern carbon ($F^{14}C$) and the mass of the associated procedural blank. Chemical isolation and radiocarbon analyses were performed at Alfred Wegener Institute in Bremerhaven, Germany, using the miniaturized radiocarbon dating system. We report the current status of carbon blanks associated with our preparation protocol for radiocarbon analysis of lignin phenols, which was determined to be 4.2 ± 0.4 μgC with $F^{14}C$ of 0.55 ± 0.04 for the entire method.

4.1. Introduction

Since Eglinton et al. (1996) first applied compound-specific radiocarbon analysis (CSRA) relying on preparative capillary gas chromatography (PCGC) for the study of lipid biomarker ^{14}C in marine sediments, the technology has developed rapidly and has been widely used in studies of aerosols, soils, rivers, lakes, oceans, and other ecological environmental systems (Matsumoto et al., 2001; Uchikawa et al., 2008; Cowie et al., 2010; Feng et al., 2013a; Eglinton et al., 2021; Kusch et al., 2021). PCGC separation technology can only be used for the isolation of compounds with low polarity and low molecular weight, such as *n*-alkanes (McNichol et al., 2000; Pearson et al., 2001). The isolation of compounds with increased polarity such as *n*-alkanoic acids requires the derivatization of such compounds and will introduce extraneous carbon that needs to be corrected for during ^{14}C isotope data processing (McNichol et al., 2000; Corr et al., 2007). To avoid the influence of derivatization carbon, high pressure liquid chromatography (HPLC) has been used to isolate polar lignin phenols (Hou et al., 2010; Feng et al., 2013b), high molecular weight GDGTs (Smittenberg et al., 2002; Shah et al., 2008) and other highly polar and high molecular weight organic compounds in plants, marine and lake sediments for CSRA (Smittenberg et al., 2002; Bour et al., 2016).

The content of biomarkers in natural environmental samples is mostly low, they are contained in a complex matrix and are difficult to isolate. Lignin is a relatively highly abundant phenolic biopolymer in sediments and originates from vascular plants, where it accounts for up to one-third of the organic matrix (Erdtman, 1971; Hedges and Mann, 1979). The lignin macromolecule consists of phenolic monomers (aldehydes, ketones, and acids of the syringyl and vanillyl group) and their relative ratios offer considerable information on vegetation source, and organic matter degradation in archives, such as sediments of lakes and marine settings (Fritz et al., 2012; Martens et al., 2020; Cao et al., 2023). Lignin-derived phenolic monomers can be obtained by alkaline CuO oxidation with a microwave digestion system (Goñi and Montgomery, 2000) and quantified by gas chromatography-mass spectrometry (GC-MS) (Ingalls et al., 2010; Hou et al., 2010; Feng et al., 2013b; Sun et al., 2020).

The separation of lignin phenols by HPLC has been improved over the last ten years (Ingalls et al., 2010; Hou et al., 2010; Feng et al., 2013b; Sun et al., 2020). The proposed method of Feng et al (2013) for CSRA involves a two-stage solid phase extraction (SPE) procedure, which first removes neutral compounds and other impurities and later separates phenolic aldehydes and ketones from their corresponding acids. The initial isolation of lignin phenols is achieved using a reverse phase ENVI-18 (octadecyl bonded endcapped silica) SPE cartridge, followed by a normal phase LC-NH_2 (aminopropyl bonded silica) SPE cartridge, where phenolic aldehydes and ketones are eluted with methanol and corresponding acids are subsequently eluted with methanol:12 M HCl (95:5 v/v). Individual lignin phenols are finally

isolated by HPLC for subsequent CSRA. Each step of this procedure may introduce contaminant carbon, deriving from the SPE separation, HPLC isolation, solvents and containers used during the procedure, which can lead to erroneous interpretation of lignin CRSA results. The SPE separation on commercially available cartridges is the most likely step to introduce extraneous carbon, as they are fabricated from plastic (e.g., polypropylene, polyethylene, and polytetrafluoroethylene) and filled with a polymer resin which both have the potential to leach carbon upon contact with solvents. In addition, the packing in the HPLC columns contains carbon that may be rinsed out with the mobile phase, suggesting that HPLC may also be a source of contaminant. The blank contribution of the SPE cartridge has so far not been quantified. Reducing the number of SPE steps not only simplifies the method for separating lignin phenols but potentially reduces the incorporation of extraneous carbon. In this study, we report a simplified procedure for the purification of lignin phenols based on the published method by Feng et al., (2013b) and evaluate the fraction of modern carbon ($F^{14}C$) and the mass of the associated procedural blank.

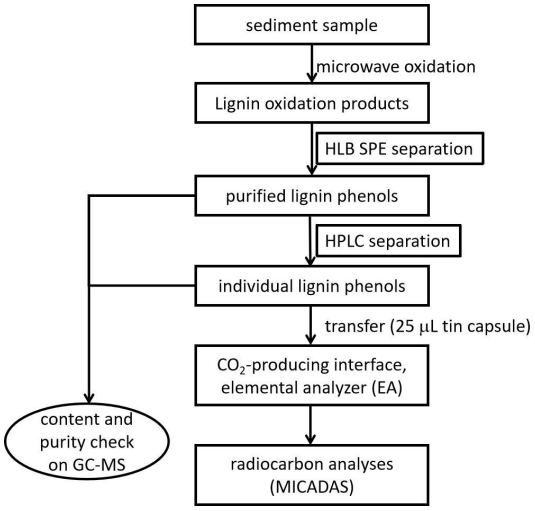

Figure 4.1. Simplified method of lignin-phenol isolation from sediments for radiocarbon analysis (using samples that have been extracted for lipid analyses). Modifications compared to the previously published method (Feng et al., 2013b) are indicated by the dotted boxes. EtAc is ethyl acetate.

4.2. Materials and Procedures

A simplified flow-path of required working steps for the purification and isolation of lignin phenols for compound-specific radiocarbon analysis is shown in Figure 4.1. All glassware used was combusted at 450 °C for 6 hours. Teflon tubes used for the microwave were rinsed with methanol (MeOH) before use. The solvents and chemicals used in this study are listed in Table 4.1.

Table 4.1 Solvents and chemicals used in this study.

Solvent	Purity grade	Manufacturer	Article No.
Ethyl acetate (EtAc)	For HPLC, ≧99.7%	Honeywell	34858-2.5L
Methanol	For GC-ECD and FID	Supelco	1.06011.2500
Hydrochloric acid (HCl)	37.3%	Merck	1.00317.2500
N,O-Bis (trimethylsilyl) trifluoroacetamide (BSTFA) with trimethylchlorosilane (TMCS)	For GC derivatization, contains 1% TMCS, 99%	Sigma-Aldrich	15238-10X1ML
Pyridine	GC, ≧99%	Merck	1.07463.0500
Acetonitrile	GC, ≧99.9%	Roth	NH44.2
Acetic acid	/	Merck	1.01830.2500
Copper oxide	/	Merck	1.02766.0100
Ferrous ammonium sulfate	/	AppliChem	A2312,0500
Sodium hydroxide	Pellets, ≧98%	Honeywell	30620-1KG
HLB solid phase extraction (SPE) cartridge (200 mg, 6 mL)	/	Waters Oasis	186000115

4.2.1. Extraction of lignin phenols from sediments

The extraction of lignin phenols was carried out following the method of Goñi and Montgomery (2000). Briefly, ~2 g freeze-dried samples, which have been extracted using organic solvents for lipids analysis (see Winterfeld et al. (2018) for more details), were oxidized with copper oxide (CuO (~500 mg) and ferrous ammonium sulfate $(NH_4)_2Fe(SO_4)_2 \cdot 6H_2O$; ~50 mg) in 18 mL 2N sodium hydroxide (NaOH) under anoxic conditions. The oxidation was conducted in a MARS5 microwave accelerated reaction system (CEM GmbH, Germany) at 150 °C for 90 minutes. The oxidation products were transferred into glass centrifuge tubes and centrifuged for 10 minutes at 2000 rpm followed by the transfer of the supernatant into 40 mL vials. The alkaline supernatant was acidified to pH 1 with 37% hydrochloric acid (HCl). Reaction products were subsequently recovered in ethyl acetate (EtAc), and the extraction was repeated a second time. The combined EtAc extracts were evaporated under a stream of nitrogen (40 ℃), then transferred into 4 mL vials with 2 mL EtAc and stored at 4 ℃ until SPE separation.

4.2.2. Purification of lignin phenols on SPE cartridges

After oxidation and extraction, lignin phenols are purified on a HLB SPE cartridge (Table 4.1). The HLB cartridges were activated first by rinsing with 6 mL methanol, and subsequently the bottoms were sealed with a cap, and 5 mL methanol was added to soak overnight. On the next day, the cartridges were successively rinsed with 6 mL Milli-Q water (twice), 6 mL methanol (twice), and 6 mL EtAc (twice).

The whole extract was evaporated under a stream of nitrogen (40 ℃), and dissolved in 1 mL of EtAc which was added onto the cartridge. The purified lignin phenol fraction was

subsequently eluted with 59 mL of EtAc. After drying of the eluent under a stream of N_2 (40 °C), the fraction was transferred to a 1.5 mL vial with 1 mL EtAc and filtered with a PTFE filter (13 mm, 0.22 μm) for the removal of particles.

Table 4.2. Standard compounds used in this study

Standard for HLB SPE cartridge recovery					
Compounds	Chemical name	Formula	Abbreviation	Manufacturer, Article No.	
Vanillin	4-Hydroxy-3-methoxybenzaldehyde	$C_8H_8O_3$	Vl	Sigma-Aldrich, W310727-SAMPLE-K	
Acetovanillone	4'-Hydroxy-3'-methoxyacetophenone	$C_9H_{10}O_3$	Vn	Sigma-Aldrich, A1,080-9	
Vanillic acid	4-Hydroxy-3-methoxybenzoic acid	$C_8H_8O_4$	Vd	Sigma-Aldrich, 94770	
Syringaldehyde	3,5-Dimethoxy-4-hydroxybenzaldehyd	$C_9H_{10}O_4$	Sl	Sigma-Aldrich, S760-2	
Acetosyringone	3',5'-Dimethoxy-4'-hydroxyacetophenone	$C_{10}H_{12}O_4$	Sn	Sigma-Aldrich, D134406-1G	
Syringic acid	4-Hydroxy-3,5-dimethoxybenzoic acid	$C_9H_{10}O_5$	Sd	Sigma-Aldrich, S6881-10G	
p-Coumaric acid	*Trans*-4-Hydroxycinnamic acid	$C_9H_8O_3$	*p*-Cd	Sigma-Aldrich, C9008-5G	
Ferulic acid	*trans*-4-Hydroxy-3-methoxycinnamic acid	$C_{10}H_{10}O_4$	Fd	Sigma-Aldrich, 12,870-8	
p-Hydroxybenzaldehyde	4-Hydroxybenzaldehyde	$C_7H_6O_2$	Pl	Sigma-Aldrich, 14,408-8	
p-Hydroxyacetophenone	4'-Hydroxyacetophenone	$C_8H_8O_2$	Pn	Sigma-Aldrich, 27,856-4	
p-Hydroxybenzoic acid	4-Hydroxybenzoic acid	$C_7H_6O_3$	Pd	Sigma-Aldrich, 24,014-1	
3,5-Dihydroxybenzoic acid	3,5-Dihydroxybenzoic acid	$C_7H_6O_4$	3,5Bd	Sigma-Aldrich, D110000-100G	
Benzoic Acid	Benzoic Acid	$C_7H_6O_2$	Bd	Roth, P738.1	
3-Hydroxybenzoic acid	3-Hydroxybenzoic acid	$C_7H_6O_3$	3HBA	Sigma-Aldrich, H20008-100G	
Standard for blank determination					
Compounds	Chemical name	Formula	Abbreviation	Manufacturer, Article No.	$F^{14}C$
trans-Cinnamic acid (natural)	3-Phenylacrylic acid	$C_9H_8O_2$	TCA	Sigma-Aldrich, W228826-SAMPLE-K	1.021 ± 0.002
3-Hydroxybenzoic acid	3-Hydroxybenzoic acid	$C_7H_6O_3$	3HBA	Sigma-Aldrich, H20008-100G	0.00

4.2.3. GC-MS analysis

A small aliquot (0.5%) of this purified phenol fraction was used to identify and quantify the individual phenols by gas chromatography-mass spectrometry (GC-MS) as described previously (Cao et al., 2023).

Before injection into the GC-MS, samples were dried and redissolved in Pyridine, and were derivatized with bis- trimethylsilyl-trifluoroacetamide (BSTFA)+1% trimethylchlorosilane (TMCS) (60 °C, 30 min). An Agilent 6850 GC coupled to an Agilent 5975C VL MSD

quadrupole MS operating in electron impact ionization (70 eV) and full scan (m/z 50–600) mode was used for analysis. The source temperature of the MS was set to 230 °C and the quadrupole to 150 °C. The GC was equipped with a DB-1 MS column (30 m×0.25 mm i.d., film thickness 0.25 μm). Helium was used as a carrier gas at a constant flow rate of 1.2 mL min^{-1}. Samples were injected in splitless mode in a split/splitless injector (S/SL) held at 280 °C. The temperature of the GC column was programmed from 100 °C (initially held for 8 min.) and ramped at 4 °C min^{-1} to 220 °C, then at 10 °C min^{-1} to 300 °C, with a final hold time of 5 minutes. These compounds were identified based on retention time and mass spectra. Quantification was achieved by peak areas of the respective compounds and using individual five point response factor equations obtained from mixtures of commercially available standards analyzed periodically. The content of lignin phenols should be around 10 ng.

4.2.4. HPLC Settings and fraction collection

Individual lignin phenols were isolated on an Agilent 1200 HPLC system coupled to a diode array detector (DAD) at a wavelength of 280 nm. The HPLC was equipped with a Phenomenex Synergi Polar-reverse phase column (4.6×250 mm; 4 μm particle size, RP column), held at 40 °C. The binary gradient of the mobile phase (solvent A: methanol/acetonitrile (1:1, v:v); solvent B: 0.2% acetic acid Milli-Q water) of the HPLC method is listed in Table 4.3. This method allows to baseline separate 11 individual lignin phenols (Pd, Pn, Pl, Vn, Vd, Sl, Sd, *p*-Cd, Fd, mBd, and 3,5Bd, see table 4.2 for abbreviations) and one lignin phenol mixture (Bd, Vn, and Sl) (Fig. 4.2). Fractions containing individual lignin phenols or the mixture were collected in 20 mL containers using time-based fraction collection from a total of 10 subsequent injections (10 μL sample volume per injection).

Table 4.3. The binary gradient of mobile phases of the HPLC method to separate lignin phenols. Solvent A: methanol/acetonitrile (1:1, v:v); Solvent B: acetic acid solution (0.2 %). Flow rate = 0.8 mL/min. Column temperature 40°C.

Time (min)	0.0	3.0	8.0	15.0	20.0	25.0	33.0	40.0	45.0	54.0	55.0	62.5
A (%)	10	10	15	20	20	25	25	30	100	100	10	10

Following HPLC fraction collection, isolated lignin phenols were transferred to 40 mL vials, and the HPLC collection containers were rinsed with 3×0.5 mL Milli-Q water and 3×0.5 mL EtAc. The lignin phenols were recovered from the washing by liquid-liquid extraction with 3×3 mL EtAc. Isolated fractions were dried under a stream of nitrogen (40 °C), then transferred to 4 mL vials with 4 mL EtAc and stored in the fridge until further processing. A

small aliquot (0.5%) of each isolated lignin phenol was derivatized and its purity checked and final amount quantified by GC-MS.

4.2.5. Radiocarbon measurement by MICADAS

Radiocarbon measurements followed the protocol described by Mollenhauer et al. (2021). Briefly, isolated lignin phenol fractions were transferred with three solvent rinses to 25 µL liquid tin capsules (Elementar, part no. S03951620, 25 µL) with a minimum amount of methanol and kept in a holding tray. Following the third transfer the holding tray was placed in a desiccator and stored evacuated (150 mbar) inside an oven (40 °C) for 48 h. An Elementar vario ISOTOPE elemental analyzer was used to combust the samples and produced CO_2 was directed to the MICADAS accelerator mass spectrometer via the gas interface system (GIS). Reference standard gas (CO_2 produced from oxalic acid II; NIST 4990C, used for the normalization of radiocarbon values) and ^{14}C-free CO_2 gas (used for the primary blank correction) were measured prior to the samples. The BATS software was used for blank correction and normalization (Wacker et al., 2010).

4.2.6. Determination and correction of processing blanks

The procedure described above introduces exogenous carbon, i.e., contaminating carbon, to the isolated compound. The amount of contamination varies depending on the method and need to be determined and corrected for in order to provide reliable radiocarbon values. Under the assumption of a constant blank for the entire method, the contamination can be determined following Sun et al (2020). Briefly, the contamination (mass of carbon; m_{blank}, and its radiocarbon value, $F^{14}C_{blank}$) can be determined by subjecting standard compounds with known and opposing radiocarbon values in varied amounts to the entire method described above.

In this case, 9 solution mixtures of in-house standards (3HBA, $F^{14}C = 0$, $n = 6$; and TCA, $F^{14}C = 1.021 \pm 0.002$, $n = 10$, see table 4.2 for details) dissolved in 1 mL EtAc containing 10−100 µgC (m) of each standard were processed and their compound-specific radiocarbon values determined. The intersection points of the resulting linear regressions ($F^{14}C$ over 1/m) for both standards define m_{blank} and $F^{14}C_{blank}$ of the method (Hwang and Druffel 2005). To account for measurement uncertainty and to robustly determine the respective uncertainties (σm_{blank}; $\sigma F^{14}C_{blank}$) a Baysian regression model was used (see Sun et al. 2020 for details.) Resulting values for m_{blank} and $F^{14}C_{blank}$ and their respective uncertainties were used to correct the raw radiocarbon values and to completely propagate uncertainties for isolated lignin phenols according to Wacker and Christl (2011).

4.3. Assessment

4.3.1 Recovery rate of HLB SPE cartridge

The recovery rate of the HLB SPE cartridge for lignin phenols was determined for 14 commercially available standards (Table 4.2). Standards were weighed into two pre-combusted 40 mL brown-glass vials and dissolved in methanol to make two stock solutions (~50 µg/mL for each compound). One stock solution contained Sl, Vn, Vd, Fd, 3HBA, 3,5Bd, Pd, Pn, and Pl, and the second Sd, Sn, Bd, p-Cd, and Vl. 0.5 mL of each stock solution was mixed and dried under N_2 (40 °C). The mixture was re-dissolved in 0.5 mL EtAc, loaded onto an activated HLB cartridge, and eluted with 59.5 mL EtAc.

Table 4.4. Recovery rates (in % relative to starting concentration) of standards after HLB SPE separation.

Compound	Recovery (%)	Standard deviation
Vl	50.9	11.5
Vd	97.1	1.2
Sn	96.6	1.6
Sd	95.0	1.1
Fd	94.1	1.1
p-Cd	92.9	1.4
Pl	77.2	4.4
Pn	91.3	2.7
Pd	95.8	1.6
3,5Bd	0	0
3HBA	90.1	1.6
Bd+Vn+Sl*	73.2	4.1

∗ composite value of the 3 compounds that co-elute during HPLC analysis on the RP column.

The eluates were dried with nitrogen (40 °C) and dissolved with 0.5 mL MeOH for HPLC analyses. Recovery rates were calculated based on the peak areas of the compounds after SPE separation in comparison to the peak areas of the original solution. The HLB SPE cartridge showed recovery rates ranging from 70% to 89%, except for 3,5Bd (Table 4.4) and are in agreement with values previously published by Arellano et al. (2018) (77 ± 4% to 95 ± 5%). However, the recovery of 3,5Bd with EtAc was low, and it could only be eluted from the cartridge with 6 mL methanol.

4.3.2. Purification capacity of HLB SPE cartridge

The CuO extraction of lignin phenols results in a highly complex mixture including unknown compounds and undefinable unresolved carbon background. The extract of a natural sample TS (test sample, sediment from a kasten core SO202-18-6, 55-57 cm, northeastern continental slope of the Bering Sea; RV Sonne cruise SO202-INOPEX (Gersonde, 2012))

appears black and its HPLC trace shows clearly elevated background levels, which preclude baseline separated isolation of individual lignin phenols (Figure 4.2). This undefinable background would potentially add significant amounts of extraneous, not lignin phenol specific, carbon to the radiocarbon analysis and needs to be removed prior to HPLC isolation. In order to test the purification capacity of the HLB SPE cartridge the TS CuO extract was dissolved in 1 mL of EtAc and added onto the activated HLB SPE cartridge. The purified lignin phenol fraction was subsequently eluted with 59 mL EtAc. The purified fraction was dried and dissolved in equal volume of MeOH as the starting TS CuO extract. The purified fraction appears much lighter in color and the HPLC trace shows a significant reduction of the background (Fig. 4.2) indicating satisfying purification capacity of the HBL SPE cartridge.

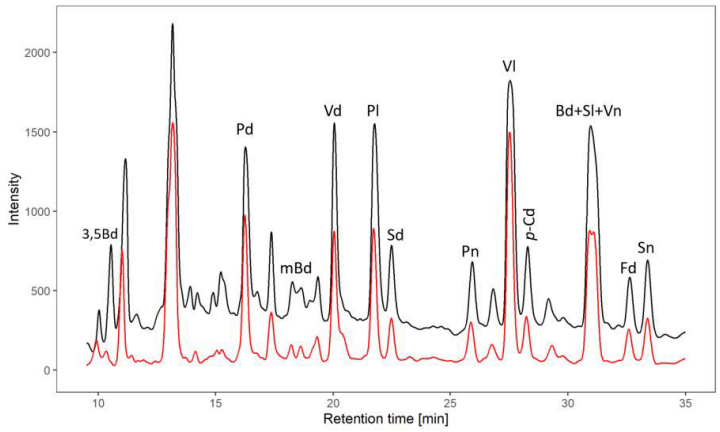

Figure 4.2. HPLC reverse phase chromatograms of the laboratory standard sediment sample (TS) before the separation by HBL SPE cartridge (black) and after (red).

4.3.3. Blank determination of SPE separation

Blank contribution of the HLB SPE cartridge were assessed by passing standards of known $^{14}C/^{12}C$ composition through the cartridge using 60 mL of EtAc. We chose TCA and 3HBA (Table 4.2) as standards. Both standards were prepared at nine different sample sizes, containing 10, 20, 30, 40, 50, 60, 70, 80, and 90 µgC per compound for final radiocarbon analysis. Recovery rates were accounted for in the calculation of the initial weight of the two standards. Each standard was placed in a 4 mL vial and dissolved with 1 mL EtAc and passed through an activated HLB SPE cartridge with 59 mL EtAc. Collections were dried under N_2 (40 °C) and transferred to 25 µL tin capsules with methanol for ^{14}C analysis.

Following the blank determination protocol as described by Sun et al. (2020), we find that HLB SPE cartridges after elution with 60 mL EtAc contribute a blank of 5.16 ± 0.16 µgC with $F^{14}C$ = 0.53 ± 0.02 (Table 4.5, Fig. 4.3), which includes the blank contribution of 25 µL tin capsules. The blank contribution of 25 µL tin capsules is 2.51 ± 0.22 µgC with $F^{14}C$ =

0.87 ± 0.05, suggesting only a small amount of carbon being introduced to the samples by the HLB SPE cartridges, and this is probably negligible if the processed sample is of sufficient size.

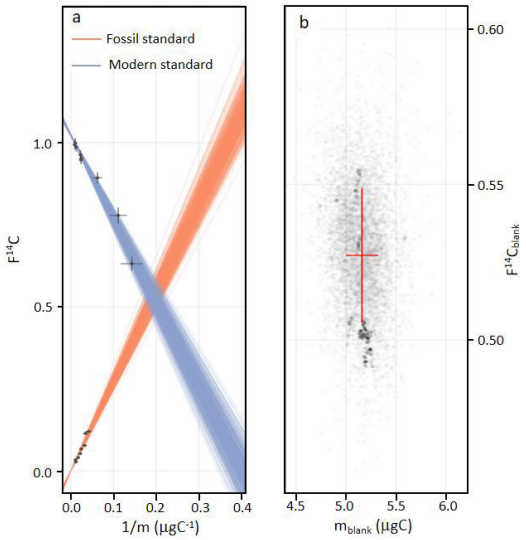

Figure 4.3. Blank assessment for the HLB SPE separation (a) a sample of 500 regression lines from the posterior distribution gives a visual check of the fitted Bayesian model. Fossil standard = 3-hydroxybenzoic acid (3HBA), modern standard = *trans*-cinnamic acid (TCA); (b) the posterior distribution of masses and $F^{14}C$ values of the procedural blank. Mass = 5.16 ± 0.16 µgC, $F^{14}C$ = 0.53 ± 0.02.

4.3.4. Blank contribution from HPLC RP column

Potential contamination sources include column bleed from the HPLC. Therefore, we collected the mobile phase of HPLC at different retention times for blank determination. For the RP column, 10×10 µL methanol was injected, and 12 mobile phase fractions were collected based on the same retention time windows as for target lignin phenols (Fig. 4.2). The collections were extracted with EtAc, as described in above. After drying, collections were transferred to 25 µL tin capsules with methanol and ^{14}C measured by MICADAS.

In our study, we have determined the RP column's blank contributions at different retention times. All blanks resulted in mass ≤ 3 µgC and we are unable to measure the $F^{14}C$ for such small samples, which is in agree with the result of Feng et al. (2013b, 2 ± 0.5 µgC), indicating that the HPLC contributes only marginally to the overall blank of the method (Hou et al., 2010; Ingalls et al., 2010).

4.3.5. Blank determination of the entire method

We assess the blank contributions of the entire lignin purification method using the two commercially available standards, TCA and 3HBA (Table 4.2), by subjecting them to all steps necessary for extraction, purification and isolation of lignin phenols from natural samples. Nine mixtures of TCA and 3HBA were prepared, each containing 10, 20, 30, 40, 50, 60, 70,

80, and 90 μgC per compound for final radiocarbon analysis. Recovery rates were accounted for in the calculation of the initial weight of the two standards.

Table 4.5* Radiocarbon contents and mass of aliquots of known lignin phenols used for blank determinations as well as estimates of mass and $F^{14}C$ of the blank for the SPE cartridge separation step and the entire lignin purification method.

	3HBA			TCA			Result
	Lab no.	Mass (μgC)	$F^{14}C$	Lab no.	Mass (μgC)	$F^{14}C$	
SPE cartridge	11404.1.1	24	0.1205±0.0022	11405.1.1	7	0.6310±0.0107	
	11404.1.2	29	0.1145±0.0021	11405.1.2	9	0.7781±0.0119	
	11404.1.3	41	0.0668±0.0017	11405.1.3	16	0.8925±0.0083	$Mass_{blank}$ = 5.16 ± 0.16 μgC,
	11404.1.4	31	0.0777±0.0019	11405.1.4	42	0.9471±0.0068	
	11404.1.5	45	0.0531±0.0016	11405.1.5	41	0.9523±0.0068	
	11404.1.6	58	0.0408±0.0014	11405.1.6	44	0.9622±0.0069	$F^{14}C$ = 0.53 ± 0.02
	11404.1.7	87	0.0277±0.0012	11405.1.7	81	0.9863±0.0070	
	11404.1.8	83	0.0287±0.0013	11405.1.8	95	0.9988±0.0071	
	11404.1.9	92	0.0340±0.0014	11405.1.9	111	0.9934±0.0071	
Entire method	10139.1.1	9	0.2232±0.0067	10140.1.1	9	0.8435±0.013	
	10139.2.1	28	0.0847±0.0026	10140.2.1	18	0.9171±0.0091	
	10139.3.1	24	0.1155±0.0031	10140.3.1	18	0.9214±0.0093	$Mass_{blank}$ = 4.17 ± 0.35 μgC,
	10139.4.1	39	0.0684±0.0026	10140.4.1	32	0.9529±0.0078	
	10139.5.1	56	0.1015±0.0026	10140.5.1	36	0.9525±0.0083	
	10139.6.1	64	0.0159±0.0019	10140.6.1	39	0.9459±0.0076	$F^{14}C$ = 0.55 ± 0.04
	10139.7.1	70	0.0288±0.0020	10140.7.1	53	0.9606±0.0077	
	10139.8.1	78	0.0341±0.0021	10140.8.1	55	0.9776±0.0079	
	10139.9.1	83	0.0251±0.0027	10140.9.1	81	0.9809±0.0077	

∗including the blank contribution of 25 μL tin capsules.

We utilized the method by Sun et al. (2020) to quantify the mass and $F^{14}C$ of contaminant carbon introduced during the purification process. The blank of the entire method was estimated at m_{blank} = 4.17 ± 0.35μgC, $F^{14}C_{blank}$ = 0.55 ± 0.04 (Table 4.5, Fig. 4.4). We observed the $F^{14}C$ value for the 20 μgC aliquot of the fossil material is different from the regression through the values for the larger aliquots would predict (Table 5 lab No. 10139.2.1, Fig. 4.4a), which may be the main reason for the relatively high uncertainty of the $F^{14}C$ value. Haghipour et al. (2019) found that sample size can affect the precision of the $F^{14}C$ value, and preparing samples for CSRA in the range of 5–20 μgC can be quite challenging, particularly for $F^{14}C < 0.6$. To improve the uncertainty of the $F^{14}C$ value, additional blank measurements are needed. The blank contribution from 25 μL tin capsules is 2.51 ± 0.22 μgC with $F^{14}C$ is 0.87 ± 0.05, suggesting that more than half of the total contamination stems from the 25 μL tin capsules. This suggests that our modification to the lignin phenol purification method by

replacing the two cartridges used by Feng et al. (2013b) with a single HLB SPE cartridge allows obtaining lignin phenols of high purity suitable for reliable radiocarbon analysis.

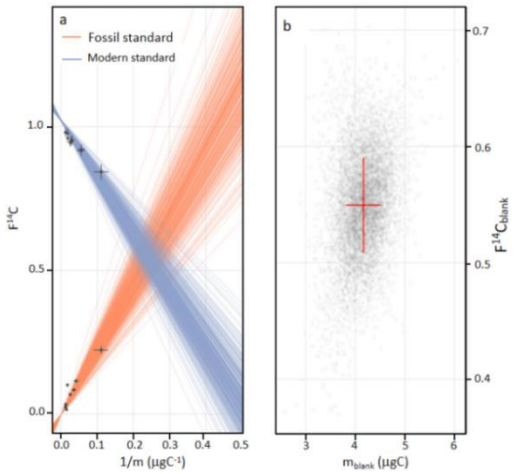

Figure 4.4. Procedural blank assessment for the entire lignin purification method: (a) a sample of 500 regression lines from the posterior distribution gives a visual check of the fitted Bayesian model. Fossil standard = 3-hydroxybenzoic acid (3HBA), modern standard = *trans*-cinnamic acid (TCA); (b) the posterior distribution of masses and $F^{14}C$ values of the procedural blank. m_{blank} = 4.17 ± 0.35 µgC, $F^{14}C_{blank}$ = 0.55 ± 0.04.

4.4. Discussion

Each step in the process may introduce blank into the sample. However, the overall method has a slightly smaller blank (4.17 ± 0.35 µgC) than that of the SPE separation (5.16 ± 0.16 µgC, Table 4.5), suggesting that the HPLC separation can remove some of extraneous carbon introduced in the previous steps and the HPLC separation of individual lignin phenols following CuO oxidation provides an efficient way to purify lignin components from sediments (Hou et al., 2010; Ingalls et al., 2010; Feng et al., 2013b). Feng et al. (2017) employed a HPLC purification method to determine radiocarbon contents of lignin phenols isolated from the dissolved organic matter from Mackenzie and Kolyma rivers. They estimated their procedural blank at 2.5 ± 0.5 µgC for eight HPLC injections, which is lower than our blank estimate. Different sample types may be the main reason for the difference, in addition, different purification processes may also lead to different blank determinations. It should be noted that the results of the blank determination are specific to our laboratory and the above-described lignin purification method. Other laboratories may obtain varying results due to different conditions despite employing the same method.

We were successful in simplifying the purification procedure of lignin phenols for compound-specific radiocarbon analysis from sediments. Our experiment has demonstrated that purification of lignin phenols can be achieved using the HLB SPE cartridge instead of the suggested combination of two cartridges according to Feng et al (2013b), suggesting that this simplified method might be more easily accessible to a broader range of users. We have

tried to use methanol as a solvent for rinsing the HLB SPE cartridges. Different from the above described method using EtAc, only 6 mL methanol was used to rinse the SPE cartridge, and the recovery rates of lignin phenol standards were higher than 70%. However, when methanol was used to examine the purification capability of the HLB SPE cartridge with TS, we found that there were more impurities in the HPLC chromatograms of the sample rinsed with methanol than in those eluted with EtAc. Therefore, the separation of phenols from non-phenol components in the extracts was achieved by using the less polar solvent EtAc instead of methanol.

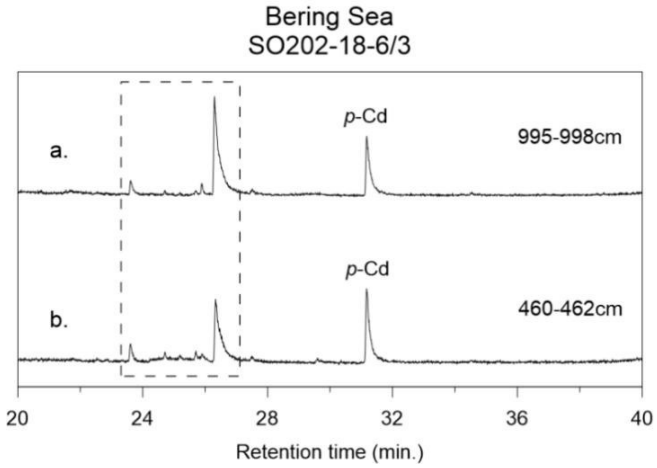

Figure 4.5. Chromatograms of GC-MS for sediment samples from Bering Sea core SO202-18-6/3 (460-462cm, 995-998cm) based on the method of lignin purification in this study. A small aliquot of purified phenols (0.5%) was used to check identity and purity by GC-MS. However, some impurities derive from the sample itself (dashed box) and cannot be separated from the *p*-Cd phenol after the two-step separation. Y axis is the relative abundance of GC-MS in intensity units.

One compound mixture (Bd, Vn, and Sl) was isolated per sample separated on the RP column of HPLC (Fig. 4.2). The mixture can be further chromatographically separated on HPLC using a ZORBAX Eclipse XDB-C18 column (4.6×150 mm; 5 μm particle size, 40 °C) of HPLC. Three compounds were collected individually after separation by a 36-minute binary gradient of mobile phases of the HPLC method. In this study, we did not measure the blank contribution of the C18 column nor the blank of the entire method which includes the two-step separation of HPLC. Therefore, only 11 individual lignin-derived phenols were isolated in this study.

It has to be noted that the above-described method cannot eliminate all impurities from natural samples. If other compounds co-elute with a target lignin phenol during the HPLC separation, they will be collected together. In several sediment samples from the Bering Sea (Fig. 4.5), we observed an additional compound in the *p*-Cd fraction when checking its purity by GC-MS, and sometimes the amount of this compound exceeds that of the phenol (Fig. 4.5). This variation in impurity levels between samples highlights the importance of evaluating the

purity of the purified samples by GC-MS after HPLC separation. According to our results of individual phenol radiocarbon data, it is recommended to aim for purified lignin phenol samples that contain at least 30 μgC to obtain reliable age estimates. Although the recovery rate of 3,5Bd was relatively low, we obtained pure 3,5Bd in some sediment samples from the Bering Sea, Okhotsk Sea, and Laptev Sea shelves, possibly because the impurities in the sample affected the separation of 3,5Bd in the HLB SPE cartridge.

4.5. Summary and Conclusions

A complete method for the purification of lignin phenols for CSRA was established after several decades of effort (Feng et al., 2013b). In this study, we simplified these authors' method and evaluated $F^{14}C$ and the mass of the associated procedural blank following the approach of Sun et al. (2020). Different from Feng's method (2013b), lignin phenols were purified only by one HLB SPE cartridge (Waters Oasis, 200 mg, 6 mL). The following single compound collection using high pressure liquid chromatography (HPLC) was also different from the published method. The HPLC was equipped with a Phenomenex Synergi Polar-RP column, and column hold at 40 °C in running. The HLB SPE cartridges had high recovery rates (>70%) and a low blank contribution. Samples were passed through the HLB cartridge with 60 mL ethyl acetate to achieve separation. It is advisable to use a small aliquot of purified phenols after HPLC isolation should to check the purity by gas chromatography-mass spectrometry. We found that the blank carbon contribution of this entire method is 4.17 ± 0.35 μgC with $F^{14}C$ of 0.55 ± 0.04.

Author contributions

The idea of the revised method was drafted by JH and GM. JH found the SPE cartridge used for lignin purification and we improved the method of SPE separation. JH improved the HPLC separation method for lignin purification of sediment samples. HG was responsible for radiocarbon analyses and blank determinations. MC prepared the extraction and purification of all the lignin standards and samples for blank determinations and improvement. MC wrote the manuscript together with comments and contributions from all co-authors.

Acknowledgments

We thank Elizabeth Bonk, Lea Phillips, Torben Gentz, Malte Hoehn and other members of MICADAS group in AWI Bremerhaven for laboratory assistance. M. Cao thanks the China Scholarship Council and POLMAR Graduate School for additional support.

5. Manuscript III

Compound-specific radiocarbon ages of lignin phenols off the Amur and the Yukon river catchments as recorders of supply pathways of terrigenous organic matter during glacial-interglacial transition

Mengli Cao[1], Jens Hefter[1], Hendrik Grotheer[1,3], Ralf Tiedemann[1,2], Lester Lembke-Jene[1], Gesine Mollenhauer[1,2,3]

[1]Alfred-Wegener-Institut, Helmholtz-Zentrum für Polar-und Meeresforschung (AWI), 27570 Bremerhaven, Germany.
[2]Department of Geosciences, University of Bremen, 28359 Bremen, Germany.
[3]MARUM-Center for Marine Environmental Sciences, University of Bremen, 28359 Bremen, Germany.

In preparation for *Global Biogoechemical Cycles*.

Abstract

Northern hemisphere permafrost stores vast amounts of organic matter in frozen form. Once thawed and remobilized, this organic matter may become bioavailable and can be respired to CO_2, contributing to the atmosphere's greenhouse gas content. However, the mechanism by which permafrost-derived organic carbon (OC) was mobilized and made bioavailable remain poorly understood. It has been observed that the age difference between co-occurring lipids and lignin phenols in recent sediments off the modern-day Arctic rivers varies with the thermal state of the permafrost in the hinterland, potentially making the pairing of compound-specific radiocarbon analysis (CSRA) of these terrigenous compounds a powerful tool to reconstruct permafrost thawing history. Previous studies on delivery of aged carbon were based on CSRA of lipids from the Yukon and Amur river basins. Here, we pair these existing data with the first downcore CSRA records of lignin-derived phenols from sediment cores retrieved off the two basins covering the early deglaciation to the Holocene. We find that the differences in ^{14}C age between the different phenols analysed in this study are consistent with the effects expected for sediment samples that receive inputs from at least two different sources characterized by different age and degradation state. Terrigenous OC contribution to

the marine sediments varied with time. Deep and surface OC pools can be transported by the same terrestrial processes, such as surface runoff and thermo-erosion. Climate warming affects the pre-depositional age of lignin phenols and lipids, and increasing surface discharge will increase the age offset between lignin phenols and lipids in the marine sediments. Age offset between lipids and lignin phenols may be used as palaeo-proxies for the changes of surface discharge in Arctic regions.

5.1. Introduction

Northern circumpolar permafrost regions hold roughly half of the global soil organic carbon (OC) pool (1300 ± 200 Gt; Tarnocai et al., 2009; Hugelius et al., 2014) of which about two-thirds are present in frozen sediments below 3 m (Hugelius et al., 2014). Warming at high latitudes is causing accelerated remobilization of this permafrost OC through gradual top-down thawing of permafrost (active layer deepening) and abrupt thaw, such as thermokarst and erosion (Lawrence et al., 2015; Schuur et al., 2015; Turetsky et al., 2020). Thermokarst occurs when warming melts ground ice, causing the land surface to collapse into the space previously occupied by ice. The landscapes in the Arctic are heterogeneous, and the degree of permafrost coverage affects the remobilization pathways of OC associated with different permafrost structures (Gustafsson et al., 2011; Feng et al., 2013a). Erosion and riverine transfer at high latitudes can lead to the long-term preservation of terrestrial particulate OC in marine sediments (Feng et al., 2013a; Hilton et al., 2015; Tesi et al., 2016; Winterfeld et al., 2018; Martens et al., 2019). On the other hand, permafrost OC is considered to be highly sensitive to microbial decomposition upon thaw and may escape to the atmosphere as carbon dioxide (Mann et al., 2015; Stapel et al., 2018; Hutchings et al., 2019), with the remainder being re-buried in soils and/or sediments (Vonk et al., 2012; Hilton et al., 2015). Since the Last Glacial Maximum (LGM), the temperature in the Northern Hemisphere has been increasing (Rasmussen et al., 2008; Clark et al., 2012), and some of the Arctic continuous permafrost has changed to discontinuous permafrost or disappeared (Vandenberghe et al., 2014; Obu et al., 2019). The last deglaciation therefore offers the possibility to assess the remobilization pathways of permafrost OC during rapid climate warming. Tesi et al. (2016) observed rapid accumulation of permafrost OC in Laptev Sea shelf sediment at the end of the deglaciation and suggested that it was supplied from the Lena River watershed via surface discharge. However, coastal erosion releasing old permafrost OC was a significant source of OC translocated to the East Siberian Sea from the Holocene to the modern day (Vonk et al., 2012; Keskitalo et al., 2017). Winterfeld et al. (2018) and Meyer et al. (2019) also suggested that shelf erosion was the dominant process for carbon mobilization during melt water pulse 1A and 1B in the Okhotsk and Bering Seas.

The transition from the LGM to the current interglacial, a period referred to as the last deglaciation, represents a temperature increase by about 3.5 °C in the Northern Hemisphere (Shakun et al., 2012). During the last deglaciation, the large continental ice sheets decayed and global sea-level rose by ~ 134 m with rates up to approximately 30 mm per year (Lambeck et al., 2014). Increasing temperature caused major reorganization of the Arctic permafrost region, including the northward shift of the permafrost boundary (Lindgren et al., 2016). There are few records of past permafrost OC remobilization in the Arctic, and our understanding of the permafrost carbon cycle during the last deglaciation remains underconstrained.

Fluvial systems form the major links between continental and oceanic OC pools. During the transport from river catchments to the oceans, permafrost OC is subjected to various physical and biogeochemical processes (e.g., sedimentation and degradation) before deposition together with autochthonous marine OC. Different terrestrial constituents have their own pre-depositional histories and abilities to survive the multiple processes of sediment transport and early diagenesis until deposition. The central challenge to detecting climate-induced mobilization of permafrost is to distinguish the old permafrost OC among the diverse OC pools during rapid climate change, which requires qualitative analysis of the sources for different OC pools in the Arctic. Source-tracing organic molecules offer a unique perspective into the fate of specific carbon pools.

Lignin is a biomarker commonly used to trace the sources and evolution of riverine OC in the land-ocean continuum. Lignin is a naturally occurring and abundant biopolymer found almost exclusively in terrestrial vascular plants, providing a large contribution to OC preserved from surface OC pools, such as higher plants vegetation, wetlands and the surface of permafrost soils (Hedges and Parker, 1976; Hedges and Mann, 1979; Opsahl and Benner, 1995; Otto et al., 2005; Feng et al., 2013a; Cao et al., 2023). Previous studies found that lignin is relatively concentrated in mineral-poor soil fractions (such as coarse soil particles or woody debris) with relatively weak mineral associations (Amelung et al., 2002; Kögel-Knabner et al., 2008; Schmidt et al., 2011) and may be more accessible to microbial degradation than mineral-bound soil organic matter. Under present climate conditions the radiocarbon ages of individual lignin phenols isolated from riverine suspended matter or sediments, flood plain and river bank deposits as well as marine sediments at river-dominated margins representing various river catchments of the world are affected by temperature and precipitation (Eglinton et al., 2021).

Different from lignin, lipids can be derived from both terrestrial plants and marine microorganisms, but high molecular weight (HMW) *n*-alkanes and fatty acids are mainly derived from higher terrestrial plants (Volkman et al., 1980; Meyers, 1997; Ficken et al., 2000). Long-chain lipids show a strong affinity to mineral surfaces through covalent or

electrostatic bonds that protect them against biological degradation (Brodowski et al., 2006; Kögel-Knabner et al., 2008; van der Voort et al., 2017). Therefore, lignin phenols may turn over more quickly than long-chain lipids in soils (Repasch et al., 2021; Jia et al., 2023), which results in disparate radiocarbon ages of these biomarkers in samples containing input from a continuum of differently aged sources in the modern Arctic river systems (Feng et al., 2013a, 2015b). Previous studies suggested that the delivery of lignin is mainly controlled by surface runoff with high contributions of young, rapidly cycling OC, and lipids predominantly trace permafrost OC which is remobilized from deep soils in the discontinuous permafrost regions (Feng et al., 2013a, 2015b). The difference in radiocarbon age between lignin phenols and long-chain lipids is therefore proposed as an indicator of hydrological changes and/or permafrost stability in the Arctic (Feng et al., 2013a).

The Yukon River and the Amur River basins were both covered by continuous permafrost during the LGM (Vandenberghe et al., 2014). After the warming during the last deglaciation, only ~ 16% of the Yukon basin remains under continuous permafrost and ~ 70% of the basin is covered by discontinuous permafrost (Brabets et al., 2000; Holmes et al., 2012), while the Amur basin is completely permafrost free at present. Here, we examine the radiocarbon signature of lignin-derived phenols (this study) and long-chain fatty acids stemming from epicuticular waxes of higher plants (Winterfeld et al., 2018; Meyer et al., 2019) in two sediment cores from the Bering and Okhotsk Sea shelves to compare the fate of various terrestrial OC pools over different temporal and spatial scales and to explore their ^{14}C signals as tracers for permafrost carbon mobilization during the last deglaciation. The objectives are three: (1) to investigate whether there is a difference of the radiocarbon age between lignin phenols and lipids during the last deglaciation in the Arctic and sub-Arctic; (2) to determine the controlling factors for the age differences; (3) to evaluate whether this difference can be used as an indicator for the thawing processes within the catchments.

5.2. Study area

The Bering Sea is located north of the Pacific Ocean (Fig. 5.1). The deglacial sediments from the Bering Sea contain records both of sea-level rise-induced erosion of the vast Bering Shelf, and of runoff from the Yukon River (Kennedy et al., 2010; Meyer et al., 2019). The Yukon River is a major watercourse in northwestern North America. The river is 3190 kilometers long and empties into the Bering Sea at the Yukon–Kuskokwim Delta. Although the annual mean discharge of the Yukon River near its mouth is around 6700 m^3/s, most of the flow occurs in the summer months from snowmelt, rainfall, and glacial melt (Brabets et al., 2000). The Yukon Basin is located between the Rocky Mountains in the north and the Pacific Mountain system to the south (Fig. 5.1) and measures approximately 8.5×10^5 km^2 in area. The Yukon Basin was mostly unglaciated during the LGM, featuring permafrost

(Vandenberghe et al., 2014), and remains mostly so until today (Brabets et al., 2000). Thawing of permafrost may increase the recharge of aquifers, thus increasing base flow in streams, which could affect the development and expansion of wetlands. Wetlands occupy about 14% of the Yukon Basin at present. Approximately 1% of the Yukon Basin is covered by glaciers (Brabets et al., 2000), and glaciers are presently found in the Alaska Range and Wrangell–St. Elias Mountains. Vegetation exerts an indirect influence on permafrost by affecting climatic and other terrain features. Needleleaf forests (54%), tall and low shrub lands (9%), broadleaf forests, lichens, barren lands, and wet herbaceous vegetation compose about 90% of the Yukon Basin (Brabets et al., 2000).

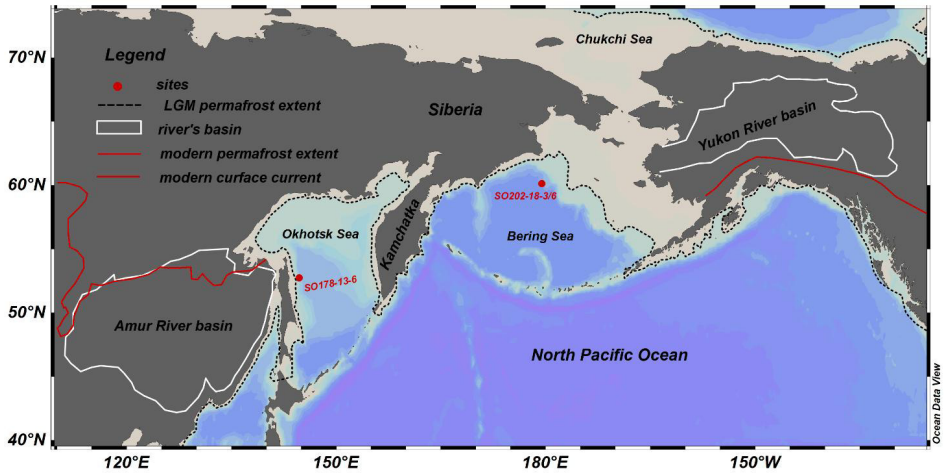

Figure 5.1 Study area. Red dots are the sediment cores used in this study (adapted from Cao et al., 2023).

The Okhotsk Sea is a marginal sea of the western Pacific Ocean (Fig.5.1), and is known as the southernmost region of seasonal sea ice in the Northern Hemisphere today. It is bordered by Russia's Kamchatka Peninsula in the east, the Kuril Islands in the southeast, Japan's island of Hokkaido in the south, the island of Sakhalin along the west, and a stretch of eastern Siberian coast along the west and north (Fig. 5.1). Large quantities of continental sediment are discharged into the sea, primarily from the Amur River. The Amur River is the longest river of the Russian Far East. The mean discharge of the Amur at its mouth is about 10,900 m^3/s, and is fed principally by the monsoon rains that fall in summer and autumn. The catchment of the Amur transitioned from complete permafrost coverage during the LGM to almost entirely permafrost-free conditions at present (Vandenberghe et al., 2012). Today, the Amur Basin holds 184,561 km^2 of wetlands (Mao et al., 2021), accounting for 9% of the whole basin area. Much of the Amur Basin lies in the taiga vegetation zone. Larch is the predominant species, particularly in boggy areas, with some pine, spruce, and fir on drier land.

5.3. Material and methods

5.3.1. Sampling

The sediment cores SO202-18-6/3 and SO178-13-6 from the Bering Sea and Okhotsk Sea are shown in Figure 5.1. Piston core SO202-18-3 and Kasten core SO202-18-6 were recovered from the continental slope of the Bering Sea in 2009 during R/V Sonne cruise SO202-INOPEX (Gersonde, 2012). The two cores are treated as one composite record (Kühn et al., 2014). It represents a continuous sedimentary sequence dated back to the Last Glacial (~ 25 kyr) (Kühn et al., 2014; see chapter 2 for more details).

The 23.7 m long piston core SO178-13-6 was collected from the Sakhalin margin in the Okhotsk Sea during the expedition SO178-KOMEX with R/V Sonne (Dullo et al., 2004), with the lowermost interval corresponding to ~ 17.5 kyr (Max et al., 2014).

5.3.2. Chronology

The chronology of the two sediment cores is constrained by accelerator mass spectrometry (AMS) ^{14}C dating of calcareous foraminifera. We used the program Calib 8.20 with the Marine 20 calibration curve (Heaton et al., 2020; Stuiver and Reimer, 1993) for initial age determinations. Radiocarbon-based age models for the two cores are revised based on Kühn et al. (2014, 2015) for core SO202-18-6/3, Max et al. (2014) and Lembke-Jene et al. (2017) for core SO178-13-6. See chapter 2 for more details. The time interval covered by the records is subdivided into six intervals: the early deglaciation (ED, 19.0–16.5 kyr), the Heinrich Stadial 1 (HS1; 16.5–14.6 kyr), the B/A (14.6–12.9 kyr), the Younger Dryas (YD; 12.9–11.5 kyr), the Pre-Boreal (PB; 11.5–9 kyr) and the Holocene (< 9 kyr).

5.3.3. Carbon isotope composition of organic carbon ($\delta^{13}C$)

The stable carbon isotope composition of organic matter ($\delta^{13}C$) was analyzed for selected samples from the two sediment cores by a Thermo Fisher Scientific Delta-V-Advantage gas mass spectrometer equipped with a FLASH elemental analyser EA 2000 and a CONFLO IV gas mixing system in the Stable Isotope Laboratory of the Alfred Wegener Institute for Polar and Marine Research in Potsdam. Sediments were freeze-dried, ground, and homogenized. Carbonates were removed by adding hydrochloric acid. An aliquot of the sample corresponding to 0.2 mg OC was weighed into a tin capsule. The carbon isotope composition was determined relative to laboratory standards of known isotopic composition. $\delta^{13}C$ values of the samples are given in ‰ relative to V-PDB. The standard deviation (1σ) was generally better than $\delta^{13}C = \pm 0.15‰$.

5.3.4. CuO oxidation for lignin extraction

The extraction of lignin phenols was carried out based on the method of Goñi and Montgomery (2000) and as described in chapter 2. Dried samples were oxidized with CuO (~ 2 g) and ~ 50 mg ferrous ammonium sulfate in ~ 18 mL 2N NaOH under anoxic conditions. The oxidation was conducted with a microwave accelerated reaction system at 150 ℃ for 90 min. Oxidation products were transferred to centrifuge tubes, and the alkaline supernatant was acidified to pH 1 with 37% HCl, and were subsequently recovered by two successive extractions with ethyl acetate (EtAc). Combined ethyl acetate extracts were evaporated under a stream of nitrogen, and stored in the fridge (4 ℃) until further processing.

5.3.5. Two-step separation of lignin-derived phenols

The two-step isolation of lignin-derived phenols was carried out as described in chapter 2. Briefly, HLB soild phase extraction (SPE) cartridges (Waters Oasis, 200 mg, 6 mL) were activated with methanol overnight. Samples were loaded onto the activated SPE cartridges with EtAc. The eluates were dried and transferred to 1.5 mL vials with 1 mL EtAc and filtered with PTFE filters (13 mm, 0.22 μm). The filtrate was dried under nitrogen (40 ℃) and subsequently re-dissolved in 150 μL methanol for high performance liquid chromatography (HPLC) separation. A small aliquot of the samples was used to check phenol content by gas chromatography-mass spectrometry (GC-MS).

Abundances of lignin phenols were determined on an Agilent 1200 HPLC system coupled to a diode array detector. The HPLC was equipped with a Phenomenex Synergi Polar-RP column (4.6×250 mm; 4 μm particle size, RP column) kept at 40 °C during runs and a binary gradient program was used to achieve chromatographic separation of 10 individual phenols. Following HPLC fraction collection, the lignin phenols were recovered by liquid-liquid extraction with 3×3 mL EtAc. Isolated fractions were dried under nitrogen (40 ℃), then transferred to 4 mL vials and stored in the fridge (4 ℃) until radiocarbon measurement. A small aliquot of purified phenols was used to check identity and purity by gas chromatography-mass spectrometry (GC-MS).

5.3.6. GC-MS analyses

The GC-MS analyses of lignin-derived phenols was carried out as described in Cao et al. (2023, chapter 2). Before injection into the GC-MS, samples were derivatized for 30 minutes at 60 ℃. An Agilent 6850 GC coupled to an Agilent 5975C VL MSD quadrupole MS operating in electron impact ionization and fullscan mode was used for analysis. The GC was equipped with a DB-1 MS column (30 m × 0.25 mm i.d., film thickness 0.25 μm). The source temperature of the MS was set to 230 ℃ and the quadrupole to 150 ℃. Helium was used as a

carrier gas at a constant flow rate of 1.2 mL min^{-1}. Samples were injected in splitless mode in a split/splitless injector held at 280 °C. The temperature of the column was programmed from 100 °C and ramped at 4 °C min^{-1} to 220 °C, then at 10 °C min^{-1} to 300 °C, with a final hold time of 5 min.

Table 5.1 Abbreviation and source of lignin-derived phenols used in this chapter.

Compounds	Abbreviation	Source	Reference
Vanillin	Vl	vascular plants	Hedges and Mann, 1979; Hedges et al., 1988; Hedges and Weliky, 1989; Opsahl and Benner, 1995;
Vanillic acid	Vd		
Syringic acid	Sd	angiosperms	
Ferulic acid	Fd	non-woody tissues of vascular plants	
p-Hydroxybenzoic acid	Pd	moss-dominated peat	Erickson and Miksche, 1974; Goñi and Hedges et al., 1995; Goñi et al., 2000
3,5-Dihydroxybenzoic acid	3,5Bd	peat	

5.3.7. Radiocarbon measurement

Radiocarbon measurements followed the protocol described in Mollenhauer et al. (2021). Briefly, isolated lignin phenol fractions were transferred (3 times) to 25 µL tin capsules with a minimum amount of methanol and kept in a holding tray (20 min.). Following the third transfer the holding tray was placed in a desiccator and stored evacuated (150 mbar) inside an oven (40 °C) for 48 h. After drying in the desiccator and oven, samples were folded as small as possible. Each tin ball was stored in a labeled 1.5 mL glass vial until analysis. Analyses were carried out by a Mini Carbon Dating System (MICADAS; Synal et al., 2007). Samples were combusted using an elemental analyzer coupled to MICADAS via the gas interface system (Wacker et al., 2013). The radiocarbon data are normalized to and corrected by standards NIST oxalic acid II and phthalic acid (see chapter 2 and 4 for more details).

Radiocarbon dating of organic matter in sediment samples was similar as described above. Briefly, freeze-dried samples were weighed into silver boats and the inorganic carbon was removed with 6 M hydrochloric acid covered and dried on a 60 °C heating plate. After carbonate removal, samples in the silver boats were folded into a tin boat to be combusted in the elemental analyzer at 950 °C. The resulting gas was transferred into the automated graphitization system (Wacker et al., 2010) for graphitization to produce graphite targets for measurement in the MICADAS. Radiocarbon data are reported as fraction modern carbon ($F^{14}C$), $\Delta^{14}C_{initial}$, and conventional ^{14}C age at deposition. See chapter 2 for the calculation of $\Delta^{14}C_{initial}$ and ^{14}C age. The measured $F^{14}C$, $\Delta^{14}C_{initial}$, and ^{14}C age of TOC and lignin-derived phenols are given in Table 5.2 and 5.3.

Table 5.2. Blank-corrected $F^{14}C$ values, $\Delta^{14}C_{initial}$ and conventional ^{14}C age at deposition of total organic carbon (TOC) in the two sediment cores.

Sediment core	Depth (cm)	Deposition age (kyr)	TOC* (%)	$\delta^{13}C$ (‰)	$F^{14}C$**	$\Delta^{14}C_{initial}$ (‰)	^{14}C age (year)
	60	4.24	0.71	n.a.	*0.3408 ± 0.0028*	*-435.49 ± 16.14*	*4879 ± 166*
	101.3	6.72	0.73	-23.98	0.2521 ± 0.0020	-436.60 ± 12.82	5258 ± 202
	200	9.63	1.08	n.a.	n.a.	/	/
	220	9.80	n.a.	n.a.	*0.1814 ± 0.0046*	*-411.00 ± 6.22*	*4971 ± 245*
SO202-18-6	305	10.40	1.14	-25.30	0.1658 ± 0.0016	-422.11 ± 4.96	5286 ± 142
	380	10.85	1.22	-24.77	0.1816 ± 0.0016	-330.90 ± 3.76	4203 ± 140
	430	11.02	0.87	-24.81	0.1484 ± 0.0015	-441.74 ± 4.69	5815 ± 141
	461	11.14	0.86	n.a.	*0.1317 ± 0.0044*	*-497.32 ± 6.50*	*6695 ± 299*
	560	11.72	0.80	-24.96	0.1238 ± 0.0014	-493.37 ± 7.05	6765 ± 188
	447	12.54	1.10	-24.80	0.1286 ± 0.0015	-418.84 ± 3.20	6032 ± 131
	481	12.79	1.07	-24.80	0.1240 ± 0.0014	-422.79 ± 3.46	5929 ± 137
	635	13.60	1.10	-24.99	0.1006 ± 0.0014	-483.21 ± 6.83	6763 ± 217
	825	14.63	1.37	-25.04	0.0570 ± 0.0012	-668.47 ± 14.01	10608 ± 347
SO202-18-3	993	15.18	1.05	-24.47	*0.0764 ± 0.0058*	*-524.65 ± 9.89*	*7994 ± 665*
	1055	15.58	0.87	-23.31	0.0769 ± 0.0013	-498.16 ± 8.42	7684 ± 292
	1136	16.67	0.82	-22.70	*0.0769 ± 0.0053*	*-427.37 ± 9.34*	*6903 ± 652*
	1144	16.82	0.81	-22.91	*0.0836 ± 0.0055*	*-365.67 ± 8.04*	*6167 ± 633*
	1425	23.39	0.97	-23.41	0.0382 ± 0.0012	-357.76 ± 5.46	6804 ± 433
	60	0.80	1.62	n.a.	*0.7395 ± 0.0035*	*-191.46 ± 12.77*	*1540 ± 64*
	700	7.40	1.17	n.a.	*0.3981 ± 0.0022*	*-27.69 ± 1.84*	*880 ± 482*
	1320	9.59	1.47	-24.16	0.2495 ± 0.0011	-210.95 ± 9.13	2541 ± 406
	1460	10.59	1.5	-24.06	*0.2401 ± 0.0018*	*-194.84 ± 6.48*	*2639 ± 347*
	1525	10.34	1.45	-24.02	0.2312 ± 0.0009	-199.58 ± 6.23	2629 ± 316
	1620	10.81	1.43	-24.31	0.2244 ± 0.0008	-177.53 ± 4.50	2487 ± 269
	1710	11.35	1.48	-24.34	0.2118 ± 0.0008	-171.56 ± 3.75	2569 ± 244
SO178-13-6	1810	12.04	1.39	-25.02	*0.1918 ± 0.0015*	*-182.81 ± 3.76*	*2999 ± 249*
	1830	12.20	1.44	-25.10	0.1840 ± 0.0007	-202.23 ± 4.13	3275 ± 245
	1910	12.84	1.37	-24.87	0.1697 ± 0.0007	-204.88 ± 4.12	3354 ± 254
	2035	13.93	1.37	-25.28	*0.1443 ± 0.0013*	*-228.22 ± 4.25*	*3568 ± 263*
	2075	14.29	1.28	-24.90	0.1411 ± 0.0006	-212.46 ± 3.72	3468 ± 250
	2130	14.78	1.14	-24.78	0.1336 ± 0.0006	-207.92 ± 3.20	3850 ± 229
	2250	15.89	1.12	-24.86	0.1166 ± 0.0006	-209.87 ± 2.25	4094 ± 174
	2340	16.68	1.02	-23.98	*0.0971 ± 0.0012*	*-275.46 ± 3.36*	*5016 ± 223*

n.a.: not analyzed

*TOC data have been published in Winterfeld et al. (2018) and Cao et al. (2023)

**Part of the $F^{14}C$ values were previously published in Winterfeld et al. (2018) and Meyer et al. (2019) and marked in italic font.

5.4. Results

5.4.1. $\delta^{13}C$ of bulk OC

The $\delta^{13}C$ values of the Bering Sea sediment samples ranged from -25.3‰ to -22.7‰ (Table 5.2). The highest (-22.7‰) and lowest (-25.3‰) $\delta^{13}C$ values are observed in the ED and PB periods, respectively (Fig. 5.2). $\delta^{13}C$ values decreased from 17.0 kyr to 14.6 kyr in the Bering Sea sediments, however, no significant change occurred from14.6 kyr to 9.0 kyr. In comparison, a narrower range was found in the Okhotsk Sea sediment samples, with values ranging from -25.3‰ to -24.0‰ (Table 5.2, Fig. 5.2), and the highest and lowest $\delta^{13}C$ values are observed in the ED and B/A period, respectively. Similar to the Bering Sea, $\delta^{13}C$ values in the Okhotsk Sea also decreased from the HS1 to B/A, and did not change significantly from the B/A to YD. However, the $\delta^{13}C$ values increased significantly after the YD.

5.4.2. ^{14}C age of bulk OC

Marine sediments exhibit a relatively wide range of initial $\Delta^{14}C$ compositions between -668.47 ± 14.01‰ and -27.69 ± 1.84‰ in the two sediment cores (Table 5.2), which correspond to conventional ^{14}C ages at deposition between 10608 ± 347 and 880 ± 482 years. The Bering Sea sediments show slightly older ^{14}C age (10608 ± 347 to 4203 ± 140) compared to the Okhotsk Sea sediments (5016 ± 223 to 880 ± 482) (Table 5.2). The youngest ^{14}C age at deposition in the core SO202-18-6/3 was fund at 10.85 kyr, and the oldest ^{14}C age was detected at 14.63 kyr, where a relatively high TOC value was found. From the ED to the early Holocene, the ^{14}C age at deposition of TOC decreased in the Okhotsk Sea sediments,with the maximum age in the ED and the minimum age in the early Holocene.

5.4.3. Radiocarbon data of individual phenols

The $\Delta^{14}C$ value and ^{14}C age used in here and after are the initial $\Delta^{14}C$ value and conventional ^{14}C age at deposition, respectively. Lignin is more difficult to degrade than lipids under the same conditions, but binding to minerals in soils protects lipids from degradation, allowing them to be stored in the soils longer than lignin (Killops and Killops, 2005; Bahri et al., 2008; Kögel-Knabner et al., 2008). Our lignin-derived phenol ages are younger than the lipids ages, consistent with literature data exiting to date. The ^{14}C compositions of lignin-derived phenols are displayed in Table 5.3 and Fig. 5.2. In the Bering Sea sediments, ^{14}C age at deposition of phenols ranged from 3048 ± 399 to 9756 ± 749 years. In comparison, a narrower range was found in the Okhotsk Sea sediment samples, with values ranging from 320 ± 474 to 4979 ± 409 years (Table 5.3, Fig. 5.2). The ^{14}C age at deposition of the non-lignin phenol 3,5Bd was generally lower than that of the lignin phenols, of which the acids Vd typically are the oldest. In the Okhotsk Sea, ^{14}C age at deposition of individual phenols decreased from the ED to the

YD, which is agreement with the change of ^{14}C age of n-C26:0 fatty acid (Fig. 5.2). The ^{14}C age at deposition of individual phenols from the Okhotsk Sea sediments decreased to a minimum of 320 ± 474 years at 7.45 kyr. V-phenols are present in all vascular plants, while C- and S-phenols are indicative of certain types of plant or plant tissues, which makes Vd the best general representative of terrestrial OC sources. Although our data set comprises more ^{14}C age data of Pd than Vd, it is considered less representative of higher plant vegetation, as the complexity of Pd sources in permafrost regions (Feng et al., 2013a) may affect its viability as a proxy for terrestrial surface OC input.

5.5. Discussion

5.5.1. Contrasting ^{14}C characteristics of individual phenols

Lignin-derived phenol ages in modern day river catchments across the globe are significantly correlated with catchment weighted mean annual temperature and precipitation, and lignin-derived phenol ^{14}C ages have been reported to increase with decreasing mean annual temperature and precipitation (Eglinton et al., 2021). After the LGM, the mean annual temperature in the Northern Hemisphere gradually increased (Rasmussen et al., 2008; Clark et al., 2012), and the ^{14}C ages of lignin-derived phenols gradually decreased in the two sediment cores from the ED to the Holocene, especially in the record from the Okhotsk Sea (Fig. 5.2). The mean $\Delta^{14}C$ value of lignin phenols in the Bering Sea (-437.5 ± 7.7‰) was higher than in the Yukon River surface sediments (-252 ± 9‰) and the results from other large Arctic river surface sediments (e.g., Lena, Ob, and Mackenzie Rivers; Feng et al., 2015b). However, the mean $\Delta^{14}C$ values of lignin phenols collected from Arctic river surface sediments reported in Feng et al. (2015) were higher than the result of core SO178-13-6 recovered from the Okhotsk Sea (-142.4 ± 4.5‰). The latitude of the Okhotsk Sea core site was lower than that of the Bering Sea core site and other Arctic river sites in Feng et al. (2015b), the mean lignin phenols age of the Okhotsk Sea was thus lower than that of the Bering Sea and Arctic river sediments. Our results are consistent with the modern pattern of lignin phenols ^{14}C age varying with differences in climate (Eglinton et al., 2021).

Table 5.3. Compound-specific radiocarbon data of lignin-derived phenols. Deposition age represents the calendar age of the respective sediment layers. $\Delta^{14}C_{initial}$ of TOC and lignin-derived phenols are referred to initial $\Delta^{14}C$-TOC and initial $\Delta^{14}C$-phenol, respectively. These values are calculated from blank-corrected $F^{14}C$ values and involve a correction for decay, and temporally variable atmospheric $\Delta^{14}C$ values are considered for age calculations (see chapter 2 for details). The content of OC for each phenol was measured by MICADAS (Mass, mg OC). ^{14}C age is the apparent initial conventional ^{14}C age calculated following Schefuß et al. (2016).

Sediment core	Depth (cm)	Deposition age (kyr)	$\delta^{13}C$ (‰)	Initial $\Delta^{14}C$-TOC (‰)	Phenol	Mass (µg OC)	$F^{14}C$	Initial $\Delta^{14}C$-phenol (‰)	^{14}C age (year)
SO202-18-6	55-57	3.97	n.a.	n.a.	Pd	44	0.3243 ± 0.0056	-471.17 ± 18.00	5339 ± 201
	200-202	9.64	n.a.	n.a.	Pd	50	0.1630 ± 0.0051	-472.02 ± 7.11	5793 ± 283
					Pd	47	0.1512 ± 0.0053	-510.32 ± 7.71	6398 ± 309
					Vd	84	0.1647 ± 0.0039	-466.75 ± 6.79	5713 ± 231
					Sd	59	0.1672 ± 0.0046	-458.47 ± 6.81	5589 ± 258
	460-462	11.14	n.a.	−497.32±6.50	Pd	78	0.1532 ± 0.0040	-405.11 ± 5.24	5342 ± 247
					Vl	56	0.1439 ± 0.0047	-441.05 ± 5.84	5843 ± 292
					Vd	50	0.1428 ± 0.0051	-445.70 ± 5.98	5910 ± 314
					Sd	36	0.1452 ± 0.0064	-436.35 ± 6.18	5776 ± 377
SO202-18-3	739-742	14.28	n.a.	n.a.	Pd	89	0.1105 ± 0.0036	-372.86 ± 7.29	5295 ± 377
					Sd	46	0.1461 ± 0.0054	-170.50 ± 3.43	3048 ± 399
					3,5Bd	31	0.1420 ± 0.0072	-194.12 ± 4.05	3280 ± 488
	995-998	15.20	n.a.	n.a.	Pd	69	0.0830 ± 0.0041	-473.50 ± 8.61	7178 ± 472
					Vl	44	0.0846 ± 0.0055	-463.46 ± 8.63	7026 ± 586

					Vd	47	0.0602 ± 0.0053	-618.04 ± 11.43	9756 ± 749
	1146-1149	16.88	n.a.	n.a.	Pd	67	0.0622 ± 0.0041	-516.01 ± 11.18	8375 ± 634
					Vd	65	0.0550 ± 0.0042	-572.61 ± 12.41	9374 ± 701
					3,5Bd	48	0.0972 ± 0.0052	-244.08 ± 5.37	4793 ± 553
SO178-13-6	55-65	0.80	n.a.	−191.46±12.77	Pd	79	0.7543 ± 0.0064	-161.51 ± 11.49	1248 ± 86
					Vd	102	0.7572 ± 0.0063	-158.24 ± 11.27	1217 ± 85
	695-705	7.45	n.a.	n.a.	Pd	56	0.4078 ± 0.0053	14.49 ± 0.93	539 ± 471
					Vl	81	0.4111 ± 0.0049	22.54 ± 1.44	476 ± 469
					Vd	61	0.3977 ± 0.0052	-10.67 ± 0.68	741 ± 471
					Fd	43	0.3978 ± 0.0058	-10.50 ± 0.67	739 ±474
					3,5Bd	38	0.4200 ± 0.0062	44.68 ± 2.87	320 ± 474
	1435-1445	9.99	n.a.	n.a.	Pd	68	0.2340 ± 0.0045	-209.40 ± 7.42	2707 ± 373
					Vl	49	0.2584 ± 0.0053	-126.94 ± 4.53	1910 ± 377
					Vd	66	0.2368 ± 0.0045	-200.05 ± 7.09	2613 ± 373
	1805-1815	12.04	-25.02	−182.81±3.76	Pd	59	0.2014 ± 0.0047	-128.11 ± 2.76	2479 ± 308
					Vl	38	0.2054 ± 0.0062	-111.02 ± 2.46	2323 ± 342
					Vd	58	0.1770 ± 0.0048	-233.79 ± 5.04	3517 ± 327
					Fd	39	0.1982 ± 0.0061	-142.12 ± 3.14	2609 ± 346

				Pd	43	0.1446 ± 0.0038	-211.90 ± 4.01	3449 ± 328
				Vl	40	0.1435 ± 0.0038	-217.82 ± 4.12	3510 ± 328
				Vd	41	0.1406 ± 0.0042	-233.49 ± 4.44	3673 ± 347
	2033-2041	13.94	n.a.	n.a.	Vd	42	0.1195 ± 0.0056	-179.16 ± 3.50	3123 ± 389
					Sd	54	0.1506 ± 0.0048	-348.56 ± 6.68	4979 ± 409
					Fd	54	0.1449 ± 0.0040	-210.16 ± 3.99	3432 ± 335
					3,5Bd	45	0.1850 ± 0.0045	8.32 ± 0.16	1470 ± 317
					Pd	102	0.1036 ± 0.0057	-215.23 ± 3.01	4371 ± 488
					Vl	109	0.1228 ± 0.0059	-69.52 ± 0.98	3003 ± 438
	2335-2342	16.67	n.a.	n.a.	Vd	75	0.1083 ± 0.0058	-179.46 ± 2.52	4013 ± 480
					Vd	45	0.1122 ± 0.0057	-149.51 ± 2.10	3725 ± 460
					3,5Bd	68	0.1296 ± 0.0054	-17.70 ± 0.25	2568 ± 395

n.a.: not analyzed

A large age difference between different lignin-derived phenols was observed in the Bering and Okhotsk Sea sediments, especially before the B/A (Fig. 5.2). Variable ages of lignin phenols may be the result of selective degradation of certain more easily degradable lignin phenols relative to more recalcitrant phenols in a sample that contains lignin from at least two different fractions of terrigenous organic matter, e.g., a rapidly cycling fraction and a slowly cycling fraction (French et al., 2018). V-phenols exists in all tissue types of terrigenous higher plant vegetation, and Vl is more easily degraded than Vd under the same conditions (Ertel and Hedges, 1985). Preferential degradation of Vl over Vd would in the above-described scenario result in an older mean age for Vd than for Vl (Fig. 5.2), particularly in samples with high acid to aldehyde (Vd/Vl) ratios (Fig. 5.3a), which is an indicator for lignin degradation. Age offset between Vd and non-lignin derived phenols (Pd and 3,5Bd) was also correlated to degradation indicator (Fig. 5.3b and c), suggesting degradation may be one important factor that affect the age offset between different phenols.

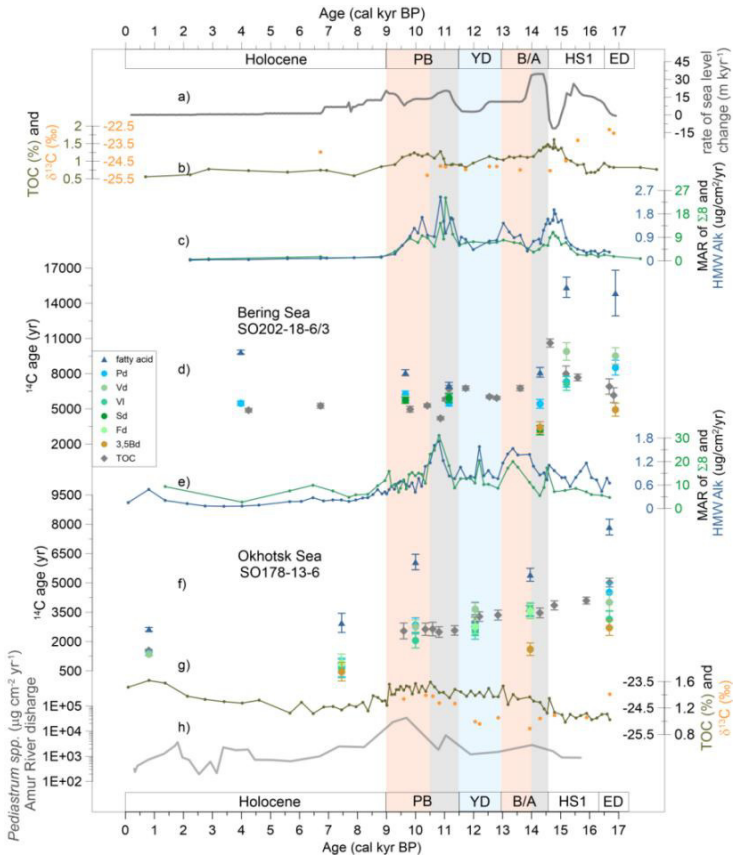

Figure 5.2 (a) Global rate of sea level change (Lambeck et al., 2014); (b) $\delta^{13}C$ of bulk OC and TOC content (Cao et al., 2023) values in the Bering Sea sediments; (c) Mass accumulation rate of lignin-derived phenols (Σ8) and long-chain *n*-alkanes (HMW Alk) in the Bering Sea sediments (Meyer et al., 2019; Cao et al., 2023); (d) Age at deposition (^{14}C age) for n-C26:0 fatty acid (blue triangles; Meyer et al., 2019), individual phenols (dots) and TOC (grey diamonds) for core SO202-18-6/3. Blue dots indicate Pd, green represents lignin phenols, brown is 3,5Bd ^{14}C age; (e) Mass accumulation rate of lignin-derived phenols (Σ8) and long-chain *n*-alkanes (HMW Alk) (Winterfeld et al., 2018; Cao et al., 2023) in the Okhotsk Sea sediments; (f) Age at deposition (^{14}C age) for fatty acid n-C26:0 (Winterfeld et al., 2018), individual phenols and TOC for core SO178-13-6; (g) $\delta^{13}C$ of bulk OC and TOC (Cao et al., 2023) values in the Okhotsk Sea sediments; (h) Accumulation rate of chlorophycean freshwater

algae *Pediastrum* spp. from core LV28-4-4 (Winterfeld et al., 2018), which are taken to represent the discharge of Amur River.

Based on reports that the degradation degree of Lena River-derived organic matter and surface sediments of Buor-Khaya Bay were similar, Winterfeld et al. (2015) suggested that the oxidative degradation of lignin occurred mainly on land. Marwick et al. (2015) described preferential decomposition of younger and more labile terrigenous OC during residence time within a river network from a global perspective. Our data only include the final deposition record of terrigenous OC in marine sediments, without any data from rivers or soils to compare, so it is difficult to accurately detect whether the degradation of terrigenous organic matter occurred on land or in the ocean during the last deglaciation.

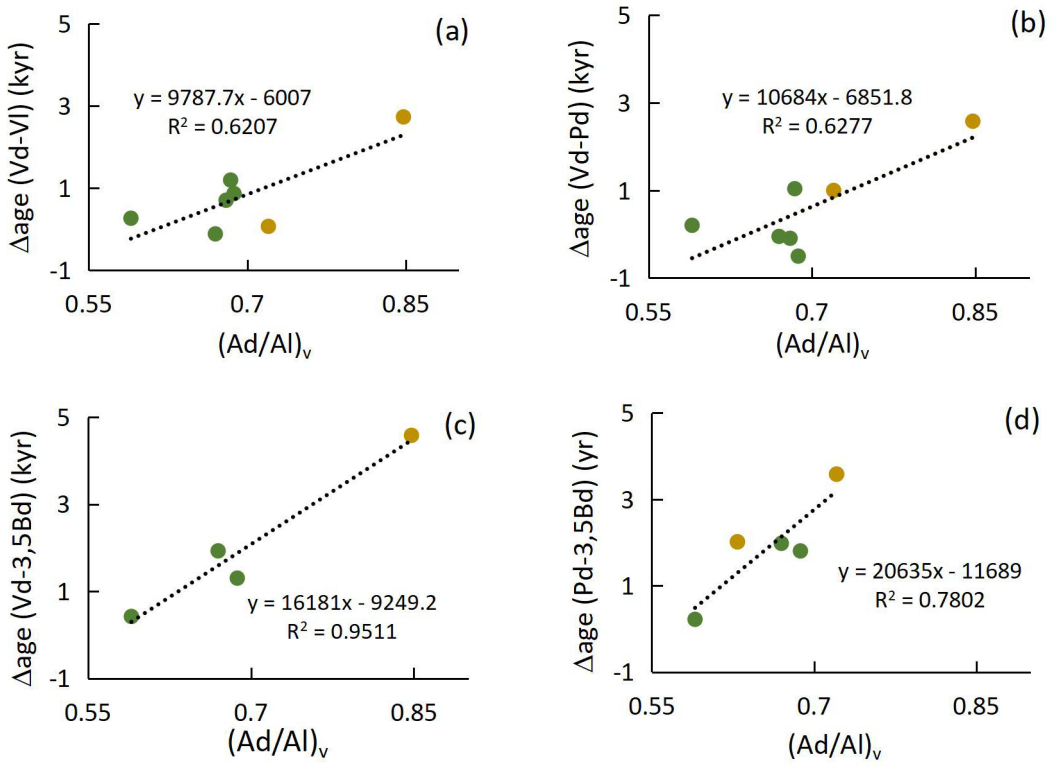

Figure 5.3 Correlation between degradation index $(Ad/Al)_v$ and (a) age offset between Vd and Vl, (b) age offset between Vd and Pd, (c) age offset between Vd and 3,5Bd, and (d) age offset between Pd and 3,5Bd in the two sediment cores during the last deglaciation. Green is Okhotsk Sea, yellow is Bering Sea.

The age of non-lignin derived hydroxy phenols (3,5Bd and Pd) could be influenced by additional processes. In our two sediment cores, the 3,5Bd age was younger than Vd and Pd, and the ^{14}C age of Vd was never lower than that of Pd (Fig. 5.2). Different from lignin phenols, Pd and 3,5Bd may derive from protein and they are enriched in *Sphagnum* and peat (Erickson and Miksche, 1974; Goñi and Hedges et al., 1995; Goñi et al., 2000; Amon et al., 2012). In Arctic rivers surface sediments, hydroxy phenol $\Delta^{14}C$ values were best correlated with the wetland coverage in the drainage basin (such as the Ob and Kalix basins), but in some watersheds with low wetland coverage (such as the Lena and Colville basins), old

hydroxy phenol inputs from deep soils are increased (Feng et al., 2013a, 2015b). The mean $\Delta^{14}C$ value of Pd in the core SO202-18-6/3 (-455.0 ± 9.6‰) was lower than the mean $\Delta^{14}C$ of hydroxy phenols in the Yukon and Ob River surface sediments (-255 ± 10‰ and -383 ± 15‰) (Feng et al., 2015b), but similar to the results from the Lena and Colville River surface sediments (-477 ± 18‰ and -486 ± 18‰) (Feng et al., 2015b). The mean wetland coverage in the Yukon Basin in the last deglaciation may be similar to that in the Lena and Colville River basins at present, but lower than in the Yukon and Ob River basins now. The surface sediment was collected from the upstream of the Yukon mouth, which means this sample was devoid of influences of coastal erosion that can release old carbon from exposed deeper soil (Feng et al., 2015b). Wetlands in the Yukon Basin began to develop at 16.5 kyr (Meyer et al., 2019; Cao et al., 2023), and ~ 14% of the basin is covered by wetlands and open water today, which is similar to the wetland coverage in the basins of Ob River basin at present (Revenga et al., 1998; Ingri et al., 2005). The coverage of wetland in the Yukon Basin during the last deglaciation may be lower than that at present, but similar to the wetland coverage in the Lena and Colville Basins today (≦1%; Revenga et al., 1998; Ingri et al., 2005).

Hydroxy phenols are better preserved than lignin phenols, especially for compounds having a terrigenous source, such as Pd and *p*-hydroxyacetophenone (Tesi et al., 2012). However, $\Delta^{14}C$ values of Pd were not lower than those of lignin phenols in our records, which may indicate that the carbon pool contributing to Pd was younger than that of lignin. 3,5Bd is more easily degraded than Pd and lignin phenols under the same conditions. Age offsets between Pd and 3,5Bd are correlated to $(Ad/Al)_v$ in the studied sediment cores (Fig. 5.3d) which means that degradation processes were the main factor affecting the age difference between Pd and 3,5Bd. Overall, the observed differences in ^{14}C age between the different phenols analyzed in this study, whose ages followed the order Vd > Pd > 3,5Bd, are therefore consistent with the effects expected for sediment samples that receive inputs from at least two different sources characterized by different age and degradation state.

5.5.2. Significance of, and age relationships between TOC, lignin phenols and long-chain fatty acids

Bulk OC and its $\Delta^{14}C$ value have to be interpreted as a mixture of materials with different ages and reactivities, where labile components tend to be younger than refractory ones. A higher relative contribution of younger labile components will result in younger ^{14}C age of bulk terrigenous OC. Using $\delta^{13}C$ and initial $\Delta^{14}C$ of bulk OC values, it is possible to estimate the mean age of terrigenous OC deposited in the marine sediments. In a first step, the relative contributions of marine and terrigenous OC can be estimated assuming end-member values for the $\delta^{13}C$ signatures of the marine and terrigenous fractions. Here we used $\delta^{13}C$-TOC values of -20.7 ± 1.6‰ (Meyers, 1994, 1997; Hobson et al., 1995; Schubert and Calvert,

2001; Tesi et al., 2016) and -26.6 ± 0.9‰ (Meyers,1994, 1997; Tesi et al., 2016) as the end-member values for marine and of terrigenous OC, respectively. A binary mixing model is employed to assess the relative contribution of marine and terrigenous OC to the marine sediments. The model is expressed by the following equations:

$$f_M \times (\delta^{13}C_{TOC\text{-}M}) + f_T \times (\delta^{13}C_{TOC\text{-}T}) = \delta^{13}C_{TOC} \quad (5.1)$$

$$f_M + f_T = 1 \quad (5.2)$$

where f_M and f_T represent the fraction of marine and terrigenous OC, respectively. $\delta^{13}C_{TOC\text{-}M}$, $\delta^{13}C_{TOC\text{-}T}$ and $\delta^{13}C_{TOC}$ represent the $\delta^{13}C$ end-member values of marine OC, terrigenous OC, and the $\delta^{13}C_{TOC}$ of the specific sample, respectively. The estimated contribution of marine and terrigenous OC is shown in Table 5.4.

In the second step, the $\Delta^{14}C$ value of terrigenous OC can be estimated based on isotopic mass balance as described by equation (5.3):

$$f_M \times (\Delta^{14}C_{TOC\text{-}M}) + f_T \times (\Delta^{14}C_{TOC\text{-}T}) = \Delta^{14}C_{TOC} \quad (5.3)$$

where $\Delta^{14}C_{TOC\text{-}M}$, $\Delta^{14}C_{TOC\text{-}T}$ and $\Delta^{14}C_{TOC}$ represent the Marine 20 $\Delta^{14}C$ value at time of deposition (Heaton et al., 2020; Stuiver and Reimer, 1993), the mean initial $\Delta^{14}C$ values of terrigenous OC, and the initial $\Delta^{14}C$ values of TOC. The calculated initial $\Delta^{14}C$ values and ^{14}C ages of terrigenous OC are shown in Table 5.4. The oldest four samples in the Bering Sea sediments are not discussed here because they received high contribution of petrogenic carbon between ~ 16.8 kyr and 15 kyr from central Alaska (Meyer et al., 2019; Wang et al., 2021), which precludes solving the equation above due to the presence of a third fraction with a distinct $\Delta^{14}C$ signature.

Table 5.4 Radiocarbon data of terrestrial OC in the Bering and Okhotsk Sea sediments estimated based on a binary mixing model. f_T and f_M are the relative contribution of terrigenous and marine OC in marine sediments. $\Delta^{14}C_{initial}$ is the initial $\Delta^{14}C$ value of TOC. ^{14}C age of terrigenous OC is calculated based on initial $\Delta^{14}C_{initial}$ of terrigenous OC.

Sediment core	Depth (cm)	Deposition age (kyr)	$\delta^{13}C$ (‰)	$\Delta^{14}C_{initial}$ (‰)	f_T (%)	f_M (%)	$\Delta^{14}C_{initial}$ of terrestrial OC (‰)	^{14}C age of terrestrial OC (yr)
SO202-18-6	101.3	6.72	-23.98	-436.60 ± 12.82	55.55 ± 10.5	44.45 ± 10.5	-853.20 ± 208.29	15413 ± 1520
	305	10.40	-25.30	-422.11 ± 4.96	77.99 ± 14.6	22.01 ± 14.6	-573.90 ± 142.86	6853 ± 1073
	380	10.85	-24.77	-330.90 ± 3.76	68.95 ± 12.9	31.05 ± 12.9	-538.05 ± 137.36	6204 ± 1034
	430	11.02	-24.81	-441.74 ± 4.69	69.59 ± 13.1	30.41 ± 13.1	-700.88 ± 174.94	9695 ± 1295
	560	11.72	-24.96	-493.37 ± 7.05	72.25 ±13.6	27.75 ± 13.6	-750.49 ± 192.20	11152 ± 1412
	447	12.54	-24.80	-418.84 ± 3.20	69.52 ± 13.0	30.48 ± 13.0	-703.96 ± 188.25	9778 ± 1386
	481	12.79	-24.80	-422.79 ± 3.46	69.52 ± 13.0	30.48 ± 13.0	-699.12 ± 181.83	9648 ± 1342
	635	13.60	-24.99	-483.21± 6.83	72.70 ± 13.6	27.30 ± 13.6	-739.50 ± 195.36	10806 ± 1433
	825	14.63	-25.04	-668.47 ± 14.01	73.55 ± 13.7	26.45 ± 13.7	-995.81 ± 260.14	43990 ± 1857
SO202-18-3	993	15.18	-24.47	-524.65 ± 9.89	63.96 ± 12.0	36.04 ± 12.0	-981.35 ± 267.57	31985 ± 1905
	1055	15.58	-23.31	-498.16 ± 8.42	n.a.	n.a.	n.a.	n.a.
	1136	16.67	-22.70	-427.37 ± 9.34	n.a.	n.a.	n.a.	n.a.
	1144	16.82	-22.91	-365.67 ± 8.04	n.a.	n.a.	n.a.	n.a.
	1425	23.39	n.a.	-357.76 ± 5.46	n.a.	n.a.	n.a.	n.a.
SO178-13-6	1320	9.59	-24.16	210.95 ± 9.13	58.58 ± 18.4	41.42 ± 18.5	-418.54 ± 182.31	4356 ± 1345
	1460	10.59	-24.06	-194.84 ± 6.48	56.95 ± 18.7	43.05 ± 18.7	-431.55 ± 199.32	4537 ± 1460

	1525	10.34	-24.02	-199.58 ± 6.23	56.28 ± 18.7	43.72 ± 18.7	-440.26 ± 203.04	4661 ± 1485
	1620	10.81	-24.31	-177.53 ± 4.50	61.24 ± 18.2	38.76 ± 18.2	-366.44 ± 160.30	3666 ± 1194
	1710	11.35	-24.34	-171.56 ± 3.75	61.65 ± 18.1	38.35 ± 18.1	-365.74 ± 164.51	3657 ± 1223
	1810	12.04	-25.02	-182.81 ± 3.76	73.23 ± 16.7	26.77 ± 16.7	-318.03 ± 126.96	3075 ± 960
	1830	12.20	-25.10	-202.23 ± 4.13	74.58 ± 16.6	25.42 ± 16.6	-339.05 ± 131.26	3326 ± 991
	1910	12.84	-24.87	-204.88 ± 4.12	70.62 ± 17.0	29.38 ± 17.0	-376.33 ± 154.90	3793 ± 1157
	2035	13.93	-25.28	-228.22 ± 4.25	77.67 ± 16.2	22.33 ± 16.2	-352.30 ± 131.50	3489 ± 992
	2075	14.27	-24.90	-212.46 ± 3.72	71.15 ± 17.0	28.85 ± 17.0	-384.90 ± 164.96	3904 ± 1227
	2130	14.78	-24.78	-207.92 ± 3.20	69.15 ± 17.2	30.85 ± 17.2	-425.23 ± 197.17	4449 ± 1446
	2250	15.89	-24.86	-209.87 ± 2.25	70.51 ± 17.1	29.49 ± 17.1	-429.60 ± 199.16	4510 ± 1459
	2340	16.68	-23.98	-275.46 ± 3.36	55.62 ± 18.8	44.38 ± 18.8	-776.85 ± 406.61	12049 ± 2741

n.a.: not available

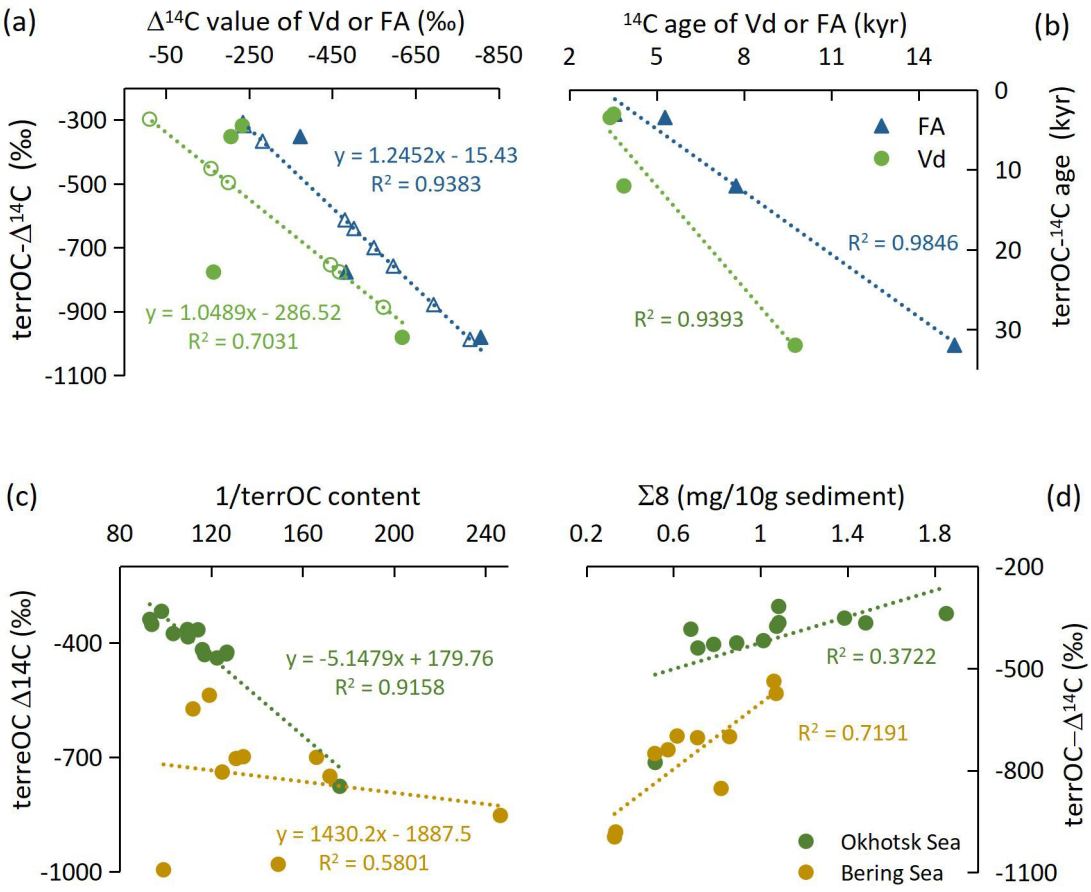

Figure 5.4 (a) Relationships between terrigenous OC $\Delta^{14}C$ value (terrOC-$\Delta^{14}C$) and Vd (green) or n-C26:0 fatty acid (FA, blue) $\Delta^{14}C$ value. Triangles and circles without fill are the interpolated $\Delta^{14}C$ values of terrigenous OC, which were calculated based on a linear regression equation between measured $\Delta^{14}C$ value of terrigenous OC and Vd or FA (circles and triangles with fill). Without the interpolated $\Delta^{14}C$ values of terrigenous OC, the R^2 of the linear regression for the blue and green are 0.86 and 0.46, respectively; (b) Relationships between terrigenous OC ^{14}C age (terrOC-^{14}C age) and Vd or n-C26:0 fatty acid ^{14}C age in the Bering and Okhotsk Sea sediments during the last deglaciation; (c) Correlation between the reciprocal of terrigenous OC content (1/terrOC content) and terrOC-$\Delta^{14}C$ in the Bering (yellow) and Okhotsk Sea (green) sediments during the last deglaciation. Terrigenous OC content was calculated from f_T multiplied with TOC%. (d) Relationships between terrOC-$\Delta^{14}C$ and lignin phenols content in dry sediment (Σ8) in the Bering and Okhotsk Sea sediment cores during the last deglaciation. $\Delta^{14}C$ value is the initial $\Delta^{14}C$ value.

The $\Delta^{14}C$ values of Vd and n-C26:0 fatty acid display positive relationships with terrigenous OC $\Delta^{14}C$ values (Fig. 5.4a), and biomarker $\Delta^{14}C$ values were higher than corresponding terrigenous OC $\Delta^{14}C$ values for most samples. This suggests the presence of an older and likely more refractory phase in terrigenous OC than what is represented by the biomarkers investigated here. This fraction likely is at least partly petrogenic or rock-derived OC. The correlation between terrigenous OC content in TOC and terrigenous OC $\Delta^{14}C$ was better in the Okhotsk Sea sediments than in the Bering Sea sediments (Fig. 5.4c), suggesting the contribution of petrogenic OC from the Yukon Basin to the Bering Sea sediments varies with time. As petrogenic OC is radiocarbon free, the $\Delta^{14}C$ of the petrogenic OC end member was defined as -1000‰. When the $\Delta^{14}C$ of terrigenous OC is -1000‰, the OC content of terrigenous was 0.62% (63% of TOC) in the Bering Sea sediments which was higher than

that in the Okhotsk Sea sediments (0.10%, ＜10% TOC) (Fig. 5.4c), but the TOC content in the Bering Sea (mean value: 0.98%) was lower than in the Okhotsk Sea sediments (mean value: 1.35%) (Table 5.2, Fig. 5.4), indicating that the influence of petrogenic OC on sediments in the Bering Sea was greater than that in the Okhotsk Sea.

Eglinton et al. (2021) found that fatty acids and lignin display similar or slightly older ^{14}C ages than corresponding catchment-weighted soils integrated from 0 to 30cm depth, and soils integrated from 30 to 100cm depth display significantly older ^{14}C ages than biomarkers. Accordingly, the majority of the terrigenous OC deposited at our core sites likely originates from deep soils (>30cm soil depth). However, the relationship between ^{14}C ages of biomarkers and terrigenous OC varied with time in our cores (Fig. 5.4b). ^{14}C ages of biomarkers were younger than the mean age of terrigenous OC in deep sediments (HS1 and ED periods) (Fig. 5.4b, ^{14}C age of terrigenous OC older than 12.0 kyr) (Table 5.3 and 5.4), and ^{14}C ages of biomarkers were slightly older or similar to the mean age of terrigenous OC in the B/A and YD (Fig. 5.4b, ^{14}C age of terrigenous OC younger than 12.0 kyr). According to the hypothesis from Feng et al. (2013), surface-derived terrigenous OC should be rich in lignin and relatively young. In accordance with this scenario, we observed an increase of lignin content in marine sediments from B/A to YD potentially reflecting the increased contribution of young terrOC from near-surface carbon pools in the last deglaciation (Fig. 5.4d), suggesting decreased erosion of deeper soils and predominant export of freshly synthesized OC (e.g., by surface runoff) (Feng et al., 2013a; Hilton, 2017; Eglinton et al., 2021).

In the Bering and Okhotsk Sea sediments, phenol ^{14}C ages were relatively older before 16.5 kyr than after 16.5 kyr (Fig. 5.2), and the $\Delta^{14}C$ offset between n-C26:0 fatty acid and Vd was high at the same time (Fig. 5.5a). The $\Delta^{14}C$ offset observed between fatty acids and lignin phenols collected from the same time may reflect differences in their sources and/or pathways of mobilization (Eglinton and Eglinton, 2008; Feng et al., 2013a). Plant wax lipids are closely associated with fine-grained minerals (Repasch et al., 2021; Jia et al., 2023) and preferentially stabilized in deep mineral soils (Xu et al., 2009). Feng et al. (2013a) found that the $\Delta^{14}C$ value of plant wax lipids is high when the watershed coverage of continuous permafrost is high in modern Arctic river systems, but younger lignin is transported by rivers with a higher mean annual runoff rate. Thermokarst and thermal erosion likely increase from perennially frozen regions to seasonally frozen zones during climate warming (Costard et al., 2007; Toniolo et al., 2009), enabling faster mobilization of deep OC from river banks and coastlines, leading to the release of old OC pools that are enriched in lipids relative to lignin (Feng et al., 2013a). Compared with the data in Feng et al. (2013a), the temporal changes in our data are consistent with the effect of permafrost stability on the $\Delta^{14}C$ offset between fatty acids and lignin-derived phenols deduced from observations in Arctic river surface sediments, which

suggested that the remobilization of permafrost will increase the $\Delta^{14}C$ offset between the lipids and lignin phenols. In the Okhotsk Sea sediments, the $\Delta^{14}C$ offset before the PB was lower than after the PB when the permafrost began to be remobilized in the Amur Basin (Winterfeld et al., 2018; Cao et al., 2023) (Fig. 5.5a). The same is true for the Bering Sea data, except that the start of permafrost remobilization in the Yukon Basin was found to be during the HS1 (Meyer at al., 2019; Cao et al, 2023) (Fig. 5.5a).

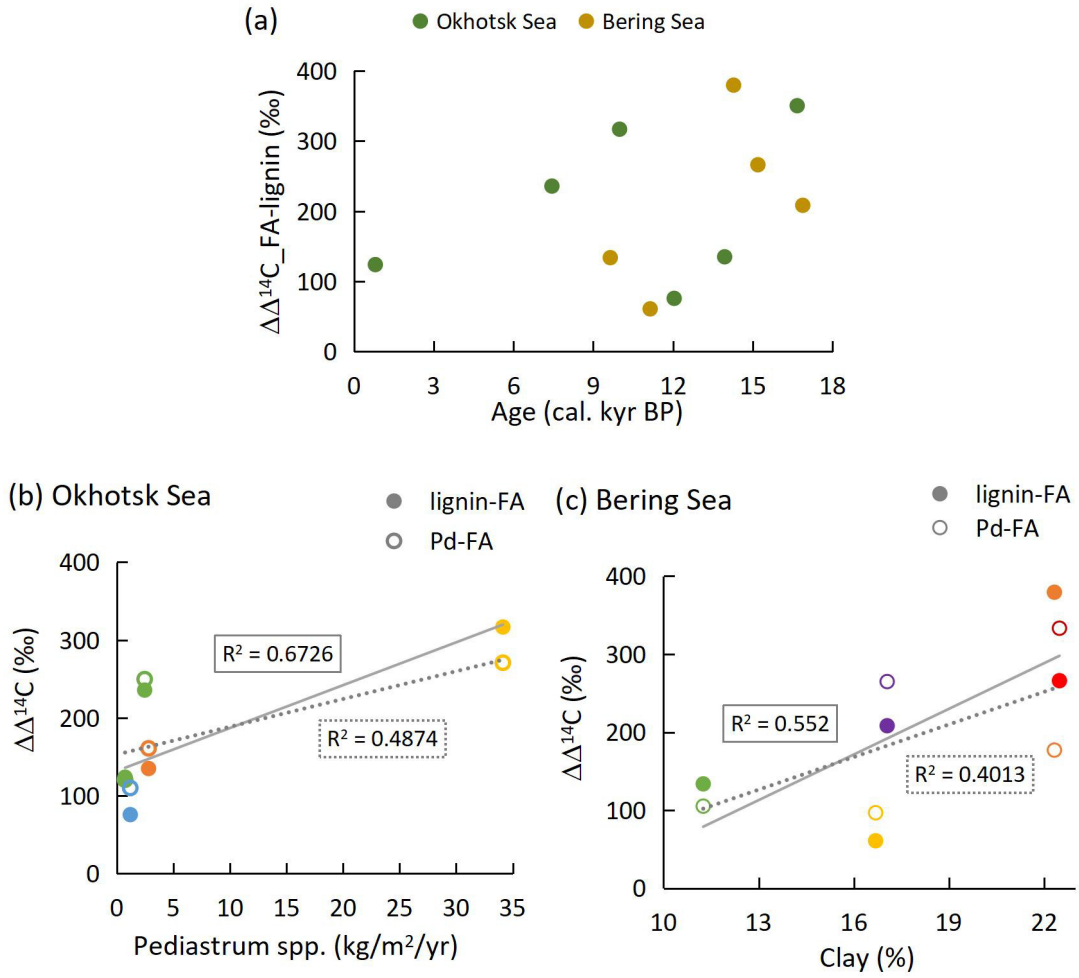

Figure 5.5 (a) Difference of $\Delta^{14}C$ value between n-C26:0 fatty acid and lignin phenols in the Bering (yellow) and Okhotsk Sea (green) in the last deglaciation. (b) Relationship between Pediastrum *spp.* (Winterfeld et al., 2018), which can be used to reflect the Amur River runoff with increasing values being indicative of increased runoff, and $\Delta^{14}C$ offset between n-C26:0 fatty acid and lignin phenols or Pd ($\Delta\Delta^{14}C$) in the Okhotsk Sea sediments. (c) Relationship between clay% (Wang et al., 2021), which can be used to reflect the Yukon River runoff with increasing value at times of increased runoff, and $\Delta^{14}C$ offset between n-C26:0 fatty acid and phenols in the Bering Sea sediments. The solid circles mark the $\Delta^{14}C$ offset between fatty acids and lignin phenols, and open circles denote the $\Delta^{14}C$ offset between fatty acid and Pd. The solid and dotted lines represent their linear regressions, and the solid and dotted boxes represent their R^2 values, respectively. In panel (b) and (c), different colors represent different periods, purple is the ED, red is the HS1, orange is the B/A, blue is the YD, yellow is the PB, and green is the Holocene.

Erosion and thermokarst may play a part in releasing lignin-rich OC pools, but this effect is likely dwarfed by surface discharge (Feng et al., 2013a). Transport of younger lignin is increased with enhancing river discharge, leading to a larger $\Delta^{14}C$ offset between lignin-

derived phenols and lipids in the Arctic river surface sediments (Feng et al., 2013a). In the Yukon Basin, the HS1 was characterized by general ice-sheet retreat in Alaska and the Brooks Range (Dyke, 2004; Pendleton et al, 2015), leading the Yukon River discharge to increase to its highest values since the LGM. The glacial meltwaters will increase the rate of deep erosion in the valleys of central Alaska (Wang et al., 2021). Accordingly, the $\Delta^{14}C$ offset between n-C26:0 fatty acid and lignin phenols in the HS1 was increased (Fig. 5.5a). The Yukon River runoff has been decreasing since the HS1, but the $\Delta^{14}C$ offset between fatty acids and lignin phenols was lower in the YD than in the PB (Fig. 5.5a). Phenol ^{14}C ages did not change much after the YD in the Bering Sea sediments (Fig. 5.2) and the difference between lipid and lignin ages are driven by the fatty acid ^{14}C ages in the PB and after. The large offset in the PB coincides with melt-water pulse 1B, suggesting that rapid flooding of the Bering Land Bridge and North Pacific shelves caused massive coastal erosion of permafrost deposits which are enriched in lipids (Manley, 2002; Meyer at al., 2019).

The ^{14}C age of lignin phenols in the Okhotsk Sea sediments decreased since the ED (Fig. 5.2). Permafrost remobilization in the PB (Winterfeld et al., 2018; Cao et al., 2023) may have resulted in increased fatty acid $\Delta^{14}C$ values which, in turn, resulted in a large $\Delta^{14}C$ offset between fatty acid and Vd at 9.99 kyr (Fig. 5.5a). The surface discharge in the two basins is correlated with corresponding $\Delta^{14}C$ offsets between fatty acid and lignin phenols (Fig. 5.5b, c) and, to a lesser degree, with the $\Delta^{14}C$ offset between fatty acid and Pd. There is a negative correlation between runoff and lignin phenol $\Delta^{14}C$ values in present-day Arctic estuarine surface sediments (Feng et al., 2013a), but the effects of glacial meltwater on runoff in these rivers are currently negligible. The discharge of the Amur River is not affected by glacial meltwater during the last deglaciation, and the positive correlation between $\Delta^{14}C$ offsets and surface runoff is better than in the Bering Sea sediments during the last deglaciation (Fig. 5.5b, c). This suggests that, similar to modern Arctic river systems, surface runoff may have a strong effect on the difference of $\Delta^{14}C$ between fatty acid and lignin phenols in the last deglaciation. Compared with lignin phenols, surface runoff had a weaker effect on the $\Delta^{14}C$ offset between fatty acid and Pd.

With increasing temperature and precipitation, the ^{14}C age of lignin phenols and fatty acids decreases globally (Eglinton et al., 2021; Fig. 5.6). The ages at deposition of fatty acid and lignin phenols in the Bering Sea from the ED to the Holocene were higher than at present at this latitude (~ 60° N, Fig. 5.6). Most high-latitude river surface samples for CSRA reported in Eglinton et al. (2021), however, come from estuaries, which means these samples are devoid of influences of coastal erosion which can release old carbon (Vonk et al., 2012), and terrigenous material in them has not been transported across a shelf system. This would explain these authors' observations of younger lipids and lignin phenols ^{14}C ages than our

results. Additionally, since the LGM, the annual temperature in the Northern Hemisphere has been increasing and the Yukon River discharge increased significantly during the past decades (Ge st al., 2013; Feng et al., 2021), which may result in a younger ^{14}C age of lignin phenols in surface sediments than in deep sediments. The range of changes of biomarker ^{14}C ages in the Bering Sea sediments since the ED is similar to the change of biomarker ages with latitude as observed today, except for the B/A period (Fig. 5.6). From the ED to the B/A, continuous summer warming in Alaska is confirmed by paleolimnological proxy records (Kurek et al., 2009; Fritz et al., 2012; Wang et al., 2021), which may have caused decreased mean biomarker ^{14}C ages in the Yukon Basin. Vegetation development and permafrost remobilization from the B/A to the PB in the Yukon Basin (Meyer et al., 2019; Cao et al., 2023) may increase the amounts of fresh lignin phenols and old plant wax lipids to be transported into the ocean (chapter 3). During the B/A, the sea level rose faster than that during the PB in the Bering Sea, which resulted in more intense coastal erosion in the B/A, but the fatty acid ^{14}C age at this time was similar to that in the PB (Fig. 5.6a). Therefore, coastal erosion is not the only pathway through which long-chain lipids are transported. Lipids derived from deep soils from inland, e.g., via river bank erosion, may also be transported into marine sediments (Hilton, 2017; Eglinton et al., 2021) during the last deglaciation. Permafrost thawing in the Yukon Basin reached its maximum during the PB period (Meyer et al., 2019; Cao et al., 2023), the contribution of deep old OC remobilized through abrupt thaw may have offset the change in fatty acid ^{14}C age due to weakened coastal erosion.

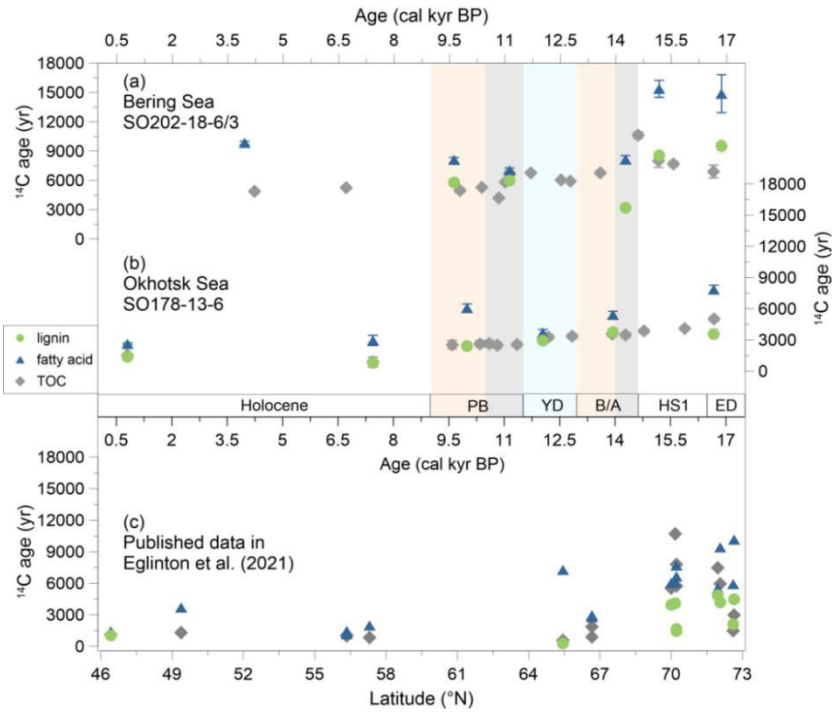

Figure 5.6 (a and b) ^{14}C age of TOC, n-C26:0 fatty acid and lignin phenols in the Bering and Okhotsk Sea sediments during the last deglaciation. (c) Reported ^{14}C age of TOC, fatty acids and lignin in Northern Hemisphere (46−73° N) at present in Eglinton et al. (2021).

In the Okhotsk Sea, the mean ^{14}C ages of fatty acids and lignin phenols are also higher than those at present at a similar latitude (~ 55° N, Fig. 5.6). The increasing temperature in the Northern Hemisphere since the LGM (Rasmussen et al., 2008; Clark et al., 2012) may be the main reason for the decreasing ^{14}C age of biomarkers in the Okhotsk Sea sediments from the ED to the Holocene (Fig. 5.6), as residence times in soils decrease with increasing mean temperature. A particularly drastic decrease in residence time would be expected upon complete permafrost loss. The remobilization of permafrost in the Amur Basin in the PB (Winterfeld et al., 2018; Cao et al.,2023) increased the ^{14}C age of fatty acid deposited at the core site, but had no significant effect on lignin age at 9.99 kyr (Fig. 5.6). As the climate warmed, the distribution of permafrost in the Amur Basin gradually decreased since the PB, and has completely disappeared at present (Obu et al., 2019). Accordingly, the ^{14}C age of n-C26:0 fatty acid in Okhotsk Sea sediments at 0.80 kyr is similar to that at present at a similar latitude (~ 55° N, Fig. 5.6). Rising air temperatures lead to increases in the atmosphere vapor holding capacity and changes in the precipitation frequency and intensity in the Amur Basin (Shin and Jung, 2015; Zhou et al., 2019; Wen et al., 2021; Yang et al., 2021). The runoff of the Amur River is mainly controlled by precipitation. As a consequence, a more pronounced influence of surface discharge on the age offset between fatty acid and lignin phenols during the last deglaciation is apparent in the Okhotsk Sea sediments than in the Bering Sea sediments (Fig. 5.5b, c). We conclude that climate change is the main factor affecting the ^{14}C age of terrigenous OC from LGM to the present. Age offset between lipids and lignin phenols can be used as palaeo-proxies for the state of permafrost, but further processes like cross-shelf transport and active coastal erosion must be considered as well.

5.6. Conclusions

Land-derived OC may be delivered to the ocean either via near-surface conduits or following deep erosion of river banks and coastal bluffs. Near-surface supply would be expected to contribute younger OC than erosion of deep ancient deposits. Lipid biomarkers are enriched in deeper soils, while lignin phenols are more abundant in near-surface deposits, and their age offsets sensitively record relative contributions of those two sources of terrigenous OC. The radiocarbon ages of phenols reflect the sediments from the Bering and Okhotsk Seas are expected to receive inputs from at least two different terrigenous sources that are characterized by different age and degradation degree during the last deglaciation. Some old and refractory terrigenous OC (such as petrogenic carbon) was exported into marine sediments, and Okhotsk Sea sediments were less affected than those in the Bering Sea. Wetland coverage may influence the age offset between lignin phenols and hydroxy phenols,

and the age offsets between lignin phenols and fatty acids were controlled by surface discharge in the Yukon and Amur Basins. Deep OC enriched in long-chain lipids can be mobilized both through coastal erosion and inland thermokarst which can be transported to marine sediments by surface runoff in the last deglaciation. Same as in the modern Arctic river systems, the radiocarbon ages of lignin phenols and long-chain fatty acids are affected by climate change, ^{14}C age offset between lipids and lignin phenols can be used as palaeo-proxies for the state of permafrost inland.

Author contributions

MC measured and compiled lignin data and wrote the manuscript with the help of all co-authors. JH and HG were responsible for all biomarker analyses and radiocarbon analyses. LLJ and RT provided samples. GM designed the study. All authors participated in the discussion of results and conclusions and contributed to the final version of the paper.

Acknowledgments

We are grateful to the crews participating in the cruises for sample collection. We thank Elizabeth Bonk, Lea Phillips, Torben Gentz, Malte Hoehn and other members of MICADAS group in AWI Bremerhaven for laboratory assistance. MC thanks the China Scholarship Council and POLMAR Graduate School for additional support.

6. Accumulation of lignin phenols and their ^{14}C age in Laptev Sea shelf sediments deposited over the last century

6.1. Introduction of Lena Basin

The Lena River is the 11th longest river in the world, with a total length of 4,400 kilometers flowing northward from its source in the Baikal Mountains, to its drainage point into the Laptev Sea. The drainage basin of the river covers an area of $2{,}49\times10^6$ km^2. About 76% of the Lena Basin is characterized by continuous permafrost and 8% is covered by discontinuous permafrost (Zhang et al., 2005; Amon et al., 2012). About 72% of the Lena Basin is covered with boreal forest or taiga, and ~ 12% is categorized as dwarf-shrub tundra and sedge or grass wetland tundra (Amon et al., 2012). Each year, the river discharges nearly 550 km^3 of freshwater and more than 20 million metric tons of suspended sediment into the Laptev Sea. About 80–90% of the freshwater and ~ 85% of the sediment are delivered through the two major channels, the Sardakhskaya–Trofimovskaya channel and the Bykovskaya channel (Fig. 6.1). The discharge of the Lena River varies throughout the seasons. The Lena River freezes over completely from early December until late April. Thawing begins from the upstream reaches in late April and then extends into the mid- and downstream regions. Runoff reaches its maximum during the spring ice breakup and snowmelt in late May to June (Ma et al., 2005; Holmes et al., 2012). The Lena Delta is the largest Arctic delta in the world, with an area of 32,000 km^2. Different from other deltas, the Lena Delta consists mainly of organomineral sediments which contain a huge organic carbon (OC) reservoir. It was formed as river sediments slowly filled in small bays that were created by transgressive phases when sea level rose during the Holocene (Bolshiyanov et al., 2015). The Bykovskaya channel drains into the Buor-Khaya Bay, which is located east of the Lena Delta and is bordered by Cape Buor-Khaya to the east (Fig. 6.1). The coastline of the Buor-Khaya Bay is largely composed of Yedoma, which is characterized by high ice and carbon content that originate from the Pleistocene (Schirrmeister et al., 2011; Zimov et al., 2006) and may be particularly vulnerable to the effects of climate change (Strauss et al., 2017). Apart from terrestrial OC transported by the Lena River, terrestrial OC derived from coastal erosion of the Buor-Khaya coast predominantly consisting of ICD is another important source of sedimentary OC in the Buor-Khaya Bay.

Over the past century, climate change in the Northern Hemisphere was in substantial changes of temperature and runoff in the Lena Basin. This is expected to lead to changes in the source and age of OC transported by the Lena river and deposited in sediments off its mouth. Here,

we present new data on lignin-derived phenol concentrations, relative composition and radiocarbon age obtained for two short sediment cores from the Laptev Sea shelf (Fig. 6.1), to distinguish the sources and degradation of organic matter transported by the Lena river. This study aims to investigate how the progress of permafrost destabilization as a result of climate change is reflected in two centennial sediment records.

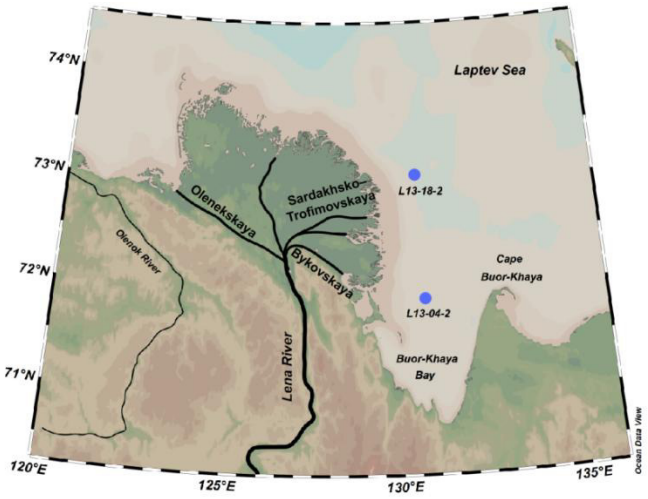

Figure 6.1. Study area. Blue dots are the sediment sites.

6.2. Sampling and methods

The sediment cores L13-04-2 and L13-18-2 were collected approximately off the mouths of the two major channels of the Lena Delta during an expedition conducted in 2013 (Fig. 6.1). Both core sites are located east of the Lena Delta in the adjacent Laptev Sea. Core L13-18-2 was 24cm long and was recovered off the mouth of the Sardakhsko–Trofimovskaya channel. Upon retrieval it was sampled every 1cm downcore. L13-04-2 was collected in the Buor-Khaya Bay, off the mouth of the Bykovskaya channel is of 25cm length and covers the last 150 years (Fig. 6.1). It was sampled at the surface (0-1cm) and downcore from there every 2 cm. All samples were put into pre-combusted glass jars and stored frozen at -20 °C until analysis.

The content of TOC, $\delta^{13}C$, and year of sedimentation (YOS) of the two sediment cores were displayed in the thesis of L. Kattein (2018). The TOC content was measured by M. Winterfeld at the Alfred Wegener Institute, Helmholtz Centre for Polar and Marine Research (AWI) in Bremerhaven in 2016. TOC was determined by high-temperature combustion after removal of carbonates as described by Goñi et al. (2003). The $\delta^{13}C$ data were obtained at Zentrum für Marine Tropenökologie Bremen in 2016. Carbonates were removed from sediments before stable isotopic analysis of OC by treating with hydrochloric acid (Goñi et al., 2003). A Thermo DeltaPlus Gas Isotope Ratio Mass Spectrometer with Thermo Flash

1112 Elemental Analyzer was used for the measurement of $\delta^{13}C$. The standard dviation is 0.13‰ based on a lab internal standard (Pepton).

The chronology of the sediment core was constructed using the constant rate of supply (CRS) model as described by Appleby and Oldfield (1978). Radiochemical extraction, separation and measurement were determined as described by Pittauer et al. (2017). Measurements for the CRS age models with the according mass accumulation rates were conducted by D. Pittauer at the University of Bremen in 2018.

Table 6.1 Abbreviation and source of phenols used in this chapter.

Compounds	Abbreviation	Source	Reference
Vanillin	Vl	vascular plants	Hedges and Mann, 1979; Hedges et al., 1988; Hedges and Weliky, 1989; Opsahl and Benner, 1995;
Vanillic acid	Vd		
Syringic acid	Sd	angiosperms	
p-coumaric acid	*p*-Cd	non-woody tissues of vascular plants	
Ferulic acid	Fd		
p-Hydroxybenzoic acid	Pd	moss-dominated peat	Erickson and Miksche, 1974; Goñi and Hedges et al., 1995; Goñi et al., 2000
p-Hydroxybenzaldehyde	Pl		
3,5-Dihydroxybenzoic acid	3,5Bd		

The lignin concentration and radiocarbon measurement were carried out by M. Cao at (AWI) in Bremerhaven in 2023, and methods were the same as described in chapter 2. Radiocarbon data are reported as fraction modern carbon ($F^{14}C$). The initial radiocarbon content ($\Delta^{14}C$) was calculated based on Schefuß et al. (2016) (see chapter 2 for more details). The abbreviations of phenols are in Table 6.1. The results of lignin flux and radiocarbon age are shown in the supplementary information below.

6.3. Results

6.3.1. Lignin concentrations and MARs

Lignin phenol concentrations were 0.86−2.03 mg/100mg OC (Λ8) or 1.36−2.89 mg/10g sediment (Σ8) in the core L13-04-2 and 2.08−16.02 mg/100mg OC or 3.90−24.35 mg/10g sediment in the core L13-18-2. The standard deviation was determined from repeated measurements of a laboratory internal standard sediment extract (n = 6), and for the carbon-normalized concentration of the sum of the eight lignin phenols (Λ8, mg/100 mg OC) it equals 0.59. Similar to the lignin concentration, the MAR of lignin was lower in core L13-04-2 (mean value is 11.75 μg/cm^2/yr) than in the core L13-18-2 (mean value is 46.28 μg/cm^2/yr) (Fig. 6.2). The maximum MAR of lignin in core L13-04-2 was 72.75 μg/cm^2/yr in 1911, and a second peak was 28.45 μg/cm^2/yr in 1897, the remaining values were all less than 14 μg/cm^2/yr. In the core L13-18-2, the maximum MAR of lignin was 131.47 μg/cm^2/yr in 1941,

and a second peak was 64.56 μg/cm^2/yr in 1964, the remaining values are between 24 and 51 μg/cm^2/yr.

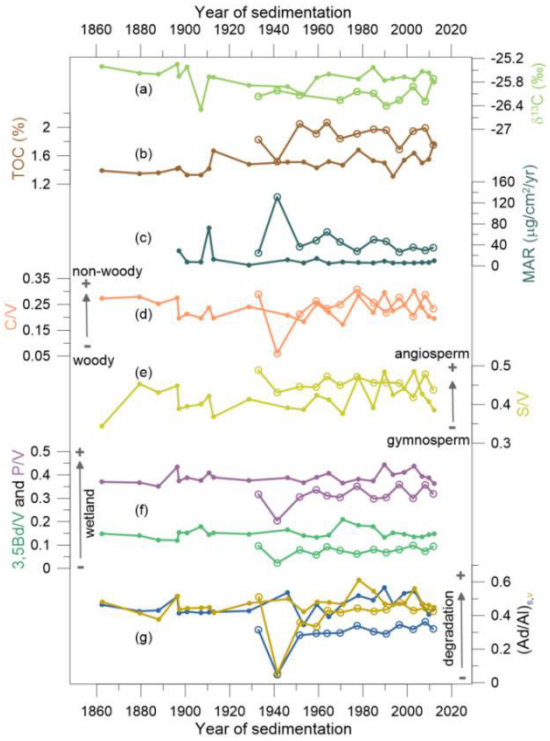

Figure 6.2. (a) $\delta^{13}C$ of core L13-04-2 (solid circles) and L13-18-2 (open circle) (Kattein, 2018); (b) TOC data in the two cores (Kattein, 2018); (c) Mass accumulation rate (MAR) of lignin in the two cores; (d-g) Records of lignin and non-lignin phenol indices in core L13-04-2 (solid circles) and core L13-18-2 (open circles); (d and e) S/V and C/V ratios reflecting different plant tissue types as sources of lignin; (f) 3,5Bd/V and P/V ratios are proxies for wetland extent; (g) The Ad/Al ratios indicate the degree of degradation of lignin. Blue is the $(Ad/Al)_s$ ratio, and yellow is the $(Ad/Al)_v$ ratio.

6.3.2. Lignin source and degradation indicators

Vegetation development can be assessed using the S/V and C/V ratios (Hedges and Mann, 1979). The S/V and C/V ratios yielded values of 0.34–0.48 and 0.17–0.30 in core L13-04-2, with mean values were 0.42 and 0.23, respectively (Fig. 6.2). The standard deviations of S/V and C/V in all samples were 0.06 and 0.12, respectively. The minimum and maximum values of S/V occurred in 1862 and 1990, respectively. The S/V and C/V ratios in core L13-18-2 ranged from 0.42 to 0.49 and 0.06 to 0.31, with the minima occurring in 2003 and 1941, respectively. Mean values of S/V and C/V ratios in core L13-18-2 were 0.45 and 0.24. The S/V ratio in core L13-04-2 was lower than that in core L13-18-2 from 1933 to 1978 (Fig. 6.2). The 3,5Bd/V and P/V ratios are proxies used to indicate the change in wetland extent in the study area (Goñi et al., 2000; Amon et al., 2012; Tesi et al., 2014; Feng et al., 2015a; Winterfeld et al., 2015). The standard deviations of 3,5Bd/V and P/V were 0.01 and 0.02, respectively. The 3,5Bd/V and P/V ratios in core L13-04-2 were higher than in core L13-18-2. In core L13-04-2, the 3,5Bd/V ratio ranged from 0.12 to 0.21, and P/V ratios yielded values

of 0.35–0.44. The 3,5Bd/V and P/V ratios ranged from 0.06–0.10 and 0.20–0.36 in core L13-18-2, and like the S/V and C/V ratios, reached minima in 1941.

$(Ad/Al)_s$ and $(Ad/Al)_v$ ratios are affected by degradation (Ertel and Hedges, 1985; Hedges et al., 1988; Otto and Simpson, 2006). The standard deviations of $(Ad/Al)_s$ and $(Ad/Al)_v$ in all samples were 0.13 and 0.17, respectively. Similar to the wetland indicators, the $(Ad/Al)_{s,v}$ ratios were higher in core L13-04-2 than in core L13-18-2. The $(Ad/Al)_s$ and $(Ad/Al)_v$ ratios yielded values of 0.34–0.57 and 0.41–0.61 in the core L13-04-2, while slightly lower ratios of 0.05–0.36 and 0.06–0.51 were obtained in core L13-18-2 (Fig. 6.2). The minima of $(Ad/Al)_s$ and $(Ad/Al)_v$ ratios in core L13-18-2 were also reached in 1941, same as other lignin indicators.

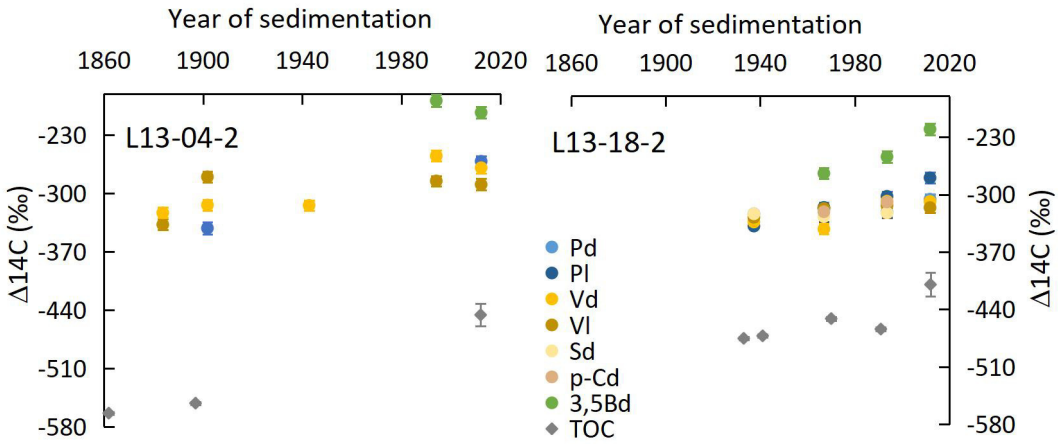

Figure 6.3 Initial $\Delta^{14}C$ values of core L13-04-2 (left) and L13-18-2 (right). Solid circles are the $\Delta^{14}C$ values of phenols, and diamonds are the $\Delta^{14}C$ values of TOC. Blue is the hydroxy phenols, yellow is the lignin phenols, and green is 3,5Bd.

6.3.3. $\Delta^{14}C$ values of TOC and individual phenols

$\Delta^{14}C$ value of TOC in the core L13-04-2 ranged from -564 ± 2‰ to -446 ± 14‰ and increased from 1862 to 2012 (Fig. 6.3). The $\Delta^{14}C$ value of TOC in the core L13-18-2 also increased with time, and ranged from -475 ± 2‰ to -409 ± 15‰.

The initial $\Delta^{14}C$ values of phenols were higher than that of TOC in the two cores. All phenols yielded values from -363.19‰ to -188.46‰ in the two cores, and $\Delta^{14}C$ values increased with time from 1884 to 2012 (Fig. 6.3). Where measured, the $\Delta^{14}C$ value of 3,5Bd is the highest of all phenols in the two sediment cores. In core L13-04-2, the ^{14}C value of Pd is lower than lignin phenols. However, in core L13-18-2, the ^{14}C value of Pd is similar to lignin phenols and the $\Delta^{14}C$ difference between different phenols is less significant than that in core L13-04-2. The $\Delta^{14}C$ values in core L13-04-2 are higher than those in core L13-18-2 in 1994 and 2012.

6.4. Discussions

6.4.1. Source and degradation of lignin

The mean C/V ratio in our samples is higher than the value in the surface sediment of Buor-Khaya Bay (mean value: 0.17, Winterfeld et al., 2015, Fig. 6.4), but the mean S/V ratio in the our samples is similar to Winterfeld et al. (2015) (mean value: 0.43). The vegetation in the Lena Basin did not change much from 1860 to 2012 based on the S/V ratios (Fig. 6.2), but the decreased C/V ratio in core L13-18-2 in 1941 may represent the type of vegetation has changed significantly. The mean value of the P/V ratio in the surface sediment of Buor-Khaya Bay is 0.43 (Winterfeld et al., 2015), which is higher than that in our samples. A typical signal of *Sphagnum*-dominated peat is the high P/V ratio (6.0, Amon et al., 2012; Tesi et al., 2014). Winterfeld et al. (2015) suggested the relatively lower P/V ratios in total suspended matter samples from the Lena Delta indicate that moss contribution is minor compared to a dominant non-woody angiosperm source. Consistent with previous studies, most of the terrestrial samples analyzed in this study exhibited low P/V ratios indicating that most of the phenols derive from vascular plant tissues.

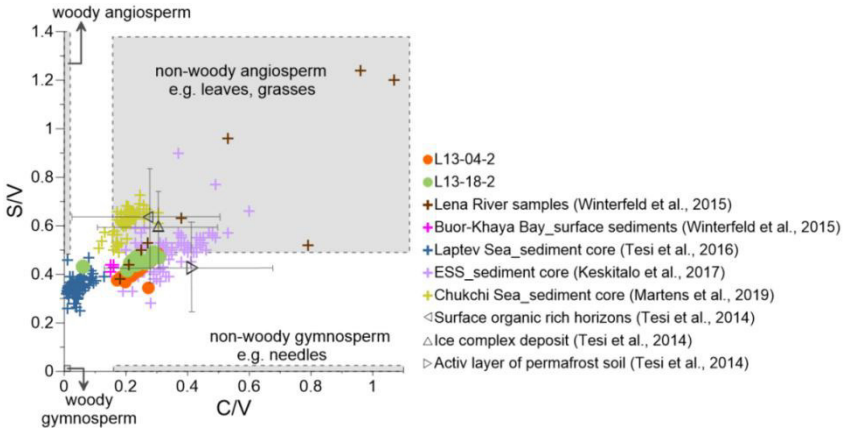

Figure 6.4 Lignin indicators of terrigenous material in core L13-04-2 (orange dots) and L13-18-2 (green dots) compared with published data (Tesi et al., 2014, 2016; Winterfeld et al., 2015; Keskitalo et al., 2017; Martens et al., 2019). Open black triangles represent the ratio of S/V and C/V from surface soils, ice complex deposits and active layer permafrost (Tesi et al., 2014). ESS is short for the East Siberian Shelf.

According to the end-member value of woody and non-woody gymnosperm and angiosperm tissues (Amon et al., 2012; Winterfled et al., 2015; Tesi et al., 2016; Cao et al., 2023), the S/V and C/V values of core L13-18-2 and L13-04-2 reflect a mixture of woody gymnosperm and non-woody angiosperm vegetation sources (Fig. 6.4). Winterfeld et al. (2015) found that the S/V and C/V ratios in the Lena Delta total suspended matter reflect a mixture of woody gymnosperm and non-woody angiosperm vegetation sources. The sediment core in Tesi et al. (2016) was retrieved from the Laptev Sea (~ 80° N). Terrigenous OC transported from the Bour-Khaya Bay to the Laptev Sea shelf edge requires ~ 3600 years, and ~ 85% terrigenous

OC was degraded during this translocation (Bröder et al., 2018). Degradation during transport from the Lena River mouth to the further offshore location may result in the difference of S/V and C/V ratios between our results and the results in Tesi et al. (2016) (Fig. 6.4).

The cinnamyl phenols are known to degrade relatively fast during early diagenesis which may result in decreased C/V ratios in 1941 (Benner et al., 1990; Opsahl and Benner, 1995), but this is not consistent with $(Ad/Al)_{s,v}$ values (Fig. 6.2). The vegetation type in the Lena Basin did not change significantly in the last century based on lignin records, the low C/V ratios in 1941 may reflect high amounts of woody tissues, such as roots, branches. In the core L13-18-2, the lignin MAR increased to the maximum in 1941 (Fig. 6.2), but no significant change was found in core L13-04-2 which is located in the Buor-Khaya Bay. Terrigenous OC transported by the Lena River may enter the Laptev Sea mainly through the Sardakhskaya–Trofimovskaya channel and the Bykovskaya channel (Fig. 6.1), instead of entering the Buor-Khaya Bay.

The mean TOC content in core L13-18-2 is 1.88% which is higher than that in core L13-04-2 (1.48%), and the mean $\delta^{13}C$ value of core L13-18-2 (-26.1‰) is lower than that of core L13-04-2 (-25.7‰) (Table S6.1). The TOC values from the two sediment cores are lower than previously published data of total suspended matter from the Laptev Sea shelf (1.67−2.47%, Winterfeld et al., 2015) and Lena River (2.6−7.1%, Ogneva et al., 2023). Organic matter degradation occurs during transport and sedimentation, as well as within the sediment, which may affect the TOC content in the shelf sediments.

The Ad/Al ratios in the core L13-04-2 are higher than that in the core L13-18-2 (Fig. 6.2). Respiration of organic matter at the sediment-water boundary is an oxygen consuming process that results in lower degradation rates in the underlying sediment. This means that the bottom water oxygen concentrations have a major driving influence on degradation rates (Hartnett et al., 1998). Semiletov et al. (2013) found very low oxygen saturations in the bottom water of the Buor-Khaya Bay and higher concentrations further north in the Laptev Sea, suggesting that the degradation rate of organic matter might be higher at the site of L13-18-2 than in core L13-04-2 (Kattein, 2018), which is contrary to our $(Ad/Al)_{s,v}$ data. Winterfeld et al. (2015) found that the strong degradation of sedimentary organic matter consisting of ICD in the Lena Basin most likely occurred after thawing on land. The bottom water oxygen concentration in seawater may not have a strong effect on degradation parameters. Vonk et al. (2012) found extensive degradation of organic matter released from Yedoma permafrost on Moustakh Island, which is located in the Buor-Khaya Bay. They discovered about 66% OC was lost during the downslope degradation occurring on the cliff slopes of the island. Therefore, we suggest that $(Ad/Al)_{s,v}$ values mainly reflect degradation processes that have occurred on land prior to, or immediately following erosion and transport to the ocean.

The minimum of Ad/Al ratios in core L13-18-2 was reached in 1941, but the $(Ad/Al)_{s,v}$ values did not change much in core L13-04-2 at the same time (Fig. 6.2). A large amount of fresh woody debris may be exported into the Lena River in 1941, which increased the MAR of lignin and decreased the the C/V ratios and $(Ad/Al)_{s,v}$ ratios in the core L13-18-2. As the Lena River discharges into the Laptev Sea mainly through the Sardakhskaya–Trofimovskaya channel and the Bykovskaya channel, the event in 1941 was not recorded in the core L13-04-2.

6.4.2 $\Delta^{14}C$ of lignin phenols in the sediments

The mean $\Delta^{14}C$ value of phenols and TOC increased with time in the two sediment cores (Fig. 6.3). The ^{14}C age of lignin phenols decreases with the increase of temperature and/or precipitation (Eglinton et al., 2021). The Arctic has warmed nearly four times faster than the globe since 1979 (Rantanen et al., 2020), and a substantial increase of precipitation in the Arctic was simulated during the twentieth century (Kattsov and Walsh, 2000). The increase of temperature and precipitation may reduce the turn over time of lignin in soils which leads to younger lignin phenols (Eglinton et al., 2021; Jia et al., 2023). Permafrost is mostly continuous except some discontinuous and sporadic patches in the southern part of the Lena Basin (Brown et al., 2002), and the mean annual air temperatures in the Lena Basin are below 0 ℃ now. Warming may increase the active layer of permafrost in the Lena Basin, but old permafrost OC remobilized from thermo-erosion may not have changed significantly over the last century. Based on the hydrogen isotope ratios and radiocarbon measurements of lipids, Kattein (2018) suggested that topsoil permafrost dominated input of organic matter in the two sediment cores. Surface runoff exerts a strong control on the $\Delta^{14}C$ values of lignin phenols in the Arctic river systems (Feng et al., 2013a), where younger lignin is transported by rivers with a higher mean annual runoff rate. The annual daily discharge of Lena River has increased by 40% from 1953 to 2013 (Tananaev et al., 2016). The $\Delta^{14}C$ value of phenols might increase proportionally over time with increasing runoff during the last century.

The mean $\Delta^{14}C$ values of lignin phenols in surface sediment of the Lena River mouth was -320 ± 46‰ (Feng et al., 2015b) which was similar to the mean $\Delta^{14}C$ value of core L13-18-2, but lower than the mean $\Delta^{14}C$ values of core L13-04-2 (-276 ± 46‰). The mean $\Delta^{14}C$ values of S-phenols in Feng et al. (2015b) is -380 ± 26‰, which is lower than our results (-324 ± 26‰). The mean $\Delta^{14}C$ values of hydroxy phenols in core L13-18-2 (-309 ± 6‰) and core L13-04-2 (-318 ± 6‰) are higher than that in the surface sediment of Lena River mouth (-477 ± 18‰, Feng et al., 2015b). The $\Delta^{14}C$ values of individual phenols from the Lena River surface sediments were lower than that in the Laptev Sea shelf sediments, which may indicate that old permafrost OC was degraded during transport from the estuary to the shelf, and the

contribution of old OC remobilized by coastal erosion on the shelf sediments may be negligible.

The $\Delta^{14}C$ offset between different phenols in the core L13-04-2 was more significant than in the core L13-18-2, and Ad/Al ratios in the former were generally higher, indicating the presence of more degraded lignin. The $\Delta^{14}C$ values of phenols in the core L13-04-2 were higher than those in core L13-18-2 in 1994 and 2012. The $\Delta^{14}C$ value of Vl in the surface sediment of Lena River mouth was -274 ± 125‰ (Feng et al., 2015b), which is higher than at the top of core L13-18-2 and L13-04-2 (Fig. 6.3). However, the $\Delta^{14}C$ values of Vd in our samples were higher than that in the surface sediment of Lena River mouth (-374 ± 37‰, Feng et al., 2015b). $\Delta^{14}C$ offsets between individual lignin phenols can be explained by differential degradation in a sample that contains lignin from at least two sources characterized by different age and degradation state. The degradation rate of 3,5Bd, which is mainly from wetlands, is faster than that of lignin phenols under the same conditions. 3,5Bd was thus younger than lignin phenols (Fig. 6.3). Feng et al. (2015b) found no correlation between $\Delta^{14}C$ values of lignin phenols and Ad/Al ratios or vegetation indicators (S/V and C/V) in surface sediments in the Lena Mouth. However, our data set reveals a positive correlation between $(Ad/Al)_v$ and $\Delta^{14}C$ values of Vl in the two cores over the last century (Fig. 6.5a), and the R^2 value in the core L13-04-2 is lower than that in core L13-18-2, indicating the degradation of lignin phenols is an important factor on the $\Delta^{14}C$ values of lignin phenols, especially for the core L13-18-2 which is more affected by Lena River than the core L13-04-2. Preferential degradation of Vl over Vd would result in an lower $\Delta^{14}C$ for Vd than for Vl, but the $\Delta^{14}C$ offset between Vd and Vl is not correlated to the $(Ad/Al)_{s,v}$ in the two sediments cores which means sources of lignin phenols may be an important factor on the $\Delta^{14}C$ offset between lignin phenols.

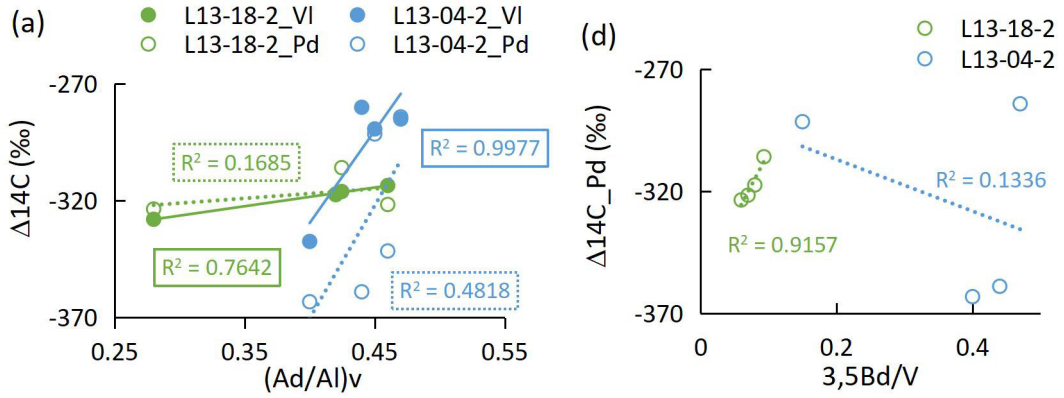

Figure 6.5 Correlation between (a) $\Delta^{14}C$ values of Vl and $(Ad/Al)_v$; and (b) C/V ratios in the two sediment cores; Correlation between (c) $\Delta^{14}C$ values of Pd and $(Ad/Al)_v$; and (d) 3,5Bd/V ratios in the two sediment cores; Green symbols are used for the core L13-18-2, and blue represents core L13-04-2 which is located in the Buor-Khaya Bay.

The correlations between $(Ad/Al)_v$ and $\Delta^{14}C$ of Pd (Fig. 6.5a) are less significant in the two cores than the correlation of $(Ad/Al)_v$ to the $\Delta^{14}C$ values of Vl (Fig. 6.5a), suggesting less degradation influence on the $\Delta^{14}C$ value of hydroxy phenols in the Lena Basin. Previous studies found that surface runoff is less efficient in supplying modern hydroxy phenols in the Lena Basin, where inputs of old hydroxy phenols from deeper soils are prominent (Feng et al., 2013a). The $\Delta^{14}C$ value of Pd was not higher than that of lignin phenols in the two sediment cores, and wetland extent as indicated by the 3,5Bd/V ratio is correlated positive to the $\Delta^{14}C$ value of Pd in the core L13-18-4 (Fig. 6.5b). Surface carbon pools (e.g., wetland) and old carbon pools (e.g., ICD) both affect the $\Delta^{14}C$ value of Pd in the core L13-18-2, but wetland contribution to Pd may be limited in the core L13-04-2. The $\Delta^{14}C$ value of bulk OC was higher in the core L13-18-2 than in the core L13-04-2 (Fig. 6.3). The contribution of old OC pools to the core L13-04-2 was likely older than to core L13-18-2. The $\Delta^{14}C$ offset between different phenols in the core L13-04-2 was larger than that in the core L13-18-2 may be relate to the different terrigenous OC source in the two sediment cores. The relative $\Delta^{14}C$ value distribution between phenols as we observe in the core L13-04-2 is consistent with lignin being predominantly supplied from an aged source containing plant tissues of various ages that has undergone some degradation, probably a deep soil, such as ICD.

6.5. Conclusions

The vegetation in the Lena Basin is a mixture of woody gymnosperm and non-woody angiosperm sources and did not change significantly from 1862 to 2012, but large amounts of woody tissues were transported into the Laptev Sea by the Lena River in 1941. Organic matter degradation occurs during transport and sedimentation, as well as within the sediment, however, we found that degradation processes of terrigenous organic matter from Lena Basin occurs mainly on land over the last century. Surface runoff has an important effect on the $\Delta^{14}C$ values of lignin phenols in shallow Laptev Sea sediments. Young and old terrigenous carbon pools both affect the $\Delta^{14}C$ values of phenols in the two sediment cores, and the $\Delta^{14}C$ values of old carbon pools may be higher in the core L13-18-2 than that in the core L13-04-2.

6.6. Supplementary information

Table S6.1. Total organic carbon (TOC) geochemical data, mass accumulation rate of lignin and lignin parameters in the two sediment cores. YOS is the year of sedimentation, and MAR is the mass accumulation rate.

Sediment core	Depth (cm)	YOS	TOC (%)	MAR ($\mu g/cm^2/yr$)	S/V	C/V	3,5Bd/V	P/V	$(Ad/Al)_s$	$(Ad/Al)_v$
L13-18-2	0-1	2012	1.75	34.77	0.44	0.23	0.09	0.32	0.32	0.42
	1-3	2008	1.99	29.43	0.48	0.29	0.07	0.36	0.36	0.45
	3-5	2003	1.95	35.29	0.42	0.20	0.10	0.30	0.32	0.43
	5-7	1997	1.69	26.54	0.46	0.28	0.08	0.36	0.35	0.48
	7-9	1991	1.96	46.71	0.46	0.22	0.07	0.30	0.29	0.44
	9-11	1985	1.97	50.36	0.46	0.26	0.08	0.30	0.30	0.43
	11-13	1978	1.91	27.44	0.47	0.31	0.06	0.35	0.34	0.44
	13-15	1970	1.84	45.75	0.45	0.25	0.08	0.30	0.30	0.42
	15-17	1964	2.07	64.56	0.47	0.23	0.09	0.31	0.29	0.43
	17-19	1959	1.91	48.32	0.45	0.26	0.06	0.34	0.29	0.33
	19-21	1952	2.05	36.59	0.45	0.21	0.08	0.30	0.28	0.36
	21-23	1941	1.52	131.47	0.43	0.06	0.02	0.20	0.05	0.06
	23-25	1933*	1.83	24.45	0.49	0.29	0.10	0.32	0.31	0.51
L13-04-2	0-1	2012	1.77	9.92	0.39	0.19	0.15	0.36	0.44	0.45
	1-2	2010	1.55	6.53	0.41	0.20	0.14	0.39	0.41	0.46
	2-3	2007	1.5	6.63	0.43	0.24	0.14	0.39	0.47	0.47
	3-4	2003	1.64	5.60	0.49	0.30	0.14	0.44	0.55	0.56
	4-5	1999	1.54	5.88	0.44	0.25	0.15	0.41	0.53	0.47
	5-6	1994	1.31	5.71	0.42	0.22	0.15	0.40	0.47	0.46
	6-7	1990	1.5	9.26	0.48	0.30	0.13	0.44	0.57	0.47
	7-8	1985	1.53	5.78	0.39	0.22	0.18	0.37	0.49	0.55
	8-9	1978	1.68	6.15	0.47	0.28	0.18	0.38	0.52	0.61
	9-10	1971	1.47	7.57	0.38	0.17	0.21	0.36	0.47	0.47
	10-11	1965	1.52	4.48	0.41	0.22	0.14	0.41	0.39	0.48
	11-12	1959	1.43	13.83	0.42	0.25	0.13	0.39	0.46	0.48

12-13	1953	1.51	6.06	0.39	0.18	0.14	0.37	0.34	0.42
13-14	1946	1.51	11.57	0.39	0.21	0.17	0.39	0.54	0.50
14-15	1929	1.48	1.74	0.41	0.24	0.15	0.38	0.43	0.47
15-16	1913	1.67	12.56	0.37	0.20	0.15	0.39	0.42	0.42
16-17	1911	1.42	72.75	0.42	0.24	0.14	0.41	0.42	0.45
17-18	1907	1.33	7.06	0.40	0.20	0.18	0.38	0.42	0.45
18-19	1901	1.33	7.57	0.39	0.21	0.15	0.39	0.42	0.44
19-20	1897	1.43	28.45	0.39	0.20	0.15	0.37	0.41	0.44
20-21	1896	1.42	n.a.	0.45	0.27	0.12	0.43	0.51	0.52
21-22	1888	1.36	n.a.	0.43	0.25	0.12	0.35	0.43	0.38
22-23	1880	1.35	n.a.	0.45	0.28	0.14	0.37	0.43	0.41
23-24	1862	1.39	n.a.	0.34	0.27	0.15	0.37	0.46	0.48

*: error of YOS is not available
n.a.: not available

Table S6.2. Compound-specific radiocarbon data of lignin-derived phenols in the two sediment cores. $\Delta^{14}C_{initial}$ of lignin-derived phenols is named as initial $\Delta^{14}C$-phenol. The content of OC for each phenol was measured by MICADAS (Mass, μg OC). YOS is the year of sedimentation.

Sediment core	Depth (cm)	YOS	Compound	Mass (μg OC)	$F^{14}C$	initial $\Delta^{14}C$-phenol (‰)
L13-18-2	surface	2012	Pl	67	0.7266 ± 0.0065	-279.65 ± 6.44
			Pd	62	0.7003 ± 0.0064	-305.79 ± 6.32
			Pd	52	0.7021 ± 0.0069	-303.98 ± 6.86
			Vl	58	0.6900 ± 0.0065	-316.01 ± 6.43
			Vl	63	0.6965 ± 0.0060	-309.50 ± 5.94
			Vd	57	0.6975 ± 0.0067	-308.52 ± 6.65
			Vd	62	0.6939 ± 0.0064	-312.08 ± 6.30
			3,5Bd	52	0.7864 ± 0.0070	-220.41 ± 6.90
	5-9	1994	Pl	85	0.7023 ± 0.0062	-302.27 ± 6.15
			Pd	68	0.6829 ± 0.0064	-321.56 ± 6.34
			Pd	72	0.6845 ± 0.0063	-319.93 ± 6.17
			Vl	55	0.6910 ± 0.0068	-313.44 ± 6.67
			Vl	67	0.6848 ± 0.0066	-319.61 ± 6.15
			Vd	64	0.6963 ± 0.0065	-308.17 ±6.47
			Vd	65	0.6789 ± 0.0063	-325.45 ± 6.43
			Sd	72	0.6819 ± 0.0063	-322.46 ± 6.26
			p-Cd	83	0.6953 ± 0.0062	-309.15 ± 6.14
			3,5Bd	45	0.7508 ± 0.0071	-254.02 ± 7.01
	13-17	1967	Pl	88	0.6865 ± 0.0061	-315.76 ± 5.97
			Pd	68	0.6849 ± 0.0065	-317.36 ± 6.37
			Pd	72	0.6747 ± 0.0064	-327.49 ± 6.30

			Vl	67	0.6851 ± 0.0064	-317.12 ± 6.33
			Vl	74	0.6686 ± 0.0064	-333.60 ± 6.29
			Vd	51	0.6601 ± 0.0064	-342.02 ± 6.31
			Vd	73	0.6769 ± 0.0058	-325.29 ± 5.71
			Sd	74	0.6752 ± 0.0061	-327.01 ± 6.06
			p-Cd	80	0.6812 ± 0.0062	-321.02 ± 6.13
			3,5Bd	45	0.7281 ± 0.0069	-274.27 ± 6.75
			Pl	74	0.6613 ± 0.0063	-338.52
			Pd	68	0.6763 ± 0.0060	-323.52
			Pd	55	0.6731 ± 0.0065	-326.66
	21-25	1937*	Vl	55	0.6719 ± 0.0065	-327.91
			Vl	59	0.6769 ± 0.0064	-322.91
			Vd	60	0.6662 ± 0.0064	-333.54
			Vd	42	0.6441 ± 0.0066	-355.67
			Sd	63	0.6762 ± 0.0060	-323.60
			Pl	83	0.7451 ± 0.0065	-261.37 ± 6.42
			Pd	61	0.7148 ± 0.0065	-291.40 ± 6.46
			Pd	44	0.7378 ± 0.0071	-268.57 ± 7.05
			Vl	53	0.7170 ± 0.0069	289.23 ± 6.83
L13-04-2	0-1	2012	Vl	65	0.7280 ± 0.0065	-278.36 ± 6.48
			Vd	69	0.7373 ± 0.0067	-269.15 ± 6.62
			Vd	53	0.7541 ± 0.0072	-252.47 ± 7.10
			3,5Bd	68	0.8043 ± 0.0066	-202.70 ± 6.51

4-7	1994	Pd	74	0.7206 ± 0.0065	-284.06 ± 6.36
		Vl	74	0.7197 ± 0.0064	-284.98 ± 6.36
		Vd	73	0.7500 ± 0.0067	-254.90 ± 6.63
		3,5Bd	54	0.8169 ± 0.0072	-188.46 ± 7.07
12-15	1943	Pd	87	0.6588 ± 0.0063	-341.47 ± 6.13
		Vd	106	0.6859 ± 0.0063	-314.29 ± 6.15
17-20	1902	Pl	36	0.6553 ± 0.0072	-341.71 ± 7.03
		Pd	88	0.6381 ± 0.0059	-358.94 ± 5.73
		Vl	56	0.7167 ± 0.0069	-279.97 ± 6.61
		Vd	66	0.6830 ± 0.0066	-313.88 ± 6.41
21-23	1884	Pd	89	0.6325 ± 0.0059	-363.19 ± 5.75
		Vl	47	0.6581 ± 0.0068	-337.38 ± 6.56
		Vd	74	0.6722 ± 0.0063	-323.20 ± 6.15

*: error of YOS is not available.

7. Summary, conclusions and outlook

7.1. Summary and conclusions

In this thesis, lignin and its ^{14}C isotope compositions were used as the major tools, combined with other biomarkers (e.g., *n*-alkanes, fatty acids, and GDGTs), isotope compositions (^{13}C and ^{14}C) of bulk OC, to reflect the characteristics of permafrost OC in the Yukon and Amur Basins during the last deglaciation and achieve the main objectives: (1) to reconstruct the past vegetation change of the two basins during the last deglaciation; (2) to explore the potentially different transport of terrestrial OM archived in sub-Arctic marine sediments during the last deglaciation; (3) to quantify the procedural blank ($F^{14}C$ and mass) of the modified purification method for lignin-derived phenols; (4) to investigate the difference of ^{14}C age between lignin-derived phenols and n-C26:0 fatty acid; (5) to study the supply and ^{14}C age of lignin-derived phenols from the Lena watershed over the past century. The key findings from the main chapters are summarized in the following:

1) The vegetation change in the Amur Basin began in the Pre-boreal based on the flux of lignin and published lipids data. This timing is different from observed changes in the Yukon basin, where wetland expansion and vegetation change occurred in the early deglaciation. In the two basins, angiosperm contribution and wetland extent all reached maxima during the Pre-boreal. Lignin parameters (e.g. S/V, C/V and 3,5Bd/V ratios) can reflect vegetation change and wetland development, but the degradation state of lignin strongly overprints these proxy signals and should be considered to be a function of temperature, transport distance and burial rate.
2) Similar to changes in vegetation, the degradation and remobilization of permafrost of the Yukon basin also occurred earlier than in the Amur basin. Retreat of sea ice coupled with increased sea surface temperatures in the Bering Sea during the early deglaciation might have promoted early permafrost mobilization. Lignin transported by surface runoff may account for significant proportions of lignin during inland warming, but the export of lignin and lipids does not always occur via different pathways, as both biomarker groups can be contributed from rapidly eroding deep deposits during phases of rapid permafrost thaw, which is in contrast to modern-day studies. This finding suggests that the fate of terrigenous organic matter in the Arctic differs on both temporal and spatial scales.
3) A revised method for the purification of lignin phenols from sediment based on a previously published method was described and the fraction of modern carbon ($F^{14}C$) and the mass of the associated procedural blank were evaluated. Different from Feng's

method (2013b), lignin phenols were purified only by one HLB SPE cartridge (Waters Oasis, 200 mg, 6 mL). The HLB SPE cartridges had high recovery rates (>70%) and a low blank contribution. Samples were passed through the HLB cartridge with 60 mL ethyl acetate to achieve separation. The following single compound collection using high pressure liquid chromatography which was equipped with a Phenomenex Synergi Polar-RP column, and column was held at 40 °C during runs. After the two-step separation, 11 lignin-derived phenols were isolated and most impurities in the sample could be removed. The current status of carbon blanks associated with the preparation protocol for radiocarbon analysis of lignin phenols was determined to be 4.2 ± 0.4 μgC with $F^{14}C$ of 0.55 ± 0.04 for the entire method. It is recommended to aim for purified lignin phenol samples that contain at least 30 μgC to obtain reliable age estimates.

4) The first downcore CSRA records of lignin-derived phenols from sediment cores retrieved off the Yukon and Amur basins covering the early deglaciation to the Holocene was provided. The radiocarbon ages of phenols reflect the sediments from the Bering and Okhotsk Seas are expected to receive inputs from at least two different terrigenous sources that are characterized by different age and degradation degree during the last deglaciation. Wetland coverage may influence the age offset between lignin phenols and hydroxy phenol, and the age offsets between lignin phenols and fatty acids were controlled by surface discharge in the Yukon and Amur Basins. Deep OC enriched in long-chain lipids can be mobilized both through coastal erosion and thermokarst inland which can be transported to marine sediments by surface runoff in the last deglaciation. Same as in the modern Arctic river systems, the radiocarbon ages of lignin phenols and long-chain fatty acids are affected by climate change, ^{14}C age offset between lipids and lignin phenols can be used as palaeo-proxies for the state of permafrost inland.

5) Over the past century, the vegetation in the Lena Basin was a mixture of woody gymnosperm and non-woody angiosperm sources and did not change significantly. The degradation processes of terrigenous organic matter from Lena Basin occurs mainly on land over the last century. Surface runoff has an important effect on the $\Delta^{14}C$ values of lignin phenols in shallow Laptev Sea sediments. Young and old terrigenous carbon pools both affect the $\Delta^{14}C$ values of phenols in the two sediment cores, but the $\Delta^{14}C$ values of lignin phenols from old carbon pools in the core L13-18-2 may be higher than that in the core L13-04-2.

7.2. Outlook

The past decades of rising temperatures in Northern Hemisphere have shown that environmental changes are long underway, now is urgency to understand the consequences and associated feedback to climate from the warming and thaw of the large permafrost carbon pool. Studies of transported terrestrial OC in the Arctic Ocean provide one of the best opportunities to trace large-scale remobilization of terrestrial OC from coastal and inland permafrost, and should therefore continue investigating changes in the circum-Arctic carbon cycle.

In this thesis, the radiocarbon age offsets between lignin phenols and long-chain fatty acids were affected by surface discharge in the Yukon and Amur Basins during the last deglaciation. If the age offset can be served as an index for surface discharge during the last deglaciation, which may help us better understand the paleo-hydrological changes of rivers. Changes in runoff may reflect climate change, especially for rivers that are heavily affected by precipitation, such as the Amur River. In modern Arctic river systems, surface discharge was correlated to the $\Delta^{14}C$ values of lignin phenols positively (Feng et al., 2013a, 2015b). In the two short cores from the Laptev Sea shelf, we found the surface discharge of Lena River may be an important control on the $\Delta^{14}C$ values of lignin phenols during the last century. More $\Delta^{14}C$ values of lignin phenols is needed to check if the lignin phenols ages or age offset between lipids and lignin phenols can be served as proxies of runoff.

Degradation affect the age offset between different lignin phenols in the Yukon and Amur Basins during the last deglaciation, but our data can not be used to explain where degradation occurs. The rate of degradation of permafrost OC and where degradation occurs is still controversial at present. Knowing more about degradation will also help us identify whether lignin ^{14}C age can be used as a reference for runoff. Further analyses of different phases of terrestrial OC in the extensive shelf seas of the Arctic Ocean will be important for understanding of degradation of terrestrial OC.

Lignin phenols are more difficult to be purified for CSRA than lipids due to its complexity and low recovery during separation, which limits the use of lignin phenols $\Delta^{14}C$ values. A simplified method of lignin purification was displayed in the thesis, but the recovery rate of lignin phenols were still low, especially for 3,5Bd. During the SPE separation, 60 mL ethyl acetate was used for one sediment sample. If new SPE cartridges and/or solvents can be found to separate lignin phenols, which may be possible to further simplify the process and improve the recovery rate of lignin phenols.

8. Acknowlagements

The past four years have been quite a journey full of great and shaping experiences. I feel deeply grateful for any aspect of it, and I believe that even stressful and frustrating times fulfilled a good purpose after all. Many of these experiences would not have happened without the people surrounding me. Finishing this PhD project would not have been possible without the support of many people, whom I am very grateful to and have had the pleasure to work with. Here, I hope to acknowledge all those who played key roles.

First, I would like to mention the great work of my supervisors, Gesine Mollenhauer and Jens Hefter. I see you both as role models and I feel lucky for having been in my spot the past four years. Thank you for all your guidance and faith. Gesine, this all would not have been possible without you and I am grateful you offering me such a great opportunity to work on this interesting project. Thank you for always being available for a good piece of advice and an answer to almost everything. Jens, I admire your commitment for your work and feel that I learned a lot from you over the years. Thank you very much for taking such good care of me. Your generosity and kindness spurred me to keep working. Besides my supervisors, I would like to thank my thesis committee members Ralf Tiedemann and Lester Lembke-jene for thoughtful feedback and inspiring advices during the meetings. I could not have imagined having better supervisors and committee members for my PhD study. Many thanks to Prof. Dr. Tommaso Tesi for reviewing my thesis.

I want to thank and greet all members of our research group. All the members created a diverse, relaxing environment, which made it very enjoyable to work in this awesome group. I would like to thank Hendrik for serving as technical advisor the past years, I appreciate working with you. Torben, great sense of humor you! Malte, you are so kindness and friendly. Liz and Lea, it’s great to have you around and it’s fun to work with you! Thanks Sara, Arnaud, Laura and Tsai-Wen for sharing the offices with me. Manuel, you are so smart and kind-hearted. Bingbing, I appreciate working with you and I look forward to more cooperation. Thanks also to all other colleagues and former group members who have by now have moved on to new challenges and adventures.

Special thanks go to all co-authors who greatly contributed to the three papers in this thesis and beyond. It was a great experience to have worked in such an professional and innovative team of scientists of the Alfred Wegener Institute for Polar and Marine Research in Bremerhaven. I am very thankful to POLMAR Graduate School for many helpful seminars, lectures and financial support that allowed me to attend international conferences.

Furthermore, I thank China Scholarship Council for offering me this opportunity to study abroad.

Thanks to anyone else at the department who has been hanging out with me over the past four years! Xianyu, we have known each other for 13 years. I hope our friendship will last forever. Defang, you are so humor and kindness. Junjie, you are very warm and thoughtful, wish you a bright future. Yunyi, I am very happy our paths crossed here in Bremerhaven. Thank you to everyone I met in the four years.

Last but not the least, I am also very grateful for a lot of support from so many people beyond work. Special thanks go to my husband, my family, my friends in Germany and home in China. Mengmeng, you are the best, thanks for being so patient with me. I would rather share one lifetime with you than face all the ages of this world alone. You complete me.

There are many more people I should have mentioned. I wish all the best to all of you, for your future careers and lives.

9. References

Abramov, A., Vishnivetskaya, T., Rivkina, E., 2021. Are permafrost microorganisms as old as permafrost? FEMS microbiology ecology 97, fiaa260.

Ager, T., 2003. Late Quaternary vegetation and climate history of the central Bering land bridge from St. Michael Island, western Alaska. Quat. Res. 60, 19–32.

Alexandrov, V.Y., Martin, T., Kolatschek, J., Eicken, H., Kreyscher, M., Makshtas, A.P., 2000. Sea ice circulation in the Laptev Sea and ice export to the Arctic Ocean: results from satellite remote sensing and numerical modeling. J. Geophys. Res. 105, 17143–17159.

Alves, E.Q., Macario, K.C., Ascough, P., Bronk Ramsey, C., 2018. The Worldwide Marine Radiocarbon Reservoir Effect: Definitions, Mechanisms, and Prospects. Rev. Geophys. 56, 278–305.

Amelung, W., Flach, K.-W., Zech, W., 1999. Lignin in particle-size fractions of native grassland soils as influenced by climate. Soil Sci. Soc. of Am. J. 63, 1222–1228.

Amelung, W., Martius, C., Bandeira, A.G., Garcia, M.V.B., Zech, W., 2002. Lignin characteristics and density fractions of termite nests in an Amazonian rain forest—indicators of termite feeding guilds? Soil Biol. Biochem. 34, 367–372.

Amon, R.M.W., Rinehart, A.J., Duan, S., Louchouarn, P., Prokushkin, A., Guggenberger, G., Bauch, D., Stedmon, C., Raymond, P.A., Holmes, R.M., McClelland, J.W., Peterson, B.J., Walker, S.A., Zhulidov, A.V., 2012. Dissolved organic matter sources in large Arctic rivers. Geochim. Cosmochim. Acta 94, 217–237.

An, Z., Porter, S. C., Kutzbach, J. E., Wu, X., Wang, S., Liu, X., Li, X., Zhou, W., 2000. Asynchronous Holocene optimum of the east Asian monsoon. Quat. Sci. Rev. 19, 743–762.

Anderson, P.M., Edwards, M.E., Brubaker, L.B., 2003. Results and paleoclimate implications of 35 years of paleoeco logical research in Alaska, in: The Quaternary Period in the United States, edited by: Gillespie, A.R., Porter, S.C., and Atwater, B. F., Elsevier, Amsterdam, 427–440.

Appleby, P.G. and Oldfield, F., 1978. The calculation of lead-210 dates assuming a constant rate of supply of unsupported ^{210}Pb to the sediment. CATENA 5, 1–8.

Arellano, A.R., Bianchi, T.S., Hutchings, J.A., Shields, M.R., Cui., X., 2018. Differential effects of solid-phase extraction resins on the measurement of dissolved lignin-phenols and organic matter composition in natural waters. Limnol. Oceanogr.: Methods 16, 22–34.

Bahri, H., Rasse, D.P., Rumpel, C., Dignac, M.F., Bardoux, G., Mariotti, A., 2008. Lignin degradation during a laboratory incubation followed by ^{13}C isotope analysis. Soil Biol. Biochem. 40, 1916–1922.

Ballantyne, A.P., Axford, Y., Miller, G.H., Otto-Bliesner, B.L., Rosenbloom, N., White, J.W.C., 2013. The amplification of Arctic terrestrial surface temperatures by reduced sea-ice extent during the Pliocene. Palaeogeogr. Palaeocl. 386, 59–67.

Bazarova, V.B., Klimin, M.A., Mokhova, L.M., Orlova, L.A., 2008. New pollen records of Late Pleistocene and Holocene changes of environment and climate in the Lower Amur River basin, NE Eurasia. Quatern. Int. 179, 9–19.

Bauer, J.E., Druffe, E.R.M., Wolgast, D.M., Griffin, S., 2002. Temporal and regional variability in sources and cycling of DOC and POC in the northwest Atlantic continental shelf and slope. Deep Sea Res., Part II 49, 4387–4419.

Bailey, R.C., 2005. Yukon River Basin, in: Rivers of North America, edited by: Benke, A.C. and Cushing, C.E., Elsevier, NewYork, 775–804.

Belt, S. T., Massé, G., Rowland, S. J., Poulin, M., Michel, C., LeBlanc, B., 2007. A novel chemical fossil of palaeo sea ice: IP_{25}. Org. Geochem. 38, 16–27.

Benner, R., Weliky, K., Hedges, J.I., 1990. Early Diagenesis of Mangrove Leaves in a Tropical Estuary−Molecular-Level Analyses of Neutral Sugars and Lignin-Derived Phenols. Geochim. Cosmochim. Ac. 54, 1991–2001.

Bianchi, T.S., Cui, X., Blair, N.E., Burdige, D.J., Eglinton, T.I., Galy, V., 2018. Centers of organic carbon burial and oxidation at the land–ocean interface. Org. Geochem. 115, 138–155.

Bigelow, N.H., 2013. Pollen Records, Late Pleistocene|Northern North America, in: Encyclopedia of Quaternary Science, 2nd Edn., edited by: Elias, S.A. and Mock, C.J., Elsevier, 39–51.

Binney, H.A., Willis, K.J. Edwards, M.E., Bhagwat, S.A., Anderson, P.M., Andreev, A.A., Blaauw, M., Damblon, F., Haesaerts, P., Kienast, F., Kremenetski, K.V., Krivonogov, S.K., Lozhkin, A.V., Macdonald, G.M., Novenko, E.Y., Oksanen, P., Sapelko, T.V., Väliranta, M., Vazhenina, L., 2009. The distribution of late-Quaternary woody taxa in northern Eurasia: evidence from a new macrofossil database. Quat. Sci. Rev. 28, 2445–2464.

Blaauw, M., 2010. Methods and code for "classical" age-modelling of radiocarbon sequences. Quat. Geochronol. 5, 512–518.

Bolshiyanov, D., Makarov, A., Savelieva, L., 2015. Lena River delta formation during the Holocene. Biogeosciences 12, 579–593.

Bour, A.L., Walker, B.D., Broek, T.A., McCarthy, M.D., 2016. Radiocarbon Analysis of Individual Amino Acids: Carbon Blank Quantification for a Small-Sample High-Pressure Liquid Chromatography Purification Method. Anal. Chem. 88, 3521-3528.

Brabets, T.P., Wang, B., Meade, R.H., 2000. Environmental and hydrological overview of the Yukon River Basin, Alaska and Canada: US Geological Survey: Anchorage, v. Water-Resources Investigations Report, series number 99-4204.

Brodowski, S., John, B., Flessa, H., Amelung, W., 2006. Aggregate-occluded black carbon in soil. Eur. J. Soil Sci. 57, 539–546.

Bröder, L., Tesi, T., Andersson, A., Semiletov, I., Gustafsson, Ö., 2018. Bounding cross-shelf transport time and degradation in Siberian-Arctic land-ocean carbon transfer. Nat. Commun. 9, 806.

Brown, J., Ferrians Jr., O.J., Heginbottom, J. A., Melnikov, E.S., 2002. Circum-Arctic Map of Permafrost and Ground Ice Conditions, National Snow and Ice Data Center/World Data Center for Glaciology, Boulder, CO, USA, Digital media.

Canuel, E.A. and Martens, C.S., 1993. Seasonal variations in the sources and alteration of organic matter associated with recently-deposited sediments. Org. Geochem. 20, 563–577.

Cao, M., Hefter, J., Tiedemann, R., Lembke-Jene, L., Meyer, V.D., Mollenhauer, G., 2023. Deglacial records of terrigenous organic matter accumulation off the Yukon and Amur rivers based on lignin phenols and long-chain *n*-alkanes. Clim. Past 19, 159–178.

Carrie, R.H., Mitchell, L., Black, K.D., 1998. Fatty acids in surface sediment at the Hebridean shelf edge, west of Scotland. Org. Geochem. 29, 1583–1593.

Caissie, B.E., Brigham-Grette, J., Lawrence, K.T., Herbert, T.D., Cook, M.S., 2010. Last Glacial Maximum to Holocene sea surface conditions at Umnak Plateau, Bering Sea, as inferred from diatom, alkenone, and stable isotope records. Paleoceanography 25, PA1206.

Church, J.A. and White, N.J., 2011. Sea-Level Rise from the Late 19th to the Early 21st Century. Surv. Geophys. 32, 585–602.

Clark, P.U., Shakun, J.D., Baker, P.A., Bartlein, P.J., Brewer, S., Brook, E., Carlson, A.E., Cheng, H., Kaufman, D.S., Liu, Z., Marchitto, T.M., Mix, A.C., Morrill, C., OttoBliesner, B.L., Pahnke, K., Russell, J.M., Whitlock, C., Adkins, J.F., Blois, J.L., Clark, J., Colman, S.M., Curry, W.B., Flower, B.P., He, F., Johnson, T.C., Lynch-Stieglitz, J., Markgraf, V., McManus, J., Mitrovica, J.X., Moreno, P.I., Williams, J.W., 2012. Global climate evolution during the last deglaciation. P. Natl. Acad. Sci. USA 109, e1134–e1142.

Corr, L.T., Berstan, R., Evershed, R.P., 2007. Optimisation of derivatisation procedures for the determination of $\delta^{13}C$ values of amino acids by gas chromatography/combustion/isotope ratio mass spectrometry. Rapid Commun. Mass Spectrom. 21, 3759–3771.

Costard, F., Gautier, E., Brunstein, D., Hammadi, J., Fedorov, A.M., Yang, D., Dupeyrat, L., 2007. Impact of the global warming on the fluvial thermal erosion over the Lena River in Central Siberia. Geophys. Res. Lett. 34.

Costard, F., Dupeyrat, L., Séjourné, A., Bouchard, F., Fedorov, A., Saint-Bézar, B., 2020. Retrogressive Thaw Slumps on Ice-Rich Permafrost Under Degradation: Results From a Large-Scale Laboratory Simulation. Geophys. Res. Lett. 48.

Couture, N.J., Irragang, A., Pollard, W., Lantuit, H., Fritzs, M., 2018. Coastal erosion of permafrost soils along the Yukon Coastal Plain and fluxes of organic carbon to the Canadian Beaufort Sea. J. Geophys. Res.-Biogeo. 123, 406–422.

Cowie, B.R., Greenberg, B.M., Slater, G.F., 2010. Determination of microbial carbon sources and cycling during remediation of petroleum hydrocarbon impacted soil using natural abundance ^{14}C analysis of PLFA. Environ. Sci. Technol. 44, 2322–2327.

Cranwell, P.A., Eglinton, G., Robinson, N., 1987. Lipids of aquatic orgnismasms portential contribution to lacustrine sediment-II. Org. Geochem. 11, 513–527.

Cranwell, P.A., 2010. Chain length distribution of *n*-alkanes from lakes sediments in relation to post-glacial environmental change. Freshwater Biol. 3, 259–265.

David, F., Marchand, C., Thiney, N., Nhu-Trang, T.-T., Meziane, T., 2019. Short-term changes in the quality of suspended particulate matter in a human impacted and mangrove dominated tropical estuary (Can Gio, Vietnam). Cont. Shelf Res. 178, 59–67.

Dittmar, T. and Stubbins, A., 2014. Dissolved Organic Matter in Aquatic Systems, in: Treatise on Geochemistry (Second Edition), edited by: Holland, H.D. and Turekian, K.K., Elsevier, Oxford, 125–156.

Dosseto, A., Bourdon, B., Turner, S.P., 2008. Uranium-series isotopes in river materials: insights into the timescales of erosion and sediment transport. Earth Planet. Sci. Lett. 265, 1–17.

Drever, J.I., 1997. The Geochemistry of Natural Waters: Surface and Groundwater Environments. Publisher Upper Saddle River, N.J.: Prentice Hall, 311–322.

Dullo, W.C., Biebow, N., Georgeleit, K., 2004. SO178-KOMEX Cruise Report: Mass Exchange Processes and Balances in the Okhotsk Sea, GEOMAR Report, GEOMAR, Germany, 110 pp.

Dunn, R.J.K., Welsh, D.T., Teasdale, P.R., Lee, S.Y., Lemckert, C.J., Meziane, T., 2008. Investigating the distribution and sources of organic matter in surface sediment of Coombabah Lake (Australia) using elemental, isotopic and fatty acid biomarkers. Cont. Shelf Res. 28, 2535–2549.

Dyke, A.S., 2004. An Outline of North American Deglaciation with Emphasis on central and Northern Canada. Quat. glaciations: extent chronology 2, 373–424.

Eglinton, G. and Hamilton, R.J., 1967. Leaf epicuticular waxes. Science 156, 1322–35.

Eglinton, T.I., Aluwihare, L.I., Bauer, J.E., Druffel, E.R.M., McNichol, A.P., 1996. Gas chromatographic isolation of individual compounds from complex matrices for radiocarbon dating. Anal. Chem. 68, 904–912.

Eglinton, T.I. and Eglinton, G., 2008. Molecular proxies for paleoclimatology. Earth Planet. Sci. Lett. 275, 1–16.

Eglinton, T.I., Galy, V.V., Hemingway, J.D., Feng, X., Bao, H., Blattmann, T.M., Dickens, A.F., Gies, H., Giosan, L., Haghipour, N., Hou, P., Lupker, M., McIntyre, C.P., Montluçon, D.B., Peucker-Ehrenbrink, B., Ponton, C., Schefuß, E., Schwab, M.S., Voss, B.M., Wacker, L., Wu, Y., Zhao, M., 2021. Climate control on terrestrial biospheric carbon turnover. P. Natl. Acad. Sci. USA 118, e2011585118.

Erdtman, H., 1971. Lignins: Occurrence, Formation, Structure and Reactions, p. 228–230. In K. V. Sarkanen and C. H. Ludwig (eds), Journal of Polymer Science Part B: Polymer Letters. John Wiley & Sons, Inc., New York.

Erickson, M. and Miksche, G.E., 1974. On the occurrence of lignin or polyphenols in some mosses and liverworts. Phytochemistry 13, 2295–2299.

Froese, D.G., Westgate, J.A., Reyes, A.V., Enkin, R.J., Preece, S.J., 2008. Ancient permafrost and a future, warmer Arctic. Science 321, 1648.

Ertel, J.R. and Hedges, J.I., 1985. Sources of sedimentary humic substances: vascular plant debris. Geochim. Cosmochim. Acta 49, 2097–2107.

FAO and ITPS. 2021. Recarbonizing global soils—A technical manual of recommended management practices. Volume 2: Hot spots and bright spots of soil organic carbon. Rome, FAO, 128–143.

Feng, X., Vonk, J.E., van Dongend, B.E., Gustafsson, Ö., Semiletov, I.P., Dudarev, O.V., Wang, Z., Montlucon, D.B., Wacker, L., Eglinton, T.I., 2013a. Differential mobilization of terrestrial carbon pools in Eurasian Arctic river basins. P. Natl. Acad. Sci. USA 110, 14168–14173.

Feng, X., Benitez-Nelson, B.C., Montluçon, D.B., Prahl, F.G., McNichol, A.P., Xu, L., Repeta, D.J., Eglinton, T.I., 2013b. ^{14}C and ^{13}C characteristics of higher plant biomarkers in Washington margin surface sediments. Geochim. Cosmochim. Acta 105, 14–30.

Feng, X., Gustafsson, Ö., Holmes, R.M., Vonk, J.E., van Dongend, B.E., Semiletov, I.P., Dudarev, O.V., Yunker, M.B., Macdonald, R.W., Montlucon, D.B., Eglinton, T.I., 2015a. Multi-molecular tracers of terrestrial carbon transfer across the pan-Arctic: comparison of hydrolyzable components with plant wax lipids and lignin phenols. Biogeosciences 12, 4841–4860.

Feng, X., Gustafsson, Ö., Holmes, R.M., Vonk, J.E., Van Dongen, B., Semiletov, I.P., Dudarev, O.V., Yunker, M.B., Macdonald, R.W., Wacker, L., Montluçon, D.B., Eglinton, T.I., 2015b. Multimolecular tracers of terrestrial carbon transfer across the pan-Arctic: ^{14}C characteristics of sedimentary carbon components and their environmental controls. Global Biogeochem. Cycles 29, 1855–1873.

Feng, X., Vonk, J.E., Griffin, C., Zimov, N., Montlucon, D.M., Wacker, L., Eglinton, T.I., 2017. ^{14}C variation of dissolved lignin in Arctic river systems. ACS Earth Space Chem. 1, 334–344.

Feng, D., Gleason, C.J., Lin, P., Yang, X., Pan, M., Ishitsuka, Y., 2021. Recent changes to Arctic river discharge. Nat. Commun. 12, 6917.

Ficken, K.J., Li, B., Swain, D.L., Eglinton, G., 2000. An *n*-alkane proxy for the sedimentary input of submerged/floating freshwater aquatic macrophytes. Org. Geochem. 31, 745–749.

Finney, B.P., Rühland, K., Smol, J.P., Fallu, M.-A., 2004. Paleolimnology of the North American subarctic, in: Long Term Environmental Change in Arctic and Antarctic Lakes, edited by: Pienitz, M.S.V. and Smol, J.P., Springer, Dordrecht, 269–317.

Fontugne, M.R. and Jouanneau, J.M., 1987. Modulation of the particulate organic carbon flux to the ocean by a macrotidal estuary: Evidence from measurements of carbon isotopes in organic matter from the Gironde system. Estuarine, Coastal Shelf Sci. 24, 377–387.

Forster, P., Ramaswamy, V., Artaxo, P., Berntsen, T., Betts, R., Fahey, D.W., Haywood, J., Lean, J., Lowe, D.C., Myhre, G., Nganga, J., Prinn, R., Raga, G., Schulz, M., van Dorland, R., 2007. Changes in Atmospheric Constituents and in Radiative Forcing. In: Climate Change 2007: The Physical Science Basis. Contribution of Working Group I to the Fourth Assessment Report of the Intergovernmental Panel on Climate Change, edited by: Solomon, S., Qin, D., Manning, M., Chen, Z., Marquis, M., Averyt, K.B., Tignor, M., Miller, H.L., Cambridge University Press, Cambridge, United Kingdom and New York, NY, USA.

Frederikse, T., Landerer, F., Caron, L., Adhikari, S., Parkes, D., Humphrey, V.W., Dangendorf, S., Hogarth, P., Zanna, L., Cheng, L., Wu, Y.-H., 2020. The causes of sea-level rise since 1900. Nature 584, 393–397.

French, K.L., Hein, C.J., Haghipour, N., Wacker, L., Kudrass, H. R., Eglinton, T. I., Galy, V., 2018. Millennial soil retention of terrestrial organic matter deposited in the Bengal Fan. Sci. Rep 8, 11997.

Friedlingstein, P., O'Sullivan, M., Jones, M.W., Andrew, R.M., Hauck, J., Olsen, A., Peters, G.P., Peters, W., Pongratz, J., Sitch, S., Le Quéré, C., Canadell, J.G., Ciais, P., Jackson, R.B., Alin, S., Aragão, L.E.O.C., Arneth, A., Arora, V., Bates, N.R.,Becker, M., Benoit-Cattin, A., Bittig, H.C., Bopp, L., Bultan, S., Chandra, N., Chevallier, F., Chini, L.P.,

Evans, W., Florentie, L., Forster, P.M., Gasser, T., Gehlen, M., Gilfifillan, D., Gkritzalis, T., Gregor, L., Gruber, N., Harris, I., Hartung, K., Haverd, V., Houghton, R.A., Ilyina, T., Jain, A.K., Joetzjer, E., Kadono, K., Kato, E., Kitidis, V., Korsbakken, J.I., Landschützer, P., Lefèvre, N., Lenton, A., Lienert, S., Liu, Z., Lombardozzi, D., Marland, G., Metzl, N., Munro, D.R., Nabel, J.E.M.S., Nakaoka, S.-I., Niwa, Y., O'Brien, K., Ono, T., Palmer, P. I., Pierrot, D., Poulter, B., Resplandy, L., Robertson, E., Rödenbeck, C., Schwinger, J., Séférian, R., Skjelvan, I., Smith, A.J.P., Sutton, A.J., Tanhua, T., Tans, P.P., Tian, H., Tilbrook, B., van der Werf, G., Vuichard, N., Walker, A.P., Wanninkhof, R., Watson, A.J., Willis, D., Wiltshire, A.J., Yuan, W., Yue, X., Zaehle, S., 2020. Global Carbon Budget 2020. Earth Syst. Sci. Data 12, 3269– 3340.

Fritz, M., Herzschuh, U., Wetterich, S., Lantuit, H., De Pascale, G.P., Pollard, W.H., Schirrmeister, L., 2012. Late glacial and Holocene sedimentation, vegetation, and climate history from easternmost Beringia (northern Yukon Territory, Canada). Quat. Res. 78, 549–560.

Fritz, M., Vonk, J., Lantuit, H., 2017. Collapsing Arctic coastlines. Nature Clim. Change 7, 6–7.

Ge, R., Yang, D., Kane, D.L., 2013. Yukon River Basin long-term (1977–2006) hydrologic and climatic analysis. Hydrol. Process. 27, 2475–2484.

Gersonde, R., 2012. The expedition of the research vessel "Sonne" to the subpolar North Pacific and the Bering Sea in 2009 (SO202-INOPEX), Berichte zur Polar- und Meeresforschung/Reports on polar and marine research, Alfred Wegener Institute for Polar and Marine Research, Bremerhaven, 323 pp.

Glaser, B., 2005. Compound-specific stable-isotope ($\delta^{13}C$) analysis in soil science. J. Plant Nutr. Soil Sci. 168, 633–648.

Godwin, H., 1962. Half-life of radiocarbon. Nature 195, 984.

Goñi, M.A., Nelson, B., Blanchette, R.A., Hedges, J.I., 1993. Fungal degradation of wood lignins: geochemical perspectives from CuO-derived phenolic dimers and monomers. Geochim. Cosmochim. Ac. 57, 3985–4002.

Goñi, M. A. and Hedges, J.I., 1995. Sources and reactivities of marinederived organic matter in coastal sediments as determined by alkaline CuO oxidation, Geochim. Cosmochim. Ac. 59, 2965–2981.

Goñi, M.A. and Montgomery, S., 2000. Alkaline CuO Oxidation with a Microwave Digestion System: Lignin Analyses of Geochemical Samples. Anal. Chem. 72, 3116–3121.

Goñi, M.A., Yunker, M.B., Macdonald, R. W., Eglinton, T.I., 2000. Distribution and sources of organic biomarkers in arctic sediments from the Mackenzie River and Beaufort Shelf. Mar. Chem. 71, 23–51.

Goñi, M., Teixeira, M., Perkey, D., 2003. Sources and distribution of organic matter in a river-dominated estuary (Winyah Bay, SC, USA). Estuar. Coast. Shelf S. 57, 1023–1048.

Grant, K.E., Galy, V.V., Haghipour, N., Eglinton, T.I., Derry, L.A., 2022. Persistence of old soil carbon under changing climate: the role of mineral-organic matter interactions. Chem. Geol. 587, 120629.

Grosse, G., Harden, J., Turetsky, M., McGuire, A.D., Camill, P., Tarnocai, C., Frolking, S., Schuur, E.A.G., Jorgenson, T., Marchenko, S., Romanovsky, V., Wickland, K.P., French, N., Waldrop, M., Bourgeau-Chavez, L., Striegl, R.G., 2011. Vulnerability of high-latitude soil organic carbon in North America to disturbance. J. Geophys. Res. 116, G00K06.

Gruber, S., and Haeberli, W., 2007. Permafrost in steep bedrock slopes and its temperature-related destabilization following climate change. Journal of Geophysical Research: Earth Surface 112, no. F2.

Guo, L., Ping, C.L., Macdonald, R.W., 2007. Mobilization pathways of organic carbon from permafrost to Arctic rivers in a changing climate. Geophys. Res. Lett. 34, L13603.

Gustafsson, Ö., van Dongen, B.E., Vonk, J.E., Dudarev, O.V., Semiletov, I.P., 2011. Widespread release of old carbon across the Siberian Arctic echoed by its large rivers. Biogeosciences 8, 1737–1743.

Haghipour, N., Ausin, B., Usman, M.O., Ishikawa, N., Wacker, L., Welte, C., Ueda, K., Eglinton, T.I., 2019. Compound-Specific Radiocarbon Analysis by Elemental Analyzer–Accelerator Mass Spectrometry: Precision and Limitations. Anal. Chem. 91, 2042–2049.

Hartnett, H., Keil, R., Hedges, J., Devol, A., 1998. Influence of oxygen exposure time on organic carbon preservation in continental margin sediments. Nature 391, 572–575.

Harvey, H.R., 1994. Fatty acids and sterols as source markers of organic matter in sediments of the North Carolina continental slope. Deep Sea Res., Part II 41, 783–796.

Heaton, T.J., Köhler, P., Butzin, M., Bard, E., Reimer, R.W., Austin, W.E.N., Ramsey, C.B., Grootes, P.M., Hughen, K.A., Kromer, B., Reimer, P.J., Adkins, J., Burke, A., Cook, M.S., Olsen, J., Skinner, L.C., 2020. Marine20—The Marine Radiocarbon Age Calibration Curve (0−55,000 cal BP). Radiocarbon 62, 779–820.

Hedges, J.I. and Parker, P.L., 1976. Land-derived organic matter in surface sediments from the Gulf of Mexico. Geochim. Cosmochim. Acta 40, 1019–1029.

Hedges, J.I. and Mann, D.C., 1979. The characterization of plant tissues by their lignin oxidation products. Geochim. Cosmochim. Acta 43, 1803–1807.

Hedges, J.I., Blanchette, R.A., Weliky, K., Devol, A.H., 1988. Effects of fungal degradation on the CuO oxidation products of lignin: A controlled laboratory study. Geochim. Cosmochim. Acta 52, 2717–2726.

Hedges, J.I. and Weliky, K., 1989. The diagenesis of conifer needles in a coastal marine environment. Geochim. Cosmochim. Acta 53, 2659–2673.

Hedges, J.I., 1992. Global biogeochemical cycles: Progress and problems. Mar. Chem. 39, 67–93.

Herndl, G.J., Reinthaler, T., Teira, E., van Aken, H., Veth, C., Pernthaler, A., Pernthaler, J., 2005. Contribution of Archaea to total prokaryotic production in the deep Atlantic Ocean. Appl. Environ. Microbiol. 71, 2303–2309.

Hilton, R.G., Galy, A., Hovius, N., Chen, M., Horng, M.J., Chen, H., 2008. Tropical-cyclone-driven erosion of the terrestrial biosphere from mountains. Nature Geoscience 1, 759–762.

Hilton, R.G., Galy, A., Hovius, N., Horng, M. J., Chen, H., 2011. Efcient transport of fossil organic carbon to the ocean by steep mountain rivers: an organic carbon sequestration mechanism. Geology 39, 71–74.

Hilton, R.G., Galy, V., Gaillardet, J., Dellinger, M., Bryant, C., O'Regan, M., Gröcke, D.R., Coxall, H., Bouchez, J., Calmels, D., 2015. Erosion of organic carbon in the Arctic as a geological carbon dioxide sink. Nature 524, 84–87.

Hilton, R.G., 2017. Climate regulates the erosional carbon export from the terrestrial biosphere. Geomorphology 277, 118-132.

Hinkel, K.M. and Nelson, F.E., 2003. Spatial and temporal patterns of active layer thickness at Circumpolar Active Layer Monitoring (CALM) sites in northern Alaska, 1995–2000. J. Geophys. Res. Atmos. 108, 8168.

Hobson, K., Ambrose Jr, W., Renaud, P., 1995. Sources of primary production, benthic-pelagiccoupling, and trophic relationships within the Northeast Water Polynya: Insights from delta super (13) C and delta super (15) N analysis. Marine ecology progress series. Oldendorf 128, 1–10.

Holmes, R.M., McClelland, J.W., Peterson, B.J., Shiklomanov, A.I., Zhulidov, A.V., Gordeev, V.V., Bobrovitskaya, N., 2002. A circumpolar perspective on fluvial sediment flux to the Arctic Ocean. Global Biogeochem. Cycles 16, 45-1–45-14.

Holmes, R.M., McClelland, J.W., Peterson, B.J., Tank, S.E., Bulygina, E., Eglinton, T.I., Gordeev, V.V., Gurtovaya, T.Y., Raymond, P.A., Repeta, D.J., Staples, R., Striegl, R.G., Zhulidov, A.V., Zimov, S.A., 2012. Seasonal and annual fluxes of nutrients and organic matter from large rivers to the Arctic Ocean and surrounding seas. Estuaries Coasts 35, 369–382.

Holmes, R.M., Shiklomanov, A.I., Suslova, A., Tretiakov, M., McClelland, J.W., Scott, L., Spencer, R.G.M., Tank, S.E., 2021. River Discharge, NOAA Technical Report OAR ARC, 21–11.

Hopmans, E.C., Weijers, J.W.H., Schefuß, E., Herfort, L., Sinninghe Damsté, J.S., Schouten, S., 2004. A novel proxy for terrestrial organic matter in sediments based on branched and isoprenoid tetraether lipids. Earth Planet. Sci. Lett. 224, 107–116.

Hou, J., Huang, Y., Brodsky, C., Alexandre, M.R., McNichol, A.P., King, J.W., Hu, F.S., Shen, J., 2010. Radiocarbon dating of individual lignin phenols: A new approach for establishing chronology of late quaternary lake sediments. Anal. Chem. 82, 7119–7126.

Houel, S., Louchouarn, P., Lucotte, M., Canuel, R., Ghaleb, B., 2006. Translocation of soil organic matter following reservoir impoundment in boreal systems: implications for in situ productivity. Limnol. Oceanogr. 51, 1497–1513.

Hu, F.S., Hedges, J.I., Gordon, E.S., Brubaker, L.B., 1999. Lignin biomarkers and pollen in postglacial sediments of an Alaskan lake, Geochim. Cosmochim. Ac. 63, 1421–1430.

Hudson, C.E. and Thompson, J.R., 2019. Hydrological modelling of climate change impacts on river flows in Siberia's Lena River Basin and implications for the Atlantic Meridional Overturning Circulation. Hydrol. Res. 50, 1577–1595.

Hugelius, G., Strauss, J., Zubrzycki, S., Harden, J., Schuur, E.A.G., Ping, C.-L., Schirrmeister, L., Grosse, G., Michaelson, G., Koven, C., O'Donnell, J., Elberling, B., Mishra, U., Camill, P., Yu, Z., Palmtag, J., Kuhry, P., 2014. Estimated stocks of circumpolar permafrost carbon with quantified uncertainty ranges and identified data gaps. Biogeosciences 11, 6573–6593.

Hussain, S.Z. and Maqbool, K., 2014. GC-MS: Principle, Technique and its application in Food Science.

Hutchings, J.A., Bianchi, T.S., Kaufman, D.S., Kholodov, A.L., Vaughn, D.R., Schuur, E.A.G., 2019. Millennial-scale carbon accumulation and molecular transformation in a permafrost core from Interior Alaska. Geochim. Cosmochim. Acta 253, 231–248.

Hwang, J. and Druffel., E.R.,2005. Blank Correction for $\Delta^{14}C$ Measurements in Organic Compound Classes of Oceanic Particulate Matter. Radiocarbon 47, 75–87.

Igarashi, Y. and Zharov, A. E., 2011. Climate and vegetation change during the late Pleistocene and early Holocene in Sakhalin and Hokkaido, northeast Asia. Quatern. Int. 237, 24–31.

Ingalls, A.E. , Ellis, E.E., Santos, G.M., McDuffee, K.E., Truxal, L., Keil, R.G., Druffel, E.R.M., 2010. HPLC Purification of Higher Plant-Dervied Lignin Phenols for Compound Specific Radiocarbon Analysis. Anal. Chem. 82, 8931–8938.

Inglis, G.N., Bhattacharya, T., Hemingway, JD., Hollingsworth, E.H., Feakins, S.J., Tierney, J.E., 2022. Biomarker Approaches for Reconstructing Terrestrial Environmental Change. Annu. Rev. Earth Planet. Sci. 50, 369–94.

Ingri, J., Widerlund, A., Land, M., 2005. Geochemistry of major elements in a pristine boreal river system; hydrological compartments and flow paths. Aquat. Geochem. 11, 57–88.

IPCC in Climate Change 2022: Impacts, Adaptation and Vulnerability-Summary for Policymakers. Working Group II contribution to the Sixth Assessment Report of the Intergovernmental Panel on Climate Change (IPCC), edited by: Pörtner, H.-O., Roberts, D.C., Tignor, M., Poloczanska, E.S., Mintenbeck, K., Alegría, A., Craig, M., Langsdorf, S., Löschke, S., Möller, V., Okem, A., Rama, B., Cambridge University Press. Cambridge University Press, Cambridge, UK and New York, NY, USA, 3056 pp.

Irrgang, A.M., Bendixen, M., Farquharson, L.M., Baranskaya, A.V., Erikson, L.H., Gibbs, A.E., Ogorodov, S.A., Overduin, P.P., Lantuit, H., Grigoriev, M.N., Jones, B.M., 2022. Drivers, dynamics and impacts of changing Arctic coasts. Nat. Rev. Earth Environ. 3, 39–54.

Jackson, R.B., Lajtha, K., Crow, S.E., Hugelius, G., Kramer, M.G., Piñeiro, G., 2017. The Ecology of Soil Carbon: Pools, Vulnerabilities, and Biotic and Abiotic Controls. Annual Review of Ecology, Evolution, and Systematics 48, 419–445.

Jakobsson, M., Pearce, C., Cronin, T.M., Backman, J., Anderson, L.G., Barrientos, N., Björk, G., Coxall, H., de Boer, A., Mayer, L. A., Mörth, C.-M., Nilsson, J., Rattray, J.E., Stranne, C., Semiletov, I., O'Regan, M., 2017. Post-glacial flooding of the Bering Land Bridge dated to 11 cal ka BP based on new geophysical and sediment records. Clim. Past 13, 991–1005.

Jeng, W.-L., 2006. Higher plant *n*-alkane average chain length as an indicator of petrogenic hydrocarbon contamination in marine sediments. Mar. Chem.102, 242–251.
Jia, J., Liu, Z., Haghipour, N., Wacker, L., Zhang, H., Sierra, C.A., Ma, T., Wang, Y., Chen, L., Luo, A., Wang, Z., He, J.-S., Zhao, M., Eglinton, T.I., Feng, X., 2023. Molecular ^{14}C evidence for contrasting turnover and temperature sensitivity of soil organic matter components. Ecol. Lett. 26, 778–788.
Jones, M.C., Berkelhammer, M., Keller, K.J., Yoshimura, K., and Wooller, M.J., 2020a. High sensitivity of Bering Sea winter sea ice to winter insolation and carbon dioxide over the last 5500 years. Sci. Adv. 6, eaaz9588.
Jones, B.M., Irrgang, A.M., Farquharson, L.M., Lantuit, H., Whalen, D., Ogorodov, S., Grigoriev, M., Tweedie., C., Gibbs, A.E., Strzelecki, M.C., Baranskaya, A., Belova, N., Sinitsyn, A., Kroon, A., Maslakov, A., Vieira, G., Grosse, G., Overduin, P., Nitze, I., Maio, C., Overbeck, J., Bendixen, M., Zagórski, P., Romanovsky, V.E., 2020b. Arctic Report Card 2020: coastal permafrost erosion.
Jorgenson, M.T., Shur, Y.L., Pullman, E.R., 2006. Abrupt increase in permafrost degradation in Arctic Alaska. Geophys. Res. Lett. 33, L02503.
Karlsson, E.S., Brüchert, V., Tesi, T., Charkin, A., Dudarev, O., Semiletov, I., Gustafsson, O., 2015. Contrasting regimes for organic matter degradation in the East Siberian Sea and the Laptev Sea assessed through microbial incubations and molecular markers. Mar. Chem. 170, 11–22.
Karner, M., DeLong, E.F., Karl, D.M., 2001. Archaeal dominance in the mesopelagic zone of the Pacific Ocean. Nature 409, 507–510.
Kaufman, D.S., Axford, Y.L., Henderson, A.C.G., Mckay, N.P., Oswald, W.W., Saenger, C., Anderson, R.S., Bailey, H.L., Clegg, B., Gajewshi, K., Hu, F.S., Jones, M.C., Massa, C., Routson, C.C., Werner, A., Wooller, M.J., Yu, Z., 2015. Holocene climate changes in eastern Beringia (NW North America)—A systematic review of multi-proxy evidence. Quat. Sci. Rev. 147, 312–339.
Kattein, L., 2018. Tracing permafrost input into the Laptev Sea by compound specific analyses of *n*-alkanoic acids. Bachelor Thesis. Department of Geosciences University of Bremen.
Kattsov, V.M., and Walsh, J.E., 2000. Twentieth-Century Trends of Arctic Precipitation from Observational Data and a Climate Model Simulation. J. Clim. 13, 1362–1370.
Kennedy, K.E., Froese, D.G., Zazula, G.D., Lauriol, B., 2010. Last glacial maximum age for the northwest Laurentide maximum from the eagle river spillway and delta complex, northern Yukon. Quat. Sci. Rev. 29, 1288–300.
Keskitalo, K., Tesi, T., Bröder, L., Andersson, A., Pearce, C., Sköld, M., Semiletov, I. P., Dudarev, O.V., Gustafsson, Ö., 2017. Sources and characteristics of terrestrial carbon in Holocene-scale sediments of the East Siberian Sea. Clim. Past 13, 1213–1226.
Killops, S. and Killops, V., 2005. Production, Preservation and Degradation of Organic Matter, in: Introduction to Organic Geochemistry (Second Edition), John Wiley & Sons, 71–116.
Kim, J.-H., van der Meer, J., Schouten, S., Helmke, P., Willmott, V., Sangiorgi, F., Koç, N., Hopmans, E.C., and Sinninghé Damsté, J.S., 2010. New indices and calibrations derived from the distribution of crenarchaeal isoprenoid tetraether lipids: Implications for past sea surface temperature reconstructions. Geochim. Cosmochim. Ac. 74, 4639–4654.
Kimura, N. and Wakatsuchi, M., 2000. Relationship between sea-ice motion and geostrophic wind in the Northern Hemisphere. Geophys. Res. Lett. 27, 2738–3735.
Kokelj, S.V., and Jorgenson, M.T., 2013. Advances in thermokarst research. Permafrost and Periglacial Processes 24, 108–119.
Kögel-Knabner, I., Guggenberger, G., Kleber, M., Kandeler, E., Kalbitz, K., Scheu, S. Eusterhues, K., Leinweber, P., 2008. Organo-mineral associations in temperate soils: integrating biology, mineralogy, and organic matter chemistry. J. Plant Nutr. Soil Sci. 171, 61–82.
Kühn, H., Lembke-Jene, L., Gersonde, R., Esper, O., Lamy, F., Arz, H., Kuhn, G., Tiedemann, R., 2014. Laminated sediments in the Bering Sea reveal atmospheric

teleconnections to Greenland climate on millennial to decadal timescales during the last deglaciation. Clim. Past 10, 2215–2236.
Kühn, H., 2015. The deglacial development of the Oxygen Minimum Zone in the Bering Sea: A study based on high-resolution laminated sediment records. PhD thesis, Universität Bremen, Fachbereich 5, Geowissenschaften.
Kupilik, M., Ulmgren, M., Brunswick, D., 2020. Bayesian parameter estimation for Arctic coastal erosion under the effects of climate change. IEEE J. Sel. Top. Appl. Earth Obs. Remote Sens. 13, 3595–3604.
Kurek, J., Cwynar, L.C., Ager, T.A., Abbott, M.B., Edwards, M.E., 2009. Late Quaternary paleoclimate of western Alaska inferred from fossil chironomids and its relation to vegetation histories. Quat. Sci. Rev. 28, 799–811.
Kusch, S., 2010. Tracing time in the ocean: Unraveling depositional and preservational timescales using compound-specific radiocarbon analysis of biomarkers from marine sediments. PhD thesis, Universität Bremen, Fachbereich 5, Geowissenschaften.

Kuzmin, Y.V., Burr, G.S., Gorbunov, S.V., Rakov, V.A., Razjigaeva, N.G., 2007. A tale of two seas: reservoir age correction values (R, Delta R) for the Sakhalin Island (Sea of Japan and Okhotsk Sea). Nucl. Instrum. Methods Phys. Res. Sect. B Beam Interact. Mater. Atom 259, 460–462.
Lambeck, K., Rouby, H., Purcell, A., Sun, Y., Sambridge, M., 2014. Sea level and global ice volumes from the Last Glacial Maximum to the Holocene. P. Natl. Acad. Sci. USA 11, 15296–15303.
Lantuit, H., Overduin, P.P., Couture, N., Wetterich, S., Aré, F., Atkinson, D., Brown, J., Cherkashov, G., Drozdov, D., Forbes, D.L., Graves-Gaylord, A., Grigoriev, M., Hubberten, H.-W., Jordan, J., Jorgenson, T., Ødegård, R.S., Ogorodov, S., Pollard, W.H., Rachold, V., Sedenko, S., Solomon, S., Steenhuisen, F., Streletskaya, I., Vasiliev, A., 2012. The Arctic Coastal Dynamics Database: A New Classification Scheme and Statistics on Arctic Permafrost Coastlines. Estuar. Coasts 35, 383–400.
Lattaud, J., Lo,L., Zeeden, C., Liu, Y.-J., Song, S.-R., van der Meer, M.T.J., Damsté, J.S.S., Schouten, S., 2019. A multiproxy study of past environmental changes in the Sea of Okhotsk during the last 1.5 Ma. Org. Geochem. 132, 50–61.
Lawrence, D. M., Slater, A. G., Tomas, R. A., Holland, M. M., Deser, C., 2008. Accelerated Arctic land warming and permafrost degradation during rapid sea ice loss. Geophys. Res. Lett. 35, L11506.
Lawrence, D.M., Koven, C.D., Swenson, S.C., Riley, W.J., Slater, A.G., 2015. Permafrost thaw and resulting soil moisture changes regulate projected high-latitude CO2 and CH4 emissions. Environ. Res. Lett. 10, 094011.
Lembke-Jene, L., Tiedemann, R., Nürnberg, D., Kokfelt, U., Kozdon, R., Max, L., Röhl, U., Gorbarenko, S.A., 2017. Deglacial variability in Okhotsk Sea Intermediate Water ventilation and biogeochemistry: Implications for North Pacific nutrient supply and productivity. Quat. Sci. Rev. 160, 116–137.
Lenton, T. M., Rockström, J., Gaffney, O., Rahmstorf, S., Richardson, K., Steffen, W., Schellnhuber, H.J., 2019. Climate tipping points—too risky to bet against. Nature 575, 592–595.
Lim, M., Whalen, D., Martin, J., Mann, P.J., Hayes, S., Fraser, P., Berry, H.B., Ouellette, D., 2020. Massive ice control on permafrost coast erosion and sensitivity. Geophys. Res. Lett. 47, e2020GL087917.
Lindgren, A., Hugelius, G., Kuhry, P., Christensen, T.R., Vandenberghe, J., 2016. GIS-based Maps and Area Estimates of Northern Hemisphere Permafrost Extent during the Last Glacial Maximum. Permafr. Periglac. Process. 27, 6–16.
Liu Z., Otto-Bliesner, B.L., He, F., Brady, E.C., Tomas, R., Clark, P.U., Carlson, A.E., Lynch-Stieglitz, J., Curry, W., Brook, E., Erickson, D., Jacob, R., Kutzbach, J., Cheng, J., 2009. Transient simulation of last deglaciation with a new mechanism for Bølling-Allerød warming. Science 325, 310–314.

Liu, B., Yang, D., 2011. Siberian Lena River heat flow regime and change. Cold Region Hydrology in a Changing Climate 346, 71–76.
Liu, J., Curry, J.A., Wang, H., Song, M., and Horton, R.M., 2012. Impact of declining Arctic sea ice on winter snowfall. P. Natl Acad. Sci. USA 109, 4074–4079.
Lo, L., Belt, S.T., Lattaud, J., Friedrich, T., Zeeden, C., Schouten, S., Smik, L., Timmermann, A., Cabedo-Sanz, P., Huang, J.-J., Zhou, L., Ou, T.-H., Chang, Y.-P., Wang, L.-C., Chou, Y.-M., Shen, C.-C., Chen, M.-T., Wei, K.-Y., Song, S.-R., Fang, T.-H., Gorbarenko, S. A., Wang, W.-L., Lee, T.-Q., Elderfield, H., Hodell, D. A., 2018. Precession and atmospheric CO_2 modulated variability of sea ice in the central Okhotsk Sea since 130,000 years ago. Earth Planet. Sc. Lett. 488, 36–45.
Lobbes, J., Fitznar, H. P., Kattner, G., 2000. Biogeochemical characteristics of dissolved and particulate organic matter in Russian rivers entering the Arctic Ocean. Geochim. Cosmochim. Ac. 64, 2973–2983.
Ma, X., Yasunari, T., Ohata, T., Fukushima, Y., 2005. The influence of river ice on spring runoff in the Lena river, Siberia. Annals of Glaciology 40, 123–127.
MacDonald, G.M. and Cwynar, L.C., 1985. A fossil pollen based reconstruction of the late quaternary history of lodgepole pine (*Pinus contorta ssp. latifolia*) in the western interior of Canada. Can. J. For. Res. 15, 1039–1044.
Mackelprang, R., Burkert, A., Haw, M., Mahendrarajah, T., Conaway, C.H., Douglas, T.A., Waldrop, M.P., 2017. Microbial survival strategies in ancient permafrost: insights from metagenomics. The ISME journal 11, 2305–2318.
Mann, P., Eglinton, T., McIntyre, C., Nikita, Z., Davydova, A., Vonk, J.E., Holmes, R.M., Spencer, R.G.M., 2015. Utilization of ancient permafrost carbon in headwaters of Arctic fluvial networks. Nat. Commun. 6, 7856.
Manley, W. F., 2002. Postglacial flflooding of the bering land bridge: a geospatial animation: INSTAAR, v1, University of Colorado, http://instaar.colorado.edu/QGISL/bering_land_bridge.
Mao, D., Tian, Y., Wang, Z., Jia, M., Du, J., Song, C., 2021. Wetland changes in the Amur River Basin: Differing trends and proximate causes on the Chinese and Russian sides. J. Environ. Manage. 280, 111670.
Marcer, M., Cicoira, A., Cusicanqui, D., Bodin, X., Echelard, T., Obregon, R., Schoeneich, P., 2021. Rock glaciers throughout the French Alps accelerated and destabilised since 1990 as air temperatures increased. Communications Earth & Environment 21, 81.
Martens, J., Wild, B., Pearce, C., Tesi, T., Andersson, A., Bröder, L., O'Regan, M., Jacobsson, M., Sköld, M., Gemery, L., Cronin, T. M., Semiletov, I., Dudarev, O.V., Gustafsson, Ö., 2019. Remobilization of old permafrost carbon to Chukchi Sea sediments during the end of the last deglaciation. Global Biogeochem. Cy. 33, 2–14.
Martens, J., Wild, B., Muschitiello, F., O'Regan, M., Jacobsson, M., Semiletov, I., Dudarev, O. V., Gustafsson, Ö., 2020. Remobilization of dormant carbon from Siberian-Arctic permafrost during three past warming events. Sci. Adv. 6, eabb6546.
Martens, J., Mueller, C.W., Joshi, P., Rosinger, C., Maisch, M., Kappler, A., Bonkowski, M., Schwamborn, G., Schirrmeister, L., Rethemeyery, J., 2023. Stabilization of mineral-associated organic carbon in Pleistocene permafrost. Nat. Commun. 14, 2120.
Marwick, T.R., Tamooh, F., Teodoru, C.R., Borges, A.V., Darchambeau, F., Bouillon, S., 2015. The age of river-transported carbon: a global perspective. Global Biogeochem. Cycles 29, 122–137.
Matsumoto, K., Kawamura, K., Uchida, M., Yasuyuki, S., Yoneda., M., 2001. Compound specific radiocarbon and $\delta^{13}C$ measurements of fatty acids in a continental aerosol sample. Geophys. Res. Lett. 28, 4587–4590.
Max, L., Riethdorf, J.-R., Tiedemann, R., Smirnova, M., Lembke-Jene, L., Fahl, K., Nürnberg, D., Matul, A., Mollenhauer, G., 2012. Sea surface temperature variability and sea-ice extent in the subarctic northwest Pacific during the past 15,000 years. Paleoceanography 27, PA3213.

Max, L., Lembke-Jene, L., Riethdorf, J.-R., Tiedemann, R., Nürnberg, D., 2014. Pulses of enhanced north Pacific intermediate water ventilation from the Okhotsk sea and Bering sea during the last deglaciation. Clim. Past 10, 591–605.

Mayorga, E., Aufdenkampe, A.K., Masiello, C.A., Krusche, A.V., Hedges, J.I., Quay, P.D., Richey, J.E., Brown, T.A., 2005. Young organic matter as a source of carbon dioxide outgassing from Amazonian rivers. Nature 436, 538–541.

McClelland, J.W., Déry, S.J., Peterson, B.J., Holmes, R.M., Wood, E.F., 2006. A pan-arctic evaluation of changes in river discharge during the latter half of the 20th century. Geophys. Res. Lett. 33, L06715.

McGuire, A.D., Anderson, L.A., Christensen, T.R., Dallimore, S., Guo, L., Hayes, D.J., Heimann, M., Lorenson, T.D., Macdonald, R.W., Roulet, N., 2009. Sensitivity of the carbon cycle in the Arctic to climate change. Ecol. Monogr. 79, 523–555.

McNichol, A., Ertel, J., Eglinton, T., 2000. The Radiocarbon Content of Individual Lignin-Derived Phenols: Technique and Initial Results. Radiocarbon 42, 219–227.

Mayer, L.M., 1994. Relationships between mineral surfaces and organic carbon concentrations in soils and sediments. Chem. Geol. 114, 347–363.

Méheust, M., Stein, R., Fahl, K., Max, L., and Riethdorf, J.R., 2016. High-resolution IP_{25}-based reconstruction of sea-ice variability in the western North Pacific and Bering Sea during the past 18,000 years. Geo-Mar. Lett. 36, 101–111,

Méheust, M., Stein, R., Fahl, K., and Gersonde, R., 2018. Sea-ice variability in the subarctic North Pacific and adjacent Bering Sea during the past 25 ka: new insights from IP_{25} and Uk'_{37} proxy records. Arktos 4, 1–19.

Menard, E., Allard, M., and Michaud, Y., 1998. Monitoring of ground surface temperatures in various biophysical micro-environments near Umiujaq, eastern Hudson Bay, Canada, in: vol. 57, Proceedings of the 7th International Conference on Permafrost, 23–27 June 1998, Yellowknife, Canada, Nordicana, edited by: Lewkowicz, A. G. and Allard, M., Univ. Laval, Quebec, Canada, 723–729.

Meyers, P.A. and Ishiwatari, R., 1993. Lacustrine organic geochemistry—an overview of indicators of organic matter sources and diagenesis in lake sediments. Org. Geochem. 20, 867–900.

Meyers, P.A., 1994. Preservation of elemental and isotopic source identification of sedimentary organic matter. Chemical Geology 114, 289-302.

Meyers, P.A., 1997. Organic geochemical proxies of paleoceanographic, paleolimnologic, and paleoclimatic processes. Org. Geochem. 27, 213–250.

Meyer, V.D., Max, L., Hefter, J., Tiedemann, R., Mollenhauer, G., 2016. Glacial-to-Holocene evolution of sea surface temperature and surface circulation in the subarctic northwest Pacific and the Western Bering Sea. Paleoceanography 31, 916–927.

Meyer, V.D., Hefter, J., Lohmann, G., Max, L., Tiedemann, R., Mollenhauer, G., 2017. Summer temperature evolution on the Kamchatka Peninsula, Russian Far East, during the past 20,000 years. Clim. Past 13, 359–377.

Meyer, V.D., Hefter, J., Köhler, P., Tiedemann, R., Gersonde, R., Wacker, L., Mollenhauer, G., 2019. Permafrost-carbon mobilization in Beringia caused by deglacial meltwater runoff, sea-level rise and warming. Environ. Res. Lett. 14, 085003.

Miner, K.R., D'Andrilli, J., Mackelprang, R., Edwards, A., Malaska, M.J., Waldrop, M.P., Miller, C.E., 2021. Emergent biogeochemical risks from Arctic permafrost degradation. Nature Climate Change 11, 809 - 819.

Mollenhauer, G., Grotheer, H., Gentz, T., Bonk, E., Hefter, J., 2021. Standard operation procedures and performance of the MICADAS radiocarbon laboratory at Alfred Wegener Institute (AWI), Germany. Nuclear Instruments and Methods in Physics Research Section B: Beam Interactions with Materials and Atoms 496, 45–51.

Monnin, E., Indermühle, A., Dällenbach, A., Flückiger, J., Stauffer, B., Stocker, T.F., Raynaud, D., Barnola, J.M., 2001. Atmospheric CO_2 concentrations over the last glacial termination. Science 291, 112–114.

Morley, J.J., Heusser, L.E., and Shackleton, N.J., 1991. Late Pleistocene/Holocene radiolarian and pollen records from sediments in the Sea of Okhotsk. Paleoceanography 6, 121–131.

Mudge, S.M., East, J.A., Bebianno, M.J., Barreira, L.A., 1998. Fatty acids in the Ria Formosa lagoon. Portugal. Org. Geochem. 29, 963–977.

Nakatsuka, T., Toda, M., Kawamura, K., and Wakatsuchi, M., 2004. Dissolved and particulate organic carbon in the Sea of Okhotsk: Transport from continental shelf to ocean interior. J. Geophys. Res. 109, C09S14.

Nitze, I., Grosse, G., Jones, B.M., Romanovsky, V.E., Boike, J., 2018. Remote sensing quantifies widespread abundance of permafrost region disturbances across the Arctic and Subarctic. Nat. Commun. 9, 5423.

Obu, J., Westermann, S., Bartsch, A., Berdnikov, N., Christiansen, H.H., Dashtseren, A., Delaloye, R., Elberling, B., Etzelmüller, B., Kholodov, A., Khomutov, A., Kääb, A., Leibman, M.O., Lewkowicz, A.G., Panda, S.K., Romanovsky, V., Way, R.G., Westergaard-Nielsen, A., Wu, T., Yamkhin, J., Zou, D., 2019. Northern Hemisphere permafrost map based on TTOP modelling for 2000–2016 at 1 km^2 scale. Earth-Sci. Rev. 193, 299–316.

Ogneva, O., Mollenhauer, G., Juhls, B., Sanders, T., Palmtag, J., Fuchs, M., Grotheer, H., Mann, P.J., Strauss, J., 2023. Particulate organic matter in the Lena River and its delta: from the permafrost catchment to the Arctic Ocean. Biogeosciences 20, 1423–1441.

Okazaki, Y., Katsunori, K., Hirofumi, A., Miyako, S., Yuriko, N., Naomi, H., 2014. Glacial to deglacial ventilation and productivity changes in the southern Okhotsk Sea. Palaeogeogr., Palaeoclimatol., Palaeoecol. 395, 53–66.

O'Leary, M.H., 1988. Carbon Isotopes in Photosynthesis: Fractionation techniques may reveal new aspects of carbon dynamics in plants. BioScience 38, 328–336.

Olefeldt, D., Goswami, S., Grosse, G., Hayes, D., Hugelius, G., Kuhry, P., McGuire, A.D., Romanovsky, V.E., Sannel, A.B.K., Schuur, E.A.G., Turetsky, M.R., 2016. Circumpolar distribution and carbon storage of thermokarst landscapes. Nature Commun. 7, 13043.

Opsahl, S. and Benner, R., 1995. Early diagenesis of vascular plant tissues: Lignin and cutin decomposition and biogeochemical implications. Geochim. Cosmochim. Acta 59, 4889–4904.

Otto, A., Shunthirasingham, C., Simpson, M.J., 2005. A comparison of plant and microbial biomarkers in grassland soils from the Prairie Ecozone of Canada. Org. Geochem. 36, 425–448.

Otto, A. and Simpson, M. J., 2005. Degradation and preservation of vascular plant-derived biomarkers in grassland and forest soils from Western Canada. Biogeochemistry 74, 377–409.

Otto, A. and Simpson, M. J., 2006. Evaluation of CuO oxidation parameters for determining the source and stage of lignin degradation in soil. Biogeochemistry 80, 121–142.

Overduin, P.P., Schneider von Deimling, T., Miesner, F., Grigoriev, M.N., Ruppel, C., Vasiliev, A., Lantuit, H., Juhls, B., Westermann, S., 2019. Submarine Permafrost Map in the Arctic Modeled Using 1-D Transient Heat Flux (SuPerMAP). J. Geophys. Res.: Oceans 124, 3490–3507.

Overland, J.E., Adams, J.M., Bond, N.A., 1999. Decadal Variability of the Aleutian Low and its Relation to High-Latitude Circulation. J. Clim. 12, 1542–1548.

Park, H., Walsh, J.E., Kim, Y., Nakai, T., Ohata, T., 2013. The role of declining Arctic sea ice in recent decreasing terrestrial Arctic snow depths. Polar Sci. 7, 174–187.

Parkes, R.J. and Taylor, J., 1983. The relationship between fatty acid distributions and bacterial respiratory types in contemporary marine sediments. Estuar. Coast. Shelf Sci. 16, 173–189.

Parkes., R.J., 1987. Analysis of microbial communities within sediments using biomarkers, in: Ecology of Microbial Communities, edited by: Fletcher, M., Gray, T.R.G., Jones, J.G., Cambridge University Press, London, 440 pp.

Pearson, A., McNichol, A.P., Benitez-Nelson, B.C., Hayes, J.M., Eglinton, T.I., 2001. Origins of lipid biomarkers in Santa Monica Basin surface sediment: a case study using compound-specific $\Delta^{14}C$ analysis. Geochim. Cosmochim. Acta. 65, 3123–3137.

Peltier, W.R., 2004. Global glacial isostasy and the surface of the ice-age earth: The ice-5G (VM2) model and grace. Annu. Rev. Earth Planet Sci. 32, 111–149.

Pendleton, S.L., Ceperley, E.G., Briner, J.P., Kaufman, D.S., Zimmerman, S., 2015. Rapid and early deglaciation in the central Brooks Range, Arctic Alaska. Geology 43, 419-422.

Peterson, B.J., Holmes, R.M., McClelland, J.W., Vörösmarty, C.J., Lammers, R.B., Shiklomanov, A.I., Shiklomanov, I.A., Rahmstorf, S., 2002. Increasing river discharge to the Arctic Ocean. Science 298, 2171–2173.

Pickart, R.S., Macdonald, A.M., Moore, G.W.K., Renfrew, I.A., Walsh, J.E., Kessler, W.S., 2009. Seasonal Evolution of Aleutian Low Pressure Systems: Implications for the North Pacific Subpolar Circulation. J. Phys. Oceanography 39, 1317–1339.

Pico, T., Mitrovica, J.X., Mix, A.C., 2020. Sea level fingerprinting of the Bering Strait flooding history detects the source of the Younger Dryas climate event. Sci. Avd. 6, eaay2935.

Pittauer, D., Tims, S.G., Froehlich, M.B., Fifield, L.K., Wallner, A., McNeil, S.D., Fischer, H.W., 2017. Continuous transport of Pacific-derived anthropogenic radionuclides towards the Indian Ocean. Scientific reports 7, 44679.

Praetorius, S.K., Mix, A.C., Walczak, M.H., Wohowe, M.D., Addison, J.A., Prahl, F. G., 2015. North Pacific deglacial hypoxic events linked to abrupt ocean warming. Nature 527, 362–366.

Rachold, V., Grigoriev, M.N., Are, F.E., Solomon, S., Reimnitz, E., Kassens, H., Antonow, M., 2000. Coastal erosion vs riverine sediment discharge in the Arctic Shelf seas. Int. J. Earth Sci. 89, 450–460.

Rantanen, M., Karpechko, A.Y., Lipponen, A., Nording, K., Hyvärinen, O., Ruosteenoja, K., Vihma, T., Laaksonen, A., 2022. The Arctic has warmed nearly four times faster than the globe since 1979. Commun. Earth Environ. 3, 168.

Rasmussen, S.O., Seierstad, I.K., Andersen, K.K., Bigler, M., Dahl-Jensen, D., Johnsen, S.J., 2008. Synchronization of the NGRIP, GRIP, and GISP2 ice cores across MIS 2 and palaeoclimatic implications. Quat. Sci. Rev. 27, 18–28.

Raymond, P.A., McClelland, J.W., Holmes, R.M., Zhulidov, A.V., Mull, K., Peterson, B.J., Striegl, R.G., Aiken, G.R., Gurtovaya, T.Y., 2007. Flux and age of dissolved organic carbon exported to the Arctic Ocean: a carbon isotopic study of the five largest arctic rivers. Global Biogeochem. Cycles 21, GB4011.

Raymond, P.A., Hartmann, J., Lauerwald, R., Sobek, S., McDonald, C., Hoover, M., Butman, D., Striegl, R., Mayorga, E., Humborg, C., Kortelainen, P., Dürr, H., Meybeck, M., Ciais, P., Guth, P., 2013. Global carbon dioxide emissions from inland waters. Nature 503, 355–359.

Repasch, M., Scheingross, J.S., Hovius, N., Lupker, M., Wittmann, H., Haghipour, N., Gröcke, D.R., Orfeo, O., Eglinton, T.I., Sachse, D., 2021. Fluvial organic carbon cycling regulated by sediment transit time and mineral protection. Nat. Geosci. 14, 842–848.

Revenga, C., Murray, S., Abramovitz, J., Hammond, A., 1998. Watersheds of the World: Ecological Value and Vulnerability, World Resources Institute and Worldwatch Institute, Washington, D. C.

Rieley, G., Coller, R.J., Jones, D.M., Eglinton, G., 1991. The biogeochemistry of Ellesmere Lake, U.K.—I: source correlation of leaf wax inputs to the sedimentary lipid record. Org. Geochem. 17, 901–912.

Riethdorf, J.-R., Max, L., Nürnberg, D., Lembke-Jene, L., Tiedemann, R., 2013. Deglacial history of (sub) sea surface temperatures and salinity in the subarctic NW Pacific: implications for upper-ocean stratification. Paleoceanography 28, 91–104.

Ruben, M., Hefter, J., Schubotz, F., Geibert, W., Butzin, M., Gentz, T., Grotheer, H., Forwick, M., Szczuciński, W., Mollenhauer, G., 2023. Fossil organic carbon utilization in marine Arctic fjord sediments by subsurface micro-organisms. Nature Geoscience 16, 625–630.

Schefuß, E., Eglinton, T.I., Spencer-Jones, C.L., Rullkötter, J., de Pol-Holz, R., Talbot, H.M., Grootes, P.M., Schneider, R.R., 2016. Hydrologic control of carbon cycling and aged carbon discharge in the Congo River basin. Nat. Geosci. 9, 687–690.

Schirrmeister, L., Kunitsky, V., Grosse, G., Wetterich, S., Meyer, H., Schwamborn, G., Babiy, O., Derevyagin, A., Siegert, C., 2010. Sedimentary characteristics and origin of the Late Pleistocene Ice Complex on north east Siberian Arctic coastal lowlands and islands-A review. Quat. Int. 241, 3–25.

Schirrmeister, L., Grosse, G., Wetterich, S., Overduin, P.P., Strauss, J., Schuur, E.A.G., Hubberten, H.-W., 2011. Fossil organic matter characteristics in permafrost deposits of the northeast Siberian Arctic. J. Geophys. Res. 116, G00M02.

Schirrmeister, L., Froese, D., Tumskoy, V., Grosse, G., Wetterich, S., 2013. Yedoma: Late Pleistocene Ice-Rich Syngenetic Permafrost of Beringia, in: The Encyclopedia of Quaternary Science, edited by: Elias, S.A., Elsevier, Amsterdam, 542–552.

Schmidt, M.W.I., Torn, M.S., Abiven, S., Dittmar, T., Guggenberger, G., Janssens, I.A., Kleber, M., Kögel-Knabner, I., Lehmann, J., Manning, D.A.C., Nannipieri, P., Rasse, D.P., Weiner, S., Trumbore, S.E., 2011. Persistence of soil organic matter as an ecosystem property. Nature 478, 49–56.

Schneider von Deimling, T., Grosse, G., Strauss, J., Schirrmeister, L., Morgenstern, A., Schaphoff, S., Meinshausen, M., Boike, J., 2015. Observation-based modelling of permafrost carbon fluxes with accounting for deep carbon deposits and thermokarst activity. Biogeosciences 12, 3469–3488.

Schouten, S., Hopman, E.C., Schefuß, E., Sinninghe Damsté, J.S., 2002. Distributional variations in marine crenarchaeotal membrane lipids: A new tool for reconstructing ancient sea water temperatures? Earth Planet. Sci. Lett. 204, 265–274.

Schubert, C.J. and Calvert, S.E., 2001. Nitrogen and carbon isotopic composition of marine and terrestrial organic matter in Arctic Ocean sediments: implications for nutrient utilization and organic matter composition. Deep Sea Res., Part I 48, 789–810.

Schuur, E.A.G., Bockheim, J., Canadell, J.G., Euskirchen, E., Field, C.B., Goryachkin, S.V., Hagemann, S., Kuhry, P., Lafleur, P.M., Lee, H., Mazhitova, G., Nelson, F.E., Rinke, E., Romanovsky, V.E., Shiklomanov, N., Tarnocai, C., Venevsky, S., Vogel, J.G., Zimov, S.A., 2008. Vulnerability of permafrost carbon to climate change: Implications for the global carbon cycle. Bioscience 58, 701–714.

Schuur, E.A.G., McGuire, A.D., Schadel, C., Grosse, G., Harden, J.W., Hayes, D.J., Hugelius, G., Koven, C.D., Kuhry, P., Lawrence, D.M., Natali, S.M., Olefeldt, D., Romanovsky, V.E., Schaefer, K., Turetsky, M.R., Treat, C.C., Vonk, J.E., 2015. Climate change and the permafrost carbon feedback. Nature 520, 171–179.

Schuur, E.A.G., Abbott, B.W., Commane, R., Ernakovich, J., Euskirchen, E., Hugelius, G., Grosse, G., Jones, M., Koven, C., Leshyk, V., Lawrence, D., Loranty, M.M., Mauritz, M., Olefeldt, D., Natali, S., Rodenhizer, H., Salmon, V., Schädel, C., Strauss, J., Treat, C., Turetsky, M., 2022. Permafrost and Climate Change: Carbon Cycle Feedbacks From the Warming Arctic. United States.

Schweger, C., Froese, D., White, J. M., Westgate, J. A., 2011. Preglacial and interglacial pollen records over the last 3 Ma from northwest Canada: Why do Holocene forests differ from those of previous interglaciations? Quat. Sci. Rev. 30, 2124–2133.

Scribe, P., Fillaux, J., Laureillard, J., Denant, V., Saliot, A., 1991. Fatty acids as biomarkers of planktonic inputs in the stratified estuary of the Krka river, Adriatic Sea: relationship with pigments. Mar. Chem. 32, 299–312.

Seki, O., Harada, N., Sato, M., Kawamura, K., Ijiri, A., and Nakatsuka, T., 2012. Assessment for paleoclimatic utility of terrestrial biomarker records in the Okhotsk Sea sediments. Deep-Sea Res. Pt. II, 61–64, 85–92.

Seki, O., Mikami, Y., Nagao, S., Bendle, J.A., Nakatsuka, T., Kim, V. I., Shesterkin, V.P., Makinov, A.N., Fukushima, M., Mossen, H.M., and Schouten, S., 2014a. Lignin phenols and BIT index distribution in the Amur River and the Sea of Okhotsk: Implications for the source and transport of particulate terrestrial OC to the Ocean. Prog. Oceanogr. 126, 146–154.

Seki, O, Bendle, J.A., Harada, N., Kobayashi, M., Sawada, K., Moossen, H., Inglis, G. N., Nagao, S., and Sakamoto, T., 2014b. Assessment and calibration of TEX86 paleothermometry in the Sea of Okhotsk and sub-polar North Pacific region: Implications for paleoceanography. Prog. Oceanogr. 126, 254–266.

Semiletov, I.P., Shakhova, N., Pipko, I.I., Pugach, S., Charkin, A.N., Dudarev, O.V., Kosmach, D., Nishino, S., 2013. Space−time dynamics of carbon and environmental parameters related to carbon dioxide emissions in the Buor-Khaya Bay and adjacent part of the Laptev Sea. Biogeosciences 10, 5977–5996.

Shah, S.R., Mollenhauer, G., Ohkouchi, N., Eglinton, T.I., Pearson, A., 2008. Origins of archaeal tetraether lipids in sediments: insights from radiocarbon analysis. Geochim. Cosmochim. Acta. 72, 4577–4594.

Shakun, J.D., Clark, P.U., He, F., Marcott, S.A., Mix, A.C., Liu, Z., Otto-Bliesner, B., Schmittner, A., Bard, E., 2012. Global warming preceded by increasing carbon dioxide concentrations during the last deglaciation. Nature 484, 49–54.

Shin, Y. and Jung, H., 2015. Assessing uncertainty in future climate change in Northeast Asia using multiple CMIP5 GCMs with four RCP scenarios. J. Environ. Impact Assess. 24, 205–216.

Smith, C.A.S., Burn, C.R., Tarnocai, C., and Sproule, B., 1998. Air and soil temperature relations along an ecological transect through the permafrost zones of northwestern Canada, in: vol. 57, Proceedings of the 7th International Conference on Permafrost, Yellowknife, Canada, Nordicana, 23–27 June 1998, edited by Lewkowicz, A. G., and Allard, M., Univ. Laval, Quebec, Canada, 1009–1015.

Smith, J.C., Galy, A., Hovius, N., Tye, A.M., Turowski, J.M., Schleppi, P., 2013. Runoff-driven export of particulate organic carbon from soil in temperate forested uplands. Earth Planet. Sci. Lett. 365, 198-208.

Smith, S.L., O'Neill, H.B., Isaksen, K., Noetzli, J., Romanovsky, V.E., 2022. The changing thermal state of permafrost. Nat. Rev. Earth Environ. 3, 10–23.

Smittenberg, R.H., Hopmans, E.C., Schouten, S., Sinninghe Damsté., J.S., 2002. Rapid isolation of biomarkers for compound specific radiocarbon dating using high-performance liquid chromatography and flow injection analysis–atmospheric pressure chemical ionisation mass spectrometry. J. Chromatogr. A. 978, 129–140.

Stabeno, P.J., Bond, N.A., Kachel, N.B., Salo, S.A., Schumacher, J.D., 2001. On the temporal variability of the physical environment over the south-eastern Bering Sea. Fish. Oceanogr. 10, 81–98.

Stapel, J.G., Schwamborn, G., Schirrmeister, L., Horsfield, B., and Mangelsdorf, K., 2018. Substrate potential of last interglacial to Holocene permafrost organic matter for future microbial greenhouse gas production. Biogeosciences 15, 1969–1985.

Strauss, J., Schirrmeister, L., Grosse, G., Wetterich, S., Ulrich, M., Herzschuh, U., Hubberten, H.-W., 2013. The deep permafrost carbon pool of the Yedoma region in Siberia and Alaska. Geophys. Res. Lett. 40, 6165–6170.

Strauss, J., Schirrmeister, L., Grosse, G., Fortier, D., Hugelius, G., Knoblauch, C., Romanovsky, V., Schädel, C., Schneider von Deimling, T., Schuur, E.A.G., Shmelev, D., Ulrich, M., Veremeeva, A., 2017. Deep Yedoma permafrost: A synthesis of depositional characteristics and carbon vulnerability. Earth-Sci. Rev. 172, 75–86.

Strauss, J., Laboor, S., Schirrmeister, L., Fedorov, A.N., Fortier, D., Froese, D., Fuchs, M., Günther, F., Grigoriev, M., Harden, J., Hugelius, G., Jongejans, L.L., Kanevskiy, M., Kholodov, A., Kunitsky, V., Kraev, G., Lozhkin, A., Rivkina, E., Shur, Y., Siegert, C., Spektor, V., Streletskaya, I., Ulrich, M., Vartanyan, S., Veremeeva, A., Anthony, K.W., Wetterich, S., Zimov, N., Grosse, G., 2021. Circum-Arctic Map of the Yedoma Permafrost Domain. Front. Earth Sci. 9, 758360.

Stuiver, M. and Polach, H.A., 1977. Reporting of C-14 data—Discussion. Radiocarbon 19, 355–363.

Stuiver, M. and Reimer, P.J., 1993. Extended ^{14}C database and revised CALIB radiocarbon calibration program. Radiocarbon 35, 215–230.

Sun, S., Schefuβ, E., Mulitza, S., Chiessi, C. M., Sawakuchi, A.O., Zabel, M., Baker, P. A., Hefter, J., Mollenhauer, G., 2017. Origin and processing of terrestrial organic carbon in the Amazon system: lignin phenols in river, shelf, and fan sediments. Biogeosciences 14, 2495–2512.

Sun, S., Meyer, V.D., Dolman, A., Winterfeld, M., Hefter, J., Dummann, W., Mollenhauer, G., 2020. ^{14}C Blank Assessment in Small-Scale Compound-Specific Radiocarbon Analysis of Lipid Biomarkers and Lignin Phenols. Radiocarbon 62, 207–218.

Synal, H.-A., Stocker, M., Suter, M., 2007. MICADAS: A new compact radiocarbon AMS system, Nucl. Instruments Methods Phys. Res. Sect. B Beam Interact. with Mater. Atoms. 259, 7–13.

Tananaev, N., Makarieva, O., Lebedeva, L., 2016. Trends in annual and extreme flows in the Lena River basin, Northern Eurasia. Geophys. Res. Lett. 43, 10764–10772.

Tarasov, P. E., Bezrukova, E. V., and Krivonogov, S. K., 2009. Late Glacial and Holocene changes in vegetation cover and climate in southern Siberia derived from a 15 kyr long pollen record from Lake Kotokel. Clim. Past 5, 285–295.

Tarnocai, C., Canadell, J. G., Schuur, E. A. G., Kuhry, P., Mazhitova, G., Zimov, S., 2009. Soil organic carbon pools in the northern circumpolar permafrost region. Global Biogeochem. Cy. 23, GB2023.

Tesi, T., Langone, L., Goñi, M.A., Wheatcroft, R.A., Miserocchi, S., Bertotti, L., 2012. Early diagenesis of recently deposited organic matter: A 9-yr time-series study of a flood deposit. Geochim. Cosmochim. Acta 83, 19–36.

Tesi, T., Semiletov, I., Hugelius, G., Dudarev, O., Kuhry, P., Gustafsson, Ö., 2014. Composition and fate of terrigenous organic matter along the Arctic land–ocean continuum in East Siberia: Insights from biomarkers and carbon isotopes, Geochim. Cosmochim. Acta 133, 235–256.

Tesi, T., Muschitiello, F., Smittenberg, R. H., Jakobsson, M., Vonk, J. E., Hill, P., Andersson, A., Kirchner, N., Noormets, R., Dudarev, O., Semiletov, I., Gustafsson, Ö., 2016. Massive remobilization of permafrost carbon during post-glacial warming. Nat. Commun. 7, 13653.

Thevenot, M., Dignac, M. F., Rumpel, C., 2010. Fate of lignins in soils: a review. Soil Biol. Biochem. 42, 1200–1211.

Tierney, J.E., Poulsen, C.J., Montañez, I.P., Bhattacharya, T., Feng, R., Ford, H.L., Hönisch, B., Inglisy, G.N., Petersen, S.V., Sagoo, N., Tabor, C.R., Thirumalai, K., Zhu, J., Burls, N.J., Foster, G.L., Goddéris, Y., Huber, B.T., Ivany, L.C., Kirtland Turner, S., Lunt, D.J., McElwain, J.C., Mills, B.J.W., Otto-Bliesner, B.L., Ridgwell, A., Zhang, Y.G., 2020. Past climates inform our future. Science 370, 6517.

Tieszen, L.L. and Boutton, T.W., 1989. Stable carbon isotopes in terrestrial ecosystem research//Rundel PW, Ehleringer JR, Nagy KA. Stable Isotopes in Ecological Research. Springer-Verlag, New York. 167–195.

Toniolo, H., Kodial, P.S., Hinzman, L.D., Yoshikawa, K., 2009. Spatio-temporal evolution of a thermokarst in Interior Alaska. Cold Reg. Sci. Technol. 56, 39–49.

Torres, M.A., Kemeny, P.C., Lamb, M.P., Cole, T.L., Fischer, W.W., 2020. Long-term storage and age-biased export of fluvial organic carbon: fled evidence from west Iceland. Geochem. Geophys. Geosyst. 21, e2019GC008632.

Turetsky, M.R., Abbott, B.W., Jones, M.C., Anthony, K.W., Olefeldt, D., Schuur, E.A.G., Grosse, G., Kuhry, P., Hugelius, G., Koven, C., Lawrence, D.M., Gibson, C., Sannel, A.B.K., McGuire, A.D., 2020. Carbon release through abrupt permafrost thaw. Nat. Geosci. 13, 138–143.

Uchikawa, J., Popp, B.N., Schoonmarker, J.E., Xu, L., 2008. Direct application of compound-specific radiocarbon analysis of leaf waxes to establish lacustrine sediment chronology. J. Paleolimnol. 39, 43–60.

Vaks, A., Gutareva, O.S., Breitenbach, S.F.M., Avirmed, E., Mason, A.J., Thomas, A.L., Osinzev, A.V., Kononov, A.M., Henderson, G.M., 2013. Speleothems Reveal 500,000-year history of Siberian Permafrost. Science 340, 183–186.

Vaks, A., Mason, A.J., Breitenbach, S.F.M., Kononov, A.M., Osinzev, A.V., Rosensaft, M., Borshevsky, A., Gutareva, O.S., Henderson, G.M., 2020. Palaeoclimate evidence of vulnerable permafrost during times of low sea ice. Nature 577, 221–225.

Vandenberghe, J., Renssen, H., Roche, D. M., Goosse, H., Velichko, A.A., Gorbunov, A., Levavasseur, G., 2012. Eurasian permafrost instability constrained by reduced sea-ice cover. Quat. Sci. Rev. 34, 16–23.

Vandenberghe, J., French, H.M., Gorbunov, A., Marchenko, S., Velichko, A.A., Jin, H., Cui, Z., Zhang, T., Wan, X., 2014. The Last Permafrost Maximum (LPM) map of the Northern Hemisphere: permafrost extent and mean annual air temperatures, 25–17 ka BP. Boreas 43, 652–666.

van der Voort, T.S., Zell, C., Hagedorn, F., Feng, X., McIntyre, C.P., Haghipour, N., Graf Pannatier, E., Eglinton, T.I., 2017. Diverse Soil Carbon Dynamics Expressed at the Molecular Level. Geophys. Res. Lett. 44, 11840–11850.

Venturini, N., Salhi, M., Bessonart, M., Pires-Vanin, A.M.S., 2012. Fatty acid biomarkers of organic matter sources and early diagenetic signatures in sediments from a coastal upwelling area (south-eastern Brazil). Chem. Ecol. 28, 221–238.

Viau, A. E., Gajewski, K., Sawada, M. C., Bunbury, J., 2008. Low- and high-frequency climatevariability in eastern Beringia during the past 25 000 years, Can. J. Earth Sci. 45, 1435–1453.

Villinski, J.C., Hayes, J.M., Brassell, S.C., Riggert, V.L., Dunbar, R.B., 2008. Sedimentary sterols as biogeochemical indicators in the Southern Ocean. Org. Geochem. 39, 567–588.

Voigt, C., Marushchak, M.E., Abbott, B.W., Biasi, C., Elberling, B., Siciliano, S.D., Sonnentag, O., Stewart, K.J., Yang, Y., Martikainen, P.J., 2020. Nitrous oxide emissions from permafrost-affected soils. Nat. Rev. Earth Environ. 1, 420–434.

Volkman, J.K., Johns, R.B., Gillan, F.T., Perry, G.J., 1980. Microbial lipids of an intertidal sediment-I. Fatty acids and hydrocarbons. Geochim. Cosmochim. Acta 44, 1133–1143.

Volkman, J.K., Jeffrey, S.W., Nichols, P.D., Rogers, G.I., Garland, C.D., 1989. Fatty acid and lipid composition of 10 species of microalgae used in mariculture. J. Exp. Mar. Bio. Ecol. 128, 219–240.

Vonk, J.E., Sánchez-García, L., Dongen, B.E., Alling, V., Kosmach, D., Charkin, A.N., Semiletov, I.P., Dudarev, O.V., Shakhova, N., Roos, P., Eglinton, T.I., Andersson, A., Gustafsson, Ö., 2012. Activation of old carbon by erosion of coastal and subsea permafrost in Arctic Siberia. Nature 489, 137–140.

Wacker, L., Christl, M., Synal., H., 2010. Bats: A new tool for AMS data reduction. Nuclear Instruments & Methods in Physics Research Section B-beam Interactions With Materials and Atoms. 268, 976–979.

Wacker, L. and Christl, M., 2011. Data reduction for small radiocarbon samples–error propagation using the model of constant contamination. Ion Beam Physics Annual Report, 36.

Wacker, L., Fahrni, S.M., Hajdas, I., Molnar, M., Synal, H.-A., Szidat, S., Zhang, Y.L., 2013. A versatile gas interface for routine radiocarbon analysis with a gas ion source. Nuclear Instruments and Methods in Physics Research Section B: Beam Interactions with Materials and Atoms. 294, 315–319.

Washburn, A.L., 1980. Permafrost Features as Evidence of Climatic Change. Earth-Sci. Rev. 15, 327–402.

Walter, K. M., Zimov, S. A., Chanton, J. P., Verbyla, D., Chapin III, F. S., 2006. Methane bubbling from Siberian thaw lakes as a positive feedback to climate warming. Nature 443, 71–75.

Walter, K.M., Edwards, M.E., Grosse, G., Zimov, S.A., Chapin III, F.S., 2007. Thermokarst lakes as a source of atmospheric CH_4 during the last deglaciation. Science 318, 633–636.

Walter Anthony, K.W., Zimov, S., Grosse, G., Jones, M.C., Anthony, P., Chapin, F.S., Finlay, J.C., Mack, M.C., Davydov, S.P., Frenzel, P., Frolking, S., 2014. A shift of thermokarst lakes from carbon sources to sinks during the Holocene epoch. Nature 511, 452–456.

Wang, R., Kuhn, G., Gong, X., Biskabrn, B. K., Gersonde, R., Lembke-Jene, L., Lohmann, G., Tiedemann, R., Diekmann, B., 2021. Deglacial land-ocean linkages at the Alaskan continental margin in the Bering Sea. Front. Earth Sci. 9, 712415.

Wegner, C., Bennett, K.E., de Vernal, A., Forwick, M., Fritz, M., Heikkilä, M., Łącka, M., Lantuit, H., Laska, M., Moskalik, M., O'Regan, M., Pawłowska, J., Promińska, A., Rachold, V., Vonk, J.E., Werner, K., 2015. Variability in transport of terrigenous material on the shelves and the deep Arctic Ocean during the Holocene. Polar Res. 34.

Weijers, J.W.H., Schouten, S., Hopmans, E.C., Geenevasen, J.A.J., David, O.R.P., Coleman, J.M., Pancost, R.D., Sinninghe Damsté, J.S., 2006a. Membrane lipids of mesophilic anaerobic bacteria thriving in peats have typical archaeal traits. Environ. Microbiol. 8, 648–657.

Weijers, J.W.H., Schouten, S., Spaargaren, O.C., Sinninghe Damsté, J.S., 2006b. Occurrence and distribution of tetraether membrane lipids in soils: Implications for the use of the TEX_{86} proxy and the BIT index. Org. Geochem. 37, 1680–1693.

Weijers, J.W.H., Schouten, S., van den Donker, J.C., Hopmans, E.C., Sinninghe Damsté, J.S., 2007. Environmental controls on bacterial tetraether membrane lipid distribution in soils. Geochim. Cosmochim. Acta 71, 703–713.

Wen, K., Gao, B., Li, M., 2021. Quantifying the Impact of Future Climate Change on Runoff in the Amur River Basin Using a Distributed Hydrological Model and CMIP6 GCM Projections. Atmosphere 12,1560.

Wiesenberg, G.L.B., Schwarzbauer, J., Schmidt, M.W.I., Schwark, L., 2008. Plant and soil lipid modification under elevated atmospheric CO_2 conditions: II. Stable carbon isotopic values ($\delta^{13}C$) and turnover. Org. Geochem. 39, 103–117.

Wild, B., Shakhova, N., Dudarevx, O., Ruban, A., Kosmach, D., Tumskoy, V., Tesi, T., Grimm, H., Nybom, I., Matsubara, F., Alexanderson, H., Jakobsson, M., Mazurov, A., Semiletov, I., Gustafsson, Ö., 2022. Organic matter composition and greenhouse gas production of thawing subsea permafrost in the Laptev Sea. Nat. Commun. 13, 5057.

Williams, C.J., Yavitt, J.B., Kelman Wieder, R., Cleavitt, N.L., 1998. Cupric oxide oxidation products of northern peat and peat-forming plants. Can. J. Bot. 76, 51–62.

Winterfeld, M., Goñi, M.A., Just, J., Hefter, J., Mollenhauer, G., 2015. Characterization of particulate organic matter in the Lena River delta and adjacent nearshore zone, NE Siberia–Part 2: Lignin-derived phenol compositions. Biogeosciences 12, 2261–2283.

Winterfeld, M., Mollenhauer, G., Dummann, W., Köhler, P., Lembke-Jene, L., Meyer, V. D., Hefter, J., Mclntyre, C., Wacker, L., Kokfelt, U., Tiedemann, R., 2018. Deglacial mobilization of pre-aged terrestrial carbon from degrading permafrost. Nat. Commun. 9, 3666.

Wong, C.S., Matear, R.J., Freeland, H.J., Whitney, F.A., Bychkov, A.S., 1998. WOCE line P1W in the Sea of Okhotsk 2. CFCs and the formation rate of intermediate water. J. Geophys. Res. 103, 15625–15642.

Wu, J., Mollenhauer, G., Stein, R., Köhler, P., Hefter, J., Fahl, K., Grotheer, H., Wei, B., Nam, S., 2022. Deglacial release of petrogenic and permafrost carbon from the Canadian Arctic impacting the carbon cycle. Nat. Commun. 13, 7172.

Xu, C., Guo, L., Ping, C.L., White, D.M., 2009. Chemical and isotopic characterization of sizefractionated organic matter from cryoturbated tundra soils, northern Alaska. J. Geophys. Res. 114, G03002.

Yang, D., Marsh, P., Ge, S., 2014. Heat flux calculations for Mackenzie and Yukon Rivers. Polar Sci. 8, 232–241.

Yang, X., Zhou, B., Xu, Y., Han, Z., 2021. CMIP6 Evaluation and Projection of Temperature and Precipitation over China. Adv. Atmos. Sci. 38, 817–830.

Ye, B., Yang, D., Kane, D.L., 2003. Changes in Lena River streamflow hydrology: Human impacts versus natural variations. Water resources research 39(7).

Yu, S.-H., Zheng, Z., Kershaw, P., Skrypnikova, M., Huang, K.-Y., 2017. A late Holocene record of vegetation and fire from the Amur Basin, far-eastern Russia. Quatern. Int. 432, 79–92.

Zazula, G.D., Schweger, C.E., Beaudoin, A.B., McCourt, G.H., 2006. Macrofossil and pollen evidence for full-glacial steppe within an ecological mosaic along the Bluefish River, eastern Beringia. Quatern. Int. 142–143, 2–16.

Zhang, T., Frauenfeld, O., Serreze, M., Etringer, A., Oelke, C., McCreight, J., Barry, R., Gilichinsky, D., Yang, D., Ye, H., Ling, F., Chudinova, S., 2005. Spatial and temporal variability in active layer thickness over the Russian Arctic drainage basin. J Geophys. Res. 110, D16101.

Zhou, S., Zhang, W., Guo, Y., 2019. Impacts of Climate and Land-Use Changes on the Hydrological Processes in the Amur River Basin. Water 12, 76.

Zimmerman, A.R. and Canuel., E.A., 2001. Bulk organic matter and lipid biomarker composition of Chesapeake Bay surficial sediments as indicators of environmental processes. Estuar. Coast. Shelf Sci. 53, 319–341.

Zimov, S.A., Schuur, E.A.G., Chapin, F.S., 2006. Permafrost and the global carbon budget. Science 312, 1612–1613.